Inaugural Dissertation

for

Obtaining a Doctoral Degree

of the

Combined Faculty of Mathematics, Engineering and Natural Sciences

of the

Ruprecht - Karls - University

Heidelberg

Presented by

M.Sci Fergus Tollervey
Born in: Bandar Seri Begawan, Brunei

Oral examination: 13-12-2023

Architecture of *C. elegans* Centrosomes as Revealed by Cryo-Electron Tomography

Referees:

Prof. Dr. Gislene Pereira

Dr. Yannick Schwab

Table of Contents

Summary 8

Zusammenfassung 10

Introduction 12

1.1 The centrosome: the anchor of mitosis 12

1.2 The centrioles: a structured regulatory keystone 16

1.3 The centriole cycle 20

1.4 The interphase centrosome 22

1.5 Centrosome maturation and disassembly 24

1.6 The supramolecular structure of the PCM 26

1.7 The role of gamma tubulin 29

1.8 Organization of microtubules at the centrosome 31

1.9 *C. elegans* microtubules 32

1.10 A minimal centrosome system 33

1.11 Cryo-electron tomography – advantages and disadvantages 35

1.12 Sample preparation: vitrification 37

1.13 Sample preparation: cryo-correlative microscopy 40

1.14 Sample preparation: cryo-focused ion beam milling 41

1.15 Sample preparation: cryo-lift out 44

1.16 Data collection: transmission electron microscopy image formation 45

1.17 Data collection: tilt series acquisition and tomographic reconstruction 47

1.18 Data analysis: denoising 49

1.19 Data analysis: segmentation 50

1.20 Data analysis: subtomogram averaging and CTF estimation. 51

1.21 Data analysis: protein structure prediction 53
2. Project motivation and open questions 55
3. Methods 57
3.1 Reagents, media, strains, equipment, and software 57
3.2 Sample preparation of protein condensates 61
3.3 Sample preparation of microtubule asters 63
3.4 Embryonic cell dissociation 65
3.5 Room temperature light microscopy 67
3.6 Plunge freezing of embryonic cells 68
3.7 Cryo-confocal microscopy 68
3.8 Cryo-focused ion beam milling 69
3.9 Cryo-ET data collection 70
3.10 Tomogram reconstruction and denoising 71
3.11 Segmentation of microtubules, centrioles, ribosomes, and membranes 72
3.12 Analysis of centrosomal zones 73
3.13 Subtomogram averaging of microtubules 74
3.14 Centriole analysis 76
3.15 Centriole subtomogram averaging 76
3.16 Gamma-TuRC subtomogram averaging 77
3.17 Subtomogram averaging of ribosomes 77
3.18 Matrix analysis 78
4. Results 80
4.1 Cryo-electron tomography of centrosomal protein condensates and asters. 80
4.2 Optimization of cell dissociation, sample preparation, and data acquisition. 89
4.3 Architectural features of the interphase centrosome 96

4.4 Architectural features of the expanded, mitotic centrosome 102
4.5 The mother and daughter centrioles display prominent structural differences 108
4.6 Microtubule organization within the centrosome 116
4.7 *C. elegans* gamma tubulin ring complexes 121
4.8 Identification of the centrosomal matrix 127
4.9 Properties of the centrosomal matrix 132
5. Discussion 143
5.1 Microtubule asters have differing architectures from *in-situ* centrosomes . 143
5.2 Dissociated cells are a viable sample for cryo-ET 145
5.3 Centrosome architecture is delineated by microtubules and gamma-TuRCs 149
5.4 Centrioles display structural heterogeneity 153
5.5 The centrosome consists of a gel-like porous meshwork 156
6. Concluding remarks 161
Contributions 163
Acknowledgments 164
List of abbreviations 166
References 168

Summary

The centrosome is an organelle responsible for the separation of DNA during mitosis in most animal cells. It consists of a pair of microtubule-based centrioles surrounded by a layer of proteinaceous Peri-Centriolar Material (PCM), responsible for polymerizing and organizing microtubules, especially in the context of the mitotic spindle. Despite decades of research, the fine molecular architecture of the centrosome, and the PCM in particular, has remained unclear. The nematode *C. elegans*, having relatively simple centrosomes, is a good well-characterized model for their study. A minimal *C. elegans* centrosome has even been reconstituted *in vitro*, with microtubules being concentrated from purified centrosomal protein into so-called asters. In this thesis, I aimed to characterize the structures within *C. elegans* centrosomes, and in doing so better understand this key organelle. To this end I made use of cryo-electron tomography (cryo-ET), which can reveal cellular structures at molecular resolution in their native state.

The data in this thesis shows that microtubule asters, although posing interesting questions about how microtubules form, are insufficient on their own to act as a model for centrosomal function. Simultaneously, I demonstrate that embryonic cells dissociated from the native embryo remain viable and are a suitable sample for cryo-ET analysis, as they are small enough to be vitrified through plunge freezing and can then be milled down to the desired thickness through use of a Focused Ion Beam (FIB). I then make use of correlative light approaches to find the centrosome inside these milled cells. Within the centrosome, I see a high level of microtubule organization, likely templated by the function of gamma-TuRC complexes which were averaged into a coherent structure. The centrioles seen within these centrosomes contained unexpected features and structural variation, which hints at the specification of their biological functions. The centrosomes themselves were divided into architectural zones: with centrioles at the heart of the organelle, surrounded by

a microtubule excluded zone and then a ribosome excluded zone. These zones contained a gel-like meshwork of PCM which functions as a selective barrier for centrosomal client proteins. Thus, my thesis builds a three-dimensional structural atlas that helps explain how centrosomes assemble, grow, and achieve function.

Zusammenfassung

Das Zentrosom ist eine Organelle, die in den meisten tierischen Zellen für die Trennung der DNA während der Mitose verantwortlich ist. Es setzt sich aus einem Paar Zentriolen zusammen, die aus Mikrotubuli bestehen und von einer Schicht proteinhaltigem perizentriolärem Material (PZM) umgeben sind, die für die Polymerisation und Organisation der Mikrotubuli verantwortlich ist, insbesondere im Zusammenhang mit der mitotischen Spindel. Trotz jahrzehntelanger Forschung bleibt die feine molekulare Architektur des Zentrosoms, insbesondere die des PZM, ungeklärt. Der Fadenwurm *C. elegans* mit seinen relativ einfachen Zentrosomen ist ein gut charakterisiertes Modell geeignet für die Untersuchung des PZMs. Das minimale Zentrosom von *C. elegans* wurde bereits in vitro rekonstituiert, indem Mikrotubuli aus gereinigtem zentrosomalen Protein zu sogenannten Astern kondensiert wurden. In dieser Arbeit charakterisiere ich die Strukturen in den Zentrosomen von *C. elegans* für ein besseres Verständnis dieser Schlüsselorganelle. Hierzu nutze ich die Kryo-Elektronentomographie (Kryo-ET), die zelluläre Strukturen in ihrem nativen Zustand mit molekularer Auflösung sichtbar macht.

Die Daten in dieser Arbeit zeigen, dass Mikrotubuli-Astern zwar interessante Fragen über die Bildung von Mikrotubuli aufwerfen, allein aber nicht als Modell für ein funktionales Zentrosom ausreichen. Gleichzeitig zeige ich, dass embryonale Zellen, die aus dem nativen Embryo herausgelöst wurden, lebensfähig bleiben und eine geeignete Probe für die Kryo-ET-Analyse darstellen, da sie klein genug sind, um durch ‘plunge freezing’ kryofixiert zu werden und dann mit Hilfe eines fokussierten Ionenstrahls (FIB) auf die gewünschte Dicke heruntergedünnt werden können. Um das Zentrosom innerhalb dieser heruntergedünnten Zellen zu lokalisieren verwende anschliessend korrelative, lichtmikroskopische Methoden. Innerhalb des Zentrosoms besteht ein hohes Maß an Mikrotubuli-Organisation, die wahrscheinlich durch die Funktion von gamma-TuRC-Molekülen, die zu einer kohärenten Struktur

gemittelt wurden, vorgegeben ist. Die Zentriolen der analysierten Zentrosomen wiesen unerwartete Merkmale und strukturelle Variationen auf, die auf spezialisierte, biologischen Funktionen hindeuten. Die Zentrosomen selbst waren in drei architektonische Zonen unterteilt: eine Zone mit Zentriolen im Zentrum der Organelle, umgeben von einer Zone ohne Mikrotubuli und schliesslich einer äußeren Zone frei von Ribosomen. Diese Zonen enthalten ein gelartiges Geflecht aus PZM, das als selektive Barriere für zentrosomale Client-Proteine fungiert. In meiner Dissertation erstelle ich einen dreidimensionalen Strukturatlas, der beschreibt, wie sich Zentrosomen zusammensetzen, wie sie wachsen und ihre Funktion ausüben.

Introduction

1.1 The centrosome: the anchor of mitosis

The centrosome is a key cellular organelle, as it is the major Microtubule Organizing Center (MTOC) of most animal cells, responsible for the assembly and organization of the mitotic spindle, and ultimately the faithful separation of chromosomes during mitosis (Lüders and Stearns, 2007; Nigg and Stearns, 2011). It was one of the earliest organelles of the cell to be described, with the first drawing of this being done in 1876 by Van Beneden, capturing only black dots labelled as “polar corpuscles”. Later work by the same researcher identified a spindle of thin fibers arising from these corpuscles, and that they separated outwards during later stages of cell division, implying a function in mitosis (Van Beneden and Neyt, 1887; Gall, 2004). The term “centrosome” however did not arise until Theodor Boveri coined it to describe this region as seen in divisions in the parasitic roundworm *Ascaris.* Additionally, he proposed the term "centriole" for the dense staining dots in the center of these centrosomes. Boveri also observed that extra centrosomes resulted in multipolar spindles and improper distribution of chromosomes (Boveri, 1900; Wilson, 1925) (Figure 1.1A). The structure of the centriole was not revealed until the 1950s when two studies described the structures of both the centriole (De Harven and Bernhard, 1956), and the centriole-derived basal body (Fawcett and Porter, 1954), while the dense region of proteinaceous material was first imaged in electron microscopy studies in the mid 1970s (Gould and Borisy, 1977) (Figure 1.1B).

Benefiting from almost a century and a half of studies, we now know that the centrosome consists of a pair of a barrel shaped, 9-fold arrangement of microtubule-based structures called centrioles, and a surrounding proteinaceous mass, called Peri-Centriolar Material, or PCM (Gould and Borisy, 1977; Kuriyama and Borisy, 1981). It is this PCM that ultimately accounts for the bulk of the centrosome, and is responsible for the nucleation of microtubules and their positioning (Wittmann,

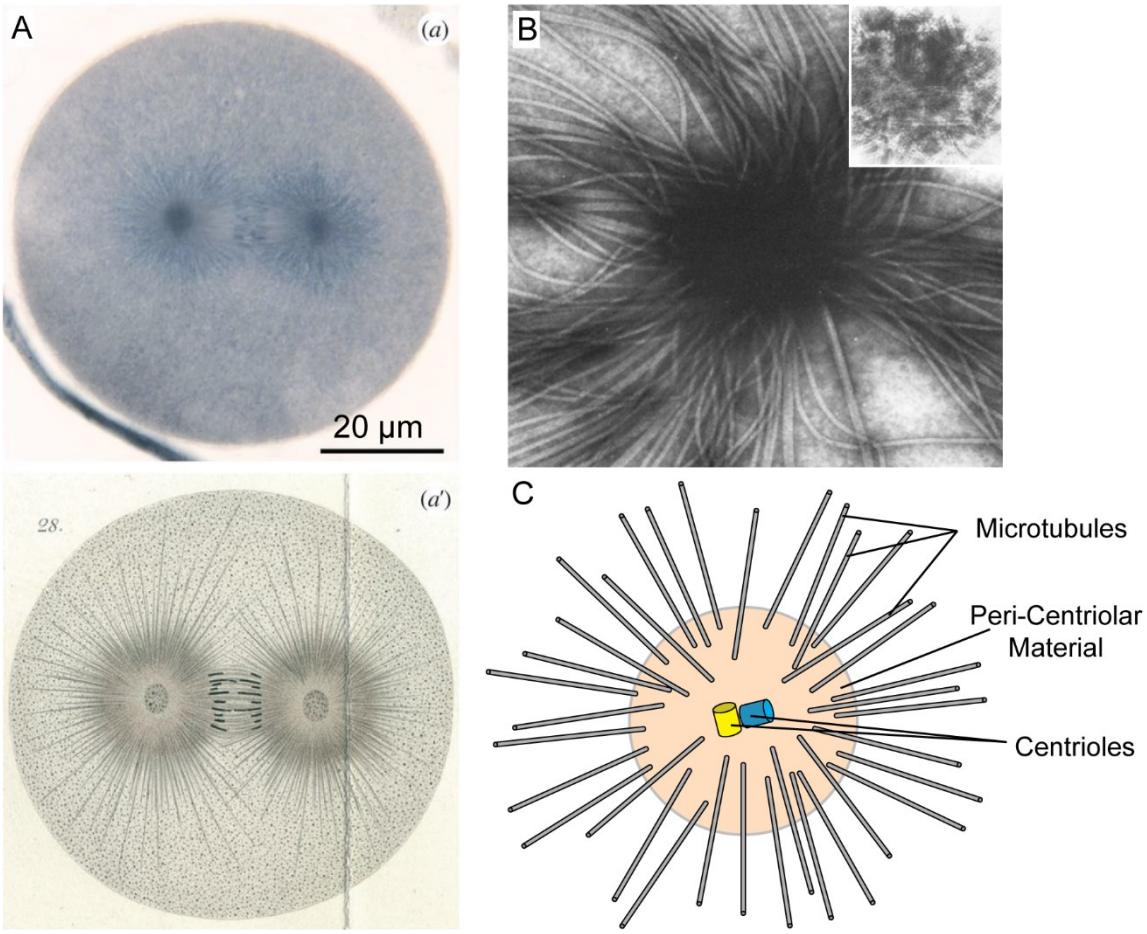

Figure 1.1: Studies and models of the centrosome. A: Top: original microscope slides from Theodore Boveri showing microtubule spindles forming around a pair of darker staining regions in a one-cell first cleavage division of Echinus microtuberculatus eggs. Bottom, Boveri's drawings on his observations. Adapted from (Scheer, 2014). B: Electron microscopy stain of centrosomes in Chinese Hamster Ovary cells, showing microtubules spreading out from an area of dense staining, consisting of PCM. The inset, at higher magnification, shows a centriole pair within the dense staining. Adapted from (Gould and Borisy, 1977). C: Schematic of the centrosome, with a centriole pair surrounded by PCM, from which microtubules are found to emerge.

Hyman and Desai, 2001) (Figure 1.1C). Previous work has speculated that the surface of the centrosome is defined by layers of gamma-tubulin (O'Toole *et al.*, 2012) or endoplasmic reticulum (Maheshwari *et al.*, 2023). Alternatively, a popular opinion is that the PCM is formed, at least initially, through phase separation (Woodruff *et al.*, 2017). Phase separation, especially in the context of biology, is the spontaneous generation of at least two distinct chemical phases, a dilute and dense phase, from a well-mixed starting solution. This dense phase can be liquid-like, demonstrating the

ability to internally rearrange, undergo transfer of material to and from the dilute phase, and fuse with other dense phase droplets; or solid-like, in which case these properties are absent or much less pronounced (Hyman, Weber and Jülicher, 2014; Alberti, Gladfelter and Mittag, 2019).

With this in mind, it has been observed that in interphase, the centrosome is a relatively small organelle, just a few hundred nanometers across (Fu and Glover, 2012; Lawo *et al.*, 2012; Mennella *et al.*, 2012; Sonnen *et al.*, 2012) As phase-separating centrosomal proteins are initially liquid-like, demonstrating internal rearrangement and droplet fusion, it is thought that the interphase centrosome is also a liquid (Woodruff *et al.*, 2017). However, during mitosis the centrosome expands 30-50 fold in volume, and in doing so nucleates many more microtubules, while becoming more solid-like in nature, losing this ability to internally rearrange and fuse (Khodjakov and Rieder, 1999; Palazzo *et al.*, 1999; Woodruff *et al.*, 2017). This process is called maturation. After mitosis, the phase changes again and the centrosome disassembles, reverting to its interphase state, ready for another round of the cell cycle (Schnackenberg *et al.*, 1998; Enos *et al.*, 2018; Mittasch *et al.*, 2020a). This growth, disassembly, and transition in function makes it an interesting example of phase separation within the cell, specifically of an organelle which undergoes multiple cyclical phase changes.

In many model organisms, the PCM consists of a stable scaffold protein, be it SPD-5 in *Caenorhabditis elegans* (Hamill *et al.*, 2002; Woodruff *et al.*, 2015, 2017), centrosomin in *Drosophila melanogaster* (Timothy *et al.*, 1999), or CDK5RAP2 in humans (Fong *et al.*, 2007; Graser, Stierhof and Nigg, 2007); as well as additional 'client' proteins that modulate centrosome function but are not thought to contribute structurally to the centrosome (Banani *et al.*, 2016; Holehouse and Pappu, 2018). These scaffold proteins self-assemble to form the supramolecular micro-scale PCM, although the exact nature of this interaction and the molecular detail of the structure formed is the result of some debate. Despite the similar function of the centrosome

across animals and some fungi (Azimzadeh, 2014), PCM scaffold proteins do not share sequence homology between species. However, there are structural similarities between these proteins that imply common functional modalities, related to their shared role in the centrosome. All of these proteins consist of a series of coiled coils connected by flexible linker regions. Due to the flexibility and difficult of working with these proteins, classical structural biology approaches, such as single particle cryo-electron microscopy and x-ray diffraction studies, are not practical on these scaffolds, although the structure of small fragments of centrosomin have been solved (Feng *et al.*, 2017). Prior to the release of Alphafold2 (Jumper *et al.*, 2021), the information on the number and location arose from secondary structure prediction software, such as PSI-PRED (McGuffin, Bryson and Jones, 2000). However, this more recent software has allowed a much more complete prediction of the individual scaffold molecules, showing their structural similarities despite their divergence in sequence.

Despite its importance in most animal cells, the centrosome is not a universal feature in eukaryotes. Lower fungi such as yeast, and most plants do not have a centrosome, with fungi having a spindle pole body, and flowering plants and conifers having an anastral mitotic spindle. Both of these differ from the centrosome as they do not contain centrioles at their core, but retain many of the key structural features of their counterpart in animal cells, such as a forming from a distinct proteinaceous core, containing many gamma Tubulin Ring Complexes (gamma-TuRCs), and retain the ability to concentrate tubulin assisting its polymerization into microtubules (Robinow and Marak, 1966; Moens and Rapport, 1971; O'Toole, Winey and McIntosh, 1999).

1.2 The centrioles: a structured regulatory keystone

Since the centriole was first identified as being a microtubule-based structure in electron micrographs back in 1956 (De Harven and Bernhard, 1956), it has been recognized as the most structured and well-ordered feature of the centrosome. In most, including mammalian, cells the centriolar microtubules are arranged as triplets (Gould and Borisy, 1977; Wang *et al.*, 2017), but there are exceptions. Notably, *Drosophila* centrioles consist of doublet microtubules (M Moritz *et al.*, 1995; Greenan *et al.*, 2018), and *C. elegans* centrioles are reported in the literature to consist of only singlets (Pelletier *et al.*, 2006; Sugioka *et al.*, 2017) (Figure 1.2). Indeed, *C. elegans* lack the delta and epsilon tubulins associated with triplet microtubules in humans (Dutcher and Trabuco, 1998; Dutcher *et al.*, 2002; Dutcher, 2003).

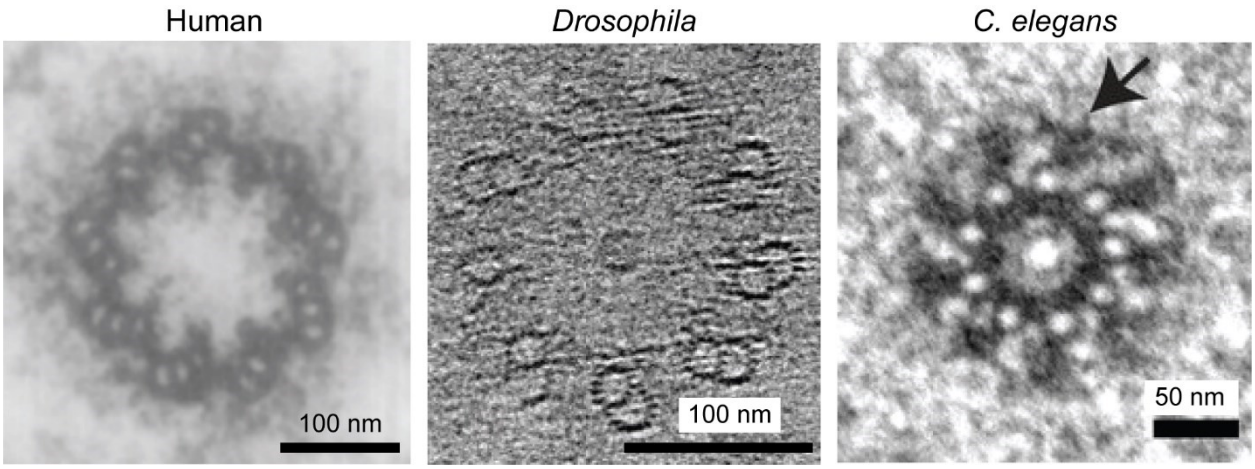

Figure 1.2 Centrioles of different organisms, showing human centrioles, *Drosophila* centrioles, and *C. elegans* centrioles. An arrow points to the paddlewheel. Adapted from (Paintrand *et al.*, 1992), (Greenan *et al.*, 2018), and (Sugioka *et al.*, 2017).

Curiously, the centriole is not vital for the formation of a mitotic spindle, as one might expect from such a large and integral centrosomal component. Not only are there many species where the centriole is absent, such as in the previously mentioned examples of fungi, conifers, and flowering plants; but mitotic divisions continue as normal in *Chlamydomonas* mutants where centrioles were forced from the PCM, or have had their assembly disrupted, However, the rate of abnormal chromosome

separation increased 100-fold (Zamora and Marshall, 2005), and mitosis was much slower (Matsuura *et al.*, 2004). Therefore, the centriole, although not strictly required for mitotic spindle assembly, is important for faithful and successful separation of chromosomes.

Since the centriole is important, but not vital, for the mitotic spindle, what does it actually do? A longstanding hypothesis was that this structure imparted physical strength to the centrosome by providing a sturdy backbone for the PCM to tether on to. There is evidence to support this, as centrosomes injected with centriole-disrupting antibodies break apart upon the onset of mitosis (Abal, Keryer and Bornens, 2005). This strength may be imposed by a helical inner scaffold, a tri-protein structure found on the inside face of the centriole, connecting to the microtubules, as this structure was found to resist deformation (Le Guennec *et al.*, 2020).

The function of the centriole does not end there, as the centriole has been found to be important in regulating centrosome replication by acting as a nucleation site for PCM. This is important, as the centriole must replicate once, and only once, during the cell cycle, else multipolar spindle formation occurs (Nigg and Holland, 2018). Studies from the 1960s identified the centriole as an attachment point for centrosomal material, as when centrioles chemically separated from the centrosome, PCM was found to re-condense around the centriole (Mazia, Harris and Bibring, 1960; Sluder and Begg, 1985). Therefore, for centrosome number to be controlled within the cell, centriole copy number must also be strictly controlled. How the this is controlled, and how it related to the cell cycle, will be addressed in section 1.3.

In order for the centriole to carry out these functions, it must remain tethered to the PCM. In *C. elegans*, this is largely carried out through the work of two proteins: PCMD-1 and SAS-7. The role of SAS-7 was identified through screens of embryonic-lethal

mutations. The loss of SAS-7 leads to defects in PCM assembly and subsequent establishment of anterior-posterior cell polarity (Sugioka *et al.*, 2017). PCMD-1, the function of which was elucidated later, was found to directly link the centriolar protein SAS-4 via PCMD-1's N terminus with the PCM protein SPD-5 via the C terminus. This function was dependent on the presence of SAS-7 within the centriole (Erpf *et al.*, 2019).

Beyond their role in the centrosome, the centriole is the basic structure from which cilia form. In ciliated cells, such as spermatozoa, the centriole will be eliminated from the centrosome and dock onto the plasma membrane, aided by centriolar appendages. Upon docking, the centriole will undergo modification to become the basal body, which in turn acts as the nucleation site for ciliary microtubules (Kobayashi and Dynlacht, 2011).

The centriole of *C. elegans* is rather different to the centriole in other organisms. The most obvious difference is their aforementioned singlet microtubules. They are also much smaller than, for example, human centrioles, which are approximately 250 nm by 500 nm in comparison to the reported dimensions of 100 nm by 150 nm in *C. elegans* (Pelletier *et al.*, 2006; Sugioka *et al.*, 2017). Most centrioles display polarity, for examples showing only certain structural features in the proximal or distal ends (Azimzadeh and Marshall, 2010; Nazarov *et al.*, 2020). This is not the case for *C. elegans*. A unique feature of the centriole in this nematode is the 'paddlewheel': a large region of poorly defined electron dense material, attached to the a-tubule and spreads along the entire length of the centriole (Pelletier *et al.*, 2006; Sugioka *et al.*, 2017; Woglar *et al.*, 2022). During the course of this thesis, a map of the proteins of the *C. elegans* centriole was published. This was carried out by using a combination of Stimulated Emission Depletion (STED) microscopy performed on expanded samples, and standard room-temperature electron microscopy, using the centriole microtubules as a registration point. This was carried out on gonad cells, and as such their centrioles were either fated to become either basal bodies in spermatozoa, or

to be eliminated entirely in ova. The combination of these two imaging approaches allowed the mapping of all known centriolar proteins to regions of electron density. The key findings include that the paddlewheel consists of the proteins SPD-5 and PCMD-1, with densities corresponding to SPD-2 and SAS-7 being found further out. SAS-1, SAS-5, and SAS-6 are all found in a series of concentric rings inside the centriole barrel (Woglar *et al.*, 2022) (Figure 1.3). These have been termed the central and inner tubes respectively in some literature (Pelletier *et al.*, 2006). However, due to the similarity of these terms, here I will refer to the inner tube as the cartwheel, as

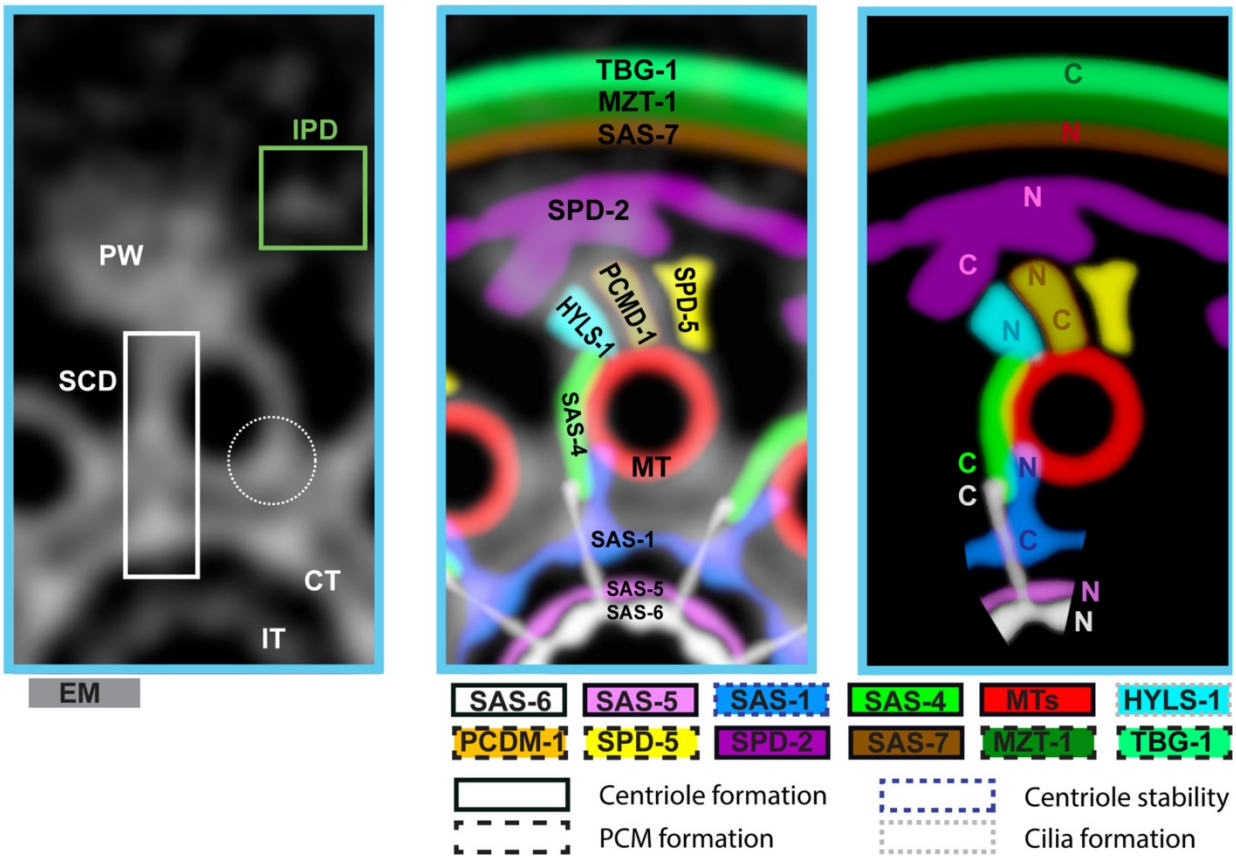

Figure 1.3: The *C. elegans* centriole. Left: subtomogram average of room-temperature stained EM of the centriole in *C. elegans* gonads, showing the Inner Tube (IT), Central Tube (CT), SAS-6/4/1 Containing Density (SCD), PaddleWheel (PW), and Inter Paddlewheel Density (IPD). Right, Stimulated Emission Depletion microscopy (STED) super-resolution light microscopy data of the localization of certain proteins within the centriole, with N ansd C termini highlighted where possible. Center, overlay of the left and right images, with proteins labelled. Adapted from (Woglar et al., 2022).

is it shares functionality with this structure in other centrioles, as is described in detail in section 1.3.

1.3 The centriole cycle

Replication of the centriole is a complicated, multi-step process, as would be expected for this complicated, multi-component structure. It is also a highly regulated procedure, as excessive centriolar replication results in multi-polar spindles and aberrant cell division, whereas a failure for centrioles to divide may result in a failure in centrosomal replication, rendering the daughter cells unable to divide.

In *C. elegans*, as in other species, centriole replication takes place at the onset of S phase (Nigg and Stearns, 2011; Firat-Karalar and Stearns, 2014; Nigg and Holland, 2018). At this point, the interphase centrosome contains only a single mother centriole, which must initiate formation of a nascent procentriole, which will eventually develop into a full daughter centriole. This daughter centriole will then mature into a mother centriole, ready to form its own daughter centriole. There are 6 essential proteins required for this process, which are recruited in a specific order. First, SAS-7 (Sugioka *et al.*, 2017) and SPD-2 (Pelletier *et al.*, 2004) are recruited, followed by the protein kinase ZYG-1. The action of ZYG-1 serves to aid recruitment of SAS-5, SAS-6, and then SAS-4 (Dammermann *et al.*, 2004; Pelletier *et al.*, 2006) to the growing procentriole. SAS-5 and SAS-6 serve as a template for microtubule growth (Leidel *et al.*, 2005; Qiao *et al.*, 2012), and after addition of SAS-4 microtubules start to form around the growing procentriole (Gopalakrishnan *et al.*, 2011) (Figure 1.4). Although this is specific to *C. elegans*, similar recruitment sequences have been reported in other model organisms.

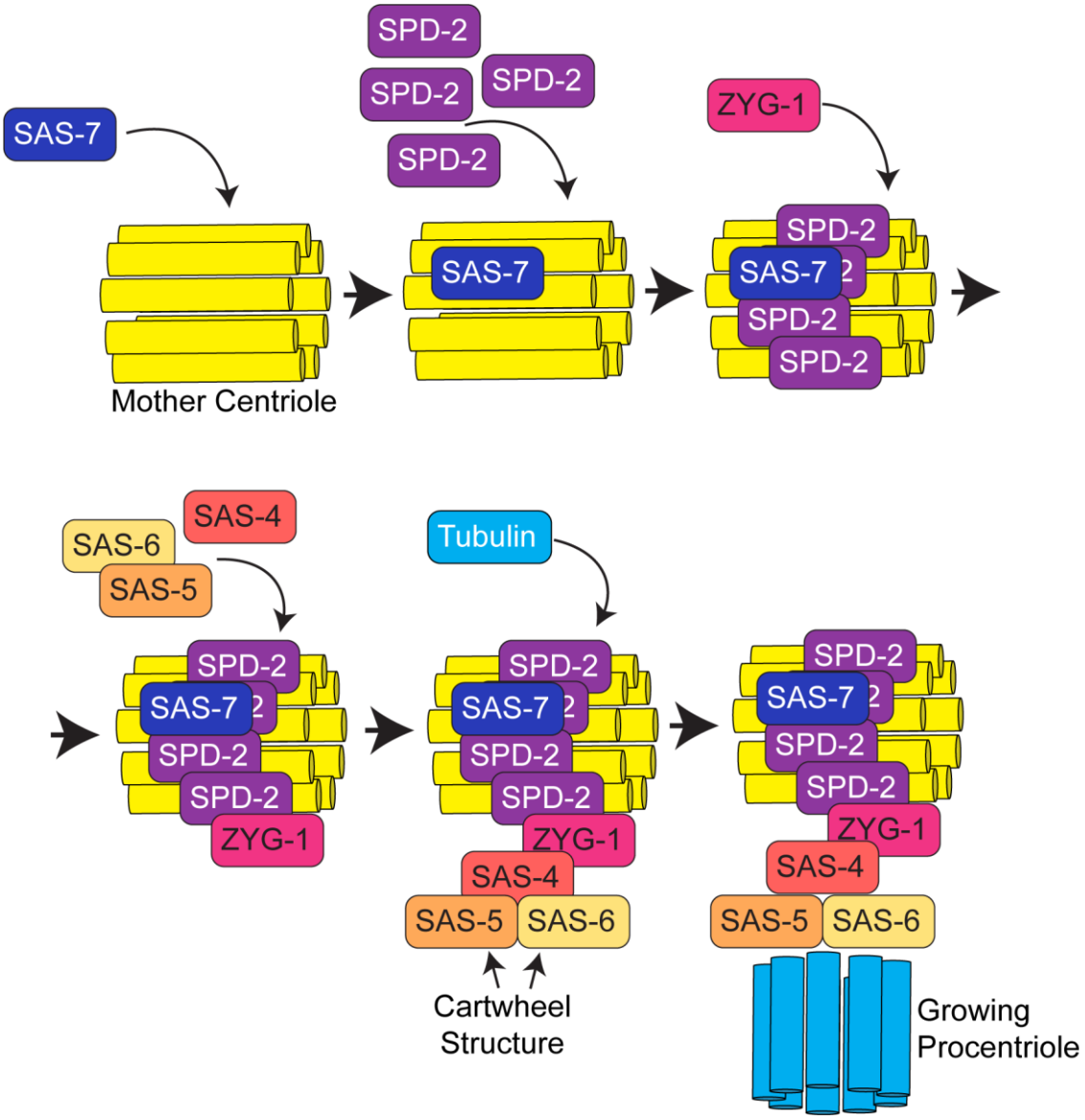

Figure 1.4: Schematic of centriole assembly. First SAS-7 is recruited to the mother centriole, followed by SPD-2 and then ZYG-9. This facilitates recruitment of SAS-5, SAS-6, and SAS4, after which tubulins for the growing procentriole can be acquired.

Of particular interest in the preceding list is SAS-6, as this is thought to be responsible for templating the highly conserved 9-fold radial symmetry of the centriole. Specifically, SAS-6 monomers are seen to multimerize into ring structures, which then stack vertically. These stacked rings are responsible for the cartwheel, or inner tube, structure seen in centrioles. *In vitro,* spokes are seen arising radially from these stacked rings. As these spokes have a 9-fold symmetry, it is thought that these spokes are responsible for imparting the symmetry of the centriole (Hilbert *et al.*,

2013; Nievergelt *et al.*, 2018; Banterle *et al.*, 2020; Hatzopoulos *et al.*, 2021). In order for this procentriole to fully develop into a centriole, additional components must yet be recruited, as PCMD-1, SAS-1, SAS-2, and SPD-5 are all found in the mature centriole (Woglar *et al.*, 2022). The process of centriole growth is complete at the time of mitosis, so each of the two centrosomes contains two centrioles, resulting in four per cell. After mitosis is complete and the mature PCM degrades, the new daughter centriole and old mother centriole within each centrosome separate, or disengage, ready to repeat the cycle once more (Tsou and Stearns, 2006).

As previously stated, it is important that this cycle is repeated exactly once every cell cycle. Of particular importance in this regard is the regulation of centriole disengagement. In humans, the breakage of this connection has been linked to PLK1, which may in turn be acting on the PCM component pericentrin to function as a separase (Matsuo *et al.*, 2012; Kim, Lee and Rhee, 2015). In *C. elegans*, the role of microtubule pulling forces in triggering centriole disengagement have been identified (Cabral *et al.*, 2013), implying a model where centriole disengagement cannot occur prior to mitosis as these pulling forces would not be present.

1.4 The interphase centrosome

Much like the centriole, the centrosome undergoes cycles of maturation, growth, and disassembly. In interphase, the centrosome has yet to go through the processes of maturation and growth, and as such remains small, in the range of a few hundred nanometers. It is also observed to be more liquid-like in this state (Woodruff *et al.*, 2017), and has been known to tether to the nuclear envelope. Specifically in humans, the nucleoporin Nup133 has been shown to anchor CENP-F, which in turn, recruits NudE/EL and dynein/dynactin to the nuclear pore at the G2/M transition. This tethering has been shown to be important for positioning the centrosomes prior to

Nuclear Envelope Breakdown (NEBD) (Bolhy *et al.*, 2011). However, such tethering has yet to be directly imaged.

What internal structure might it have in this state? Light microscopy has been carried out on the interphase centrosome in both *Drosophila* and humans. Specifically, Structured Illumination Microscopy (SIM) and STochastic Optical Reconstruction Microscopy (STORM) was used to observe sub-compartmentalization of proteins within the organelle. In *Drosophila,* it was found that there was specific layering of the PCM components surrounding the centriole, in what was described as "patterned layers". In *Drosophila*, a Pericentrin Like Protein (Dplp) layer was seen immediately surrounding centrioles, existing in extended fibrils of the protein. Spd-2 and Sas-4 werer found to be associated with this layer. In mother centrioles only, this was in turn surrounded by additional layers of Dplp, Asterless (Asl), Plk4, Centrosomin (Cnn), and gamma tubulin, followed by a layer of gamma tubulin, Polo, Spd-2, and Cnn. Many of the proteins, in particular Cnn, are required for the recruitment of gamma tubulin, while the extended conformation of Dplp was suspected to physically support the 3D shape of the centrosome. In the daughter centriole, only the first pattered layer of proteins was seen, at least until the onset of metaphase. This demonstrates that the mother and daughter centrioles may have different functions within the centrosome (Fu and Glover, 2012; Mennella *et al.*, 2012).

Similarly, the studies on human cells also observed specific sub-localization of PCM around the centriole, but in a notably different pattern. Rather than simple specific zones, dot-like and ring-like patterns were observed around the centrioles. Proteins such as Centrin, Sas-6, STIL, and Plk4 appeared as compact dots, while Pericentrin and NEDD1 formed toroid patterns around the centrioles. The proteins were grouped into inner, intermediate, and outer PCM based on their ring diameters, much like in *Drosophila* (Lawo *et al.*, 2012; Sonnen *et al.*, 2012). Since the publishing of these results over 10 years ago on the interphase centrosome, little light microscopy work has been published on the mitotic centrosome. This may indicate that light

microscopy work is inappropriate to study this system. Direct, unlabeled imaging of the centrosome at molecular resolution may therefore assist in our understanding of protein patterning outlined in these two models.

1.5 Centrosome maturation and disassembly

For the centrosome to go from the small organelle described previously to a structure capable of nucleating the many hundreds of microtubules in the mitotic spindle and resist the pulling forces of mitosis, it must undergo drastic changes, termed maturation (Palazzo *et al.*, 1999). The process of centrosomal maturation is well-documented in *C. elegans*, with PLK-1 being of particular importance (Ohta *et al.*, 2021; Nakajo *et al.*, 2022). The self-interaction of SPD-5 has been known to be modified by PLK-1 mediated phosphorylation, with phosphorylation increasing the assembly rate, but not scaffolding function of, SPD-5. Specifically, *C. elegans* embryos expressing both endogenous SPD-5 and SPD-5 mutants that had phosphorylation sites shown to be crucial for centrosome growth (Woodruff *et al.*, 2015) blocked via an ectopically expressed transgene were examined. Although mutant SPD-5 was found to localize to the interphase centrosome, it failed to expand it, resulting in centrosomes that were 58% smaller upon NEBD than in wild type embryos. It was therefore suggested that PLK-1 mediated phosphorylation biased SPD-5 towards an 'assembly competent' state, which in turn allowed the PCM scaffold to rapidly grow upon the onset of mitosis (Wueseke *et al.*, 2014, 2016), accounting for the observed increase in centrosome size. Similarly, a combination of pulling forces and the phosphatase PP2A were found to trigger centrosome disassembly (Enos *et al.*, 2018). PLK-1 was found to exit the centrosome at the metaphase-anaphase transition, where centrosome integrity was also found to be compromised (Mittasch *et al.*, 2020a). Taken together, this creates a model where centrosome growth driven by self-assembly of the centrosome scaffolds, are primarily modulated by phosphorylation of the PCM scaffolds.

However, PLK-1 is far from being the only factor acting upon the PCM scaffold to influence maturation. SPD-2 also plays an important role here, as well as its previously described role in centriolar development. For example, depletion of SPD-2 via RNAi results in a failure of the centrosome to mature. This property arises specifically due to interactions between SPD-2 and SPD-5, as SPD-5 depletion prevents SPD-2 accumulating in the centrosome (Pelletier *et al.*, 2004; Decker *et al.*, 2011). It is therefore thought that SPD-2 acts as a centrosomal cross-linker, joining already interconnected sections of SPD-5 polymer, aiding the centrosome in its growth and maturation.

Although the experiments above give an outline of the components required for centrosome maturation and disassembly, they do little to explore the changing material landscape of the centrosome over the course of maturation and mitosis. Thankfully, with modern techniques it is now possible to explore this within a living and dividing cell. Focused Light-indUced Cytoplasmic Streaming (FLUCS) microscopy is a recently-developed technique that uses thermal gradients induced by a laser to introduce a flow within a very small volume, such as the cell (Mittasch *et al.*, 2018). When applied within the *C. elegans* 1-cell embryo, this can effectively be used to pull apart the centrosome under varying conditions, thus determining the strength and ductility of the organelle at different time points. It was observed that the ability of the centrosome to deform increased at the point of metaphase-anaphase transition, with the centrosome turning from a hard ball that resisted deformation, into something that could be more easily stretched apart by cytoplasmic flow. Both PLK-1 and SPD-2 were important in reinforcing this strength and ductility, in line with the previous studies (Pelletier *et al.*, 2004; Decker *et al.*, 2011; Wueseke *et al.*, 2014, 2016). Of specific importance is the fact that PLK-1 levels were found to sharply drop at the metaphase-anaphase transition, while at the same time point PP2A levels rise. This builds on the previous model of SPD-5 posttranslational modification affecting PCM growth, by also demonstrating how phosphorylation modifies the properties of

the PCM as required by the centrosome at each specific cell stage. SPD-2 departure, which occurs at late anaphase/early telophase, was also found to correlate with a loss of centrosome ductility. Other PCM components, such as gamma tubulin and SPD-5, were found to be associated with the centrosome until telophase, when the centrosome falls apart, although it has been observed that gamma tubulin exited the centrosome following PLK-1 inhibition (Haren, Stearns and Lüders, 2009). Taken together, this forms a model where the combined effect of these activities determines the overall mechanical properties of the PCM during the cell cycle, a form of mechanical regulation the authors referred to as "transient reinforcement". This enables cell cycle-regulated PCM assembly, function, and disassembly as required (Mittasch *et al.*, 2020a).

1.6 The supramolecular structure of the PCM

Although the primary factors resulting in the centrosome's growth, maturation, and disassembly have been well identified and discussed, there is still much debate as to the architecture of the expanded PCM. Debate is centered around the contrasting merits and weaknesses of three models. First, a lattice model was put down as a result of work on salt-stripped centrosomes. Salt stripping removed most, but not all, of the centrosomal protein, leaving behind a diminished centrosome with no capacity to nucleate microtubules. When incubated with oocyte cytoplasmic extract, the scaffold regained the ability to form microtubules. Negative-stain electron microscopy of the salt-stripped centrosome revealed a loosely organized 3D fibrous network, composed of a series of 12-15 nm long fibers. It was assumed that this formed the skeleton of the centrosome, onto which other PCM molecules would bind. The authors also observed pores within similar salt stripped centrosomes, with a diameter matching that of a gamma Tubulin Ring Complex (gamma-TuRC), which was presumed to be where these complexes were forced from the lattice upon salt-stripping (Schnackenberg *et al.*, 1998; Schnackenberg and Palazzo, 1999). In a

similar system, gamma-TuRCs were found to reliably bind to salt stripped centrosomes and restore some microtubule binding property (Moritz *et al.*, 1998). Although fibers of these length have not been seen under other experimental circumstances, the very low rates of SPD-5 exchange to and from the mitotic *C. elegans* centrosome imply solidity of this structure (Laos, Cabral and Dammermann, 2015), as liquids have a much greater turnover (Zwicker, Hyman and Julicher, 2015). Although it is questionable if the authors originally intended for their discovery to be interpreted this way, many have taken this to mean that the centrosome contains a rigid, crystalline lattice acting as a skeleton, providing material strength to the entire centrosome, around which other PCM factors can bind to modulate its properties.

By contrast, evidence also exists suggesting the centrosome grows solely through liquid-liquid phase separation, as has been suggested by theoretical modelling of PCM growth kinetics throughout maturation. This model also provides two separate explanations for the spherical shape of centrosome. As a liquid, it will always relax into a sphere due to the effect of surface tension. Furthermore liquids are capable of isotropic growth, also resulting in a spherical shape (Zwicker *et al.*, 2014). Further biological evidence for this model is the observation that SPD-5 is added throughout the volume of the PCM in the early stages of maturation (Laos, Cabral and Dammermann, 2015; Alvarez-Rodrigo *et al.*, 2019), and isotropic growth is a telltale property of intracellular liquid condensates.

A third model suggests a more-gel like or ‘arrested condensate’ conformation, and is supported by work with *in-vitro* SPD-5 condensates. It is observed that SPD-5 condensates, although initially liquid-like and displaying dynamic exchange between the mixed and demixed phases and isotropic growth, rapidly harden and become less dynamic with time (Woodruff *et al.*, 2017). This process of condensate ‘ageing’ is observed elsewhere (Alberti and Hyman, 2016), and is thought to arise when the self-interacting domains of a phase separating protein become saturated (Ranganathan and Shakhnovich, 2020). This model also may explain the observed and previously

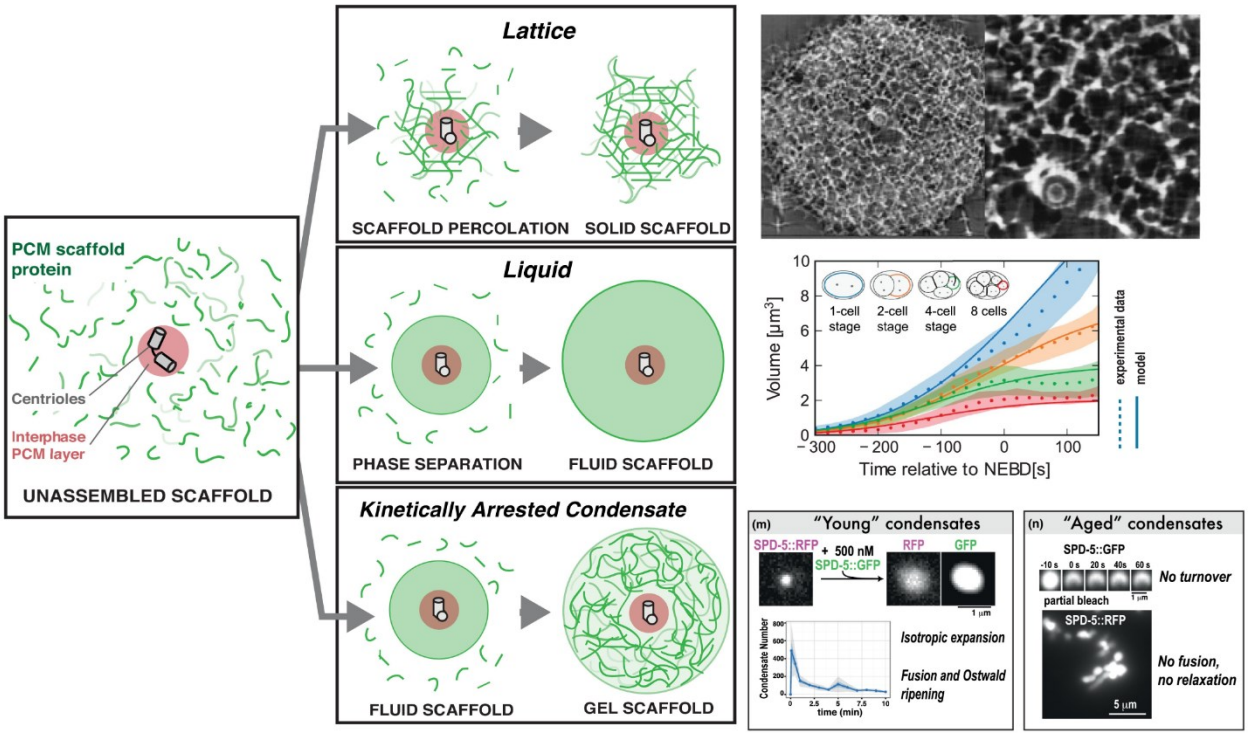

Figure 1.5: Differing models of PCM structure, adapted from (Woodruff, 2021). In the lattice model, upon maturation, scaffold proteins come together to form an interconnected, cohesive network. The scaffold within the PCM expands as new proteins diffuse and assemble onto the exposed surface of the existing lattice. Evidence for this is shown on the right, in the form of a centrosomal lattice as seen in *S. solidissima*, adapted from (Schnackenberg et al., 1998). In the liquid model the centrosome forms purely via liquid-liquid phase separation. Evidence on the right shows the comparison between the mathematical models of the purely liquid model, and observed growth kinetics of the PCM in embryogenesis, adapted from (Zwicker et al., 2014). A gel model, although scaffolds initially have the opportunity to rearrange, they are soon locked in a gel-like cross-linking interacrtions. Evidence on the right shows partial photobleaching of SPD-5 condensates, which initially can recover but over time as the condensates solidify, lose this ability, adapted from (Woodruff et al., 2017).

mentioned low turnover of SPD-5 between the centrosome and surrounding cytoplasm during metaphase. The gel model is reinforced *in vivo* through use of the previously described FLUCS experiments. Although metaphase centrosomes were able to resist the shear force introduced by these flows, anaphase centrosomes could be deformed without breakage. This infers that SPD-5 can undergo local rearrangements, as is seen in viscoelastic gels (Mittasch *et al.*, 2020a). It could also

be suggested that a gel such as this would be more resistant to microtubule pulling forces than either a hard lattice or fully liquid centrosome (Figure 1.5).

Although all of these models have their own strengths, the evidence at present is most consistent with an arrested condensate, or gel model, as this explains the spherical nature of the centrosome, observed protein turnover, and can explain how the structure withstands pulling forces. Again, direct observation of a centrosomal mesh either *in vivo* or *in situ* would help judge the merit of said models.

1.7 The role of gamma tubulin

Although much has been said about the assembly and structural properties of the PCM, its role in organizing microtubules has yet to be addressed. A key complex responsible for this is gamma-TuRC, which has been thought to be responsible in templating microtubules. It is now known that the whole ring complex consists of multiple gamma-tubulin containing tetramers, termed gamma-Tubulin Small Complexes (gamma-TuSC). The importance of gamma-TuRC for this task was first outlined in studies in the 1990s, which identified 25-30 diameter ring shapes in microtubule-free *Drosophila* centrosomes. It was also observed when microtubules were regrown from these centrosomes, they had short, blunt ends which matched the dimensions stated. Immuno-gold labelling targeting gamma tubulin subsequently revealed that gamma tubulin forms these ring shapes within the centrosome, and at the minus ends of growing microtubules (Michelle Moritz *et al.*, 1995). Simultaneously, the same structure was seen purified from *Xenopus* through negative-stain electron microscopy: a capping structure on the minus ends of microtubules, capable of nucleating microtubules (Zheng *et al.*, 1995).

Later studies improved on the structures shown in these preliminary works. Platinum etching and tomography generated a crude (by modern standards) but workable

structure showing the interactions between gamma-tubulin and Dgrip proteins within the complex. The overall topography of the complex, forming a ring of gamma tubulin and Drgip dimers, was found to be similar to the ends of microtubules. This suggests that the gamma-TuRC acts as a template for microtubule nucleation. Onto this ring, a cap of more Dgrips was found (Moritz *et al.*, 2000). Improvements in technology over the years has allowed for molecular resolution structures to be developed. Single-particle cryo-electron microscopy of the complete human-gamma tubulin ring complex revealed that it is composed of 14 subunits that resemble individual gamma-TuSC subcomplexes. It was observed the helical symmetry of the gamma tubulin molecules in the complex did not match that of microtubules, leading to speculation that conformational changes within the ring would be required for ring closure. There is also a large, unclassified density in the central 'plug' of the gamma-TuRC cone, of unknown function (Wieczorek *et al.*, 2020).

Curiously, within the centrosome, gamma-TuRC seems to be less responsible for the nucleation of microtubules, and more for their organization. Not only is the PCM capable of concentrating tubulin itself (Woodruff *et al.*, 2017; Baumgart *et al.*, 2019), but RNAi-mediated knockdown of gamma-tubulin in *C. elegans* does not result in fewer microtubules being formed in the spindle, instead resulting in its disorganization. In wild type centrosomes, centrioles are seen surrounded by a microtubule free volume. However upon gamma tubulin RNAi this is lost, and microtubules pass very close to the centrioles. This indicates that rather than having a role in concentrating tubulin for templating microtubules, the complex is responsible for the positioning and orienting microtubules. The same paper presents a model where the surface of the centrosome is defined as a patterned layer of gamma-TuRCs (O'Toole *et al.*, 2012).

1.8 Organization of microtubules at the centrosome

In order for the centrosome to work effectively, the microtubules must be assembled into a spindle that can anchor microtubules and ultimately separate chromosomes. To this end, the microtubules must be correctly oriented and have their minus ends pointing towards the centrosome, and their growing plus ends facing outwards in the aster. Additionally, as part of the wider mitotic spinde, microtubules are seen branching off from existing microtubules (Petry *et al.*, 2013; Ishihara *et al.*, 2014), and from a fibrous corona surrounding the kinetochores of the chromosome (Kops and Gassmann, 2020). Thankfully, a biological tool exists which allows one to examine the process of microtubule growth: so-called EB2 comets. As opposed to the gamma-TuRC stabilized minus ends, microtubule's growing plus ends are stabilized by a 'stabilizing cap', consisting of GTP-bound tubulin (Bowne-Anderson *et al.*, 2013) onto which a family of proteins have been known to bind. One of the most useful in determining microtubule dynamics is End Binding protein 2 (EB2), one of a family of three proteins. As such, the growth of microtubules at the non-gamma tubulin stabilized plus end can be observed by tracking EB2, as they move in a characteristic 'comet' shape (Grigoriev *et al.*, 2008). Tracking EB2 comets in the *C. elegans* centrosome reveals that not only do most microtubules grow away from the center of the centrosome, but it was even possible to observe their growth rate from the centrosome, being 0.34 ± 0.02 μm s^{-1} away from the spindle.

The same study examining comets in *C. elegans* (Redemann *et al.*, 2017) managed to image the entire mitotic spindle in this nematode, through plastic-embedded serial section tomography. Although this technique cannot reveal the molecular detail of the centrosome itself, it does provide a wealth of information on how the centrosome organizes its microtubules into a spindle. A key finding was that rather than microtubules directly bridging the kinetochore and the centrosome, most microtubules existed as part of a larger microtubule network. Only 22% of microtubules that were bound to a kinetochore ended within a few microns of the

centrioles, which was interpreted as being part of the centrosome. The remaining 78% of kinetochore microtubules connected to spindle microtubules via connections at their minus end, with a distance of 30-50 nm and an angle of 5-45° between them. Depolymerization of these minus ends was predicted through mathematical modelling to be particularly important in facilitating the separation of the chromosomes. Despite the importance of these kinetochore microtubules, the majority of microtubules were still found to originate from the centrosomes, and it was thought that the formation of centrosome-based microtubules was in fact outcompeting other forms of microtubule nucleation (Redemann *et al.*, 2017). Although this has revealed much about the overall arrangement of microtubules, the nature of the chemical stains required means that the molecular details of the centrosome, as well as properties such as the protofilament numbers within the microtubules, was lost in this dataset.

1.9 *C. elegans* microtubules

Now it is known how microtubules themselves are organized within the centrosome, the microtubules themselves can be examined. Microtubules themselves are formed of alpha and beta tubulin monomers, arranged sequentially head-to-tail into protofilaments. In most organisms 13 of these protofilaments arrange into a microtubule (Tilney *et al.*, 1973). *C. elegans* microtubules have been studied and found to be rather different to canonical microtubules. Touch receptor neurons in the nematode have 15 protofilaments, but most cell types, including the embryo, have 11 protofilaments (Chalfie and Thomson, 1982; Chaaban *et al.*, 2018). This has been examined by plastic-embedded tomography, followed by radial averaging of the microtubules. Although 11 protofilaments was the average number of protofilaments, there were outliers, with the total spread being from 9 to 13. *In vitro* however, *C. elegans* tubulin was found to exist in a variety of protofilament numbers, of which 12 was the most common. This implies some sort of controlling system

extant *in vivo* that is required for 11 protofilament formation. This tubulin was also found to be highly dynamic, undergoing assembly and catastrophe at a greater rate than any other known tubulin (Chaaban *et al.*, 2018).

1.10 A minimal centrosome system

In many species, including humans, the centrosome consists of many hundreds of proteins, responsible for the scaffolding, regulation, modulation, and organization of the mitotic spindle (Jakobsen *et al.*, 2011; Conduit, Wainman and Raff, 2015). Thankfully, not every organism has centrosomes this complicated. In particular, *C. elegans* is famed for having relatively simple centrosomes. Genetic work over the years has identified a small set of essential proteins for PCM assembly *in vivo*, with the PCM scaffold SPD-5 (Hamill *et al.*, 2002), the protein kinase PLK-1 (Decker *et al.*, 2011), and the PCM cross-linker SPD-2 (Pelletier *et al.*, 2004), all playing crucial roles. Of these, SPD-5 was observed to form dense irregular networks *in vitro* (Woodruff *et al.*, 2015), leading to the idea that it may be possible to reconstitute centrosomal function within a test tube. To this end, the authors attempted to discover what set of minimal proteins was required to facilitate tubulin concentration and microtubule polymerization. First, SPD-5 was found to phase separate into spherical, micron-scale condensates under conditions of molecular crowding, which more accurately simulates the dense protein-rich cytoplasm of the cell than simple buffer (Fulton, 1982; Ellis and Minton, 2003; Woodruff *et al.*, 2017). These condensates were found to mimic some of the properties of the centrosome, such as becoming stiffer and less ductile with age. Furthermore, the condensates were found to act as a selective compartment where PCM client proteins partition via interactions with SPD-5, just as the *in vivo* centrosome was found to concentrate tubulin. Two of the proteins capable of selectively partitioning into these SPD-5 droplets were the microtubule nucleation factors ZYG-9 (Matthews *et al.*, 1998) and TPXL-1 (Özlü *et al.*, 2005). With these also portioned into the condensates, it is possible for tubulin,

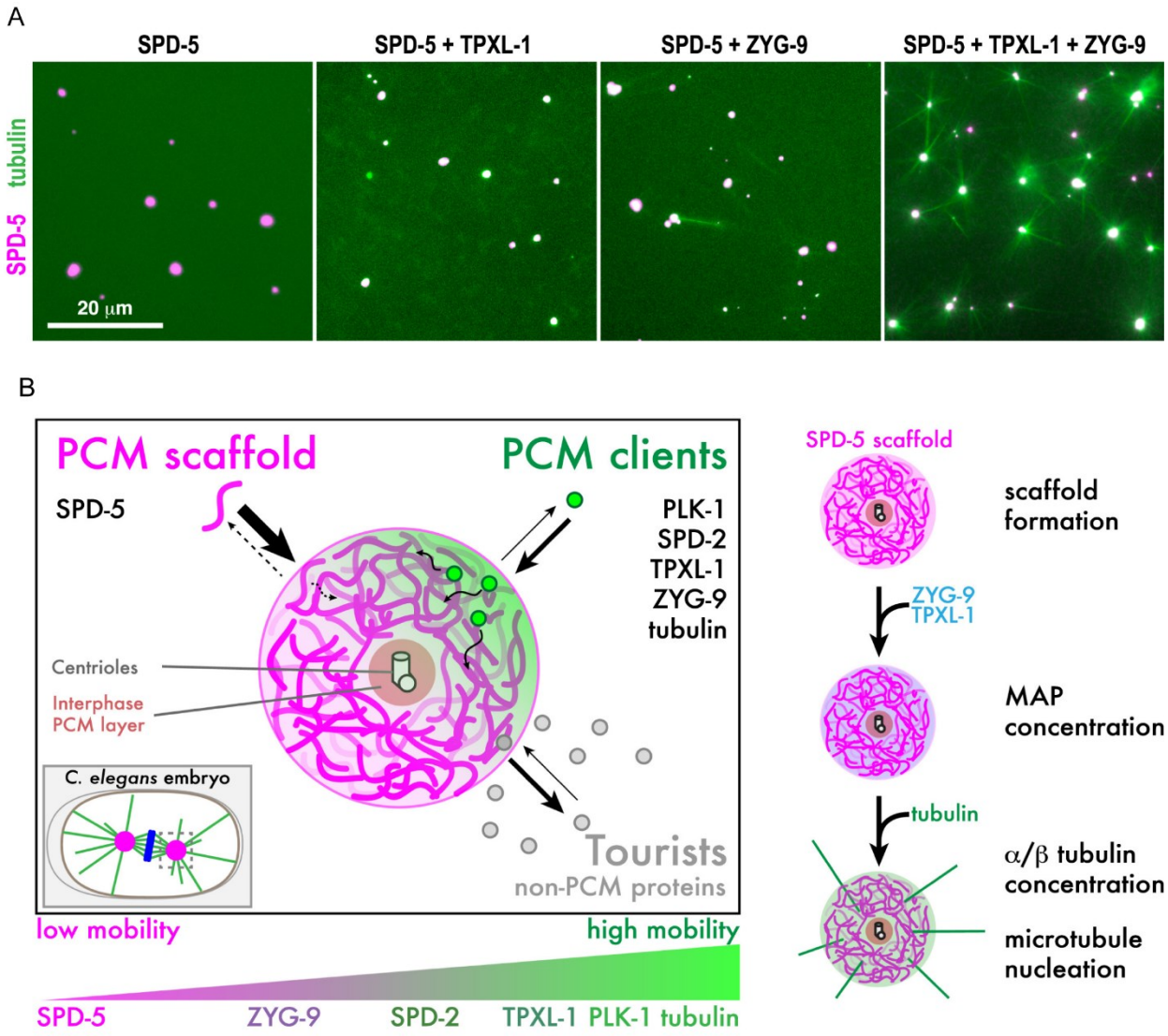

Figure 1.6: The *C. elegans* minimal microtubule system. A: the formation of microtubule asters using a combination of αβ-tubulin, SPD-5, TPXL-1, and ZYG-9. All images taken after 10 minutes of incubation. B: schematic of the *C. elegans* centrosome. Phase separation of SPD-5 forms a layer of mitotic PCM scaffold around the centrioles, which can selectively accumulate additional PCM proteins, while allowing "tourist" proteins, unrelated to centrosomal function, to pass through. Adapted from (Woodruff et al., 2017).

sourced from pig brain, to be both concentrated in the droplets, and for it to then polymerize into stable microtubules without the use of taxol or any other microtubule stabilizing agents. Crucially, concentration of tubulin present in solution was below the minimum threshold required for spontaneous microtubule polymerization *in vivo* (Mitchison and Kirschner, 1984), meaning the polymerized microtubules must arise

from the effect of tubulin concentration and microtubule stabilization in the condensate (Woodruff *et al.*, 2017) (Figure 1.6). These *in-vitro* minimally reconstituted centrosomes not only demonstrate the simplicity of the centrosome in this model organism, but also provide a powerful tool in which the properties of centrosomal proteins can be investigated in a controlled environment mimicking the native condition.

1.11 Cryo-electron tomography – advantages and disadvantages

Cryo-Electron Tomography (cryo-ET) is a rapidly evolving technique which can be used to generate molecular-resolution volumes of biological samples. When applied to cells, it can be used to unveil macromolecular structures and meso-scale assemblies contained within the cellular volume. This means that any imaged molecules are retained within their native context, allowing the effects of the molecular sociology of the cell be studied (Robinson, Sali and Baumeister, 2007; Engel *et al.*, 2015; Beck and Baumeister, 2016; Mahamid *et al.*, 2016; Pfeffer and Mahamid, 2018; Berger, Premaraj, *et al.*, 2023). This puts it in contrast with more traditional structural biology approaches, such as x-ray crystallography, where molecules are restricted in a crystal lattice. Being label-free, it is not necessary to decide which specific molecules will be imaged, instead the whole cellular milieu is captured. This, in turn, gives it great versatility, as it has been effectively employed on isolated viruses (Adrian *et al.*, 1984; Li, 2022), in vitro phase-separated protein condensates (Patel *et al.*, 2015; Wheeler *et al.*, 2016; Guillén-Boixet *et al.*, 2020; Tollervey *et al.*, 2022), whole small bacterial cells such as *Mycoplasma* (O'Reilly *et al.*, 2020), the thin periphery of larger cells (Weber, Wojtynek and Medalia, 2019; Wang, Wojtynek and Medalia, 2023), and thin slices of whole cells, called lamella (Rigort *et al.*, 2012; Villa *et al.*, 2013; Mahamid *et al.*, 2016; Schaffer *et al.*, 2017; Lam and Villa, 2021; Berger, Premaraj, *et al.*, 2023). Furthermore, the lack of chemical

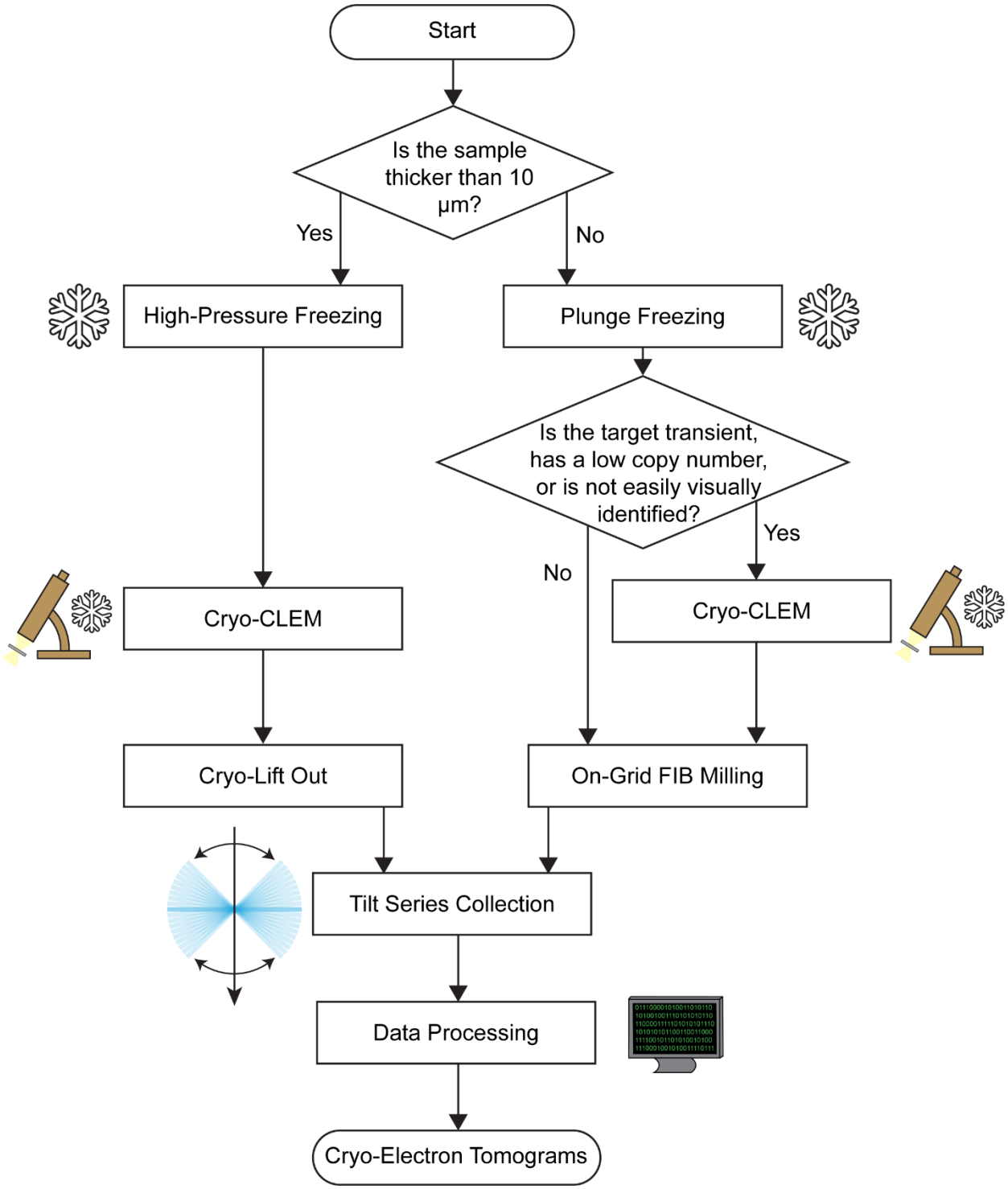

Figure 1.7: Sample preparation pipeline for cryo-ET, suitable for a variety of different biological targets. Not included is any further data processing and analysis that may be necessary on obtained tomograms, such as image segmentation and subtomogram averaging.

stains results in the molecular structures being directly imaged. This means that, given a high enough copy number, reoccurring macromolecules and complexes can be aligned and averaged together to yield higher resolution structures. Indeed, recent advancements have allowed for near-atomic resolution structures of proteins within a cell using this technique (Tegunov *et al.*, 2021; Oosterheert *et al.*, 2022). It therefore seems clear that employing cryo-ET to tackle the unknowns of the centrosome, specifically the molecular structure of the PCM, and how it partitions gamma-TuRCs, microtubules, and other clients, would be highly advantageous. However, it is not without its drawbacks and challenges. Sample preparation is highly challenging, as the sample must be rapidly frozen to maintain the ice's amorphous property, which in turn requires the sample to be thin, under a few microns (Adrian *et al.*, 1984; Dubochet *et al.*, 1987, 1988). The sample then must be rendered even thinner, under a few hundred nanometers, to be transparent to electrons, without introducing compression or cutting artefacts (Han, Sedat and Agard, 1995). Great care must then be taken at all steps to maintain the sample at cryogenic temperatures (i.e. under 135 ^{o}K / -138 ^{o}C, (Dubochet and McDowall, 1981)) while reducing surface ice contamination. Once sample preparation is complete, the data collection is a highly technical process requiring specialized equipment and expertise (Figure 1.7). Data processing can be computationally expensive. All of this means that the entire process is low throughput and not suitable for screening large numbers of conditions. In the next section, I will describe the cryo-ET workflow and best practices in detail.

1.12 Sample preparation: vitrification

A fundamental challenge of electron microscopy is that the sample must be maintained in a high vacuum, as electrons cannot travel through atmosphere without being scattered and lost. Traditional electron microscopy studies overcame this problem by embedding the sample in plastic after use of chemical fixatives (Dawes,

1971; Graham and Orenstein, 2007). However, this, and the deformations resulting from it (Kellenberger *et al.*, 1992; Murk *et al.*, 2003), can be avoided by freezing the sample. Under normal conditions, ice expands upon freezing as the water molecules arrange in a crystalline pattern. This would irreparably damage the sample. Thankfully this effect can be avoided, by locking molecules, in biological samples primarily water, in their amorphous state through incredibly rapid freezing. This state of water, termed vitreous ice, preserves biological molecules and potentially small organisms in their native state, while rendering them vacuum compatible (Dubochet and McDowall, 1981; Dubochet *et al.*, 1982).

Vitrification of samples can be achieved in one of two ways: plunge freezing (Adrian *et al.*, 1984) and high-pressure freezing (Moor, 1987; Dubochet, 1995). Plunge freezing involves applying the sample, be it protein solution, phase separated condensates, small organelles, or whole cells, on an Electron Microscopy (EM) grid. EM grids are circular, small, thin, and flat specimen holders. They are usually constructed of metal in a grid pattern within the circle, often gold or copper due to their good thermal conductivity. On top of the grid pattern, a foil of just a few nanometers thick is layered. Foils can be made of a wide variety of materials, such as carbon, gold, or silicon dioxide, often contain regularly spaced holes to allows liquid to pass through, and are there to physically support the sample. Once the sample is applied to the grid, excess liquid is blotted away, and the whole sample is plunged rapidly into liquid ethane, or an ethane/propane mix (Tivol, Briegel and Jensen, 2008), held at around -185^{o}C (Adrian *et al.*, 1984). Blotting away excess liquid is needed, as in order to trap ice in the vitreous state it must be cooled at a rate of at least 10^{4} K.s^{-1} (Brüggeller and Mayer, 1980), meaning only a few nanolitres of material can be left on the grid, else too much heat will be retained and damaging crystalline ice will form. This means the bulk of material will be lost in the blotting process. In freezing whole cells, EM grids are usually blotted from the back. Grids are plunged into propane or an ethane/propane mix as plunging into liquid nitrogen would be ineffective. Boiling nitrogen forms an insulating layer of gas between itself

and the warm surface, called the Leidenfrost effect. Plunge freezing is an effective and relatively cheap way of achieving sample vitrification, and for non-cellular samples usually requires no sample thinning, as the ice produced should already be thin enough to be electron transparent (Han, Sedat and Agard, 1995; Passmore and Russo, 2016). However, the great rates of temperature change required render it ineffective at sample thicknesses over roughly 10 μm (Adrian *et al.*, 1984; Dubochet *et al.*, 1987, 1988). The growth of in-cell cryo-ET in recent years has spurred a demand for more sophisticated approaches to freezing whole-cells on grid. Adherent cells may be cultured directly on grids, but the grids themselves must be made of a biocompatible material such as gold or titanium (Mahamid *et al.*, 2016). Oxidation of copper will result in toxic ions being released into solution. More recent developments have allowed grids to be micro-patterned, to ensure that adherent cells remain on the grid foil and not the electron-opaque grid bars (Toro-Nahuelpan *et al.*, 2020).

For samples thicker than 10 μm, such as larger cells, organoids, and small organisms including *C. elegans*, it is necessary to turn to High Pressure Freezing (HPF). Rather than trapping ice just through rapid temperature change, the sample is held under high pressure (2100 atmospheres) during the freezing process (Moor, 1987; Liu, Pokrovskaya and Storrie, 2023). This prevents ice crystal formation as the extreme pressure prevents expansion during the freezing process. As the fragile EM grids would be destroyed by the forces enacted on them in this process, sturdier planchettes, usually made of aluminium, are used in their stead. EM grids can be high pressure frozen in the so-called waffle method, in which the delicate EM grid is shielded between the planchettes (Kelley *et al.*, 2022). High pressure freezing allows samples between 100 μm and 300 μm to be effectively vitrified. However, this process has its drawbacks. Firstly, being embedded in a relatively thick block of ice contained within a metal planchette, the sample is totally electron opaque. As such, the sample must be removed from the planchette, and somehow sectioned into electron transparent slices, and then mounted onto EM grids for imaging. How this

can be done at cryogenic temperatures, which involves a process called the lift-out will be discussed in section 1.14.

1.13 Sample preparation: cryo-correlative microscopy

If, when performing *in-situ* cryo-ET, a specific region must be targeted, Correlative Light and Electron Microscopy (CLEM) may be employed. This may be because the target of interest is present at a low copy number, a subpopulation of cells, or is dynamic, all of which means it may be difficult to target it within the lamella or confirm said target's presence within the final tomogram. As a lamella typically contains less than 1% of the volume of a eukaryotic cell, there is no guarantee a lamella will contain sparsely occurring features unless specifically guided (Plitzko, Rigort and Leis, 2009; Arnold *et al.*, 2016). If the target is fluorescently tagged, it can be imaged in a light microscope first, and then correlated with either Focused Ion Beam (FIB) or Transmission Electron Microscopy (TEM) images, to track the target. However, it is a fundamental challenge of this approach that as soon as the sample has been frozen, it must be kept at cryogenic temperatures, or else the sample will devitrify and be destroyed (Dubochet *et al.*, 1982). This means that any imaging performed after cryofixation must be performed on microscopes, widefield or confocal, with specialized stages capable of holding EM grids at liquid nitrogen temperature. This also precludes the use of any oil or water immersion objective lenses, although a small number of cryo-immersion liquids exist (Faoro *et al.*, 2018). Correlations carried out prior to freezing are possible, but are rarely helpful for targeted regions that may move prior to and during the plunge freezing process.

Cryo-CLEM is regularly applied by endogenously tagging a target protein within a cell, then acquiring a z-stack in a cryo-confocal microscope. Fiducials visible in both the light and electron microscopes should also be added immediately prior to plunge freezing. These are commonly fluorescent beads. After taking images of the same

sample in the FIB, the z-stack can then be deconvolved (Shaw, 2006), resliced, and transformed in such a way that the fiducials align in both images. This allows the region of interest to be identified within FIB images for targeted milling of lamella (Arnold *et al.*, 2016). The same principle can be applied to TEM images to locate regions of interest in the field of view (Klein *et al.*, 2021).

Several major new developments have arisen in this area. One is improvement of the cryo-fluorescence microscopy techniques, with new super-resolution microscopy techniques, including cryo-SIM (Phillips *et al.*, 2020) and cryo-PhotoActivated Localization Microscopy (cryo-PALM) (Tuijtel *et al.*, 2019) being applied to cryogenic samples, although the latter requires switchable fluorophores at cryogenic temperatures. The aim of this is to bridge the gap in resolution between diffraction limited light microscopy (~200 nm) and electron microscopy (less than 1 nm), although correlating images can remain challenging. Another area of development is improving identification of molecules in cryo-electron tomograms. This would require a fluorescent tag also easily visible within the tomogram. GFP tagged proteins linking to Genetically-Encoded Multimeric particles (GEMs), based on icosahedral encapsuling proteins, are being employed to this end (Fung *et al.*, 2022). These provide both fluorescence signal and can be tracked back into the tomogram, a process aided through particle localization software (de Teresa-Trueba *et al.*, 2023).

1.14 Sample preparation: cryo-focused ion beam milling

In a 300 kV transmission electron microscope, electrons can travel only 280 nm before interference, in particular inelastic scattering, damages image quality and significantly lowers the Signal-to-Noise Ratio (SNR), a property called the mean free path. Indeed, the thinner the sample is, the greater the SNR (Passmore and Russo, 2016). Although certain samples, in particular proteins in solution, small phase separated condensates, dissociated organelles and small bacterial cells, may be

under this limit, eukaryotic cells are too large and therefore must be thinned. Historically this was done through use of a cryo-ultramicrotome (Al-Amoudi *et al.*, 2004), but this is very labor intensive, technically challenging, and error prone. Even if successful, knife marks and compression artefacts may render the sections produced unsuitable for molecular resolution analysis (Al-Amoudi, Studer and Dubochet, 2005), although there has been limited success in performing subtomogram averaging on microtomed sections (Pierson *et al.*, 2011; Bharat, Hoffmann and Kukulski, 2018). Ultimately, said artefacts will inevitably affect quantitative analysis of samples, and impair direct comparison between different samples.

A less laborious approach that prevents such artefact formation is cryo-FIB milling. Here, Ga^{+} ions are used to ablate away material above and below the region of interest, while keeping the sample well vitrified (Marko *et al.*, 2007) (Figure 1.8). Ideally the thin slices, or 'lamella' produced should be around 200 nm. Although thinner lamella result in a higher SNR, if too thin important biological context may be removed. A Scanning Electron Microscope (SEM) is built into the same machine to allow observation and tracking of the target, and information from this instrument can be combined with light microscopy data. Larger samples may be prepared on this instrument using the cryo-lift out (Mahamid *et al.*, 2015; Schaffer *et al.*, 2019), to be addressed in the next section, or through serial section imaging (Spehner *et al.*, 2020). Classically this is performed with samples vitrified on EM grids using specialized shuttles and cooling stages to prevent heating. Samples are coated with a layer of organometallic platinum to prevent damage from the ion beam, and sputtered with platinum before and after milling to enhance conductivity (Schaffer *et al.*, 2017; Wagner *et al.*, 2020). Although not enough to introduce devitrification, lamella do heat slightly upon milling, and the resulting thermal expansion can cause them to bend and break. Different compression ratios of vitreous ice and grid materials can also introduce internal stresses, which may also cause lamella breaking (Booy and Pawley, 1993; Naydenova, Jia and Russo, 2020; Thorne, 2020).

This is alleviated by milling small 'micro expansion joints' on either side of the lamella to allow reduced lamella breakage by giving them space to expand as needed (Wolff *et al.*, 2019).

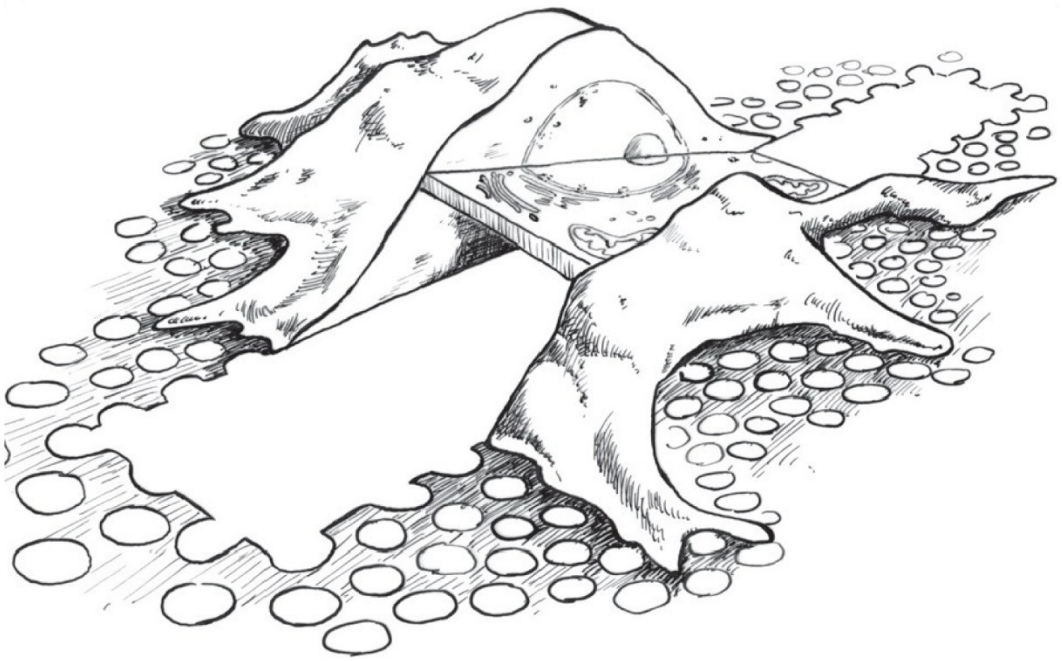

Figure 1.8: Illustration of a eukaryotic cell after cryo-FIB milling. The cell, shown on the holey foil of an EM grid, has had the area above and below a central slice of cell milled away using Ga^+ ions, leaving behind a central slice of cell, or lamella, free to be imaged in the TEM. Adapted from (Villa et al., 2013).

Several technological advances have been made to improve the effectiveness of FIB milling. As with many technical procedures, FIB milling requires much expertise. Recent advancements in automation have reduced the labor involved in making lamella, while improving reliability and reducing the time required (Zachs *et al.*, 2020; Klumpe *et al.*, 2021; Tacke *et al.*, 2021). As contaminating water ice will slowly deposit on the surface on lamella the longer the grid remains in the FIB, the reduced milling time associated with automation also translates to more lamella per grid being feasible. Later FIB instruments have improved vacuum chambers with reduced water deposition (Tacke *et al.*, 2021). FIBs are now being modified to include in-built cryo-light microscopy equipment, with commercial options becoming available

(Gorelick *et al.*, 2019; Bieber *et al.*, 2021; Boltje *et al.*, 2022). This allows correlations to be performed instantly on a sample without the associated contamination and damage associated with transferring a grid to different instruments (Thompson *et al.*, 2016).

A developing area is the use of plasma FIBs, which use the plasma of gasses such as oxygen, nitrogen, xenon, or argon, which may allow for faster milling at high currents owing to a smaller probe size at higher currents (Smith *et al.*, 2006; Berger, Dumoux, *et al.*, 2023). It is thought that these instruments will allow for much quicker lamella milling, allowing both more lamella to be milled per grid, and for thicker samples to become amenable to FIB milling.

1.15 Sample preparation: cryo-lift out

Although the procedure described in the previous section is suitable for samples prepared by direct plunge freezing on an EM grid, it is less appropriate for samples that have been high-pressure frozen. Not only does the bulk of the ice make the milling time impractical, the planchette required for HPF is made material that cannot be milled through on a reasonable timescale. Therefore, generating lamella directly from a HPF sample is impractical. An alternative approach has accordingly been developed: cryo-lift out. This procedure already existed for room temperature approaches in the material sciences (Langford and Clinton, 2004), and has more recently been applied towards biological samples (Mahamid *et al.*, 2015; Schaffer *et al.*, 2019). The lift out involves first milling wide and deep trenches on either side of the region of interest, to create a thick (several micron wide) slab. Use of correlative approaches are of particular importance here, as physical specimen features in HPF samples are harder to see in the FIB than those frozen in a grid, buried as they are in the bulk ice. Micromanipulators, either in the form of grippers or a needle probe, can then come in and make contact with the slab and physically remove it from the bulk

specimen, placing it on a specialized EM grid, containing holders for these samples. This slab can then be further polished down to the desired ~200 nm for cryo-ET imaging. Recent modifications to this procedure mean more lamella can be obtained from a single block, allowing for cryo-semi-serial sections of a thick specimen (Schiøtz *et al.*, 2023). However, the lift out remains technically challenging. The micromanipulators require very fine control else the sample will be damaged or lost, or in more extreme cases, the manipulators themselves may be destroyed. This means that any work involving the lift out can be slow, expensive, and dependent on highly-trained operators. Improvements in FIB automation have allowed milling to be automated, but at present sample transfer remains manual.

1.16 Data collection: transmission electron microscopy image formation

The basic principle of all transmission microscopy is that radiation passes through the sample, is modified, and then captured on a detector. In transmission electron microscopy, electrons pass through a thin biological sample, and are scattered by its Coulomb potential. This scattering can be elastic or inelastic in nature. Elastic scattering means the transmitted electrons leave the sample with the same energy they entered with. By contrast inelastically scattered electrons transfer some energy into the sample. Inelastically scattered electrons, do not transfer information to the image in TEM and instead contribute to the noise, although they are used in Scanning Transmission Electron Microscopy (STEM) (Elbaum, Wolf and Houben, 2016). The thicker the sample the more inelastic scattering events there will be, hence the requirement for thin samples to maximize SNR (Henderson, 1995; Glaeser *et al.*, 2016). Use of an energy filter can remove the inelastically scattered electrons, improving image quality (Egerton, 2009; Fukuda *et al.*, 2015).

Contrast in images arises from a combination of both amplitude and phase contrast (Orlova and Saibil, 2011). As biological samples are made primarily of light atoms similar to the vitreous ice background, mostly hydrogen, carbon, nitrogen, and oxygen; very few electrons are absorbed or deflected, and amplitude contrast only contributes to around 7% of the image (Penczek, 2010). Instead, phase contrast contributes to much of the image. Phase contrast arises from the interference between the elastically scattered and inelastically scattered electrons at the image plane within the microscope, resulting in an induced phase shift, giving contrast in the final image. However, this is interference, and thus contrast, is very low when the microscope is at focus. Images are therefore taken at a defocus of between 1 and 5 μm, which results in greater phase modulation and thus contrast (Glaeser *et al.*, 2016). However, this modulation, or Contrast Transfer Function (CTF) must also be accounted for, and will be discussed in a later section.

The phase of the beam can be modulated more through use of a Volta phase plate. This works by introducing a known phase shift into the electron beam, by passing it through a region of amorphous carbon that has been pre-treated by exposing it to electrons. This generates electrostatic potential, which in turn introduces a 90^{o} phase shift in the scattered electron beam. The phase shift enhances the low-frequency contrast when recombined at the image plane (Danev *et al.*, 2014; Danev and Baumeister, 2016; Danev, Tegunov and Baumeister, 2017), although this is not recommended for very high resolution, i.e., sub 6 Å, studies as information higher frequency than this may be lost, or image quality may be impacted by charging effects (Buijsse *et al.*, 2020; Turoňová *et al.*, 2020). Laser phase plates, currently under development, may introduce the phase shift without the loss of this high resolution information (Schwartz *et al.*, 2019).

Data are recorded on direct electron detectors. Rather than recording static images, these record short movies, which can then have their frames aligned to account for beam-induced motion of the specimen once exposed to electrons and then averaged

together (Brilot *et al.*, 2012; Li *et al.*, 2013). As noise is random but signal is not, the noise in each frame will be averaged out, increasing the SNR of the resulting averaged movie. However, it is important to correctly account for the movement of the stage and beam induced motion of the sample between frames to prevent blurring of the final result (Scheres, 2014; Zheng *et al.*, 2017).

1.17 Data collection: tilt series acquisition and tomographic reconstruction

The end goal of the data collection is the recreation of the 3D volume of the biological specimen, from 2D projection images. Consequently, the sample is physically tilted at different angles within the microscope, with images taken at each angle. Given the thin, flat shape of the sample, this functionally increases the thickness of the sample at high tilts, and reduces the SNR of the produced projection images (Glaeser, 2013; Glaeser *et al.*, 2016). This effect combined with the physical limitations of the stage mean that tilts are limited between +60° and -60° within the microscope. This produces a gap within the data, most noticeable in Fourier space, termed the 'missing wedge' (Wan and Briggs, 2016a) (Figure 1.9).

As with all forms of structural biology, one must be mindful of the electron dose when performing cryo-ET, as radiation damage is the ultimate limiting factor of resolution (Glaeser and Taylor, 1978). With tomography, not only is resolution further limited by the Crowther criterion (i.e. tomographic resolution is limited by the number of views, with smaller particles in particular requiring more views (Crowther, DeRosier and Klug, 1970)) but the electron dose must be spread across ~61 individual projection images, dependent on one's tilt scheme. Although a dose-symmetric scheme can result in the thinnest and thus highest SNR images having the lowest accumulated dose (Hagen, Wan and Briggs, 2017), it is still important to minimize the dose on the acquisition area as much as possible. This can be done by acquiring focus

and tracking information between tilts at an area adjacent to the acquisition area, parallel to the tilt axis. This saves electrons for image acquisition. Overall, 100-120 electrons per square angstrom should be used per tilt series, to prevent the worst effects of radiation damage.

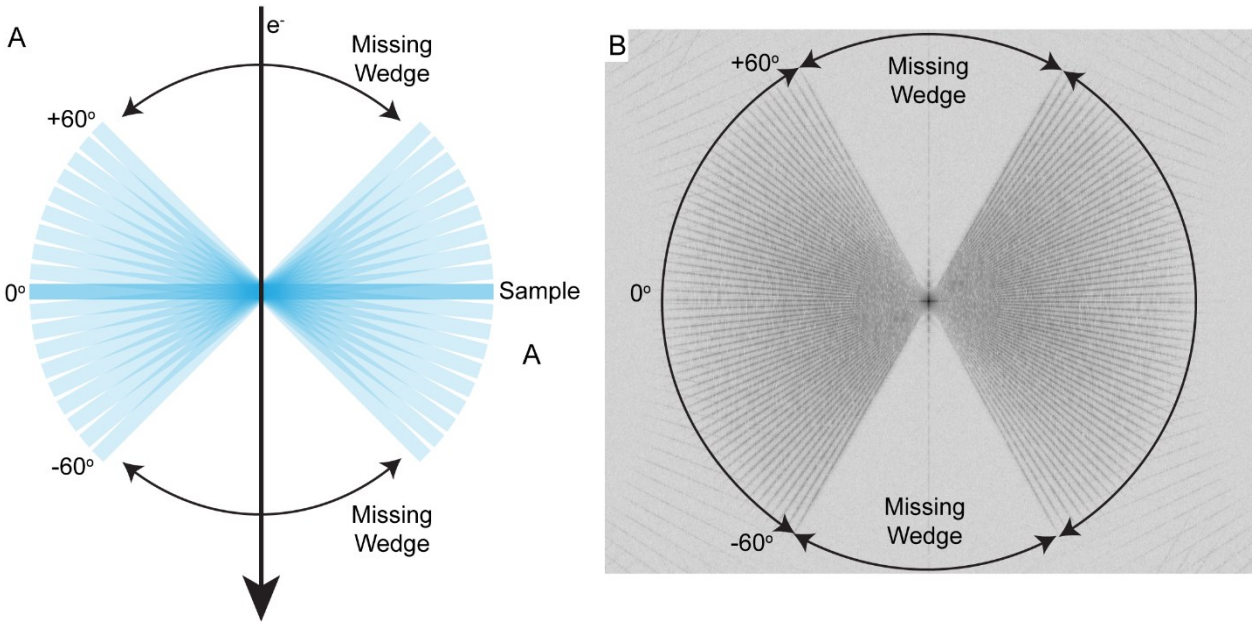

Figure 1.9: Sample tilting and missing wedge formation. A: Schematic showing sample titling from -60° to +60° in the TEM, with the gap in real space data shown. Electron path is shown by an arrow labelled with an e^-. B: missing wedge in the Fourier transform of a real data set. Each tilt image can be seen as a black line. The gap between black lines corresponds to the tomogram's missing wedge.

Once a tilt series has been acquired, it must be reconstructed into a 3D tomogram. This is normally done via a weighted back projection (Figure 1.10), but can also be done via other approaches which boost the SNR in the final tomogram by emphasizing low-frequency signals such as Simultaneous Iterations Reconstructions Technique (SIRT). It is important to align individual tilts before alignment, as the alignment quality will affect the overall quality of the tomogram. Ideally this is done using high-contrast fiducials such as 10 nm gold nanoparticles. However, this is not always possible, especially with lamella, where applying a fiducial to an already vitrified sample after milling is often impractical. In these cases, small patches of each image are tracked between tilts. Although the widely used software for tilt-

series alignment is Etomo, part of the IMOD package (Mastronarde and Held, 2017), the newly developed Aretomo (Zheng *et al.*, 2022) offers much of the same alignment functionality in a more automated fashion.

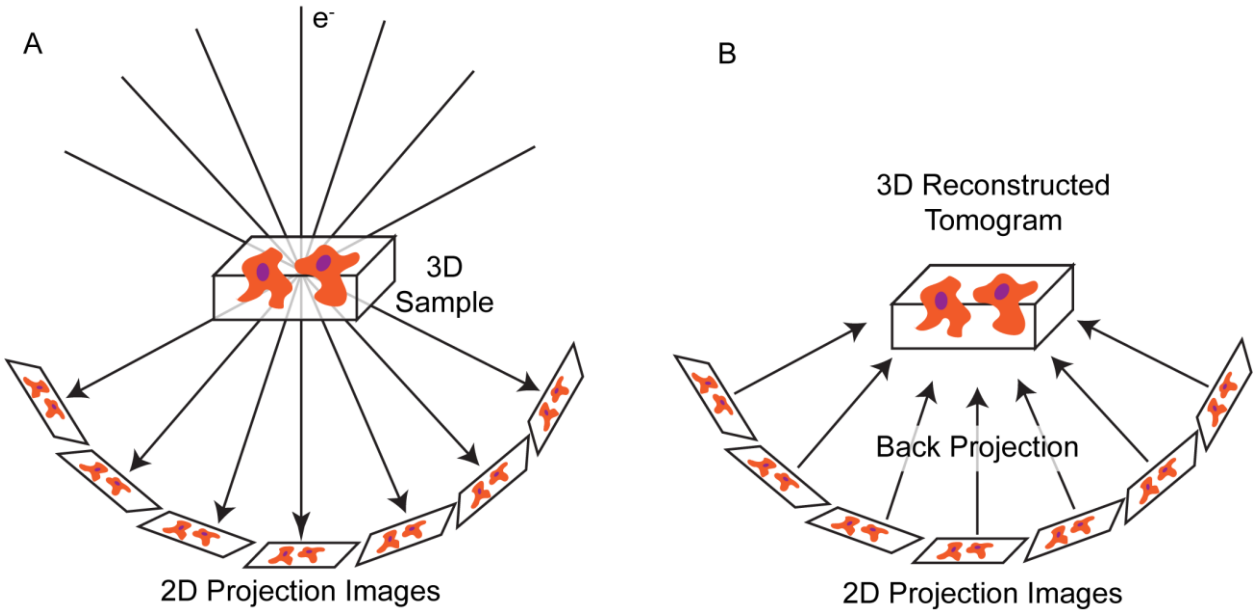

Figure 1.10: Tilt series collection and tomogram reconstruction. A: during data collection, sample tilting creates a series of images at different angles. B: during tomogram reconstruction, the images are back-projected into a 3D volume.

1.18 Data analysis: denoising

Although the tomograms generated may contain a wealth of biological information, the low SNR inherent to this technique can obscure much of it. Various denoising approaches can be applied to improve SNR, although these often come at a cost of damping high frequency, high resolution information. Basic denoising approaches might involve a simple mathematical function, such as applying a Gaussian filter a few voxels wide over the entire tomogram. More advanced denoising approaches involve deep learning methods, such as Content-Aware image REstoration, or cryo-CARE. This requires two sets of independent noise, so the system can learn to differentiate signal from noise. This can be provided by generating two tomograms,

generated from either odd or even tilts, or odd and even frames from the detector. From these, a model is trained using predefined network architecture. The trained model is then applied to complete tomograms, where it enhances signal while repressing noise (Buchholz *et al.*, 2018; Weigert *et al.*, 2018). Denoised tomograms should not be used for subtomogram averaging studies due to loss of high-resolution information, and to prevent denoising artefacts persisting in the data.

1.19 Data analysis: segmentation

Tomograms, even well denoised tomograms, only show the Coulomb potential of the volume imaged, and as such cannot be used to show cellular structures and macromolecules without a labelling step. This assignment of voxels, called segmentation, is a challenging bottleneck of analysis due to the low SNR of tomograms complicating automated procedures, while manual approaches are very time consuming and may not be as reproducible. Regardless, automated approaches have been attempted.

The traditionally used method for localizing macromolecules in a tomogram is template matching. As the name would suggest, template matching requires a pre-existing template based on the known structure of interest, be it an already solved macromolecular structure such as a ribosome (Böhm *et al.*, 2000; Wu *et al.*, 2019; Lucas *et al.*, 2021), or a simple geometric shape in the case of microtubules or actin (Rusu *et al.*, 2012; Redemann *et al.*, 2014). In the case of existing molecular structures, they are often low-pass filtered to ensure that only the low frequency information, such as overall particle shape, is carried forward, rather than trying to fit high resolution noise. A 3D cross correlation function is then run using this template on the entire tomographic volume: a highly computationally expensive procedure. This is only applicable on large easily detectable macromolecular complexes; smaller complexes are likely to be missed. Furthermore, this technique is prone to picking a

large number of false positives, which must be then inspected and removed in a lengthy manual process (Böhm *et al.*, 2000; Nickell *et al.*, 2005; Hrabe *et al.*, 2012; Wan and Briggs, 2016a).

More developed segmentation techniques involve, once again, the use of deep learning. These have been used to automatically annotate tomograms, streamlining the procedure, and reducing manual input, as well as in some cases being less computationally expensive (Chen *et al.*, 2017; Lee *et al.*, 2018; Wang *et al.*, 2022). Recently a tool called Deep Picker in Context (DeePiCt) has been developed to this end and has been used to great effect. After training on tomograms and binary maps corresponding to the cellular features of interest, the program uses convolutional neural networks for pattern recognition, allowing for the detection of less abundant and harder to detect structures, such as the hollow-caged shape fatty acid synthase complex. This is less computationally expensive and requires less input than template-based approaches, but requires already segmented tomograms to train models (de Teresa-Trueba *et al.*, 2023).

1.20 Data analysis: subtomogram averaging and CTF estimation.

The low SNR of tomograms acts as a limitation on how much information can be gleamed from otherwise very high-resolution data. The resolution of repeating structures, such as the many ribosomes inside a cell or the repeating units of a microtubule, can be greatly increased through use of subtomogram averaging. These units, henceforth particles, can be extracted from the data, either by simply cropping them out of the larger volume or by performing a local reconstruction from the original tilt series (Pyle and Zanetti, 2021). Particles are then cross correlated in Fourier space to a reference structure, either from an extant map, or from an original unaligned average of the subtomograms. This cross correlation is then used to

determine a series of shifts and rotations required to best orient the particles to the reference (Wan and Briggs, 2016b). This process can be continued iteratively, either simply using the assigned averages from the highest cross correlation score, or by using maximum likelihood approaches where all orientations contribute to the average, but are weighted according to the probability of each individual orientation (Scheres, 2010; Stölken *et al.*, 2011). It is necessary to compensate for the missing wedge to prevent particles erroneously matching onto the wedge (Wan and Briggs, 2016b).

When aligned and averaged in this way, a single average with higher resolution and SNR can be obtained, which in turn reveals the molecular properties of the complex (Wan and Briggs, 2016a) (Figure 1.11). Particles can also be classified into sub-populations which in turn can be used to remove falsely picked particles or identify heterogeneity of particles within cells. Many computational tools exist to aid one in this process (Nickell *et al.*, 2005; Castaño-Díez *et al.*, 2012; Hrabe *et al.*, 2012; Galaz-Montoya *et al.*, 2015; Himes and Zhang, 2018; Wan *et al.*, 2020; Kimanius *et al.*, 2021).

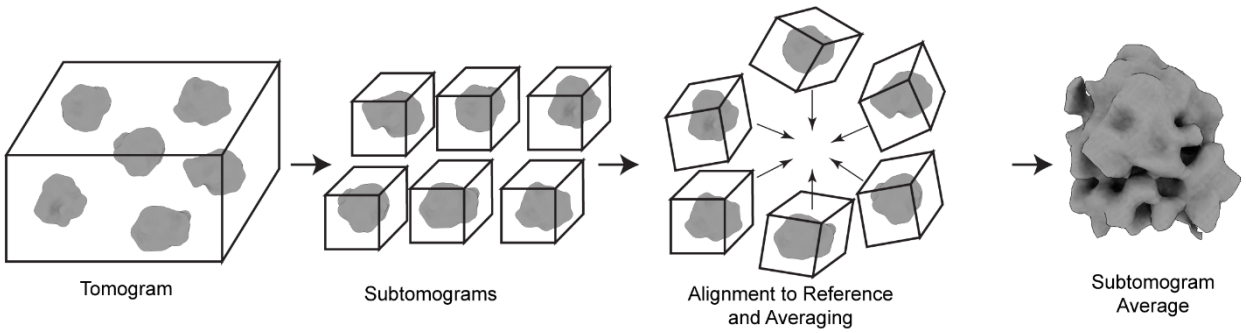

Figure 1.11: Subtomogram averaging procedures. Repeating units are cropped from the whole tomogram, aligned to one another, and averaged into a subvolume with a greater SNR and resolution than the original tomogram. This process can be repeated iteratively. Inspired by (Wan and Briggs, 2016).

For this to be carried out to best effect, it is necessary to account for the image modulations arising from defocus, phase shift, and optical aberrations within the

microscope. This cumulative effect is called the Contrast Transfer Function (CTF), and can be computationally corrected for. In tomography, as a sample tilts, different objects will be held at different heights relative to one another, resulting in a defocus gradient along the tilting axis. Although various packages exist for CTF estimation and correction (Rohou and Grigorieff, 2015; Zhang, 2016; Turoňová *et al.*, 2017; Tegunov and Cramer, 2019), the basic principle of all of them is that a radial average of the Fourier spectrum in TEM images is fit against a CTF model under certain conditions. From this the individual modulations can be determined and corrected for in the data.

Recently, *in-situ* subtomogram averages have approached near-atomic resolution, in both small *Mycoplasma* cells and lamella from eukaryotes (Tegunov *et al.*, 2021; Oosterheert *et al.*, 2022). To reach this more extreme resolutions, it is necessary to perform both per-particle CTF estimation (Turoňová *et al.*, 2017; Tegunov and Cramer, 2019), and to consider per-particle physical deformations of the sample during imaging (Himes and Zhang, 2018).

1.21 Data analysis: protein structure prediction

Determining a protein's structure from its primary protein sequence has long been a challenge of molecular biology. Thankfully, recent developments have largely solved this long-standing question. AlphaFold2 is a reliable piece of protein prediction software that can be used to accurately predict a protein's structure from just its sequence, using both bioinformatics data and physical restrictions (Jumper *et al.*, 2021). Crucially it is capable of assigning confidence scores to its predictions, meaning poor quality estimations can be quickly identified. Additionally, AlphaFold2 has been applied to multimers, which can be used to see which normally unstructured proteins adopt a regular conformation upon multimerization (Evans *et al.*, 2022). This has been a boon for the world of tomography, as previously

unidentified densities can be assigned molecular identity based on their similarity to these predicted structures, if high enough resolution maps of the density can be obtained using averaging (Chen *et al.*, 2022).

2. Project motivation and open questions

Despite over a century of work, no study to date has been able to show the molecular detail of the centrosome, and specifically the PCM, at a molecular level. Being able to do so would answer long-standing questions about the material nature of the PCM, and how it functions within the centrosome. In order to do this, I set about applying cryo-electron tomography. Unlike fluorescence-based approaches, ET is label-free, allowing one to see all the centrosomal components simultaneously. However, traditional room temperature electron microscopy involves both fixing and embedding the sample in plastic, followed by application of heavy metal stains. This respectively allows for the sample to survive the vacuum of the electron column, and for it to have enough contrast to be properly interpreted. Working with cryogenic samples involves neither, as the sample is held in a near-native state, and thus prevents the sample warping, deformation, and effects of imperfect staining inherent to room temperature samples (Adrian *et al.*, 1984; Kellenberger *et al.*, 1992; Murk *et al.*, 2003). Furthermore, as there already exists a method to reconstitute a minimal centrosome *in vitro* (Woodruff *et al.*, 2017), I attempted to view this at molecular resolution to investigate its effectiveness as a tool for centrosomal study as a complement for the complex in vivo scenario. As such, the aims of this thesis are:

1. To perform cryo-electron tomography and analyze SPD-5 condensates and asters under a variety of conditions
2. Develop a workflow through which *C. elegans* embryos can regularly be subjected to cryo-ET
3. Obtain tomograms of the *C. elegans* centrosome, at various points of the cell cycle
4. From these tomograms, determine:
   4.1. The overall structure of the centrosome
   4.2. The role the centrosome has in organizing microtubules

4.3. The location, orientation, and structure of gamma-TuRCs within the centrosome

4.4. The molecular architecture and structural properties of the PCM

3. Methods

3.1 Reagents, media, strains, equipment, and software

Table 3.1: all compounds and reagents used in this study

Compound	Source	Notes/Use
HEPES	Sigma-Aldrich	Condensate buffer
KCl	Sigma-Aldrich	Condensate buffer
DTT	Thermo Fischer Scientific	Condensate/aster buffer
Tris-HCl	Sigma-Aldrich	Aster buffer
CHAPS	Sigma-Aldrich	Aster buffer
Glycerol	Merck	Aster buffer
NaCl	Sigma-Aldrich	Aster buffer
Adenosine Triphosphate	Sigma-Aldrich	PLK-1 substrate
$MgCl_2$	Sigma-Aldrich	ATP stabilization/BRB80
PEG-3350	Sigma-Aldrich	M9 media/molecular crowding agent
Paraformaldehyde	Sigma-Aldrich	Fixative
K-PIPES	Sigma-Aldrich	BRB80
EGTA	Sigma-Aldrich	BRB80
Guanosine triphosphate	Thermo Fischer Scientific	Tubulin polymerization
Agar	Thermo Fischer Scientific	NGM plates
Peptone	Thermo Fischer Scientific	NGM plates
$CaCl_2$	Sigma-Aldrich	NGM plates
Cholesterol	Sigma-Aldrich	M9 media
KH_2PO_4	Sigma-Aldrich	M9 media
Na_2HPO_4	Merck	M9 media
$MgSO_4$	Merck	NGM plates/M9 media
L15-Media	Thermo Fischer Scientific	Without phenol red
Fetal Bovine Serum	Gibco	Modified L-15 Media
Pen-Strep mix	Gibco	Modified L-15 Media
Sucrose	Thermo Fischer Scientific	Modified L-15 Media
5% bleach	Thermo Fischer Scientific	Bleaching solution
NaOH	Merck	Bleaching solution
Chitinase	Sigma-Aldrich	Digestion of eggshell
Accutase	Stemcell Technologies	Cell protease
HCl	Merck	Acid washing coverslips
Poly-l-lysine	Sigma-Aldrich	Cell substrate

Table 3.2: all media and buffers prepared in this study

Buffer/Media	Composition	Notes
Condensate Buffer	25 mM HEPES pH 7.4, 150 mM KCl, 0.5 mM DTT	Keep on ice until ready. DTT must be added fresh
Aster Buffer	50 mM Tris pH 7.4, 500 mM NaCL, 0.1% Chaps, 1 % Glycerol, 0.5 mM DTT	As above. From (Woodruff *et al.*, 2017)
BRB80 Buffer	80 mM K-PIPES, 1 mM $MgCl_2$, 1 mM EGTA	For tubulin polymerization. From ('BRB80 (5x)', 2016)
NGM Media	3 g NaCl, 17 g agar, 2.5 g peptone, 1 ml 1 M CaCl, 975 ml H_2O. Autoclaved and supplemented with 1ml 5 mg/ml cholesterol, 1 ml 1 M $MgSO_4$, 25 ml 1 M KPO_4	After autoclaving, use sterile technique. Pour into petri dishes while still hot, then allow to cool. Once formed, should be refrigerated until use. From (Brenner, 1974)
M9 Media	3 g KH_2PO_4, 6 g Na_2HPO_4, 5g NaCl, 1 mM $MgSO_4$, 0.1% PEG 3350, made up to 1 L with H_2O	Autoclave after preparation. From (Brenner, 1974)
Modified L-15 Media	L-15 media without phenol red (Thermo Fischer Scientific), 10% FBS, 50 U/ml pen-strep mix (Thermo Fischer Scientific), sucrose up to 340 mOsm	Filter sterilize after preparation. Keep cold until use. From (Strange, Christensen and Morrison, 2007)

Table 3.3: proteins used in this study

All proteins provided by Jeff Woodruff of UT Southwestern, expressed in and purified from SF+ insect cells, except for tubulin which is purified from pig brain.

Protein	Concentration as provided
SPD-5	5 µM
SPD-5::RFP	500 nM, for condensates
SPD-5::GFP	5 µM, for asters
Phosphomimetic SPD-5::GFP	500 nM
PLK-1, constitutively active	500 nM
Pig brain tubulin	95 µM
TAMARA labelled tubulin	200 µM
TPXL-1	10 µM
ZYG-9	5 µM

Table 3.4: *C. elegans* strains used in this study

Geotype	Source	Identifier
unc-119(ed9) III; ltSi202[pVV103/ pOD1021; Pspd-2::GFP::SPD-5 RNAiresistant;cb-unc-119(+)]II; ltIs37 [(pAA64) pie-1p::mCherry::his-58 + unc-119(+)] IV.	(Mittasch *et al.*, 2020)	JWW69
spd-2(or293) I; unc-119(ed9) III; ltSi202[pVV103/ pOD1021; Pspd-2::GFP::SPD-5 RNAiresistant;cb-unc-119(+)]II; ltIs37 [(pAA64) pie-1p::mCherry::his-58 + unc-119(+)] + him-8(e1489) IV	Cross between EU780 (O'Rourke *et al.*, 2011) and JWW69. From the Woodruff lab.	JWW159

Table 3.5: Laboratory consumables used in this study

Article	Source
7x20 mm ultracentrifuge tubes	Beckman Coulter
Protein A 10 nm gold fiducials	Aurion
35 mm low-type µ dishes, polymer coverslip	Ibidi
Carbon foil holey R 2/1 200 copper mesh EM grids	Quantifoil Micro Tools
Grid boxes	Subangstrom
100 mm petri dishes	
40 µm cell strainer	Falcon
1.5 ml safe lock tubes	Eppendorf
20 µm cell strainer	Pluristrain
10 µm cell strainer	Pluristrain
SiO2 foil holey R 1/4 Au Grid 200 mesh EM grids	Quantifoil Micro Tools
Autogrids and clip rings	Thermo Fischer Scientific

Table 3.6: Laboratory equipment used in this study

Article	Source	Description/Use
TLA-100 rotor	Beckman Coulter	Centrifuging protein mixes
Optima MAX-TL ultracentrifuge	Beckman Coulter	Centrifuging protein mixes
Zeiss Axio Observer	Zeiss Microscopy	Examining condensates, asters, and cells prior to freezing
Plan-apochromat 64x oil immersion objective	Zeiss Microscopy	N.A 1.4. Examining condensates and asters prior to freezing
PELCO easiGlow	Ted Pella	Glow discharger, for rendering EM grids hydrophilic
VitRobot mark 4	Thermo Fischer Scientific	Plunge freezer. Vitrifying protein condensates and asters
Centrifuge 5424 R	Eppendorf	Benchtop centrifuge
Thermomixer compact	Eppendorf	Benchtop thermomixer
LD Plan-Neofluar 20x air immersion objective	Zeiss Microscopy	N.A 0.4. Examining cells prior to freezing
Zeiss 780 NLO microscope	Zeiss Microscopy	Live cell imaging
Plan-apochromat 63x oil immersion DIC objective lens	Zeiss Microscopy	N.A 1.2. Live cell imaging
Leica EM GP2	Leica Microsystems	Plunge freezer. Vitrifying cell cultures
Leica TCS SP8, with prototype cryo-stage	Leica Microsystems	Prototype cryo CLEM
HC PL APO 50x cryo air immersion objective	Leica Microsystems	N.A 0.95. For cryo CLEM
Aquilos 1 dual beam microscope	Thermo Fischer Scientific	Focused ion beam
Titan Krios	Thermo Fischer Scientific	Cryo-TEM
Quantum post column energy filter	Gatan	Cryo-TEM energy filter
Volta phase plate	Thermo Fischer Scientific	Cryo-TEM phase plate
K2 summit direct electron detector	Gatan	Cryo-TEM camera

Table 3.7: All software used in this study

Software	Description
Zeiss ZEN pro 2.3	Zeiss microscope control
Leica Application Suite X 3.5.5	Leica microscope control
Maps 2.5	Navigation within the Aquilos
Fiji 2.9.0	Image analysis
SerialFIB 1.0	Automatic FIB milling
SerialEM 3.8	Cryo-ET image acquisition and TEM control
Warp 1.0.9	CTF correction, tomogram and subtomogram reconstruction
IMOD 4.1.1	Tilt series alignment
cryoCARE 0.2.1	Tomogram denoising
MATLAB 2016/2019a	Programing environment
TOM toolbox	MATLAB based toolkit for subtomogram averaging
Amira 2021.1	Imaging processing and segmentation
DeePiCt	Automated segmentation
Chimera	3D depiction and visualization
ChimeraX	3D depiction and visualization
Dynamo 1.1.514	MATLAB based toolkit for subtomogram averaging
RELION 4.0.1	Cryo-Electron Microscopy (cryo-EM) averaging
Ilastik 1.3.3	Learning and segmentation toolkit
Python 3.11	Programing environment
Skan 0.11	Skeleton analysis
Graphpad Prism 9.5.1	Graphing software

3.2 Sample preparation of protein condensates

All proteins were kindly provided by my collaborator Jeff Woodruff of UT Southwestern Medical Center. Prior to sample preparation, condensate buffer was prepared (25 mM HEPES, pH7.4, 150 mM KCl, 0.5 mM fresh Dithiothreitol (DTT)), and kept on ice until needed. All steps are carried out on ice unless otherwise stated. For experiments with wild-type aged and young SPD-5, 5 µl of condensate buffer, 0.5 µl of 4 mM ATP and 200 mM $MgCl_2$, 0.5 µl of 10 mM DTT, 1 µl of 500 nM SPD-5::GFP, and 3 µl of 30% polyethylene glycol (PEG) molecular weight 3350, were added in that order to make 10 µl final solution. Phosphomimetic SPD-5 condensates were prepared identically, except wild-type SPD-5 was swapped for the phosphomimetic. PLK-1 phosphorylated SPD-5 was prepared with 4 µl of condensate buffer, 0.5 µl of

4 mM ATP and 200 mM $MgCl_2$, 0.5 µl of 10 mM DTT, 1 µl of 500 nm SPD-5::GFP, 1 µl of 500 nM PLK-1 and 3 µl of 30% PEG. Young condensates were plunge frozen immediately, whereas all other proteins, and for light microscopy experiments, condensates were left to age for 15 mins in a test tube at room temperature. In later experiments, i.e. after a full dataset had been collected on SPD-5, the SPD-5 solution was first ultracentrifuged in a TLA-100 rotor (Beckman Coulter) using cold 7x20 mm ultracentrifuge tubes (Beckman Coulter) at 80,000 RPM and 4°C for 5 minutes in an Optima MAX-TL ultracentrifuge (Beckman Coulter), and the supernatant retained to remove protein aggregate, and a final concentration of 0.05% paraformaldehyde (PFA) added to the condensate solution. 2 µl of protein A 10 nm gold fiducials (Aurion) per grid frozen was centrifuged at 14,000 RPM at 4°C, until the fiducials collected in the pellet. The supernatant was then replaced with an equal volume of condensate buffer supplemented with 9% PEG.

Before plunge freezing, protein condensates were investigated in a Zeiss Axio Observer (Zeiss Microscopy) to ensure that condensates were both forming correctly, and settling on an EM grid. A 64x oil immersion objective (Numerical Aperture (NA) 1.4) was used to image 4 µl of condensate solution and 2 µl of fiducials, either under a converslip, or on an EM grid. To image condensates on a grid, Quantifoil R 2/1 on 200 copper mesh grids (Quantifoil Micro Tools) were plasma cleaned on both sides in a PELCO easiGlow (Ted Pella) for 45 seconds at 0.37 mBar and 15 mA. A grid was then placed in an Ibidi 35 mm low-type µ dishes with a polymer coverslip (Ibidi), which was then place in the microscope chamber. 4 µl of condensate solution was added, and the protein allowed to settle. In particular, I was looking for condensates not settling to the bottom of the grid, or dissolution of condensates on the grid, as this would require conditions to be altered.

Plunge freezing of grids was done in a VitRobot mk 4 (Thermo Fischer Scientific). This machine produces a gradient of ice thickness across the grid, ensuring at least one section will have appropriate ice thickness for cryo-TEM imaging. 4 µl of condensate

solution and 2 µl of fiducials were added per grid. Grids were blotted at blot force 0 and a blot time of 3 seconds, with no wait or drain time. Chamber conditions were 22°C and 90% humidity. Grids were plunged into ethane cooled by liquid nitrogen and immediately transferred into grid boxes (Subangstrom) until ready for tilt series acquisition.

3.3 Sample preparation of microtubule asters

Rather than growing asters in a test tube, it was decided to grow asters directly on an EM grid to reduce the damage of shear forces arising from pipetting. To prevent evaporation of the solution on the grid, due to the very low volumes involved, the grid was mounted on tweezers and placed inside an airtight plastic container padded with damp tissue paper. For light microscopy screening, this was done in a droplet on an EM grid in an Ibidi 35 mm low-type µ dish with a polymer coverslip (Ibidi), also padded with damp tissue.

All of the following is carried out on ice unless otherwise stated. Asters were prepared by first preparing the following working solutions: aster buffer was prepared to final concentrations of 50 mM Tris pH 7.4, 500 mM NaCl, 0.1% CHAPS, 1% glycerol, 0.5 mM DTT. A SPD-5 work solution was prepared by mixing 8 µl of 5 µM unlabeled SPD-5 and 1 µl of 5 µM SPD-5::GFP. 5.6 µl of this was mixed with 19.4 µl cold aster buffer in an ultracentrifuge tube. A tubulin work solution was obtained by mixing 10.5 µl of 95 µM unlabeled tubulin, 1.25 µl of 200 µM TAMRA labelled tubulin, and 13.25 of 20 mM GTP in an ultracentrifuge tube. The two were spun in a TLA-100 rotor (Beckman Coulter) at 80,000 RPM and 4°C for 5 minutes, and the supernatant retained to remove protein aggregate. While this was being done, TPXL-1 and ZYG-9 work solutions were made by mixing 2 µl of 20 µM TXPL-1 with 18 µl of dH2O and 4 µl 5 µM ZYG-9 with 16 µl dH2O respectively. Additionally, 30% PEG, 10 mM DTT, 5x BRB80, and 20 mM DTP solutions were prepared and kept on ice. It is

important for the GTP and DTT to both be prepared fresh, of if frozen they cannot be refrozen after thawing. Fiducials were also prepared by centrifuging 2 µl of protein A 10 nm gold fiducial (Aurion) per grid frozen at 14,000 RPM at 4°C, until the fiducials collected in the pellet. The supernatant was then replaced with an equal volume of aster buffer supplemented with 9% PEG.

For every sample, asters were prepared individually in droplets at room temperature, with components added in the following order: 0.8 µl of dH2O, 0.8 µl of 5x BRB80, 0.2 µl of 20 mM GTP, 0.2 µl 10 mM DTT, 0.4 µL 25 µM SPD-5 mix, and 1 µl of 30% PEG. Wait 30 seconds for condensates to form, then add 0.2 µl of 2 µM TPXL-1 and 0.2 µl of 2 µM ZYG-9. Wait 2 minutes for TPXL-1 and ZYG-9 to concentrate into the condensates, then add 0.2 µl of 50 µM tubulin solution. At this point, wait either 0, 5, or 10 minutes for microtubules to nucleate, before adding 1.4 µl of fiducial mix and 0.6 µl of 0.5% PFA to stop the reaction.

Light microscopy was carried out on a Zeiss Axio Obsersver fluorescence light microscope using a 64x oil immersion objective (NA 1.4), either directly on an ibidi dish or on an Quantifoil R 2/1 on 200 copper mesh grid (Quantifoil Micro Tools), plasma cleaned on both sides in a PELCO easiGlow (Ted Pella) for 45 seconds at 0.37 mBar and 15 mA.

Plunge freezing was carried out using a VitRobot mk 4 at blot force 0 and a blot time of 3 seconds, with no wait or drain time. Back blotting only was used, so the front filter paper was replaced with a Teflon pad. Chamber conditions were 22°C and 90% humidity. Grids were plunged into ethane and immediately transferred into grid boxes (Subangstrom) until ready for tilt series acquisition.

3.4 Embryonic cell dissociation

Fluorescent and temperature sensitive worm strains were generously provided by my collaborator Jeff Woodruff of UT Southwestern Medical Center. To conduct the experiments, except for work on temperature-sensitive mutants, *C. elegans* worms expressing GFP::SPD-5 and H2B::mCherry were cultured at 22°C on Nematode Growth Media (NGM) with OP50 until they reached the adult gravid stage, following the protocols described in (Brenner, 1974; Porta-de-la-Riva *et al.*, 2012). The temperature-sensitive SPD-2 strain (or293ts, from (O'Rourke *et al.*, 2011)) was maintained at 15°C and transferred to 25°C for 4 hours before dissociation.

For each preparation, at least four 100 mm petri dishes with worms were grown until the bacteria were almost fully consumed to ensure a higher number of worms without starving them. The plates were washed off with M9 media, supplemented with 0.1% polyethylene glycol (PEG) 3350 (Sigma Aldrich). The washed material was then passed through a 40 µm cell strainer (Falcon) to remove leftover bacteria, laid eggs, and larvae. The retained material on the strainer was washed into 1.5 ml safe lock tubes (Eppendorf, henceforth Eppendorf tubes) and centrifuged three times at 600 RCF for 6 minutes at 22°C. After each centrifugation, the supernatant was aspirated, and 1000 µl of M9 with 0.1% PEG was added.

Fresh bleaching solution was prepared each day by combining 750 µl H2O, 600 µl 5 M NaOH, and 450 µl 5% bleach (Thermo Fischer Scientific). After 1 round of centrifugation and supernatant removal as described above, the worms were split, and approximately 10 µl of worm pellet was visible per tube. To each Eppendorf tube, 450 µl M9 with 0.1% PEG and 150 µl bleaching solution were added. The tubes were shaken on a thermomixer compact (Eppendorf) at 1400 RPM and 22°C for 13 minutes. The resulting mixture was immediately transferred to a benchtop centrifuge 5424 R (Eppendorf) and spun at 600 RCF for 6 minutes at 22°C. The supernatant was removed, and the embryos were resuspended in M9 with 0.1% PEG. This process was repeated once. The M9 media was then replaced with L-15 media without phenol

red (Thermo Fischer Scientific), supplemented with 50 U/ml pen-strep mix (Gibco), 10% Fetal Bovine Serum (FBS) (Gibco), and sucrose (Thermo Fischer Scientific) up to 340 mOsm. This was done by centrifuging under the previously described conditions and replacing the supernatant with modified L-15, repeating the process three times. After the last centrifugation, the embryos were pooled into a single Eppendorf tube, spun again, and the bottom 200 µl, containing the embryos was retained.

The following procedure was adapted from (Christensen *et al.*, 2002; Strange, Christensen and Morrison, 2007) to better suit a cryo-ET workflow. To the embryo suspension, 200 µl of 4 mg/ml chitinase (Sigma Aldrich) dissolved in supplemented L-15 media was added and rocked for 15 minutes. This was followed by two rounds of centrifugation at 300 RCF for 3 minutes at 22^{o}C, with the supernatant being replaced with supplemented L-15 each time. As removing the eggshell has exposed the cells of the embryo, the more gentle centrifugation is required to prevent damage. After the final centrifugation, only the bottom 50 µl was left in the Eppendorf tube, meaning the chitinase was removed, while retaining cells and media.

Cell dissociation was performed by gently aspirating and dispensing the cells in a 200 µl pipette tip for 10 minutes. Then, 25 µl of accutase solution (Stemcell Technologies) was added to disrupt cell-cell connections, and incubated at room temperature for 10 minutes while gently shaken. Cells were passed through a 200 µl pipette tip for an additional 10 minutes to remove larger cell clumps and persistent cellular detritus. To further eliminate any remaining clumps, cells were filtered through both a 20 µm and 10 µm cell strainer (pluriSelect). Under a 20x air objective (NA 0.4), cells were examined to ensure sufficient cell separation, and that any cell clumps were smaller than 20 µm in diameter to allow for vitrification. If needed, cells were aspirated and dispensed again until only clumps of the desired size remained.

For room temperature light microscopy experiments, the above procedure was carried out under a sterile cell culture hood, to prevent bacterial contamination throughout the imaging procedure.

3.5 Room temperature light microscopy

Prior to dissociation, Ibidi 35 mm low-type µ dishes with a polymer coverslip (Ibidi) were prepared by acid washing overnight in 1 M HCl at 50°C, in order to enhance the effectiveness of substrate coating. They were then washed with dH2O, left to dry for 1 hour under a sterile cell culture hood, and incubated with 300 µl of 0.1% poly-l-lysine (Sigma-Aldrich) for 1 hour. This was followed by five washes with 300 µl of dH2O, to remove excess substrate, as this may prove toxic to cells. The dissociated *C. elegans* cells were pipetted into the treated dishes, and the total volume was adjusted to 200 µl using modified L-15 media. After settling for 1 hour, the cells were drained of media and washed five times with 200 µl of fresh media to remove any unattached cells.

Imaging was performed using a Zeiss 780 NLO microscope with a plan-apochromat 63x oil immersion DIC objective lens, NA 1.2, and the chamber set to 21°C, using Zeiss ZEN pro 2.3 software (Zeiss Microscopy). Chamber temperature controls were vital, as otherwise the sample would heat significantly during the imaging process, causing cell death. Regions containing cell clumps were imaged with the following parameters: pixel spacing of 0.264 µm, image size of 512 x 512 pixels (134.95 µm x 134.95 µm), pixel dwell time of 3.14 µs, pinhole set to 288 µm, and 8 z steps of 0.5 µm. The power of the 561 nm laser was set to 2.5%. Images were taken at 5-minute intervals for 100 minutes.

3.6 Plunge freezing of embryonic cells

Plunge freezing was performed within an hour of cell dissociation to ensure cell viability, and without placing the cells on ice to prevent microtubule depolymerization (Fygenson, Braun and Libchaber, 1994; Li and Moore, 2020). Quantifoil Holey SiO2 R 1/4 Au Grid 200 mesh EM grids (Quantifoil Micro Tools) were plasma cleaned on both sides in a Pelco easyglow for 45 seconds at 0.37 mBar and 15 mA. Plunge freezing was carried out using a Leica EM GP2. This device produces a more even ice layer than the VitRobot, making it more suitable for FIB milling applications. The chamber temperature was set to 22°C, and the humidity was set to 70%. A volume of 4 µl of cell suspension was added to the front of the grid (the support film side), and 2 µl of supplemented L-15 media was added to the back side to aid blotting (by assisting media to flow through onto the blotting paper). This prevented a situation where blotting would fail due to media not passing through or around the grid onto the blotting paper, which would in turn result in the full 6 µl of cells and media being plunged into ethane producing excessively thick ice. The grids were back-blotted for 3 seconds and then immediately plunged into liquid ethane at -185°C. The grids were stored in grid boxes (Subangstrom) until ready for use.

3.7 Cryo-confocal microscopy

Before correlative microscopy, the grids were clipped into Autogrids modified for shallow angle milling, under liquid nitrogen, in a dry environment to minimize surface ice contamination. Light microscopy was conducted using a Leica TCS SP8 microscope modified with a prototype cryo-stage and a 50x NA 0.95 air objective (Leica Microsystems). Grid overviews in epifluorescence mode were acquired and montaged using the Mosaic stitching module in Leica Application Suite X 3.5.5 to generate a map from which regions of interest, containing small cell clumps or individual cells, were identified. These regions were imaged as a confocal stack with

the following settings: image size of 1056 x 1056 pixels (182.65 µm x 182.65 µm), 4x line integration, and mirror set to speed 200 Hz, resulting in a pixel dwell time of 2.03 µs. The pinhole was set to 91.95 µm with 55 z steps of 0.37 µm, covering a total depth of 20.11 µm. The 488 nm and 552 nm lasers were set to 50% power, and detection was performed from 492 to 540 nm for mCherry signal and 596 to 719 nm for GFP signal.

3.8 Cryo-focused ion beam milling

FIB milling was conducted using an Aquilos 1 (Thermo Fisher Scientific). Prior to milling, an overview image of the grid in the FIB was manually overlaid with the montage from correlative light microscopy, and the grid squares containing cells of interest were defined. Milling positions were determined using Maps software (Thermo Fischer Scientific). Light microscopy stacks were z-projected in Fiji 2.9.0 (Schindelin *et al.*, 2012), and the z-projection was manually overlaid onto the FIB data. Cells of interest, as seen in the light microscopy data, were identified in both electron beam images before milling.

Milling was carried out at a 20° angle on a shuttle with a 45° pretilt at 30kV. Initial rough milling was performed at currents of 1 nA, then 500 pA and 300 pA at distances of 5 µm, 3 µm, and 1 µm from the final lamella, respectively, above and below the region of interest. At a later point, I also introduced micro-expansion joints of 300 nm width, milled on both sides of the region of interest before further milling to reduce the effects of stress caused by thermal expansion (Wolff *et al.*, 2019). This reduced the bending of the lamella, resulting in a more accurately milled target and greater milling success. Polishing was done at a current of 100 pA, first milling below the lamella and then above it. Polishing both above and below simultaneously was found to result in a higher rate of lamella breakage for this sample rich in difficult-to-mill yolk granules. Initial lamellae were manually milled, but for subsequent data

collection, rough milling was carried out automatically using SerialFIB (Klumpe *et al.*, 2021).

3.9 Cryo-ET data collection

Data collection was performed on a Titan Krios (ThermoFisher Scientific) cryo-TEM at 300 kV, equipped with a field-emission gun, a quantum post-column energy filter (Gatan), a K2 Summit direct electron detector (Gatan), and a Volta phase plate. A grid montage at 233.046 nm/pixel and lamella maps at 2.223 nm/pixel were collected. Both were overlaid with the light microscopy montage and stack, respectively, to aid target localization for tomographic data collection.

SerialEM (Mastronarde, 2018) was used in nanoprobe mode to collect dose-fractionated, zero-loss tilt-series images from -60° to +60° in 2° increments in a dose-symmetric scheme (Hagen, Wan and Briggs, 2017), with the sample pre-tilted to the FIB milling angle. The pixel size used was 3.3702 Å/pixel. The total electron dose was 120 e-/Å^2. The defocus range was set between 2.5 µm and 4.5 µm. A total of 144 tilt series of *C. elegans* embryonic cells were successfully collected, all using the phase plate. All of these were also reconstructed into tomograms, of which 13 were of centrosomes useful for the study (i.e. not containing beam damage or heavily contaminated by ice). Tilt series on protein condensates were taken using the same setup, but without the necessity of a pretilt, as there was no FIB milling for these samples. 205 condensate tilt series were collected, of which 92 were reconstructed into tomograms.

3.10 Tomogram reconstruction and denoising

Motion correction and CTF estimation were performed using Warp 1.0.9 (Tegunov and Cramer, 2019), starting from processing the original frames. Tilt-series alignment was carried out using etomo, part of the IMOD package, (Mastronarde and Held, 2017), using stacks written within Warp. Final tomogram reconstruction was conducted in Warp, and the tomograms were reconstructed with a voxel size of 13.4808 Å/pixel, or 4x binning, to enhance the signal-to-noise ratio and reduce the overall tomogram size. For condensate tilt series, addition of gold fiducials meant that fiducial based alignment was possible. However, for lamella data this was less straightforward. Where available, platinum specks on the lamella surface were used as fiducials to guide alignment. However, this was not always possible due to a lack of or non-ideal positioning of these fiducials (i.e., all the fiducials appearing in one side of the field of view). In these cases patch tracking within etomo was used. Reconstructed tomograms were inspected in 3dmod (Kremer, Mastronarde and McIntosh, 1996) to ensure reconstruction was successful and there were no misaligned regions.

To improve the signal-to-noise ratio, especially for segmentation of the centrosome matrix, denoising was performed using cryoCARE 0.2.1 (Buchholz *et al.*, 2018). For each tomogram, two tomograms were reconstructed using odd and even frames, respectively. These tomograms were also deconvolved in Warp and a lamella mask, created in MATLAB 2016a (Mathworks), that removed the volume of noise above and below the lamella in the tomogram was applied. This ensured training was carried out on the actual lamella volume and not random noise. For tomograms with stronger curtaining effects, a thick darker stripe was visible through the data due to unequal lamella thickness. To resolve this, TOM toolbox's (Nickell *et al.*, 2005) tom_filter with a kernel size of 10 was applied to the denoised tomogram. This strongly filtered tomogram was then subtracted from the original tomogram to obtain a more equal background to aid viewing and analysis.

3.11 Segmentation of microtubules, centrioles, ribosomes, and membranes

Segmentation of microtubules in the first 11 mitotic tomograms was performed using Amira 2021.1's cylinder correlation function (Stalling, Westerhoff and Hege, 2005). Raw 4-bin tomograms were Gaussian filtered with a kernel of 3 voxels before segmentation using the TOM toolbox (Nickell *et al.*, 2005), to improve the signal-to-noise ratio of these large discrete structures. Cylinder correlation was run with following specific parameters: cylinder length of 53.92 nm (40 voxels), angular sampling of 8 degrees, mask cylinder radius of 13.48 nm (10 voxels), outer cylinder radius of 12.13 nm (9 voxels), and inner cylinder radius of 6.7404 nm (5 voxels). Missing wedge correction was set in the y-tilt axis from -60^{o} to +60^{o}. These parameters were set based on the dimensions of microtubules as seen in the dataset. Correlation tracing had a minimum seed correlation of 60, minimum continuation quality of 60, direction coefficient of 0.3, minimum distance of 24.27 nm (18 voxels), and minimum length of 53.92 nm (40 voxels). The search cone was 53.92 nm (40 voxels) long and 37^{o} wide, with a minimum step size of 10%. Results were manually examined in the filament tab, and erroneous results were removed.

To smooth out the results and connect breaks in the microtubules shown in the segmentation, but not in the data analyzed, the output was rerun through cylinder correlation. A surface for the first round of cylinder correlation was extracted with a tube scale of 8. This surface was then converted into a volume, which was again subjected to cylinder correlation with the same conditions as above but with the inner cylinder radius set to zero. The results from this output were both much smoother than the previous iteration, and more closely matched the data seen. This required less curation than trying to manually fix breaks in microtubules.

For the last tomogram, binary masks corresponding to the output of the first 11 tomograms were used to train a DeePiCt model for microtubules (de Teresa-Trueba *et al.*, 2023). The outputs of this trained model (11cents5inter6mitotic_pp, bundled with DeePiCt) were applied to the remaining tomograms, and the results were once again cleaned in Amira to remove false positives.

Centriole microtubules were manually traced in Amira 2021.1 within the filament tab. The start and stop points came from the same side for every centriole. The centriolar microtubules were assumed to be entirely straight, matching what was seen in data.

Membranes and ribosomes were segmented in all tomograms using DeePiCt. The pre-trained models ribo_model2_IF4_D2_0 and full_vpp_memb_model_IF4_D2_BN were used for ribosomes and membranes respectively. The results were also cleaned in Amira to remove false positives.

Segmentations were depicted in Chimera (Pettersen *et al.*, 2004) and ChimeraX (Pettersen *et al.*, 2021). To better depict the biology reflected by these segmentations, subtomogram averages for both mother and daughter centrioles, microtubules, gamma-TuRCs, and ribosomes were projected back into the data using a custom script in python 3.10, kindly shared by my colleague Rasmus Jensen. Averages were masked using a tight lamella mask before being projected into the data, and to reduce clash from adjacent particles, microtubules were cropped from a box length of 72 voxels to 36 voxels.

3.12 Analysis of centrosomal zones

The analysis was conducted using MATLAB 2019a (Mathworks), using tools from TOM (Nickell *et al.*, 2005) and dynamo 1.1.514 (Castaño-Díez *et al.*, 2012). Centroids for the ribosome-excluded and microtubule-excluded regions were calculated as

follows: Binary segmentations were averaged along the z-axis to obtain a 2D projection. The diameter and approximate center of the excluded region were estimated from this projection. A circle with a diameter approximately 50% larger than the estimated excluded region was drawn from the estimated center, masking out everything outside. The region within this mask was inverted, assigning a value of zero to the signal and one to the background. The centroid from this masked region was calculated, and as signal had been inverted, the centroid was calculated to be the region furthers from microtubules or ribosomes, i.e. placing it in the center of the excluded region. A new mask of the same diameter was drawn from this centroid, and a new centroid from that mask calculated. This process was repeated iteratively until convergence shifting the mask with each iteration and finally obtaining the centroid coordinates in x and y. To determine the centroid value in z, a single round of the above process was performed in 3D, with x and y values fixed to the 2D output to prevent drifting, but the z value free to change. Spheres were then grown concentrically from these centroids. Whenever a sphere encountered density from the binary segmentation, the sphere's radius and the number of voxels were recorded, to measure the radius of each cellular feature at the distances from the centroid.

3.13 Subtomogram averaging of microtubules

Coordinates and initial Euler angles of particles were obtained from microtubule segmentations using a custom script in MATLAB 2019a. The script generated a table file for use in dynamo 1.1.514 (Castaño-Díez *et al.*, 2012) and a STAR file for use in Warp 1.0.9 (Tegunov and Cramer, 2019). The table file included unique identifiers for each tomogram, as well as each microtubule within the tomogram. Particles were picked every 8.09 nm (6 voxels) accounting for the expected size of a tubulin dimer. The particles were then reconstructed in Warp with a pixel spacing of 6.7404 Å/voxel (or 2x binning) and a box size of 72 voxels. These particles were imported into

dynamo via the dynamo GUI. The third Euler angle was randomized prior to alignment, to counter the effects of the missing wedge. Microtubules were aligned in dynamo through 2 rounds of 5 iterations each. In the first round, particles were aligned around the new z-axis with a 30° search cone but no azimuthal searches. In the second round, particles were only searched around the azimuth with a 33° (360/11) search range. Both rounds allowed 53.92 Å (8 voxel) shifts, with limits determined from the center of the first iteration. The resolution of this average was estimated via drawing an FSC curve. As the two half-sets of data were not processed independently throughout the alignment procedure, a cut-off score of 0.5 had to be used (Scheres and Chen, 2012), giving a resolution of 24 Å.

Once the average was generated, per-microtubule averages were calculated using the unique microtubule identifiers in the table. To enhance contrast, these per-microtubule averages were averaged along the z-axis to create a 2D average of size 72x72 pixels. The protofilament number was automatically determined in MATLAB 2019a by comparing each average to reference structures of microtubules with 9 to 15 protofilaments, taken from EMDB accession codes EMD-5191 to EMD-5195, from (Sui and Downing, 2010). These were then resampled to the 6.7404 Å pixel size of my average in EMAN2 (Galaz-Montoya *et al.*, 2015). Each average was rotated until it achieved the highest possible cross-correlation coefficient with each structure. The highest output was recorded as the protofilament number for the microtubule. The microtubule polarity was determined by comparing each 2D average projection to a representative average for each polarity. The longest microtubule in all data was found, and its average projection used as a template for a positively oriented microtubule. This template was also flipped along z to create a template for negatively oriented microtubules. Each microtubule average was then compared to these two templates as in the protofilament determination step.

3.14 Centriole analysis

Centrioles were circularized and 9-fold symmetrized in Fiji (Schindelin *et al.*, 2012) using CentrioleJ (Guichard *et al.*, 2013). To determine the lengths of different features within the centriole, the tomogram was opened in 3dmod and positioned in the slicer window to fully visualize the feature of interest along each microtubule. Line scans were then run in Fiji, and the length of each feature was determined as the distance in the scan where the mean pixel value was lower than the mean pixel value of the entire image. The average length and corresponding standard deviation was calculated for each of these feature lengths to give a more representative result.

3.15 Centriole subtomogram averaging

Similar to microtubule subtomogram averaging, coordinates and initial Euler angles of particles were obtained from segmentations using a custom MATLAB script in MATLAB 2019a, which generated both a STAR (for use in RELION and Warp) and table (for use in dynamo) file. Particles were picked every 8.09 nm (6 voxels). The particles were then reconstructed in Warp 1.0.9 (Tegunov and Cramer, 2019) with a voxel spacing of 6.7404 Å/voxel and a box size of 180 voxels. The table contained unique identifiers for the tomogram number, centriole number, and microtubule number within the centriole. The third Euler angle for particles within each centriolar microtubule was initially fixed relative to one another, to allow easier manipulation of this value and to aid initial reconstructions. To align these microtubules initially, particles in each microtubule had their third Euler angle rotated 40 ($360^{o}/9$) relative to the previous microtubule, resulting in a more confident initial average. An alignment job was then run in dynamo 1.1.514 (Castaño-Díez *et al.*, 2012), consisting of 12 iterations allowing shifts of 40.44 Å (6 voxels), with cone and azimuth search ranges of 27.7^{o}. The resolution of this average was estimated via drawing an FSC curve. As the two half-sets of data were not processed independently throughout the

alignment procedure, a cut-off score of 0.5 had to be used (Scheres and Chen, 2012), giving a resolution of 44 Å. The average generated was then split into the different centrioles using the table identifiers, and each was further averaged along the z-axis to improve contrast.

3.16 Gamma-TuRC subtomogram averaging

281 particle coordinates and initial angles were manually identified from 4-bin denoised tomograms using dynamo 1.1.514 (Castaño-Díez *et al.*, 2012). Particles were picked with a dipole for initial Euler angle assignment. These particles were then reconstructed in Warp 1.0.9 (Tegunov and Cramer, 2019) with voxel spacings of 13.4808 Å/pixel and 6.7404 Å/pixel (4-bin and 2-bin) and box sizes of 74 and 148 voxels, respectively. In RELION 4.0.1 (Kimanius *et al.*, 2021), the 4-bin particles underwent a 2-class classification job, resulting in all 281 particles being assigned to a single class. The results were then refined at 2-bin, with a 450 Å spherical mask covering the tip, resulting in the final average at a resolution of 38 Å. Resolution determination was performed using RELION postprocessing. As the data was processed as two independent half-sets throughout, a gold-standard FSC cut-off score of 0.143 was used (Scheres and Chen, 2012).

3.17 Subtomogram averaging of ribosomes

Although not immediately relevant to this project, ribosomes were aligned and averaged to improve the quality of depictions and make them more reflective of the biological reality, as opposed to merely showing spheres in the segmentations. Using coordinate data for ribosomes as described in the segmentation section, 10,220 particles were picked and reconstructed in Warp 1.0.9 (Tegunov and Cramer, 2019)

at 10 Å/px and with a box length of 44 voxels. This was then subject to 1 round of 3d refinement in RELION 4.0.1 (Kimanius *et al.*, 2021), with no mask and under default conditions. As this was simply for depiction's sake, an FSC curve to determine resolution was not calculated.

3.18 Matrix analysis

Much of the below, including most of the branch analysis, was carried out with assistance from Frosina Stojanovska. Only 4 tomograms, 2 with metaphase centrosomes and 2 with anaphase centrosomes were subject to this analysis, as these were the tomograms in which the matrix could be most clearly seen. Denoised tomograms were used for matrix segmentation. Centrioles, microtubules, ribosomes, and membranes were removed by expanding their segmentations by 24 voxels (32 nm) for centrioles, 11 voxels (15 nm) for microtubules, 8 voxels (11 nm) for ribosomes, and 4 voxels (5 nm) and using the resulting volume as a mask that could be subtracted from the lamella volume. A strict lamella mask, cutting off the very edge of the lamella itself as well as any curtained regions, was applied.

Two models for the matrix were generated using Ilastik 1.3.3 (Berg *et al.*, 2019). One utilized 3D Pixel Classification with all features and 7 labels, of which 2 corresponded to the matrix, and 5 of which corresponded to other tomographic structures (e.g. the masked volume, cytosol). The other model used 2D Autocontext, also with all features, trained on the central 50 xy slices of the tomogram, but later applied to the entire volume. 7 labels were used on the first iteration of Autocontext, but the second iteration had only two, corresponding to the matrix volume and everything else. The outputs of the Ilastik modalities were combined and binarized in MATLAB 2019a (Mathworks) to obtain the final matrix model.

Pore sizes were determined by running a distance transformation and identifying regional maxima in MATLAB 2019a. The radii of the pores were calculated by multiplying the distance transformation by the regional maxima. A Gaussian fit of the whole data was applied using Graphpad Prism 9.5.1 (Dotmatics). Pore radii at distances from the centroid were calculated in a similar fashion to how centrosomal zones were determined; spheres were grown sequentially out from the centroid, and whenever a regional maximum (corresponding to a pore center) was encountered, its pixel value (corresponding to the pore radius) was recorded.

The matrix was skeletonized using a Skeleton3D function (Kollmannsberger *et al.*, 2017) in MATLAB 2019a before determining the number of branch points and segment lengths. Branch points were identified using a custom script. First bwmorph was used to identify all branchpoints, and a box was cropped out around each branchpoint. The number of branches was then determined by counting the number of voxels in the box. Segment lengths were calculated using the Skan toolbox (0.11.0) (Nunez-Iglesias *et al.*, 2018) in Python 3.10.9, considering only segments between junctions. A second python script was used to create masks for filaments of a predefined length, and was used to identify very short (>2 voxel) segments within the matrix. As a result of the information from this script, segments shorter than 2 voxels were removed from the data, as these were found to represent knubs at branchpoints arising from a skeletonization artefact rather than actual connections. Both these scripts were kindly written by Frosina Stojanovska. Plots and fitting to the data was performed in Graphpad Prism 9.5.1, using the sum of two Lorentzian fits to describe the distribution of segment lengths.

4. Results

4.1 Cryo-electron tomography of centrosomal protein condensates and asters

Although *in-situ* cryo-electron tomography is a highly effective means of determining the in-cell architecture of organelles and cellular complexes, it is plagued by difficulties in sample preparation, requiring technical expertise and specialized equipment. This makes wider screens of different conditions currently impractical. As such, cryo-electron tomography of individual centrosomal protein condensates, plunge frozen on an EM grid, allows relatively quick and easy modification and examination of different conditions. It was hoped that tomography on these condensates would in turn provide a reflection of how the PCM appears in the native cell.

I performed cryo-ET on SPD-5 droplets under a variety of conditions. Prior to freezing samples for cryo-ET, it is essential to thoroughly characterize the protein condensate being studied. In my case, SPD-5 had already been well classified in conditions under a cover slip suitable for light microscopy, which I was able to replicate (Figure 4.1.1A). However, when compared to reconstitutions conducted in bulk solution typically observed using light microscopy on a glass surface, the conditions of an EM grid can have an impact on the reliable formation and stability of condensates. The elevated surface area to volume ratio inherent to the grid can potentially lead to protein denaturation at the interface between air and water (D'Imprima *et al.*, 2019). Additionally, surface charges present on the grid may induce aggregation or dissolution of the condensates. Furthermore, it may require some time for the condensates to settle on the grid which must be factored into plunge freezing conditions. The cost associated with using a TEM make it impractical to check all of these at cryogenic temperatures. As such, every experimental condition had to be

checked to ensure protein condensates both formed and settled on an EM grid prior to plunge freezing (Figure 4.1.1B).

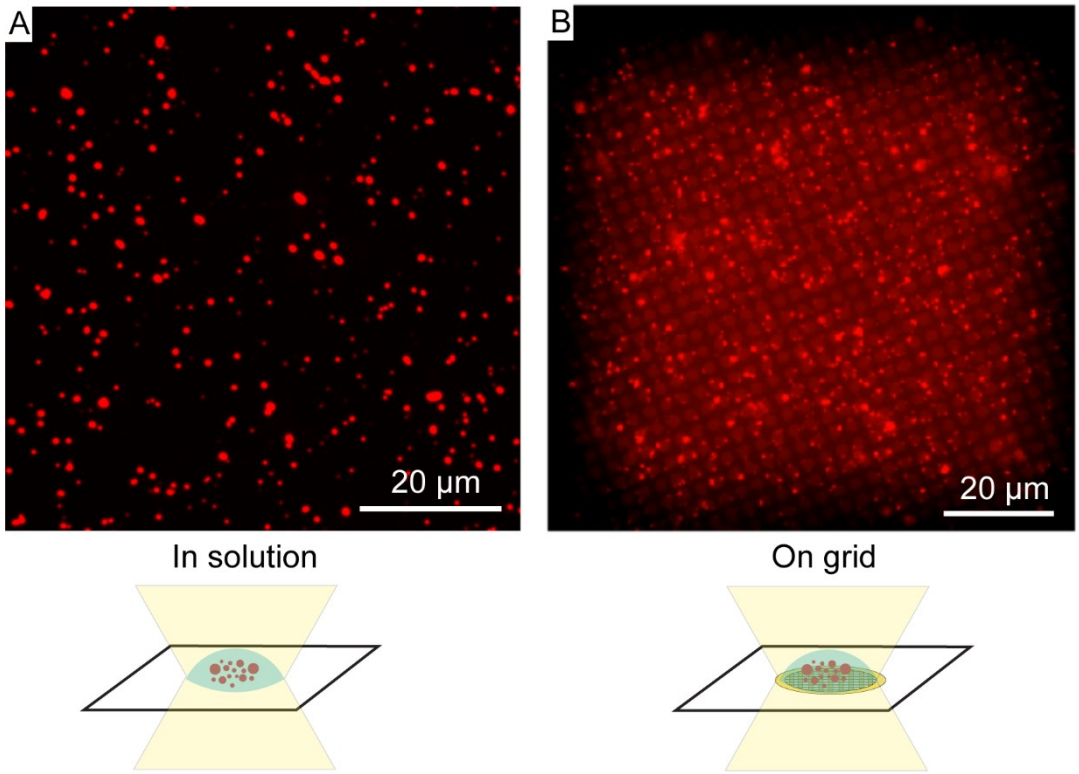

Figure 4.1.1: Light microscopy screening of SPD-5 condensates. A: SPD-5 condensates settled on a glass coverslip. B: SPD-5 condensates settled on the bottom of an EM grid.

Self-assembly of SPD-5 is affected by both the 'age' of the condensate, and the phosphorylation state of the protein (Wueseke *et al.*, 2016; Woodruff *et al.*, 2017). I therefore aimed to compare the meso-scale assembly of 'young' (plunge frozen immediately), 'aged' (left to age for 15 mins prior to plunge freezing) condensates, as well as phosphomimetic SPD-5, in which 4 phosphorylated serines were mutated to glutamates, and SPD-5 phosphorylated with PLK-1.

Initial examination of this data yielded noticeable results. All condensates examined were seen to be squashed to the overall thickness of the ice layer, between around 150 and 250 nm. As older condensates are stiffer and exhibit less internal

rearrangement (Woodruff *et al.*, 2017; Ranganathan and Shakhnovich, 2020), it was expected these may protrude from the ice after blotting, and although the droplets are thicker than the ice layer, they are still squashed down and are not spherical. In young condensates I also noticed a subset of droplets that were wetted onto the surface of the ice, and as such were much thinner and broader than other condensates. Given their location at the periphery of the ice, it is likely their shape is influenced by the air-water interface. However, as wetting is an inherently liquid property, which demonstrates the liquid-like nature of younger SPD-5 droplets. By contrast, not only is no wetting seen in the aged SPD-5 condensates, I see droplets that have fused, but fail to relax back into a sphere, indicating the stiffening of said assemblies.

Both phosphomimetic and PLK-1 phosphorylated SPD-5 share many morphological similarities. Firstly, in both I see a series of multiple droplets that have fused, but not relaxed into spherical droplets. Secondly, I also see large regions of dense contracted material, which appears to form a fibril-like interconnected network (Figure 4.1.2). This is reminiscent of what was seen in previous work carrying out cryo-ET on SPD-5 without crowding agent, where a condensed droplet phase was not seen (Woodruff *et al.*, 2015). This networked state seen in the phosphorylated or phosphomimetic (and as such more assembly competent (Wueseke *et al.*, 2016)) SPD-5 may be reflective of an important biological reality, or may be a result of small protein aggregates too small to be seen by light microscopy but that are resolvable in the final tomogram. Thus, two changes were made to the experimental procedure. Firstly, proteins were ultracentrifuged at 80k RPM at 4^{o}C for 5 min, and only the supernatant retained to more effectively remove any potentially aggregated protein. Secondly, a final concentration of 0.05% PFA was added to the condensate mix, to better preserve the stability of condensates through the shear forces associated with the blotting process (Armstrong *et al.*, 2020) and ensure greater survivability, while minimizing the detrimental effects of fixation in introducing artefacts into the fine molecular structure.

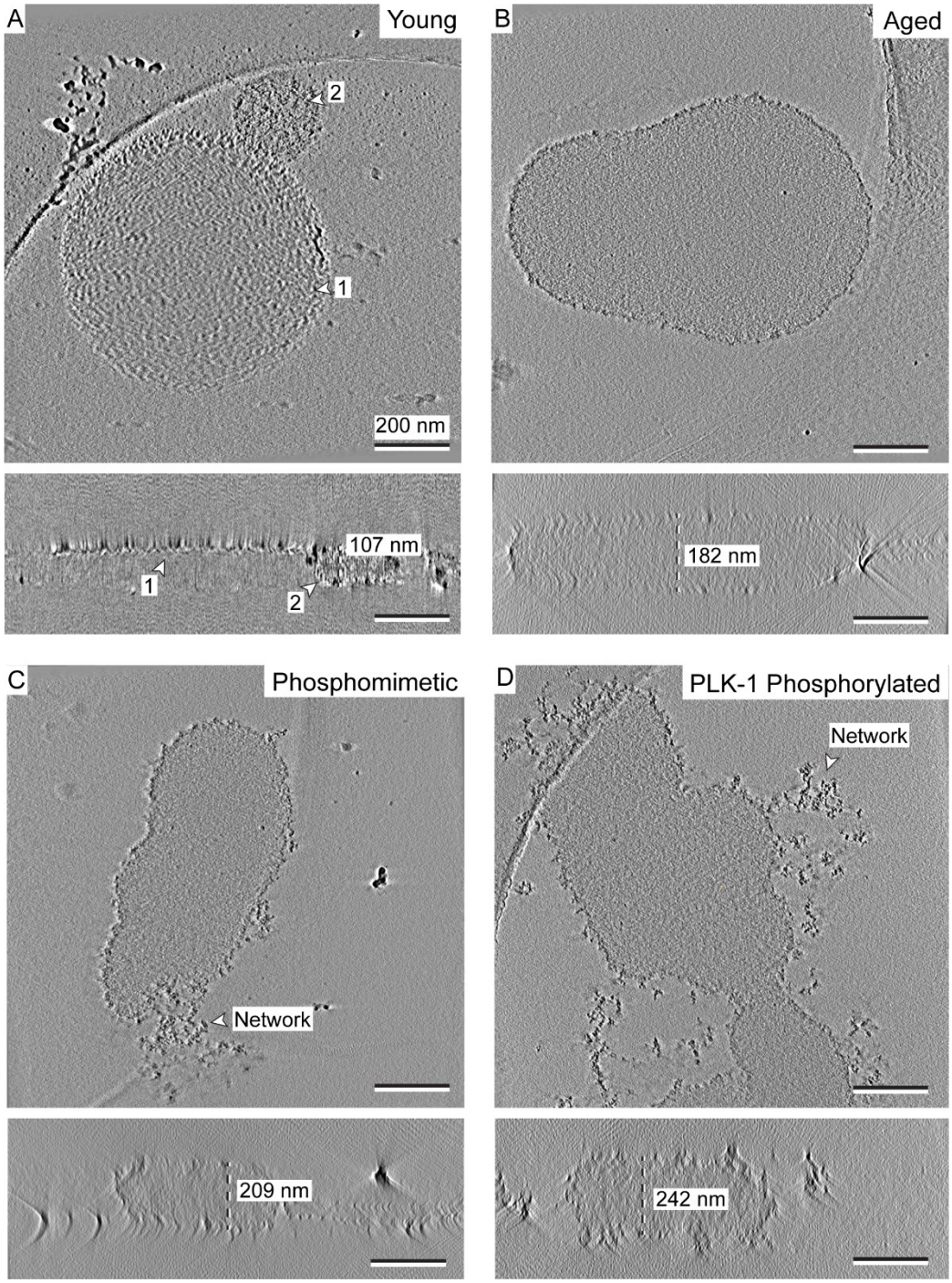

Figure 4.1.2: Tomograms of SPD-5 condensates. For each tomogram an XY view is shown on top, with a cross-section view on the bottom, with the condensate thickness highlighted by a dashed white and black line. A: Young condensates, with two in the field of view. The first (labelled with 1) is very thin and flat, wetted onto the surface of the ice. The second (labelled with a 2) is smaller and stiffer. B: Aged condensates, showing two that have merged but not yet relaxed into a spherical shape. C and D: Phosphomimetic and PLK-1 phosphorylated SPD-5, with protein 'network' identified.

Under these conditions, I examined wild type, phosphomimetic, and PLK-1 phosphorylated SPD-5. In all three conditions, several droplets that had fused, but not relaxed, were seen. Furthermore, the denser protein network that was seen under previous conditions is absent. Therefore, it was concluded that rather than reflecting some sort of biological reality, this represented random protein aggregation that was removed through ultracentrifugation, and should not be considered. Ultimately, under these preparation conditions, it was not possible to visually distinguish between wild type, phosphomimetic, and PLK-1 phosphorylated SPD-5 without prior information (Figure 4.1.3).

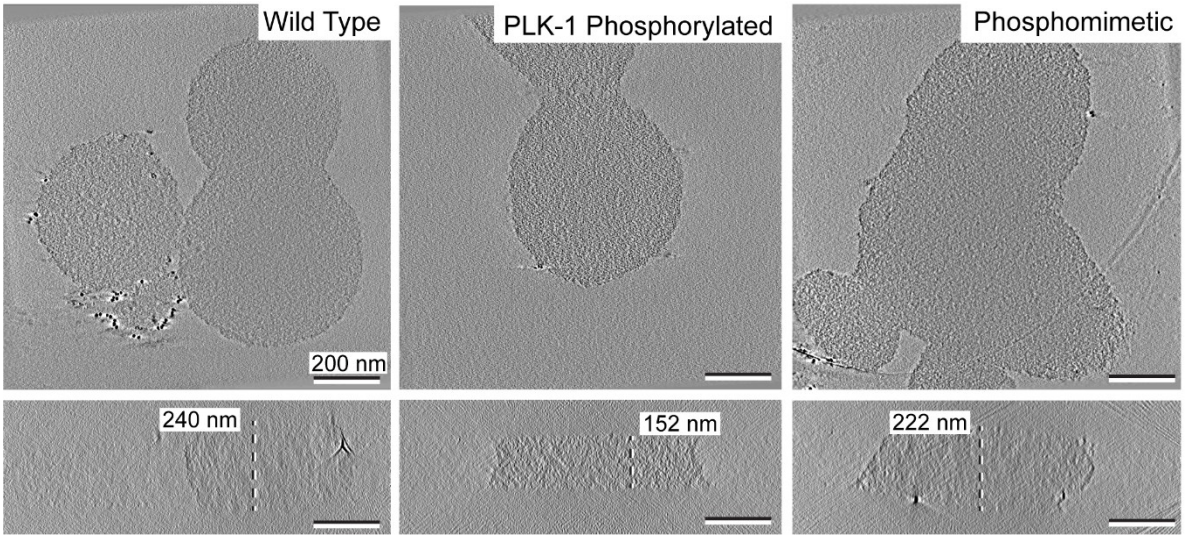

Figure 4.1.3: Tomograms of SPD-5 condensates, after the removal of aggregate protein. XY planes are shown on top, with XZ planes shown underneath with condensate thickness highlighted by a dashed white and black line.

As there exists a model of the centrosome where it consists of a gel (Woodruff *et al.*, 2017; Mittasch *et al.*, 2020), it was expected that a two-phase system within condensates would be seen, with a networked gel phase and a dilute phase. This was not seen in this case, with all condensates consisting of a single, continuous, smooth phase, with no internal structures. As such, tomography of *in-vitro* SPD-5 condensates cannot lend support to a gel model of the centrosome. However, individual SPD-5 condensates are not the most faithful recreation of the centrosome possible, even within the context of a test tube. An *in vitro* minimal aster system

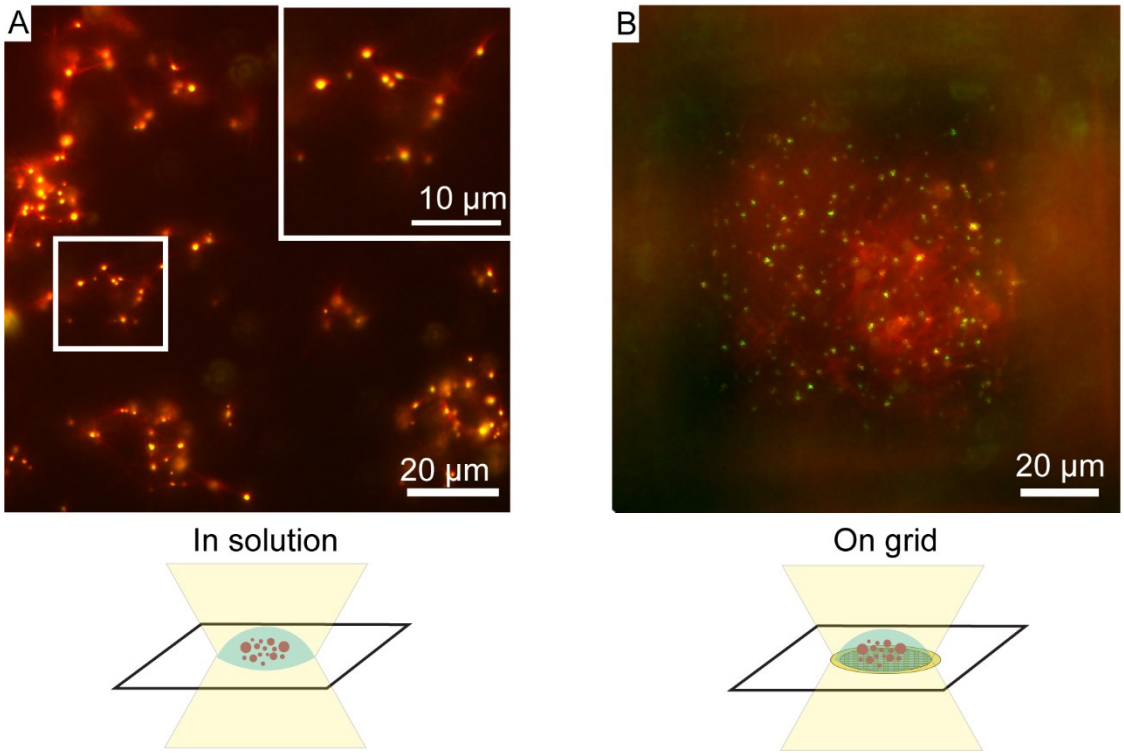

Figure 4.1.4: Light microscopy of SPD-5 microtubule asters. A: Asters settled on a glass coverslip. B: Asters settled on the bottom of an EM grid.

exists, consisting of SPD-5 condensates supplemented with ZYG-9 and TPXL-1, which can condense pig brain tubulin and nucleate microtubules (Woodruff *et al.*, 2017). I was able to recreate this minimal aster system (Figure 4.1.4A). I aimed to develop snapshots of this aster as it aged and solidified throughout the maturation process, as well as to investigate where, when, and how microtubule nucleation took place. I took tilt-series of asters from 0 mins, 5 mins, and 10 mins after the addition of tubulin. After 10 minutes, asters have fully matured. Great care was taken to ensure aster structure was maintained as faithfully as possible throughout the preparation and blotting stages. For example, rather than growing asters in a test tube and pipetting them onto an EM grid, asters were grown directly on an EM grid. This also meant imaging asters that had been grown directly on a grid in a fluorescence light microscope was needed (Figure 4.1.4B). Direct growth on the grid reduced the shear force from pipetting that could have removed the microtubules from the condensates. This in turn required special considerations: instead of copper grids, gold grids had to be used as copper grids may oxidize and introduce damaging

ions into solution. Furthermore, leaving a few microliters of solution on an EM grid for several minutes at a time would result in evaporation of water and subsequent changes in concentration of protein in the remaining material. To prevent this unwanted effect, grids were placed inside a plastic box, padded with damp tissue paper to create a humid environment to minimize evaporation. Finally, to lessen the damage caused by shear forces during the blotting process, samples were spiked to a final concentration of 0.05% PFA immediately before plunging, once again to stabilize condensates slightly, while minimizing fixation damage. Finally, only back blotting was used in an attempt to maximize the amount of material left on the grid.

I examined these asters under all 4 time points: frozen 0, 2, 5, and 10 minutes after the addition of tubulin. The 0 and 2 min asters do not appear to have formed correctly. Despite condensates being clear and present, they had not yet relaxed into the spherical conformations seen in later time points. Furthermore, microtubules are not seen, showing microtubule nucleation and polymerization within droplets take place on a timescale of minutes and not seconds (Figure 4.1.5A, Figure 4.1.5B). After 5 minutes, microtubules were seen emanating from the asters, although many more microtubules were seen in the ice that did not appear to originate or terminate from a SPD-5 droplet. As the concentration of tubulin in solution (2.5 μM) is lower than the concentration required for spontaneous polymerization of microtubules (15 μM, (Mitchison and Kirschner, 1984)), these must arise from concentration from within a condensate. Taken together, this implies some microtubules are still being removed from the condensate through blotting induced shear forces despite the effort undertaken to preserve this property. Regardless, many asters were seen at both 5 and 10 minutes with many microtubules formed around a condensate. As well as normally formed microtubules, larger ring-like structures were observed throughout the data. These rings were ~50 nm in diameter, and appeared throughout the periphery of the asters, forming large clouds. What could the identity of these rings be? The strictly controlled nature of these *in-vitro* experiments means there the only things it could be are SPD-5, TPXL-1, ZYG-9, and tubulin; of which only tubulin is

known to form discrete, regular molecular structures. Tubulin rings have long been a suspected intermediate in microtubule disassembly, as the depolymerizing microtubule fragments into individual protofilaments that peel back into ring shapes (Nogales and Wang, 2006). But here I see this structure in polymerizing microtubules, implying this structure may be an assembly intermediate (Figure 4.1.5C).

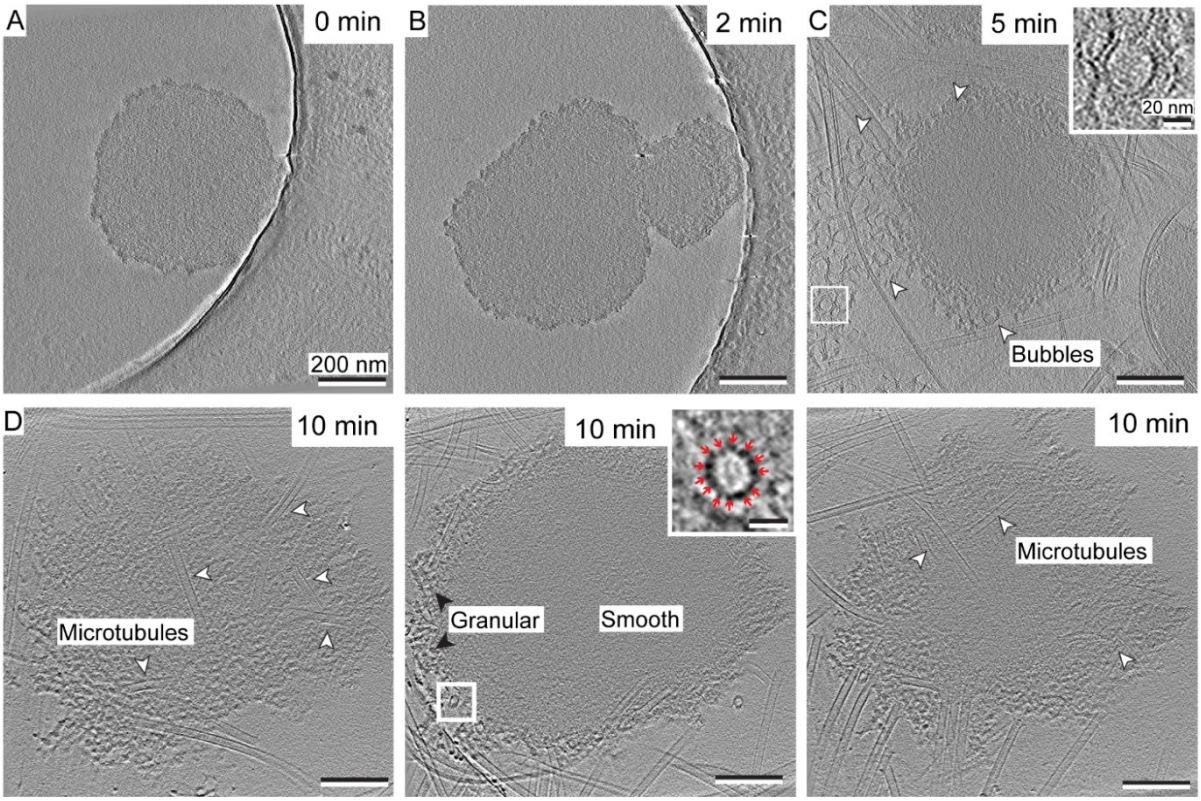

Figure 4.1.5: Tomograms of SPD-5 microtubule asters. A: Microtubule aster immediately plunge frozen after the addition of tubulin. B: Microtubule aster plunge frozen two minutes after the addition of tubulin. C: Microtubule aster plunge frozen five minutes after the addition of tubulin. Bubble structures can be seen throughout the periphery of the aster, and have been highlighted with arrows. The inset is a magnification of the region delineated by a white box and shows one of these 'bubbles' in more detail. D: Microtubule aster plunge frozen ten minutes after the addition of tubulin. Three images of the same aster are shown, with 'top' (left), middle (center), and 'bottom' (right) views. Microtubules can bet seen forming on the periphery of the aster, and some are highlighted with white arrows. The central slice shows a peripheral granular zone and a central smooth zone. The inset shows a single microtubule with the 13 protofilaments highlighted with red arrows.

In both 5- and 10-minute old asters, I observed two apparent zones in the aster, a smooth inner phase with no apparent internal structure, and a more granulated external phase. As this external phase is structurally similar to the aggregated protein seen in phosphomimetic and PLK-1 phosphorylated SPD-5, it might appear that this is aggregated protein as well. However, unlike earlier experiments examining individual protein condensates, SPD-5 and tubulin were both ultracentrifuged prior to experimentation in all aster data sets, and as such no aggregation would be expected, as is also the case for later condensate tomograms. Furthermore, all the observed microtubules arose from this denser phase. I therefore suspected that this granular phase represented a region with greater protein, likely tubulin, concentration. Finally, microtubules seen were formed of 13 protofilaments, as opposed to the 11 seen in most commonly in *C. elegans* (Chalfie and Thomson, 1982; Chaaban *et al.*, 2018). As 13 protofilament pig brain tubulin is used in aster formation due to its relative availability and low cost, this finding is not unexpected, but demonstrates that SPD-5 based asters are not sufficient on their own to template the 11 protofilaments of *C. elegans* microtubules (Figure 4.1.5D).

Ultimately, although tomography on SPD-5 protein condensates and microtubule asters were able to reveal limited information about their morphologies, relative stiffness, and how microtubules are polymerized, it was in no means sufficient to probe the properties of the centrosome. As such, I had to move onto systems more reflective of the biological reality within in the cell, that is to say carry out tomography of the centrosome within its native environment.

4.2 Optimization of cell dissociation, sample preparation, and data acquisition

In order to carry out electron tomography of the centrosome, the sample bust first be preserved in such a way that it will survive the vacuum environment of the microscope. Traditionally, this was done with fixation, dehydration and plastic embedding followed by use of heavy metal stains. This has been used to great effect to image, for example, the entire mitotic spindle in *C. elegans* (Redemann *et al.*, 2017), or even the entire brain of *Drosophila* (Zheng *et al.*, 2018). However, plastic embedding has been known to distort the sample, and heavy metal staining is imperfect and obscures fine molecular details. Cryo electron microscopy circumvents these issues, but simple plunge freezing approaches are limited to a sample of around 10 μm thickness (Adrian *et al.*, 1984; Dubochet *et al.*, 1988), much less the 100 μm of an adult gravid nematode. Although high pressure freezing can vitrify samples up to 300 μm thick (Moor, 1987; Dubochet, 1995; Liu, Pokrovskaya and Storrie, 2023), but the specimen is subsequently contained within a thicker ice block which is not suitable for standard on-grid FIB milling approaches applied to single cells. Cryo-lift out procedures, which involve extracting regions of interest from the ice, were established as proof-of-principle applications (Mahamid *et al.*, 2015; Schaffer *et al.*, 2019). However, at the time of this work, the limited availability of lift-out apparatus rendered this impractical for my purposes. Although limited work was done attempting to set up these pipelines at EMBL Heidelberg, this was ultimately dropped given the success of alternative methodology. In the time since data collection for this thesis was carried out, the lift-out has started to become more routine at our institute, providing a promising route for future high-resolution studies of thicker samples.

Since I could not reliably vitrify the entire worm in a manner amenable to available workflows, I instead decided to focus on only vitrifying parts of the whole. Since *C.*

elegans embryos are readily obtained from gravid adults through bleaching in established procedures (Brenner, 1974; Porta-de-la-Riva *et al.*, 2012), I investigated if the much smaller *C. elegans* embryo, being only 40 μm thick can be reliably plunge frozen (Figure 4.2.1). Although this is also too thick for the 10 μm thickness for plunge freezing, it was hoped that the periphery of this embryo might still be vitrified, even if the center retained observable cell damage. However, after plunge freezing, FIB milling, and observation in the TEM, it was clear by simple visual inspection that even the very edges of the embryo were severely damaged by crystalline ice formation (Figure 4.2.2).

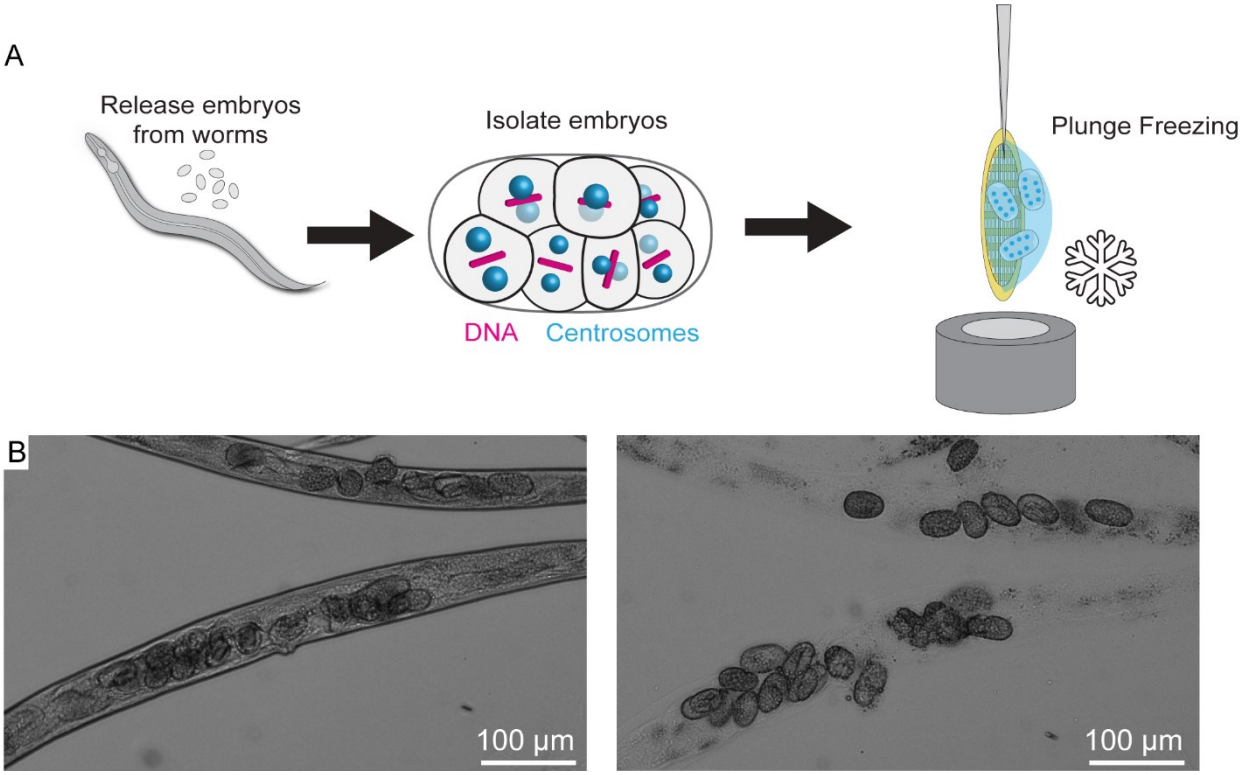

Figure 4.2.1: Obtaining embryos for cryo-ET studies. A: Schematic of the plunge freezing protocol used in this case. B: Transmission light microscopy images of two adult gravid *C. elegans* worms before and after treatment with bleach, leaving behind the embryos.

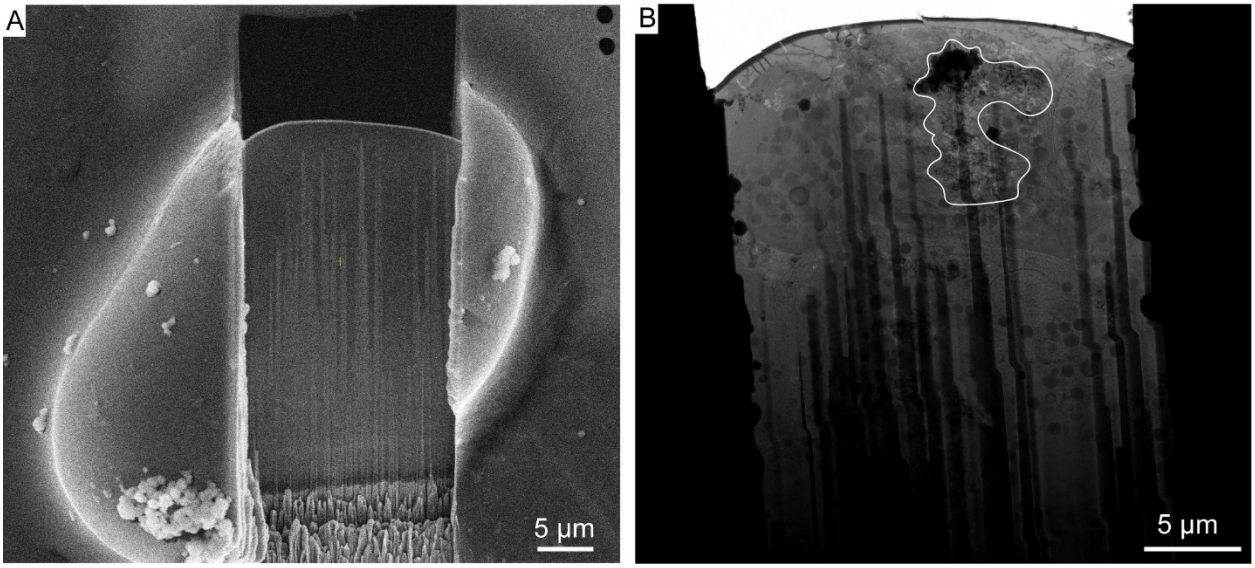

Figure 4.2.2: Attempted FIB milling of a whole *C. elegans* embryo. A: FIB view of the embryo, as seen after lamella milling. B: TEM view of the same lamella. A region of particularly bad ice damage, near the front of the lamella, has been highlighted in white.

As such I needed an even thinner sample, that was still a good model for centrosomal studies (i.e., the sample must retain the ability to undergo cell divisions). Previous work had successfully obtained individual cells from *C. elegans* embryos, which would then be differentiated into neuronal cells for use in patch clamp experiments. This was done by digesting the protective chitin eggshell in commercially available chitinase, followed by mechanically separating the cells in a fine needle tip (Christensen *et al.*, 2002; Strange, Christensen and Morrison, 2007). Although well optimized for this purpose, modifications to these procedures were required to render them more suitable for use in cryo-ET experiments. Specifically, my sample needed larger, undifferentiated cells from earlier embryos, with less waste and debris in the remaining media, and a higher concentration of overall cells which can continue to divide. As the majority of material is blotted away and removed from the grid as a part of the plunge freezing procedure, many more cells must be added to the grid prior to freezing than will actually be retained through in later sample preparation steps. As plunge freezing even a large number of grids only requires a few microliters of solution, it is better to have a little of more concentrated cell mix than the reverse.

Detritus in the sample, which may be acceptable for patch clamp work, when frozen would obscure views and make target identification much harder, and may prevent proper vitrification. Finally, I needed cells from younger embryos, as these have the larger centrosomes of early-stage cell divisions, which are better described in the literature.

To this end, I modified the procedures described previously. Worms washed off from NGM plates were placed in a 40 μm cell strainer, and washed thoroughly with M9 media. Doing this removed all embryos that had already been laid, meaning only 44 cell embryos and earlier are retrained, as eggs are laid at around the 30 cell stage and the onset of gastrulation (Gilbert, 2000). I observed that the larger cells were also more likely to rupture and lyse during the mechanical dissociation steps, and decided that this should be gentler. I moved from a needle tip, to passing the cell suspension through a p200 pipette tip, as this both reduced the shear forces on the cell and was easier to handle considering the small volumes in use. Additionally, I made use of the commercial protease accutase to digest away at cell-cell connections, reducing the amount of shear force and thus number of passages to separate cells. Accutase was used as it is effective at 22°C, the temperature of these cells prior to plunge freezing, hence its use in favor of other proteases active at 37°C, such as trypsin. Finally, the removal of persistent waste material, such as segments of worm carcass that were retained throughout all steps, were removed by passing the suspension consecutively through a 20 μm and then a 10 μm cell strainer. This generated a cell suspension of individual cells and small cell clumps of up to roughly 5 cells, free from detritus, which would be suitable for use in existing cryo-ET pipelines (Figure 4.2.3A).

It is still necessary to ensure that room-temperature cell divisions and proper vitrification, milling, and cryo-ET are possible. Proper cell divisions were investigated by allowing the cells to adhere to a poly-l-lysine substrate, which has previously been shown to facilitate cell adhesion (Strange, Christensen and Morrison, 2007). As the

worms used in these studies, and subsequently the dissociated cells, had endogenous tags for SPD-5 and H2B, I were able to observe these cells undergoing proper and regular cell divisions as part of small cell clumps for up to 50 minutes after plating onto the substrate (Figure 4.2.3B).

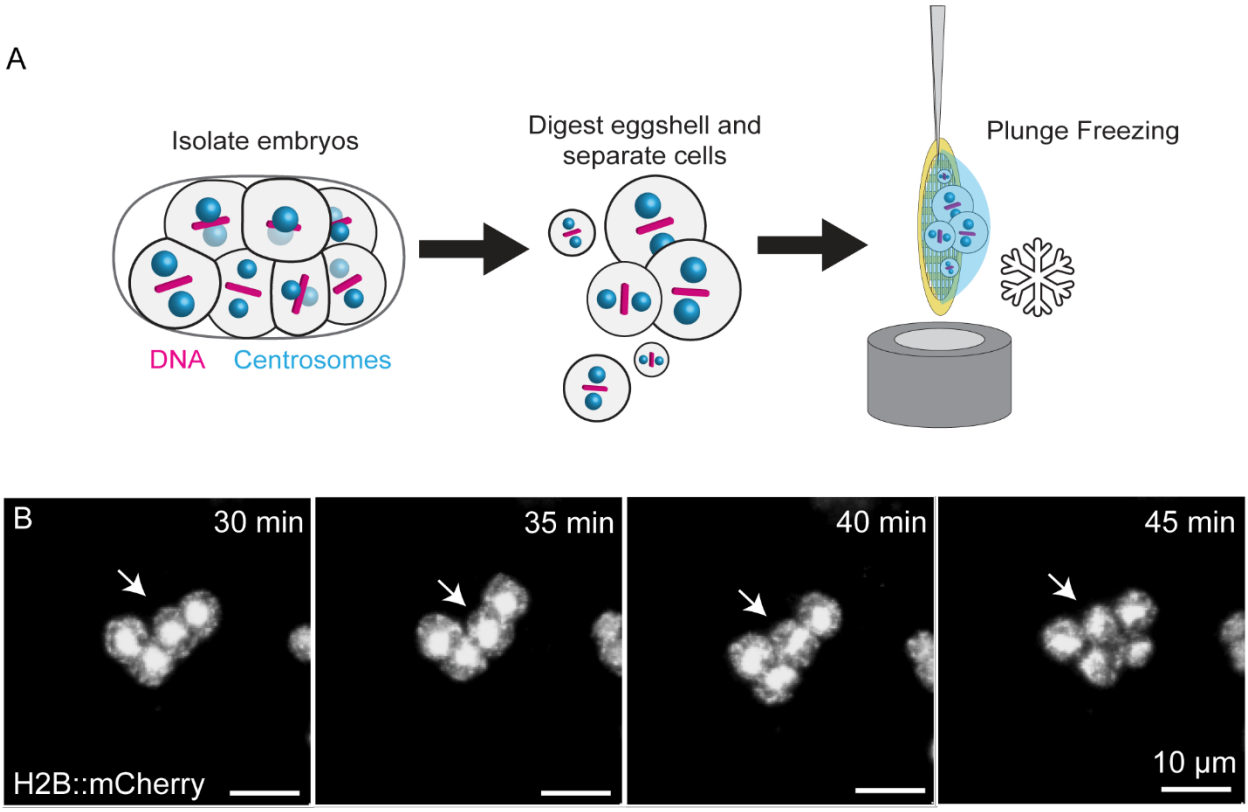

Figure 4.2.3: Obtaining viable embryonic cells for cryo-ET studies. Schematic of the plunge freezing protocol of dissociated embryonic cells. B: Fluorescence imaging of dissociated cells dividing. Time points indicate time since cell attachment to the cover slip. The dividing cell in this field of view is highlighted by a white arrow.

When plunge frozen and examined within the FIB, cells were clearly visible, both individually and as a part of clusters (Figure 4.2.4). Initially, I simply wanted to check the validity of this approach in generating suitable lamella for cryo-ET, and as such no correlative light microscopy was applied. When a lamella was milled into a cell as part of this process and loaded into the TEM, an interphase centrosome was noticed immediately within this lamella (Figure 4.2.5). As such, I not only concluded that working with these dissociated cells is an effectual method to perform cryo-electron tomography of *C. elegans* cells in a more cost effective and simple way than the lift-

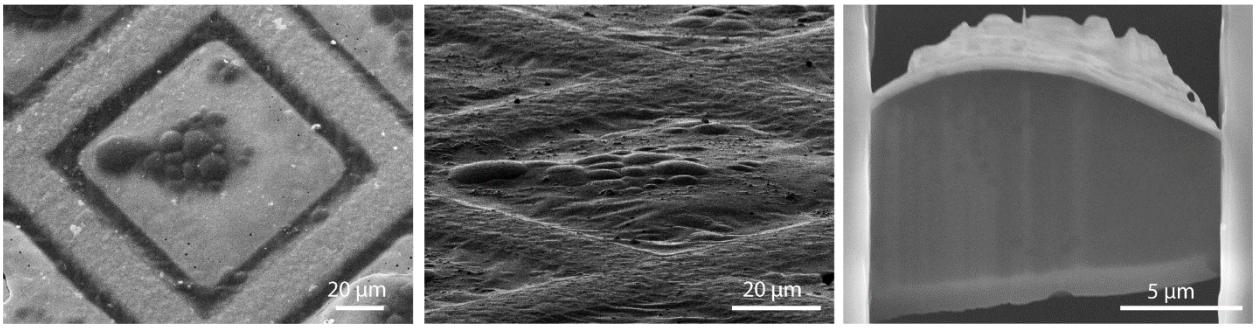

Figure 4.2.4: Dissociated embryonic cells in the FIB. Left image shows cells in the SEM view, center image in the FIB view. The rightmost image shows a lamella in the SEM view after milling.

out, but can be used directly for centrosomal studies. Given the small size of the interphase centrosome, it was decided that targeting this using CLEM approaches would be very challenging. 75 tilt series were successfully taken from lamella milled in this fashion and reconstructed into tomograms. Of these tomograms, 5 were of interphase centrosomes, featuring a whole or partial centriole. As the thickness of a lamella (around 200 nm) is around the same as the dimensions of the centriole (100 nm by 150 according to (Pelletier *et al.*, 2006)), it is likely that the centrioles will be at least partially removed by the ion beam during sample preparation. Regardless, each of these interphase centrosomes contained at least a partial centriole.

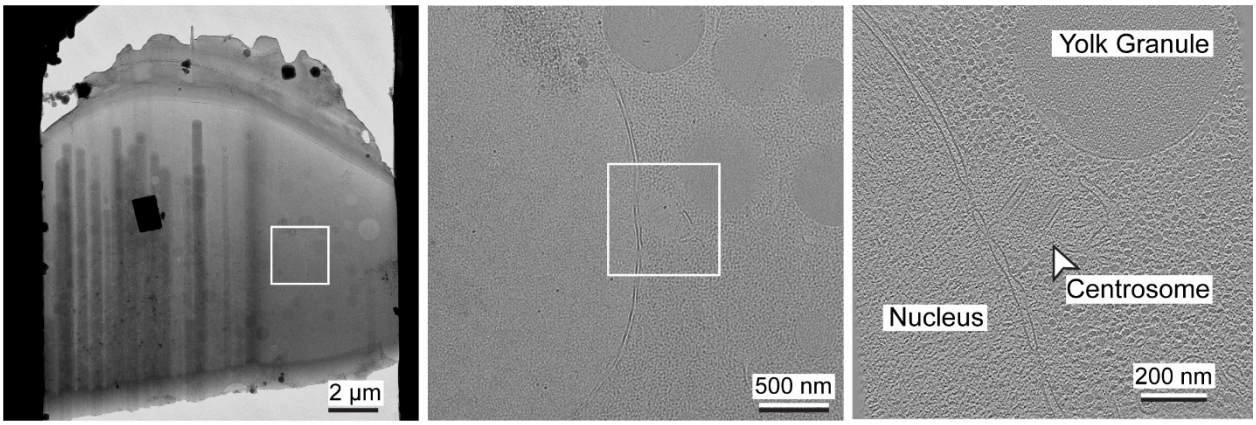

Figure 4.2.5: Identification of interphase centrosomes within a lamella. Left view shows an overview of the entire lamella in the TEM. The lamella shown is the same as in Figure 4.2.4. The region highlighted in the white square is shown in the center panel. The center panel has a small ribosome excluded region, itself being an interphase centrosome, adjacent to the nucleus, highlighted by another white square. The right panel shows a tomographic slice of this centrosome.

Although uncorrelated milling proved effective in collecting tomograms of the interphase centrosome, I was still missing the mitotic centrosome, with its expanded PCM being the focus of a large part of this thesis. To image this, I had to integrate light microscopy to my approach. A histone tag endogenous to the strain was working with also allowed me to identify cell stage, enabling targeting of mitotic cells. If a mitotic cell is seen, I was also able to conclude which stage of mitosis it is in. Therefore, after freezing, I examined grids on a prototype Leica cryo-confocal microscope, which allowed accurate localization of the SPD-5::GFP and H2B::mCherry signals from the cells while maintaining them at cryogenic temperatures. Unfortunately, I experienced

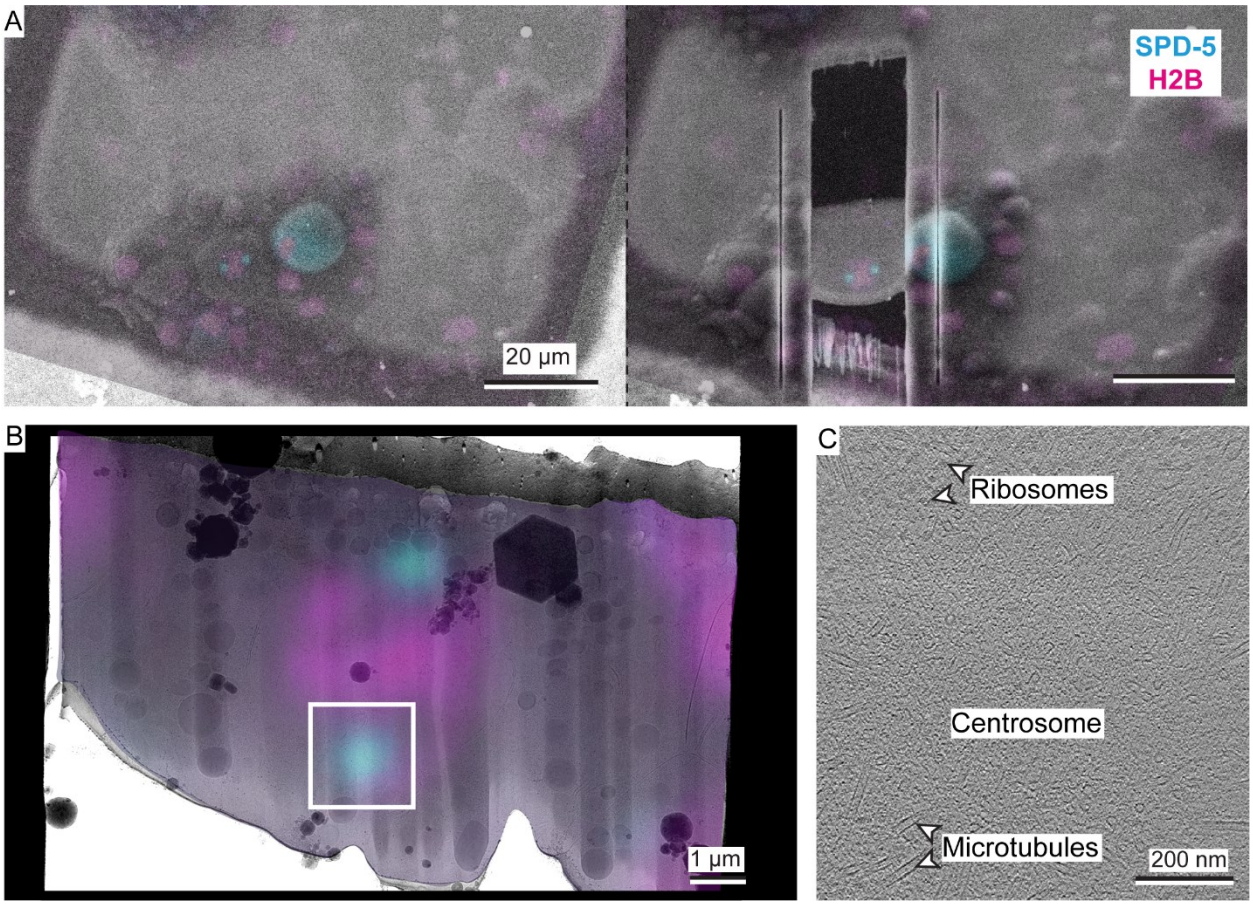

Figure 4.2.6: Identification of mitotic centrosomes. A: overlay of FIB SEM image and cryo-confocal fluorescence images, both before and after milling, showing one cell in metaphase. B: overlay of fluorescence and TEM images from a different lamella, showing the location of the mitotic centrosome within the lamella outlined by a white box. C: Tomographic slice of the centrosome obtained from this data.

problems in mapping the light microscopy data back into the ion beam data in three dimensions, related to the warping of the sample under the ion beam and consequent movement of my target (Klumpe *et al.*, 2021). Subsequently, I mapped the data back in x and y only (Figure 4.2.6). As this process is much quicker, it allowed many more lamella to be milled, increasing the chances of a successful hit on a centrosome. Of the correlated lamella successfully taken into the TEM without lamella breakage or prohibitively bad ice contamination, a total of 8 mitotic centrosomes were seen in the data, covering prophase through telophase (Table 4.2.1). One of these mitotic centrosomes was from a temperature sensitive mutant, and is not considered as part of the main dataset in PCM analysis. Additional 56 tomograms were reconstructed from areas of these targeted lamella not corresponding to centrosomes.

Table 4.2.1, centrosomes collected in this study.

Cell Stage	Number of Tomograms
Interphase	5
Prophase	1
Metaphase	3
Anaphase	2
Telophase	1
Total	12

4.3 Architectural features of the interphase centrosome

All five of the interphase centrosomes shared a number of common features. Each centrosome consists of a centriole surrounded by a small, unstructured, ribosome-excluding region (Figure 4.3.1A). A small number of microtubules were seen budding off from the surface of these centrosomes. I could not discriminate between microtubule-free and ribosome-free zones, with them having approximately the same radius from the center of the centrosome. Furthermore, not only is every centrosome connected to the nuclear envelope, so that this ribosome excluding region is in direct contact with this structure, but there is a Nuclear Pore Complex (NPC) also connecting to this region. Although some densities could be seen in the

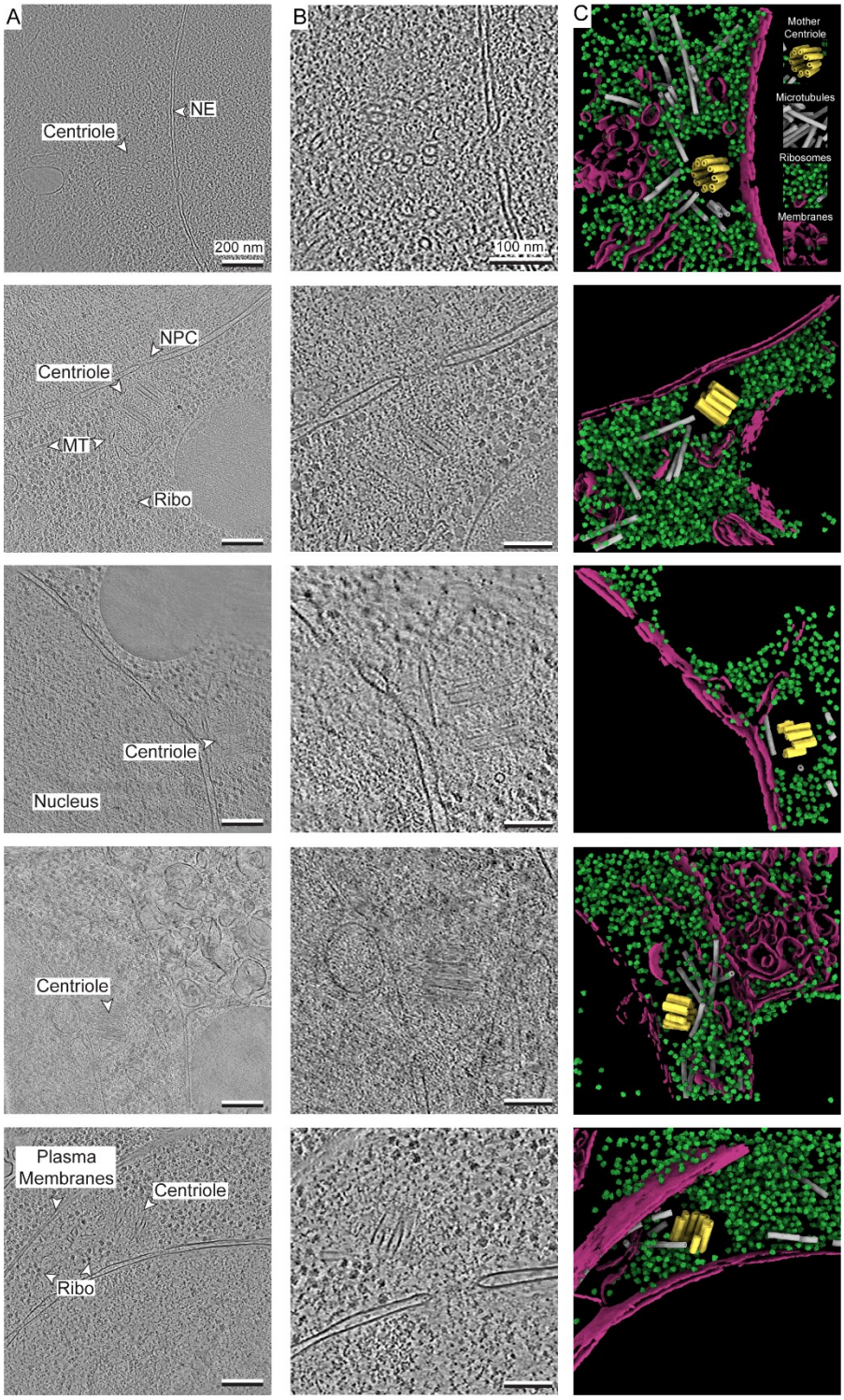

Figure 4.3.1: overview of the interphase centrosome. A: tomographic slices of all interphase centrosomes collected in this study. Certain features such as the centriole, plasma membranes, ribosomes (Ribo), microtubules (MT), nuclear envelope (NE), the nuclear pore complex (NPC), are identified. B: magnified section of regions immediately adjacent to the centrioles shown in A. C: Segmented images of interphase centrosomes, with centrioles in yellow, microtubules in grey, ribosomes in green, and membranes in purple.

excluded region, they were too sparse and difficult to differentiate from background to be effectively segmented (Figure 4.3.1B). The centriole itself featured several novel structures, which are described in detail in section 4.5.

To aid quantitative analysis of the spatial arrangement of the different cellular structures, I performed segmentation of centrioles, microtubules, membranes, and ribosomes, using a combination of semi-automated correlation-based segmentation in Amira (Stalling, Westerhoff and Hege, 2005), and deep-learning based annotation with DeePiCt (de Teresa-Trueba *et al.*, 2023). Specifically, membranes and ribosomes were localized in the volume using pre-trained DeePiCt models. Unfortunately, the only existing model, at the time of me starting this analysis, for microtubules was ineffective at picking up microtubules in the centrosome, as it only picked microtubules along a single axis instead of out of an aster. Initially therefore, I resorted to the more traditional means of segmenting by running cylinder correlations in Amira, and tracing the results. The centrioles were traced manually, as they are small and have a copy number of just one in the interphase tomograms, which does not justify the use of more sophisticated but initially technically challenging approaches. The output of these segmentations are shown in Figure 4.3.1C.

As it appeared that microtubules were present only at the very periphery of the ribosome excluded region, I decided to use my segmentations to explore this in a quantitative manner. I defined the center of the interphase centrosome as the centroid of the ribosome excluding region. Centroids were calculated by generating a sphere about 50% bigger than the volume that excludes ribosomes based on their segmentation at its widest point, and iteratively repelling it away from ribosomes until convergence, so that the centroid was at a local point most repelled by ribosomes. The initial sphere had to be made slightly larger than the excluded zone, otherwise the sphere would ‘stall’ at a random point in the middle of the void without being repelled to a true centroid. The occupancy of microtubules, ribosomes, and

membranes were determined at increasing radii from this centroid, once discovered, and I defined the excluded region for each at the last radius at which no voxels corresponding to the feature were found. Through these means, I found that the radius of the centrosome, measured as the ribosome excluded region, was 87.6 nm to 114.6 nm. Furthermore, the mean difference between the microtubule and ribosome excluded radii was only 8.9 nm, although standard deviation was fairly high at 37.9 nm. This confirmed the observation that microtubules are only seen right at the surface of interphase centrosomes (Figure 4.3.2, Table 4.3.1).

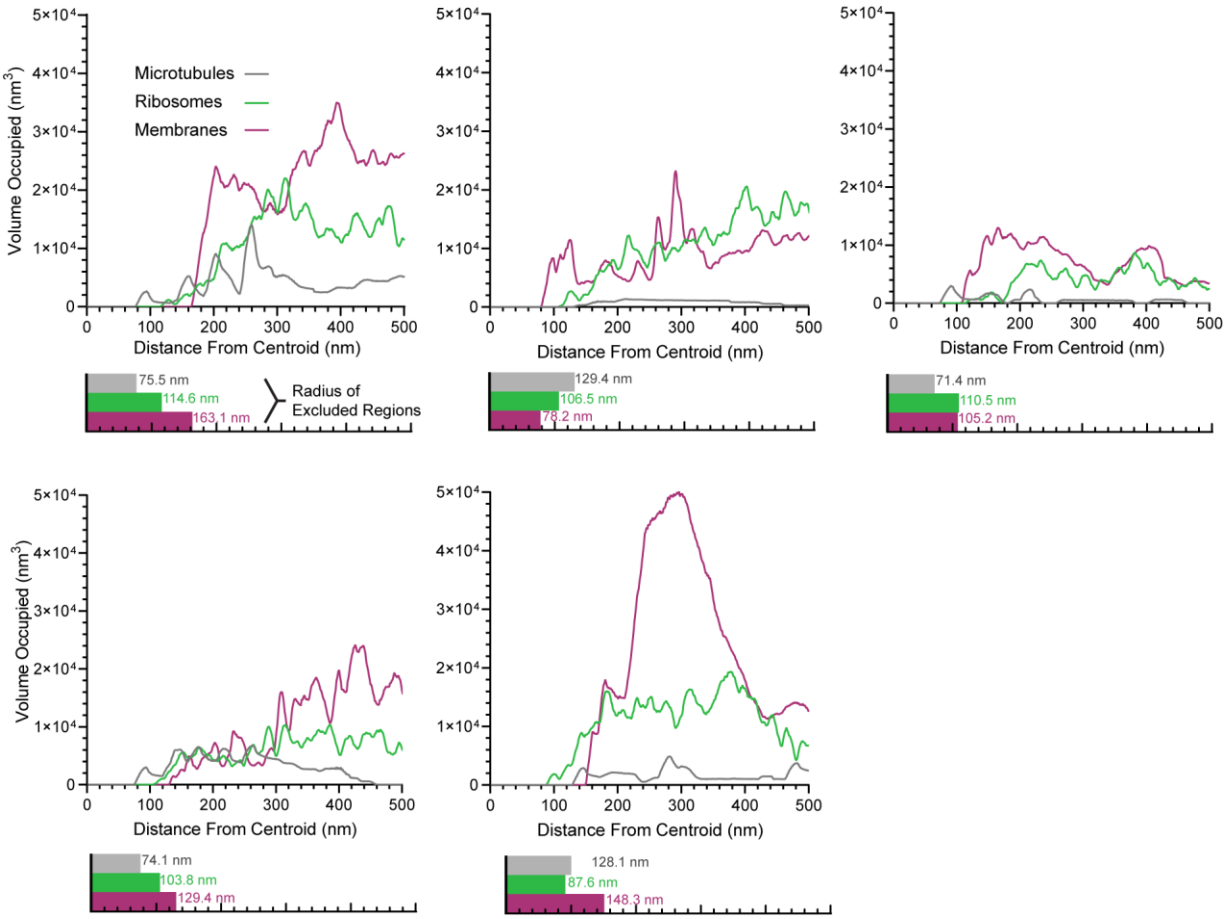

Figure 4.3.2: Volume of microtubules, ribosomes, and membranes at distances from the centrosome centroid for each of these features. The excluded zone, defined as the last distance at which no volume of this feature is detected, is recorded below.

Table 4.3.1, parameters of all interphase centrosomes analyzed in this study.

Cell Stage	Microtubule Excluded Radius (nm)	Ribosome Excluded Radius (nm)	Membrane Excluded Radius (nm)	Difference Between Ribosome and Microtubule Exclusion (nm)	Mean Ribosome /Microtubule Difference (nm)	Ribosome /Microtubule StDev (nm)	Mean Membrane /Ribosome Difference (nm)	Membrane /Ribosome StDev (nm)
Interphase	75.5	114.6	163.1	39.1	8.9	37.9	20.2	37.0
	129.4	106.5	78.2	-22.9				
	71.4	110.5	105.2	39.1				
	74.1	103.8	129.4	29.7				
	128.1	87.6	148.3	-40.5				

As previously stated, an NPC is seen connecting to the microtubule excluded region in all interphase tomograms. I probed the distances between the manually picked center of the NPC to the centroid of the segmented centriole mask. This was found to be very consistent, with a mean distance of 191.5 ± 5.0 nm (Figure 4.3.3, Table 4.3.2). This lack of variability implies the presence of some sort of physical tether, as shown in the literature (Bolhy *et al.*, 2011; Hashizume *et al.*, 2013), connecting these two structures. However, no density for such tether was visible in the centrosomal milieu.

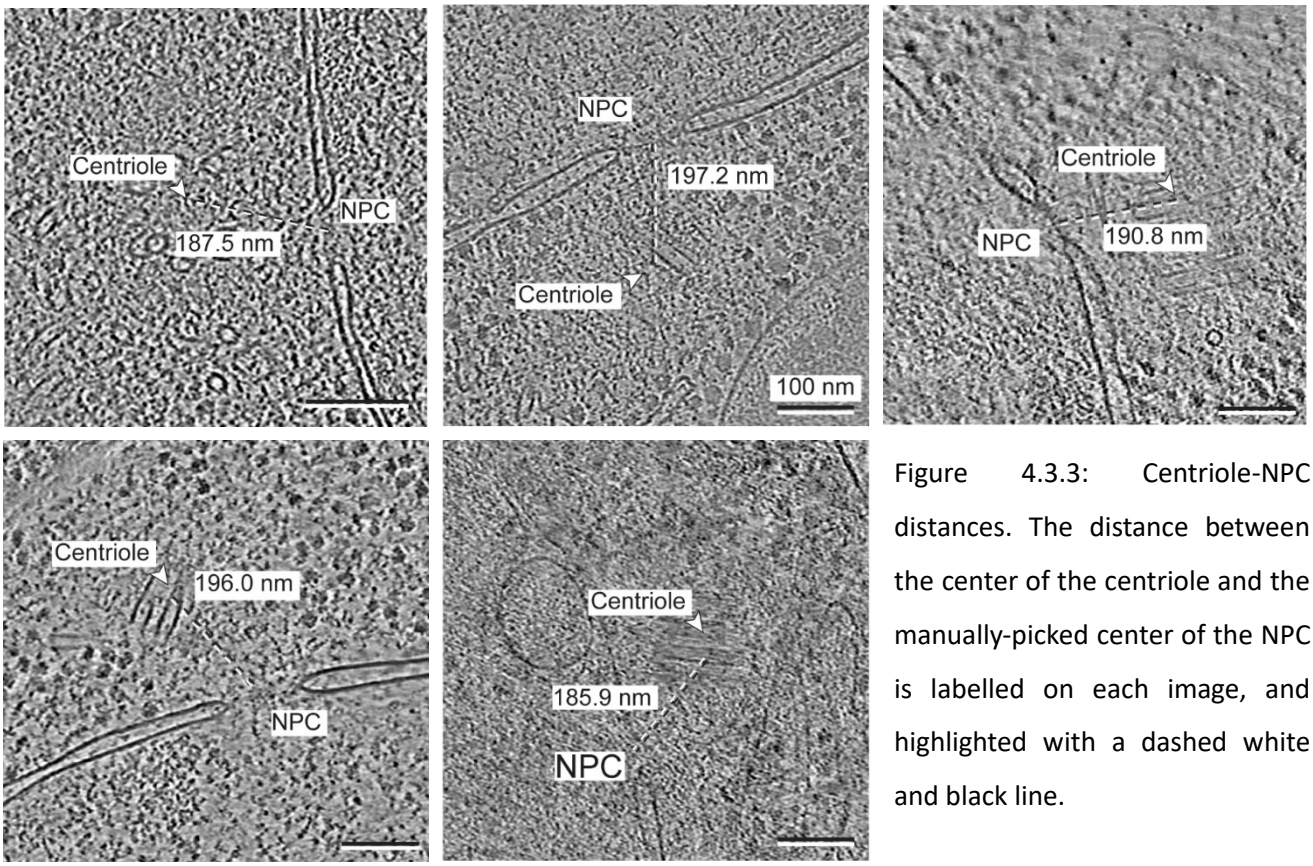

Figure 4.3.3: Centriole-NPC distances. The distance between the center of the centriole and the manually-picked center of the NPC is labelled on each image, and highlighted with a dashed white and black line.

Table 4.3.2, centrosome-NPC distances.

Centrosome Number	NPC-Centriole Distance (nm)
1	187.5
2	197.2
3	190.8
4	185.9
5	196.0
Mean	191.5
Standard Deviation	5.0

The interphase centrosome is understood to be liquid-like in nature (Woodruff *et al.*, 2017). It would therefore be expected that this structure would form spherically, but be capable of deforming under pressures. None of the interphase centrosomes, as demarked by the ribosome edge, are perfectly spherical, appearing instead as elongated droplets (Figure 4.3.4). This suggests that there might be some physical forces acting on centrosomes even in interphase.

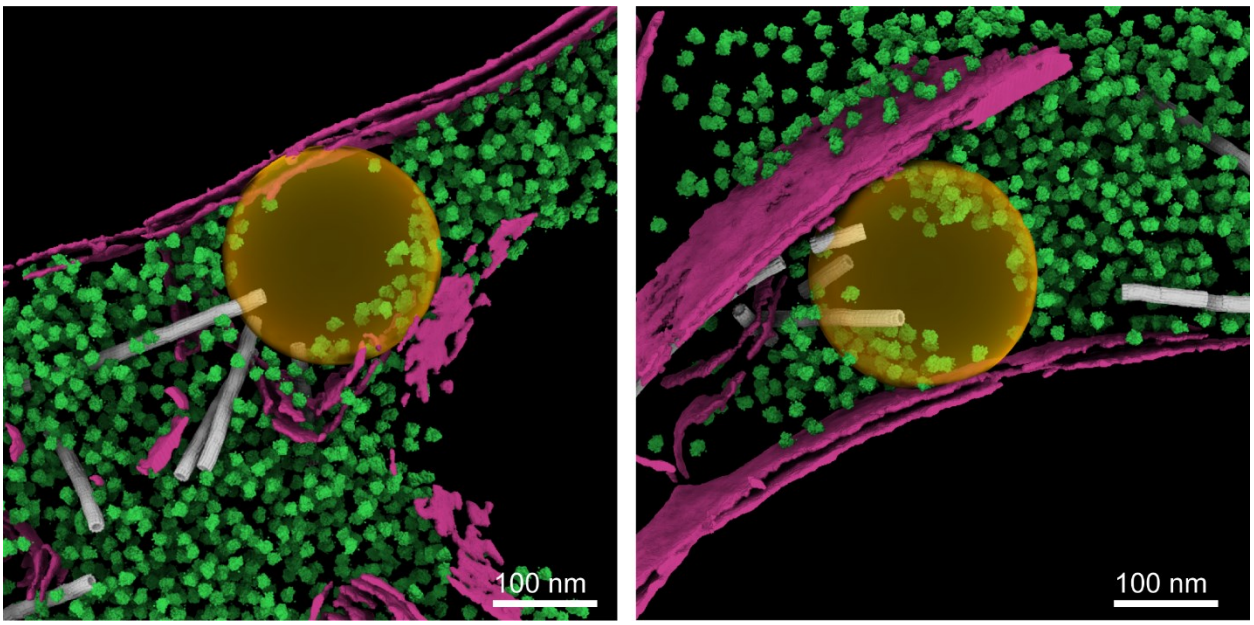

Figure 4.3.4: Interphase centrosome sphericity. Segmentations from two interphase centrosomes are shown. Orange spheres were grown from the centroid to best encompass the ribosome excluded region. As the centrosome is not spherical, some ribosomes can still be seen within this orange sphere.

4.4 Architectural features of the expanded, mitotic centrosome

Using the correlative approach, I was able to acquire 7 tomograms of mitotic centrosomes. Two more were collected that contained flaws attributed to problems in the sample preparation procedures, such as contaminating ice on the surface of the lamella, beam damage, or extreme curtaining during the FIB milling procedure. As these caused major issues in tomogram reconstruction, and rendered high resolution analysis impossible, they were not included in the shown datasets. The data that was retained includes tomograms from prophase, metaphase, anaphase, and telophase (Figure 4.4.1). However, the one telophase tomogram seen in this dataset contained no centrioles, and I could not define a region of microtubule exclusion, although ribosome exclusion was still present. This suggests a view along the very edge of the centrosome, cutting into only the very periphery of the organelle. As such, only limited information on the architecture of telophase centrosomes could be obtained.

As in interphase centrosomes, it was important to segment these tomograms to both aid visual interpretation of the inherently noisy volumes, and to allow quantification of the data (Figure 4.4.2). Although segmentation of membranes, ribosomes, and centrioles was carried out in mitotic centrosomes exactly in interphase, microtubules were traced slightly differently. The many more microtubules seen in mitosis stressed the importance of a more automated approach for particle picking that does not depend on the labor-intensive and computationally expensive Amira-based approaches. As such, I decided to use deep learning approaches for picking out mitotic microtubules. 6 of the 7 mitotic tomograms had their microtubules semi-manually traced in Amira. The output from 6 of these semi-manually traced tomograms was used to train a new DeePiCt model, which was much better at tracing microtubules in multiple directions, in contrast to pre-existing models which only

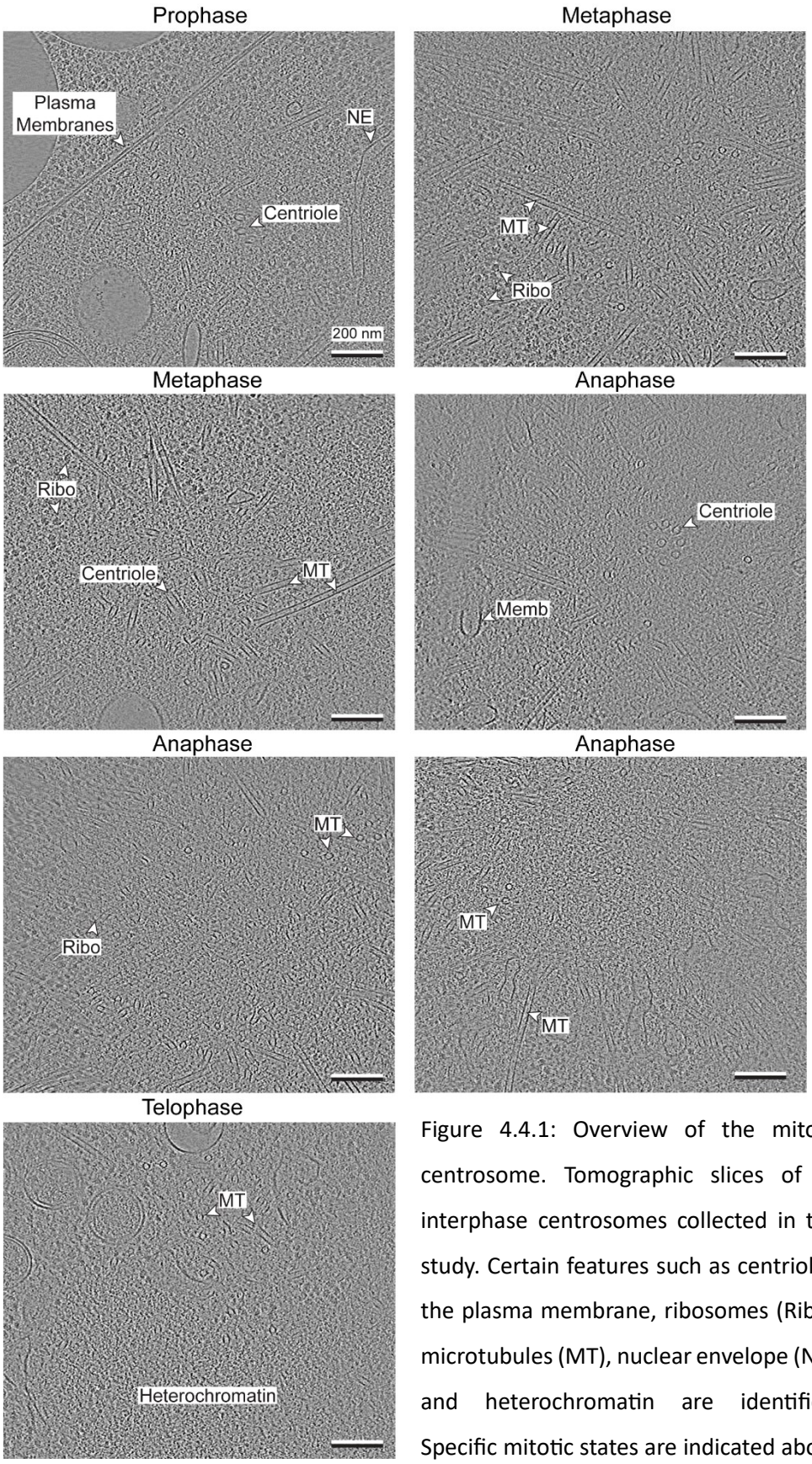

Figure 4.4.1: Overview of the mitotic centrosome. Tomographic slices of all interphase centrosomes collected in this study. Certain features such as centrioles, the plasma membrane, ribosomes (Ribo), microtubules (MT), nuclear envelope (NE), and heterochromatin are identified. Specific mitotic states are indicated above each tomogram.

traced microtubules along a single axis. This was also shown to be effective in tracing microtubules in HeLa cells (Mahamid *et al.*, 2016; de Teresa-Trueba *et al.*, 2023). This trained model was publicly released with DeePiCt for microtubule tracing.

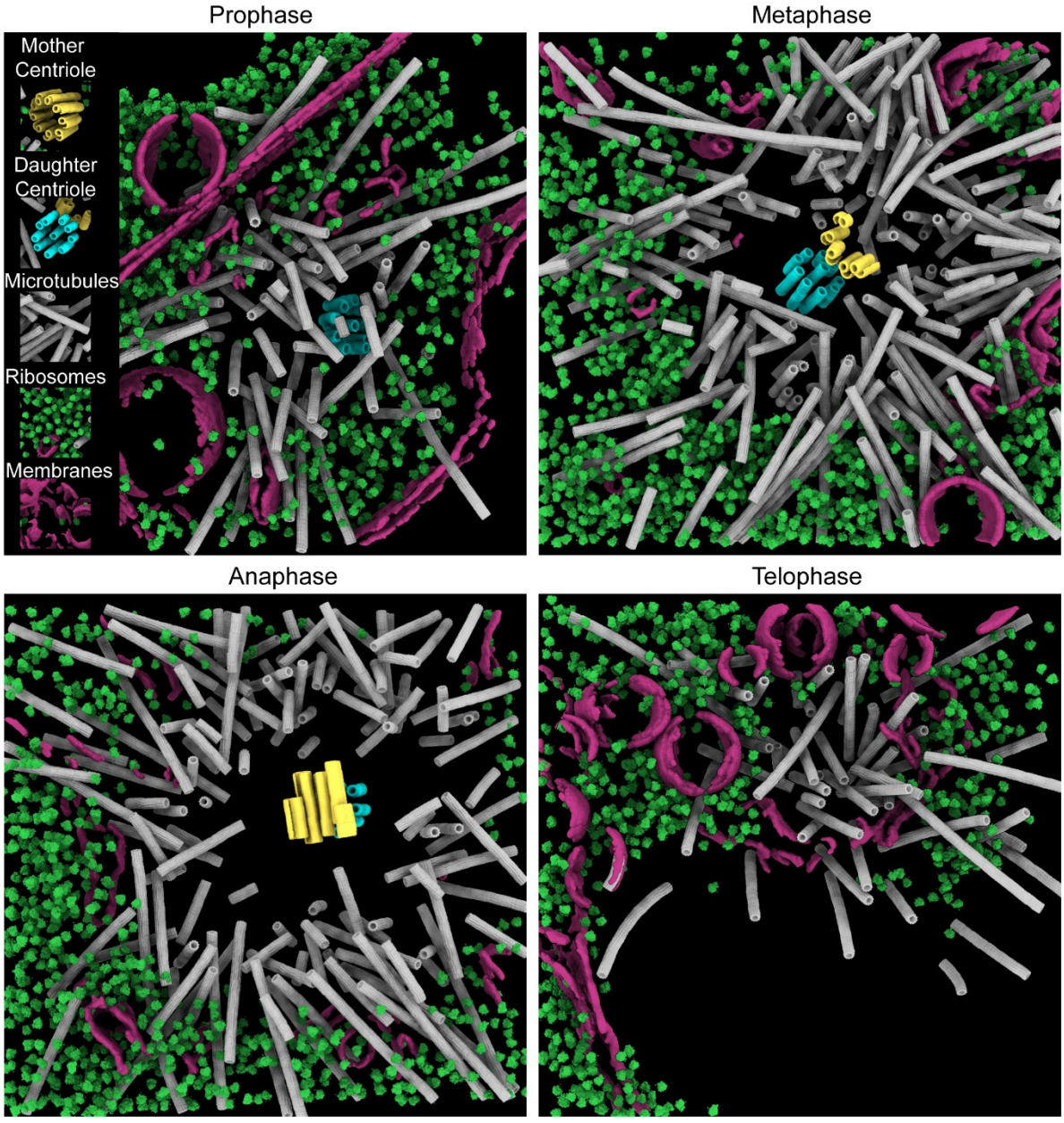

Figure 4.4.2: Segmentations of mitotic centrosomes. One segmented tomogram for each of the four major stages of mitosis are shown. Mother centrioles are in yellow, daughters in blue, microtubules in grey, ribosomes in green, and membranes in purple.

An internal arrangement can be observed surrounding the centrioles. This arrangement consists of two regions with distinct characteristics. The first region,

previously described as the Microtubule Excluded Zone (MEZ), encompasses the immediate vicinity of the centrioles. The MEZ is surrounded by a region rich in microtubules, but devoid of ribosomes, aptly named the Ribosome Excluded Zone (REZ). As mitosis progresses, a phenomenon becomes apparent—the radius of the MEZ relative to the REZ undergoes a discernible increase. In the initial stages of mitosis, specifically during prophase, the microtubule-excluded radius of the centrosome measures approximately 29.7 nm. Concurrently, the ribosome-excluded region, which can serve as a representative measure of the overall centrosomal volume observed through tomographic imaging, spans about 161.8 nm. Consequently, there exists a notable discrepancy of 132.1 nm between these two regions during prophase. As mitosis advances into metaphase, the discrepancy between the MEZ and the REZ further widens. The mean difference increases to approximately 215.3 nm during metaphase. Finally, in anaphase, the difference reaches its peak at approximately 262.2 nm (Figure 4.4.3, Table 4.4.1), highlighting the dynamic nature of the centrosome during this critical stage of cell division. These observations are consistent with prior investigations conducted on centrosomes using room temperature electron microscopy. Specifically they align with the findings from light microscopy studies, which have demonstrated the continuous addition of PCM proteins to the centrosome throughout mitosis in *Drosophila* and *C. elegans* (Alvarez-Rodrigo *et al.*, 2019; Mittasch *et al.*, 2020a). These findings shed light on the structural changes occurring within mitotic centrosomes and provide valuable insights into the complex mechanisms underlying the progression of centrosome maturation.

This data shows some evidence to add to the discussion around the concept of the "centriculum" (Maheshwari *et al.*, 2023). According to this model, the centrosome possesses a surrounding membrane structure derived from endoplasmic reticulum that serves to filter out shorter microtubules and prevent them passing out of the centrosome. I have observed that as one moves away from the centroid of the centrosome, membranes are encountered at nearly the same distance as ribosomes.

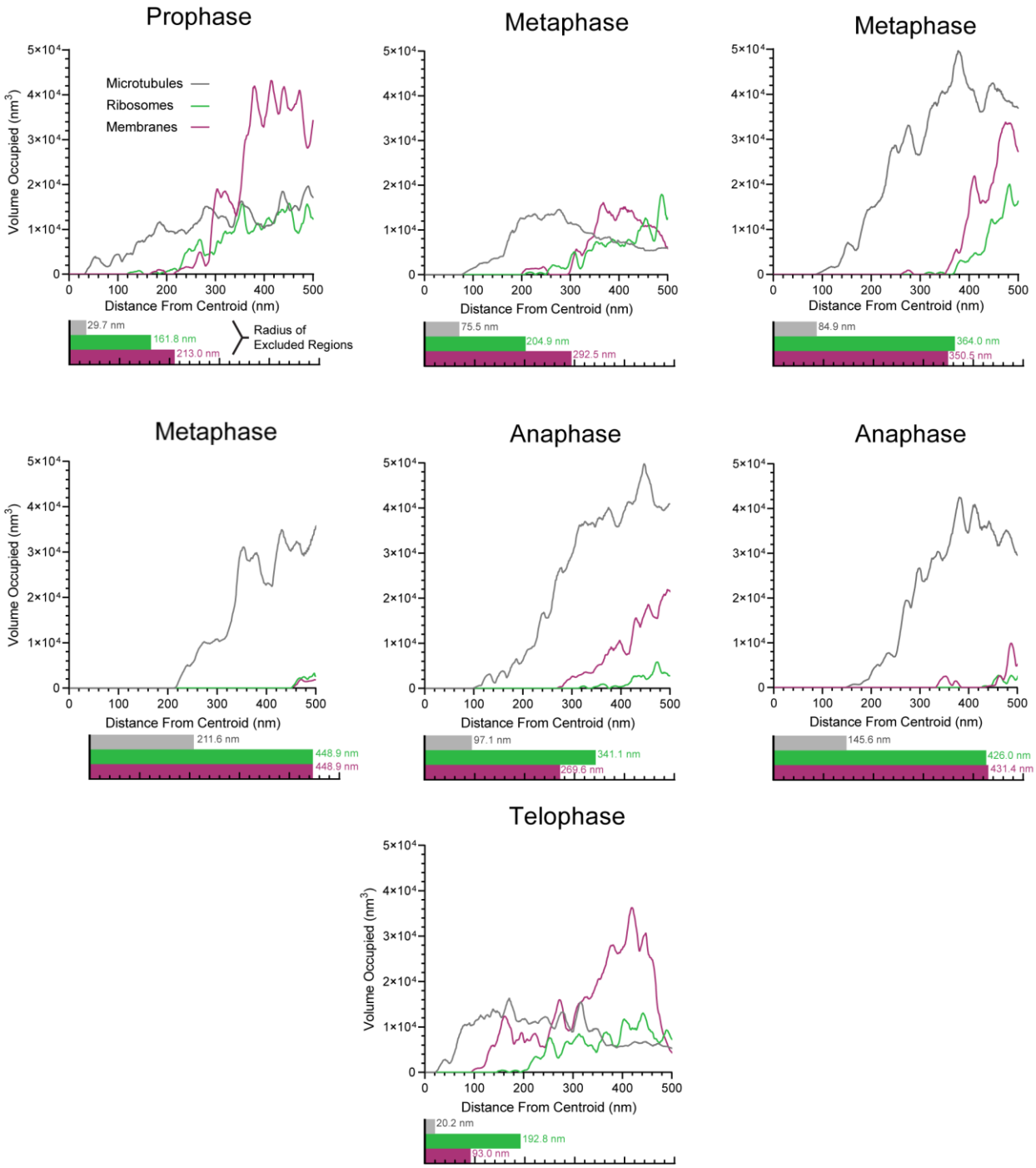

Figure 4.4.3: Volume of microtubules, ribosomes, and membranes at distances from the centrosome centroid for each of these features. The excluded zone, defined as the last distance at which no volume of this feature is detected, is recorded below.

Table 4.4.1, parameters of all mitotic centrosomes analyzed in this study.

Cell Stage	Microtubule Excluded Radius (nm)	Ribosome Excluded Radius (nm)	Membrane Excluded Radius (nm)	Difference Between Ribosome and Microtubule Exclusion (nm)	Difference Between Membrane and Ribosome Exclusion (nm)	Mean Ribosome /Microtubule Difference (nm)	Ribosome /Microtubule StDev	Mean Membrane /Ribosome Difference (nm)	Membrane /Ribosome StDev (nm)
Prophase	29.7	161.8	213.0	132.1	51.2	132.1	n/a	-5.8	65.0
Metaphase	84.9	364.0	350.5	279.1	-13.5	215.3	77.3		
	75.5	204.9	292.5	129.4	87.6				
	211.6	448.9	448.9	237.3	0.0				
Anaphase	145.6	426.0	431.4	280.4	5.4	262.2	25.7		
	97.1	341.1	269.6	244.0	-71.5				
Telophase	20.2	192.8	93.0	172.6	-99.8	172.6	n/a		

Indeed, during mitosis, there exists a difference of merely 5.8 nm between the radii of the ribosome-excluded region and the membrane-excluded region within the centrosome (Table 4.4.1). However, it is crucial to note that despite the presence of these membranes, they do not appear fully enclose the centrosome (Figure 4.4.4). It becomes evident that a model solely based on complete membrane enclosure fails to provide an adequate explanation for the intricate compartmentalization of centrosomes within the cellular context. Another explanation, more consistent with the data shown here, is that both the membranes and the ribosomes themselves may be excluded by the PCM material, rather than either forming a confining surface.

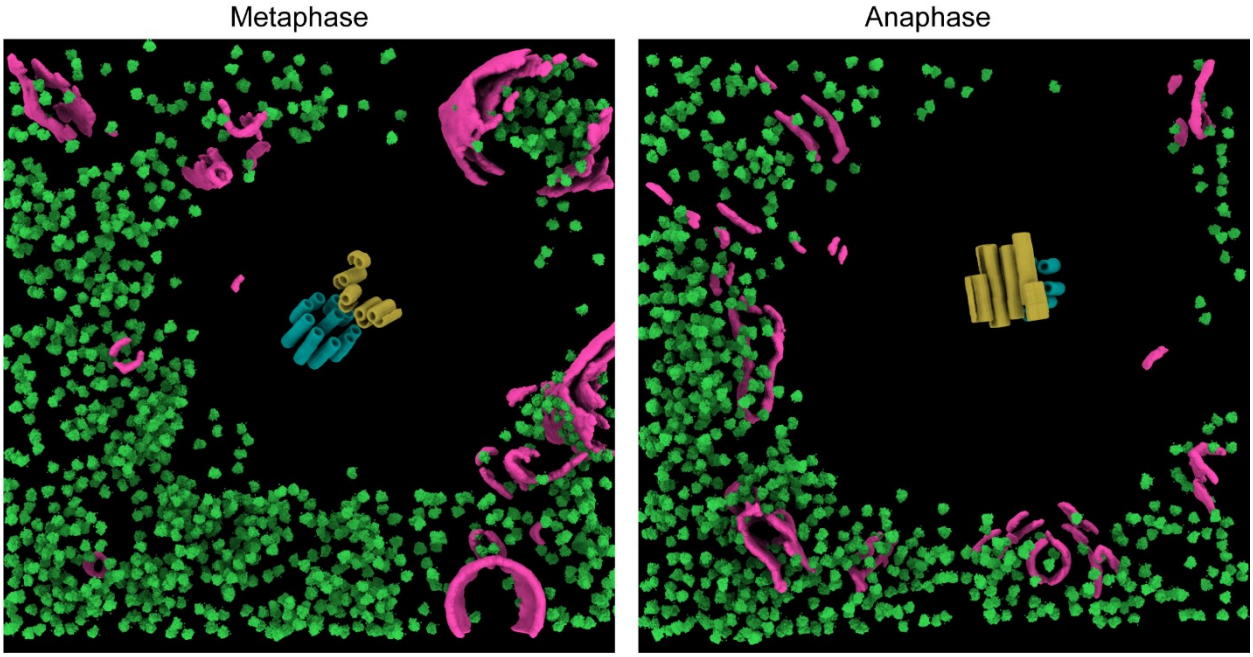

Figure 4.4.4: Evidence relevant to the centriculum model. Ribosomes (green) and membranes (purple) are shown to be equally excluded from the centrosome. Centrioles are included as a reference point.

I conclude that centrosomes are defined by concentric zones defined by the presence of centrioles (zone 1), a region free of microtubules (MEZ, zone 2), and a region rich in microtubules that exclude ribosomes (REZ, zone 3). My results indicate that the outer edge of Zone 3 defines the interface between PCM and the cytoplasm, while zones 2 and 3 expand during centrosome maturation. The PCM also acts as a selective filter that excludes ribosomes, allows entry of centrosome proteins, and permits exit of microtubules.

4.5 The mother and daughter centrioles display prominent structural differences

Much research has been dedicated to the investigation of the centriole's ultrastructure in *C. elegans* using electron microscopy techniques at room temperature. These studies have yielded a wealth of knowledge concerning the detailed organization and morphology of the centriole (Dammermann *et al.*, 2004; Pelletier *et al.*, 2004, 2006; Sugioka *et al.*, 2017; Woglar *et al.*, 2022). However, it must be acknowledged that the methodology of room-temperature EM may introduce artifacts that could potentially influence the accurate depiction of the centriole's intricate features. For instance, previous work has shown that the centriolar "paddlewheel" structure appeared fuzzy and disordered, which could be attributed to limitations in the chemical stains used during the staining process. In contrast, cryo-fixation techniques preserve cellular material in a state that closely resembles its native condition. By utilizing cryo-ET, I was able to gain unprecedented insights into the precise ultrastructure of the centriole.

During the examination of tomograms where two centrioles were simultaneously visible, one centriole was positioned at a 90-degree angle relative to the long axis of the other centriole. This distinctive spatial arrangement allowed for the

differentiation between the mother and daughter centrioles by observing the growth of the daughter centriole from the mother's cylinder wall (Azimzadeh, 2014) (Figure 4.5.1). The structural features observed within the daughter centriole were found to be similar to those described in the existing literature based on studies utilizing room temperature EM. These features included the presence of singlet microtubules and a cartwheel structure, sometimes referred to as the "inner tube" in certain literature (Pelletier *et al.*, 2006). Furthermore, the size and shape of the cartwheel structure observed in the centrioles aligned with the findings from previous studies on the protein SAS-6 (Hilbert *et al.*, 2013; Hatzopoulos *et al.*, 2021; Woglar *et al.*, 2022).

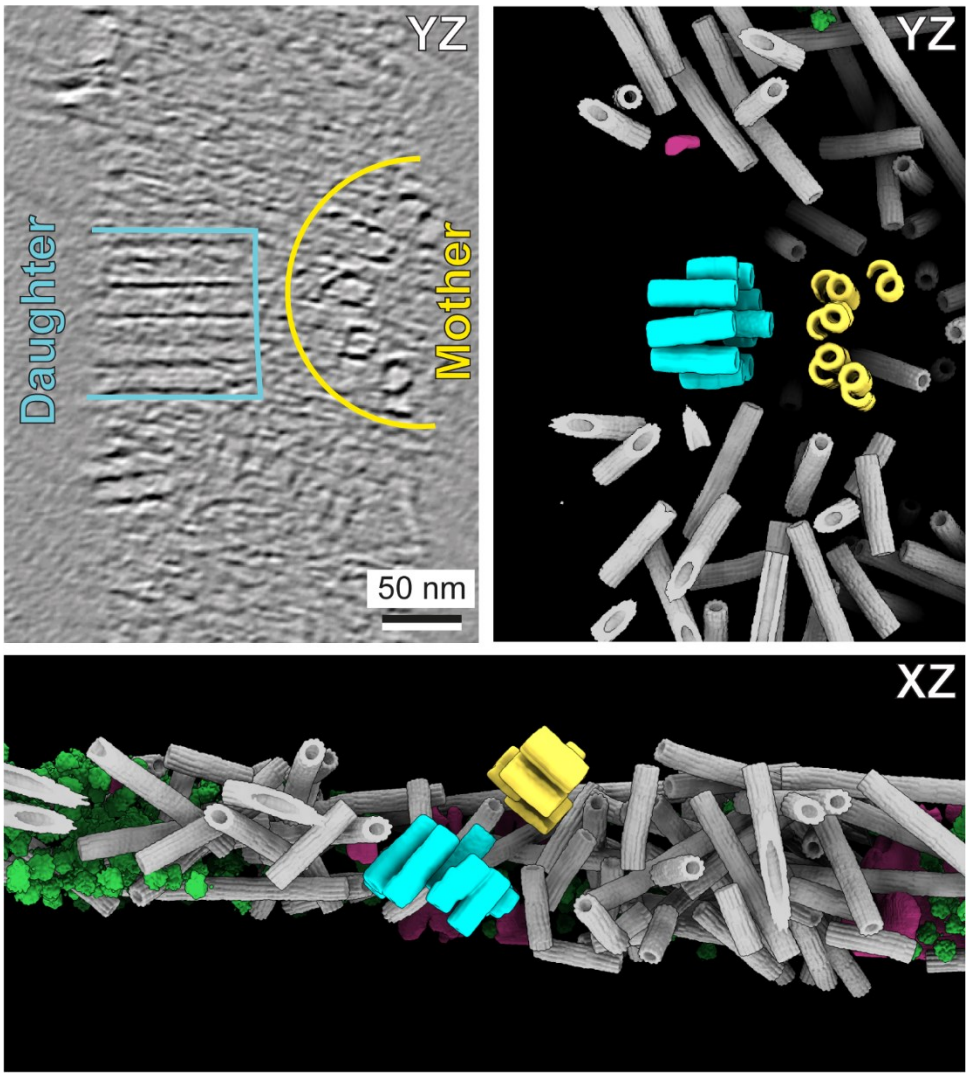

Figure 4.5.1: Segmentations of the tomogram allow identification of the mother and daughter centrioles. The daughter centriole's positioning at a 90° angle off the side of the mother centriole in both the XY and YZ planes. Daughter centrioles are shown in blue, mothers in yellow.

However, the examination of the mother centriole revealed previously unknown characteristics. Notably, the distinct "paddlewheel" structure typically associated with the centriole was instead observed as a partial b-tubule. Additionally, a star-shaped density protruded from each b-tubule, encircling the entire circumference of the centriole. This star density exhibited particular prominence at the junction between the a- and b-tubules, known as the "star joint," as well as just beyond the tip of the b-tubule, referred to as the "star tip." Furthermore, the presence of the central tube within the *C. elegans* centriole was confirmed, as described in previous literature (Pelletier *et al.*, 2006; Woglar *et al.*, 2022). This central tube emitted projections I termed "tube spikes" toward the centriole microtubules. Although these spikes were also observed in the daughter centriole, they were too faint to be meaningfully interpreted or analyzed (Figure 4.5.2).

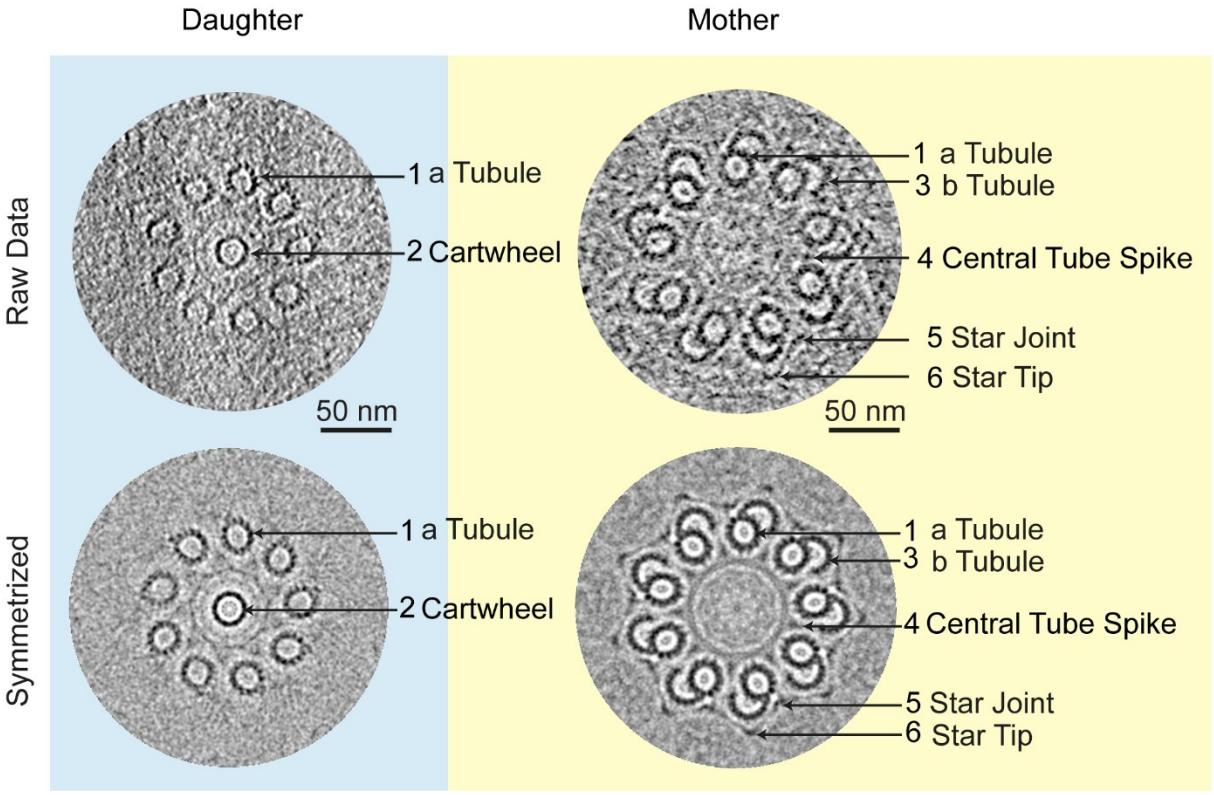

Figure 4.5.2: Cross-sectional views of the mother and the daughter centrioles, both unsymmetrized and symmetrized. Arrows point to key features including: the a tubule (1), cartwheel (2), b tubule (3), central tube spikes (4), outer star joint (5), and outer star tip (6).

Despite the limited number of particles available arising from the shortness of these centrioles, I successfully generated subtomogram averages of the centrioles, with particles sampled along the a-tubule, to identify potential differences between the mother and daughter centrioles based on 2D projections of per-centriole averages (Figure 4.5.3). This approach yielded a resolution of 45 Å in the final 3D reconstruction (Figure 4.5.4), prior to splitting into per-centriole models and 2D projection. While the features of the daughter centriole remained consistent, the mother centrioles exhibited heterogeneity. The number of protofilaments in the b-tubule varied from 3 to 9, and no discernible pattern was observed to correlate the number of protofilaments with the cell stage or stage of mitosis. None of the observed cases demonstrated complete closure of the b-tubule onto the a-tubule. An intriguing finding is the presence of 13 protofilaments in the a-tubule of both the mother and daughter centrioles of *C. elegans*. This contrasts with the widely observed prominence of 11 protofilament microtubules within this organism (Chalfie and Thomson, 1982; Chaaban et al., 2018). The close proximity of the 13 protofilament centrioles to the 11 protofilament centrosomal microtubules suggests the existence of a tightly regulated and spatially controlled mechanism for microtubule templating (Figure 4.5.5).

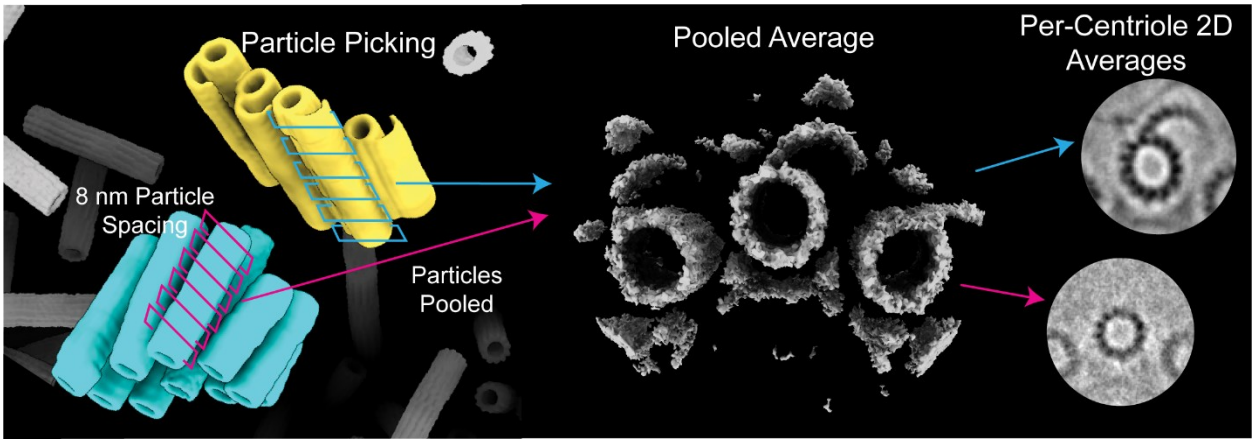

Figure 4.5.3: Schematic of centriole subtomogram averaging: particles are sampled 8 nm along each centriole a microtubule, and then pooled together for alignment. After, averages are separated into per-centriole models and averaged along the long axis of the centriole to boost SNR.

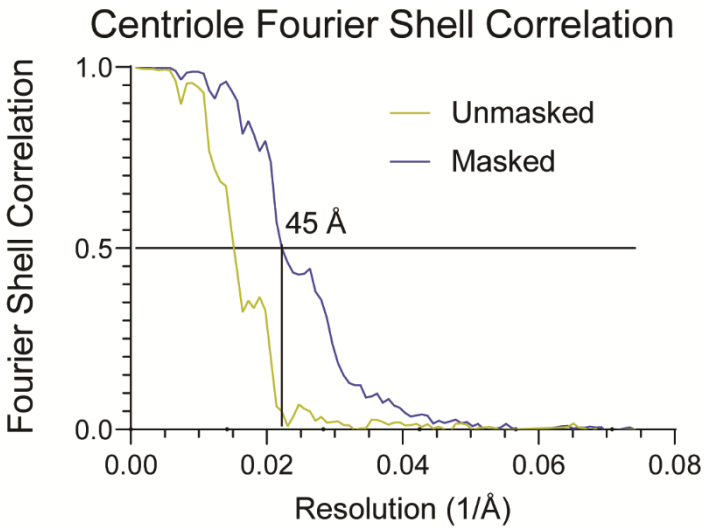

Figure 4.5.4: Fourier Shell Correlation (FSC) curves for both the masked and unmasked centriole subtomogram averages. FSC cutoff taken at 0.5 giving a resolution of 45 Å.

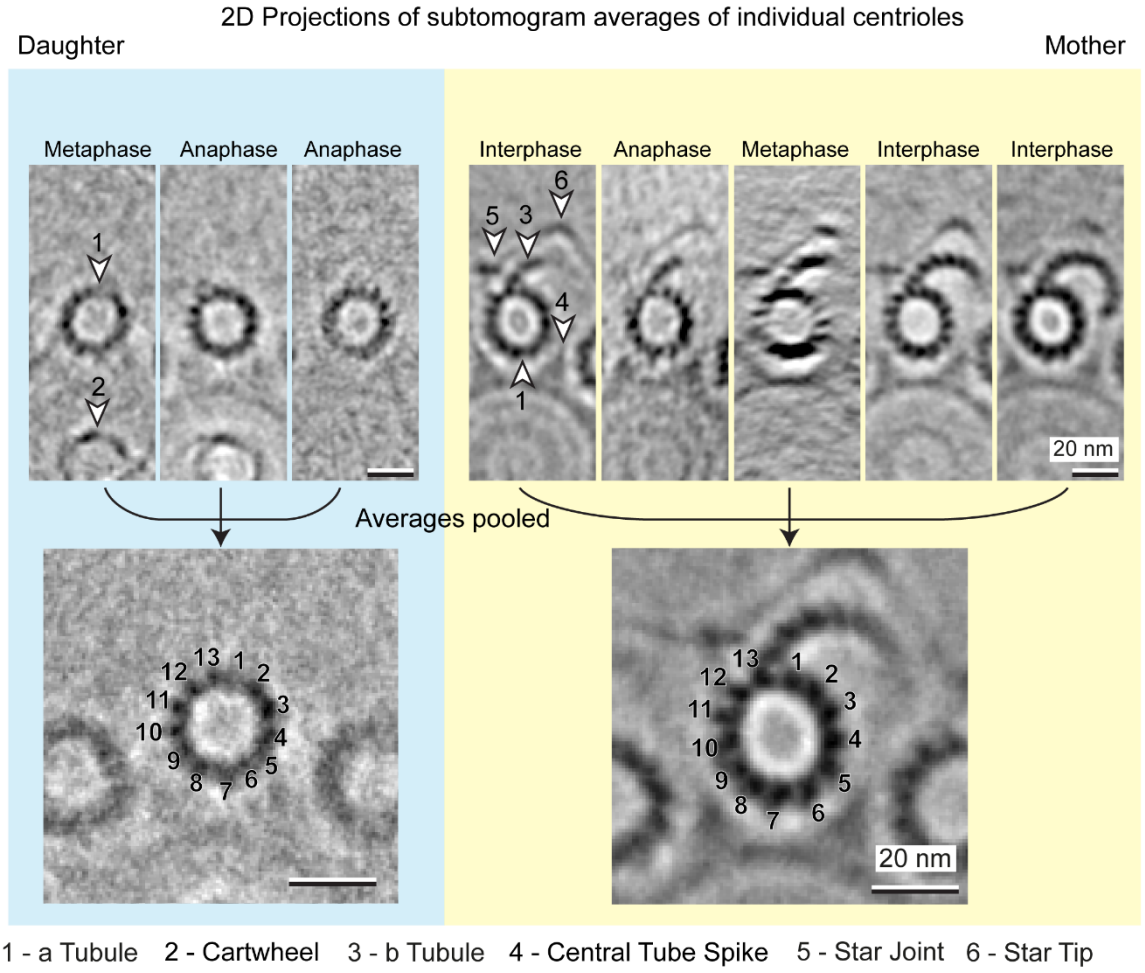

Figure 4.5.5: Gallery of 2D projections of per-centriole subtomogram averages. Numbers relate to the same features as figure 4.5.2. Cell stage is written above. Below are pooled 2D averages, with protofilament numbers labelled next to them.

To quantify the sizes and spatial distribution of the newly identified structures, line scans were performed, and intensities were measured in the original denoised tomograms. However, due to physical constraints, it was not feasible to perform these measurements on all centrioles or features. For instance, complete daughter centrioles could not be fully resolved in this study as they all were partially cut off by the lamella edge. Consequently, the total length of the a-tubules within daughter centrioles could not be determined. In many tomograms, the star tip, joint, and tube spikes were obscured by the missing wedge, resulting in a lower number of measurements from which distances can be determined. Regardless, I was able to observe the lengths of these features through this approach.

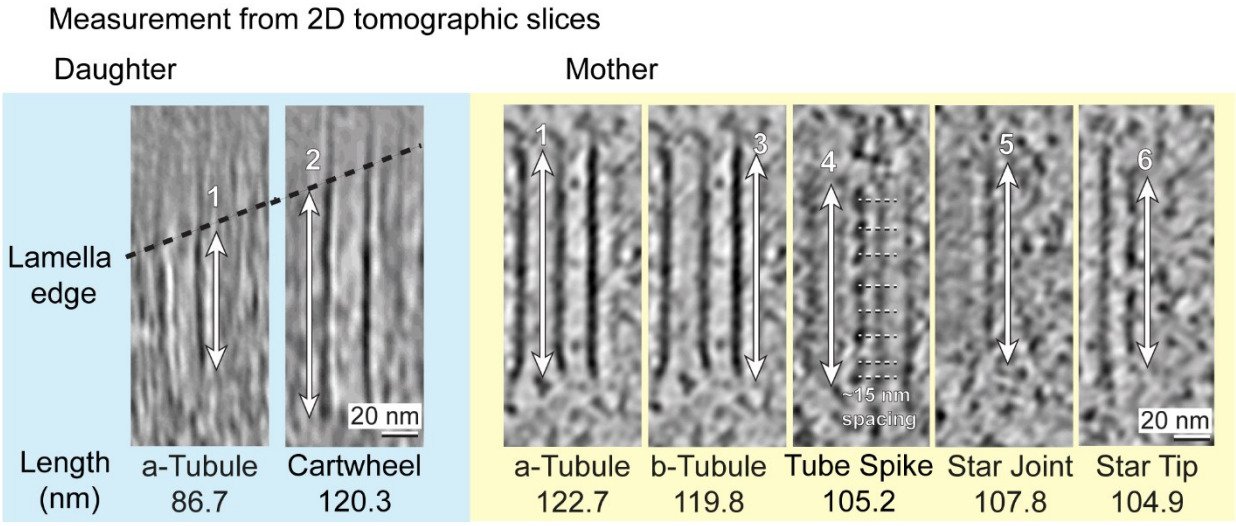

Figure 4.5.6: Lengths of centriole structural features. Distances indicated are from the averages shown in Table 4.5.1. Dashed lines in the Tube spike indicate the approximate 15 nm spacing between densities.

The analysis of the mother centriole unveiled a total length of 122.7 nm on the a-tubule, with the b-tubule spanning 119.8 nm, accounting for nearly the entire length of the a-tubule. The spikes of the central tube extended along the centriole for a length of 105.2 nm and have spacing of approximately 15 nm, while the star joint covered 107.8 nm, and the star tip discontinuously covered 104.9 nm. Notably, each of these features exclusively found in the mother centriole (b-tubule, barrel spikes, star joint, and star tip) appeared at an equal distance from the proximal and distal

ends of the centriole, indicating a lack of polarity. This characteristic aligns with previous literature in *C. elegans* (Pelletier *et al.*, 2006; Woglar *et al.*, 2022) but contrasts with other model organisms such as *Drosophila* and humans, which have clear structural differences between the proximal and distal ends (Bowler *et al.*, 2019; Klena *et al.*, 2020; Nazarov *et al.*, 2020)(Figure 4.5.6, Table 4.5.1). Despite attempts to perform subtomogram averaging of these newly identified features, the limited number of particles resulting from the short length of the centriole prevented the generation of useful maps.

Table 4.5.1, centriole feature lengths

Mother			
	Mean	**Standard Deviation**	**N**
A Tubule Wall	122.7	8.1	15
B Tubule Tip	119.8	11.4	9
Central Tube Spike	105.2	5.4	5
Outer Star Joint	107.8	7.7	4
Outer Star Tip	104.9	3.2	5
Daughter			
	Mean	**Standard Deviation**	**N**
A Tubule Wall*	86.7	8.3	18
Cartwheel*	120.3	7.2	4

To investigate the molecular identity of the recently discovered "star" structure, I turned to recent literature, which involved expansion microscopy of *C. elegans* gonad cells. This literature indicated that SPD-2 localized at the star position (Woglar *et al.*, 2022). To further explore this connection, a temperature-sensitive mutant strain of *C. elegans* was utilized. Under permissive conditions at 16°C, the worms displayed a normal phenotype. However, when exposed to 25°C, the worms experienced a rapid reduction in SPD-2 levels, becoming undetectable within the centrosome under fluorescence light microscopy within 1.5 minutes, as inactivation of SPD-2 during mitosis forces it from the centrosome. (Cabral *et al.*, 2019). Subsequently, the correlative cryo-ET pipeline, as described previously, was performed on SPD-2 mutants that had been kept at 25°C for 4 hours in order to eliminate SPD-2. Although 4 hours may have been excessive, it was decided that this would provide a stronger

guarantee that the embryos would be free from SPD-2, as eggs are laid after just 150 minutes. Under these conditions, the single centriole containing tomogram acquired revealed that the centrioles maintained the star density. Curiously and unexpectedly the b-tubule was absent, whereas the outer star remained clear and visible (Figure 4.5.7). The fluorescence signal for SPD-2 did not localize to the area associated with the b-tubule, and as such this cannot be easily explained. However, the cartwheel structure appeared more prominent than expected for a mother centriole, suggesting that this particular centriole was in a very early stage of development compared to other mother centrioles. If indeed it is in an early stage, it could be before the development of the b-tubule but after formation of the star. Alternatively, as SPD-2 plays myriad roles in both centrosome and centriole biology, it is possible its elimination has had unexpected effects downstream, resulting in this phenotype. Ultimately, SPD-2 is highly unlikely to be the primary component of the outer star. Given its localization within the centriole as determined by light microscopy, and its biological function, SAS-7 remains a likely candidate for the identity of this outer star (Sugioka *et al.*, 2017; Woglar *et al.*, 2022).

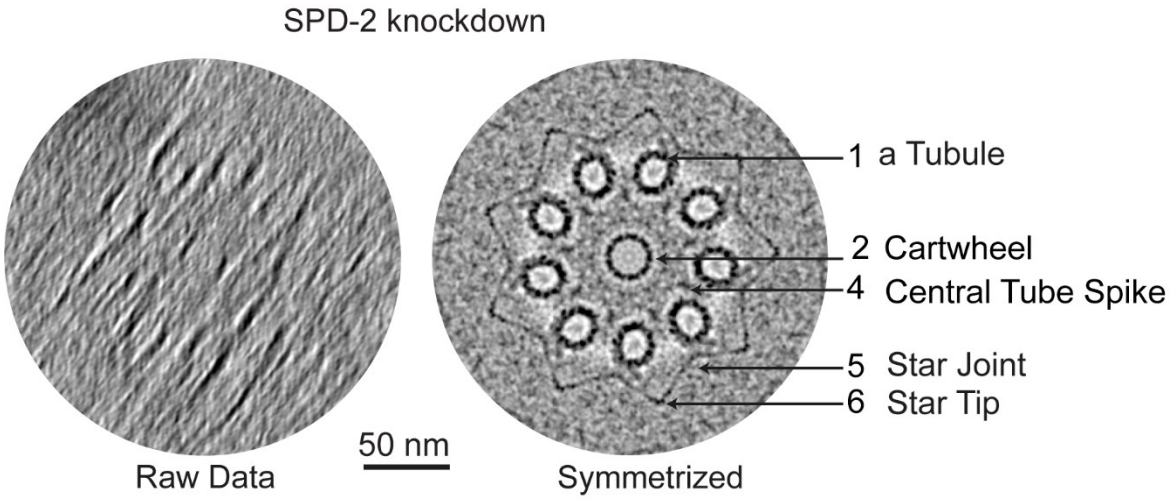

Figure 4.5.7: Features as seen in a SPD-2 knock-down mutant, both symmetrized and unsymmetrized.

4.6 Microtubule organization within the centrosome

The Mitotic PCM is responsible for nucleating and organizing numerous microtubules, which are essential for the construction of a functional spindle. As I aimed to further understand how these microtubules were organized, I decided to investigate their properties. Specifically, I was interested in exploring the uniformity of microtubule protofilament numbers, and the polarity of the microtubules in question relative to the centrosome.

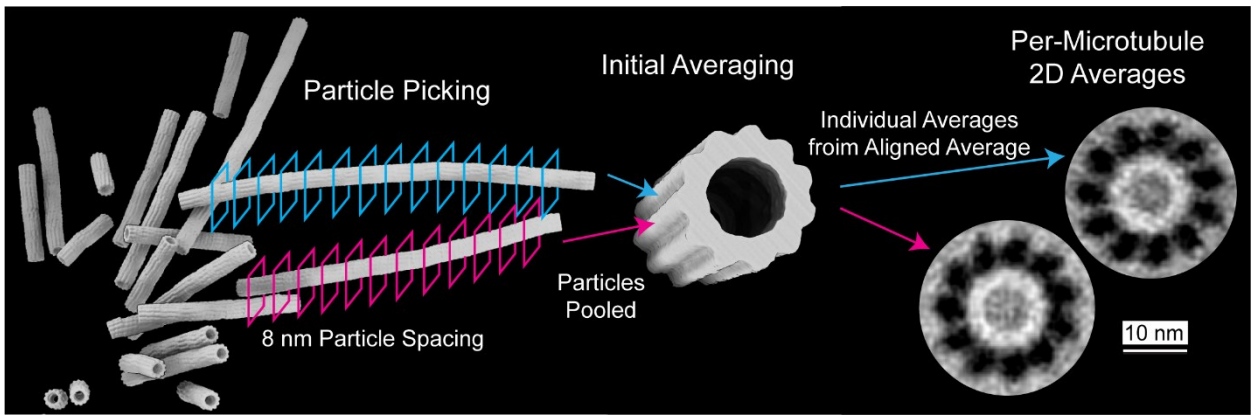

Figure 4.6.1: Schematic of microtubule averaging workflow: microtubule sampling takes place at 8 nm spacing along each microtubule, before being pooled into a single average for alignment. Once aligned, these are separated back into per-microtubule averages, which are then projected along z to increase signal/noise ratio.

Previous studies have shown that microtubules in *C. elegans* neurons and embryos contained 11 protofilaments (Chalfie and Thomson, 1982; Chaaban *et al.*, 2018). To verify this, I conducted the analysis by sampling 8 nm segments along the length of the microtubules (Figure 4.6.1). These particles were then aligned and averaged to generate a comprehensive map with a resolution of 24 Å (Figure 4.6.2). As this average involves particles from all microtubules and cannot say anything about individual filaments, I then divided the data into individual maps for each microtubule. Each individual map was then projected along the long axis, and the 2D projections of these averaged maps were cross correlated to references representing a range of 9-15 protofilaments, and the result of the highest cross correlation score

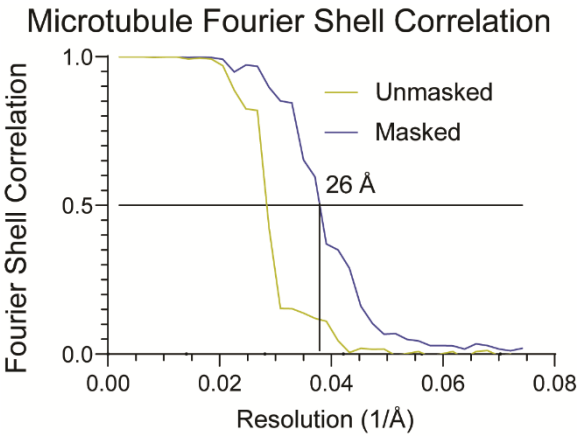

Figure 4.6.2: FSC curves for both the masked and unmasked microtubule subtomogram averages. FSC cutoff taken at 0.5 giving a resolution of 24 Å.

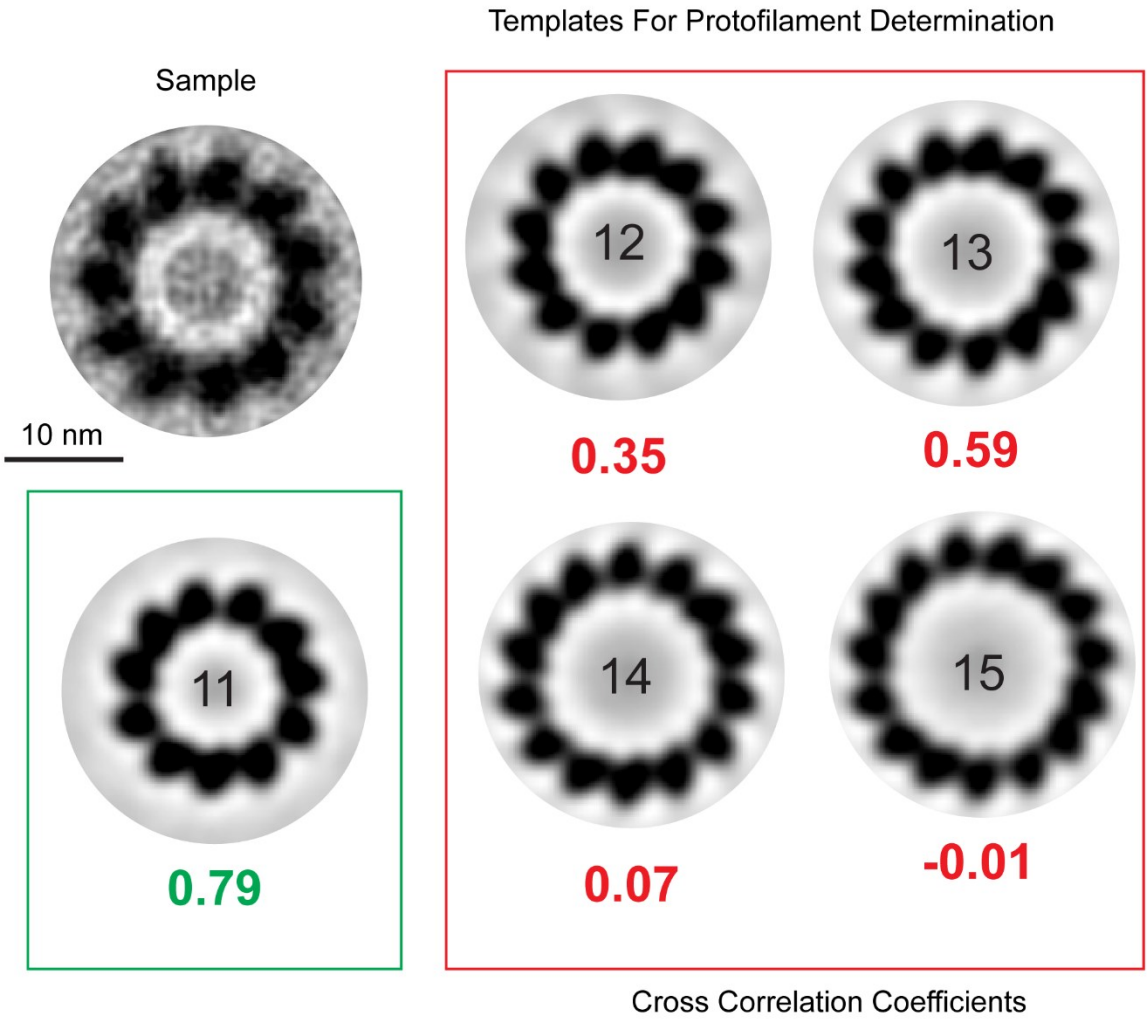

Figure 4.6.3: Application of per-microtubule averages to determine protofilament number. Each microtubule average is rotated and cross correlated with templates corresponding to 11, 12, 13, 14, and 15 protofilament microtubule templates, and the result with the highest cross correlation score is recorded as the protofilament number.

was saved as the protofilament number for the microtubule. 2D projections were taken as this improves the signal to noise ratio of the data, without affecting accuracy of protofilament assignment. The reference maps were obtained from previous electron microscopy studies (EMDB accession codes EMD-5191 to EMD-5195, from (Sui and Downing, 2010)) (Figure 4.6.3). In total, I analyzed 830 microtubules, comprising all the mitotic microtubules seen in all datasets, with an average length of 149 nm and a standard deviation of 109 nm. Apart from two microtubules, all exhibited 11 protofilaments (Table 4.6.1). This observation shows a high degree of conservation in protofilament number within *C. elegans* embryonic cells, higher than observed in plastic embedded data taken also from the embryo (Chaaban *et al.*, 2018). It is worth noting once again that this number differs from the 13 protofilaments found in centrioles, suggesting distinct nucleation mechanisms or interaction partners for these newly identified microtubule subpopulations.

Table 4.6.1, microtubule protofilament numbers

Cell Stage	Total Microtubules	11 Protofilaments
Prophase	72	72
Metaphase	169	168
	49	49
	162	161
Anaphase	132	132
	196	196
Telophase	50	50
All	830	828

I next examined the preservation of microtubule polarities. As the microtubule averages were randomly oriented in the data, it was first necessary to arrange them relative to the mitotic spindle. Particles in a microtubule model were subsequently rearranged so the first particle is closest to the previously identified centroid of the microtubule-excluded zone, meaning every average was functionally ‘pointing away’ from the centroid. Next, I made use of the existing observation that the polarity of microtubules can be determined by examining the skew of microtubules seen down a cross sectional view of the filament. As such I analyzed the protofilament skew in

the 2D averages of each rearranged microtubule and compared it to two distinct models: one corresponding to a microtubule with a positive orientation, where the microtubule plus end points away from the centroid and appears to exhibit a clockwise skew, and the other corresponding to a negative orientation, which displays a counter-clockwise skew (Sosa and Chrétien, 1998) (Figure 4.6.4).

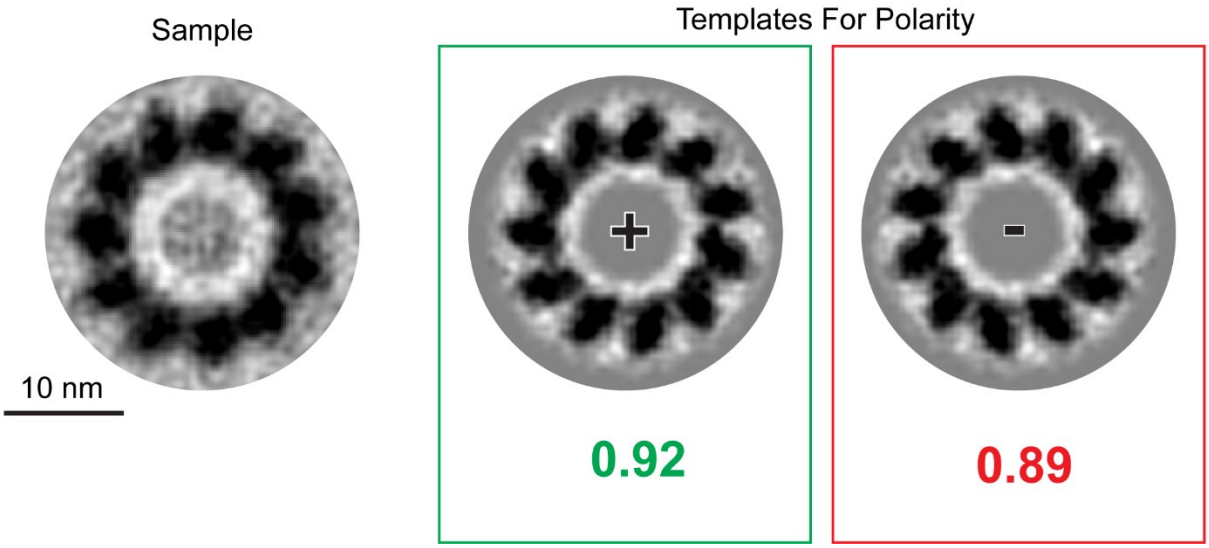

Figure 4.6.4: Application of per-microtubule averages to determine microtubule polarity. Each microtubule average is rotated and cross correlated with images corresponding to a 2D projection of the longest single microtubule in the data, and the same projection flipped. These act as templates for positive and negative microtubule polarity. The result with the highest cross correlation score is recorded as the microtubule polarity.

Table 4.6.2, microtubule polarities

Cell Stage	Number of Positively Oriented Microtubules	Percentage of Positively Oriented Microtubules
Prophase	50/72	69%
Metaphase	145/169	86%
	38/49	76%
	114/162	70%
Anaphase	100/132	76%
	183/196	93%
Telophase	37/50	74%
All	667	80%

I found that 80% of all microtubules were oriented with their plus ends pointing away from the centroid (Table 4.6.2). These microtubules with a positive orientation were

longer compared to those with a negative orientation, with positively oriented microtubules having a mean length of 217.8 ± 110.9 nm, compared to the negatively oriented microtubules having a mean length of 124.5 ± 10.5 nm. This was found to be statistically significant (p-value of $2.62*10^{-23}$; calculated using a one-tailed two-sample t-test). Moreover, the negatively oriented microtubules, being considerably

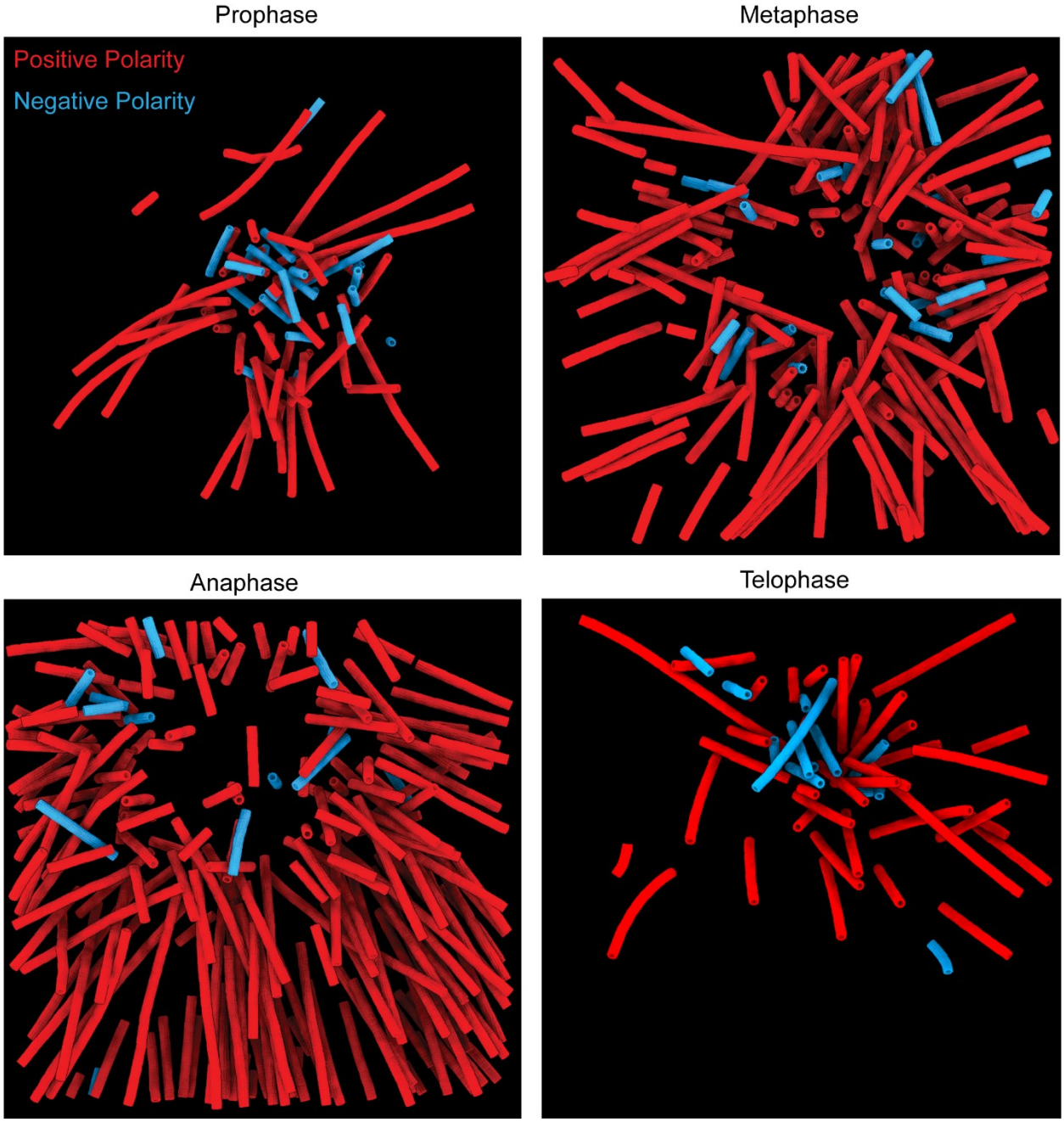

Figure 4.6.5: Microtubule polarities shown in the data. Microtubule segmentations, shown previously, are colored according to their polarity with positive in red and negative in blue. All 4 major mitotic states are shown.

shorter, were predominantly located within the microtubule-rich core of the centrosome's ribosome excluded zone, and did not extend beyond it toward the mitotic chromosomes (Figure 4.6.5). These observations suggest that the assembly state and orientation of spindle microtubules are tightly regulated within the PCM. This specific property of the PCM is attributed to the presence of gamma-TuRCs, as attributed to previous sources (Michelle Moritz *et al.*, 1995; Zheng *et al.*, 1995; Moritz *et al.*, 2000; O'Toole *et al.*, 2012).

In summary, the findings reveal that not only is the number of protofilaments highly conserved in the microtubules, but their orientations are also controlled at the PCM. This further highlights the intricate and precise mechanisms underlying microtubule organization within the mitotic spindle.

4.7 *C. elegans* gamma tubulin ring complexes

While tracing out microtubules within the ribosome excluded zones of the centrosome, I observed that there were small stretches of structures resembling microtubules, that did not form discrete tubes and were very short (under 40 nm) in length. These were even more commonplace within the microtubule excluded region. It was also noted these structures contained a cone-shaped capping structure, something I suspected to be a gamma-TuRC (Figure 4.7.1). As gamma-TuRCs had never been characterized before either in *C. elegans* or *in-situ*, I reasoned this represented an excellent opportunity to boost understanding of the active form of this complex under native conditions. Doing so may also increase our understanding of how centriolar microtubules are 13 protofilaments, but spindle microtubules are 11.

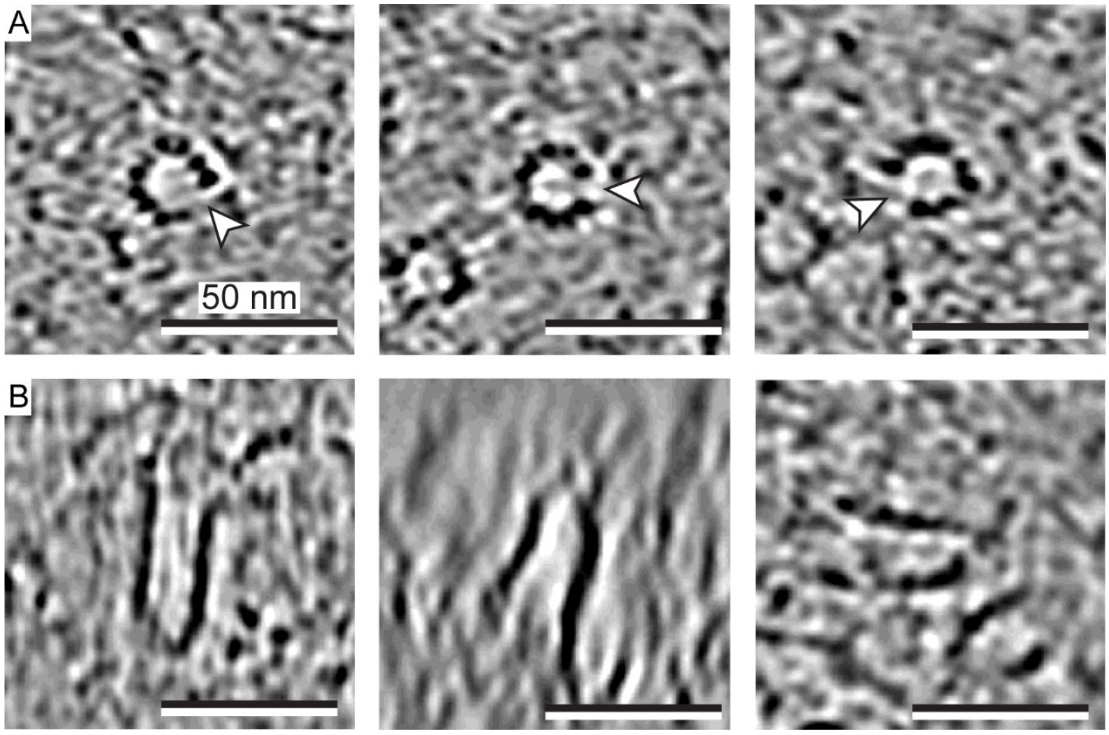

Figure 4.7.1: Identification of short or incomplete microtubule segments within the tomogram. Top: microtubules with a small discontinuity in them (indicated by white arrows). Bottom: short (under 50 nm) microtubule sections ending with a capping structure.

Template matching for gamma-TuRC complexes was attempted, but was ultimately unsuccessful, due to a large number of false positives that proved prohibitively difficult to manually distinguish from noise. A large portion of these false positives were believed to actually consist of PCM matrix material (see section 4.8). Indeed, template matching historically has proven challenging for all but a handful of cellular complexes, such as ribosomes. As a result, I resorted to manually picking 281 particles in dynamo (Castaño-Díez *et al.*, 2012): representing all the complexes observed in the analyzed data. Despite this low number of particles, reaching an interpretable 3D structure was attempted using RELION (Kimanius *et al.*, 2021), resulting in an average with a resolution of 38 Å (Figure 4.7.2). Classifying this average into smaller subpopulations however was unsuccessful, despite a number of masks and conditions tested. This may be due to the low particle numbers, or it may arise from a bona-fide lack of structural variation.

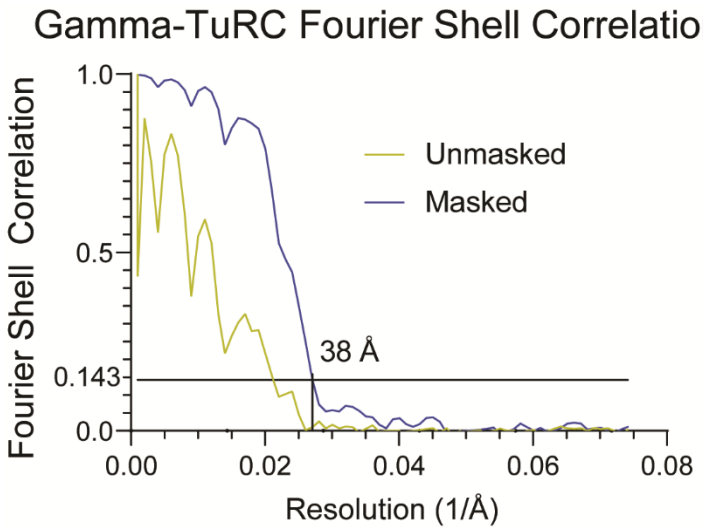

Figure 4.7.2 FSC curves for both the masked and unmasked Gamma-TuRC subtomogram averages. FSC cutoff taken at 0.143 giving a resolution of 38 Å.

This average revealed a 30 nm long segment of microtubule, which was connected to a circular cap region. Notably, the orientation of protofilaments skew within the short microtubule region indicated that the minus end was located at the circular cap. Given the role of gamma-TuRC in templating and stabilizing microtubule minus ends (Michelle Moritz *et al.*, 1995; Zheng *et al.*, 1995; Moritz *et al.*, 2000), this lends credence to the idea that the average does in fact depict an active gamma-TuRC complex templating a short microtubule segment. This short microtubule segment had 11 protofilaments, as seen in almost all of the microtubules of the mitotic spindle (Figure 4.7.3). The microtubules of the mitotic spindle are capped themselves by gamma-TuRC (O'Toole *et al.*, 2012), but no capping structures can be seen in the centrioles captured in the same data, and *in vitro C. elegans* microtubules nucleate into a range of protofilament numbers (Chaaban *et al.*, 2018). Taken together with my observations, this may indicate that it is these gamma-TuRCs that are responsible for templating the 11 protofilaments of *C. elegans* microtubules.

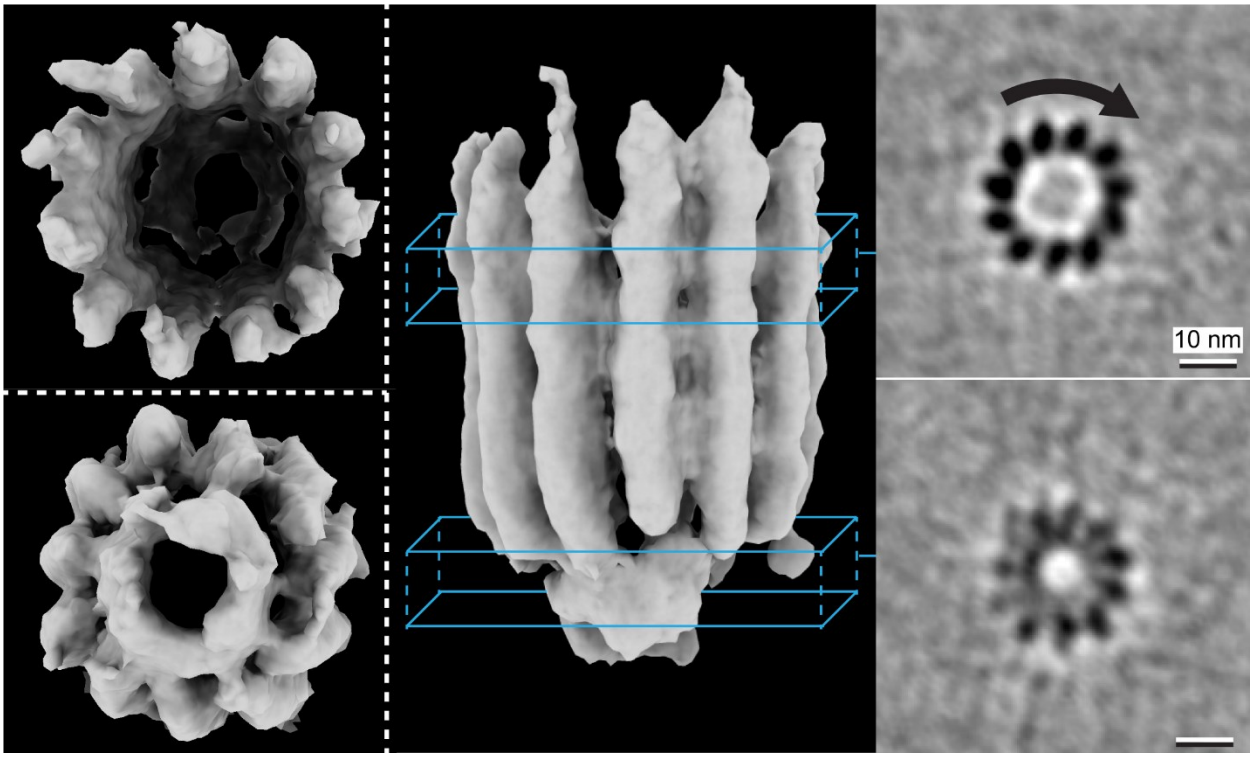

Figure 4.7.3: Average of gamma-TuRCs, with a small capping region at the bottom and a wider microtubule bound section at the top. Two images on the left show the top and bottom images of the average. Highlighted area on the center image indicates the regions shown on the left. The microtubule skew in the projection of the microtubule bound region of the gamma-TuRC, indicating positive polarity. A projection of the lower capped region of the average, shows a clear ring structure.

While no high-resolution structures of gamma-TuRC complexes specifically for *C. elegans* are available, structures for the human complex have been reported (Wieczorek *et al.*, 2020). Unfortunately, there is a difference in microtubule protofilament number between humans (typically 13) and *C. elegans* (11), making it challenging to fit the entire human gamma-TuRC structure to my average. Regardless, the gamma-TuRC ring, consisting of the N-terminal domains of the GCP subunits, aligned well with my average (Figure 4.7.4). This alignment, combined with the observed microtubule polarity, suggests that these structures are likely gamma-TuRCs bound to short microtubule segments. *C. elegans* has just two GCP genes, aptly named *gpc-1* and *gpc-2* (Jansen, Weinkove and Plasterk, 2002). These proteins have never been imaged before, nor has the presence of the gamma-TuRC ring been shown

in this species. As such, this average contains the first evidence for a GPC ring within gamma-TuRC in *C. elegans*.

Although my map aligns with the atomic model for human gamma-TuRC, there is a noticeable difference seen between the human complex and the average from this dataset. In the human version, a large plug density is seen occupying the end region of the cone in electron density maps only, although this is not present in the atomic models shown in figures due to uncertainty over its identity and its relatively low resolution. In contrast, in this region a prominent hole is seen in this dataset, making my complex more of a conical frustum than a simple cone. The authors of the human study were unable to assign this plug density to any specific protein, and as such it was not possible do a bioinformatics search on any homologues the plug may be in *C. elegans*. Consequently, it is not clear if the absence of the plug in this dataset's average is due to a species dependent difference, or if it arises from gamma-TuRC being in an active, microtubule binding conformation.

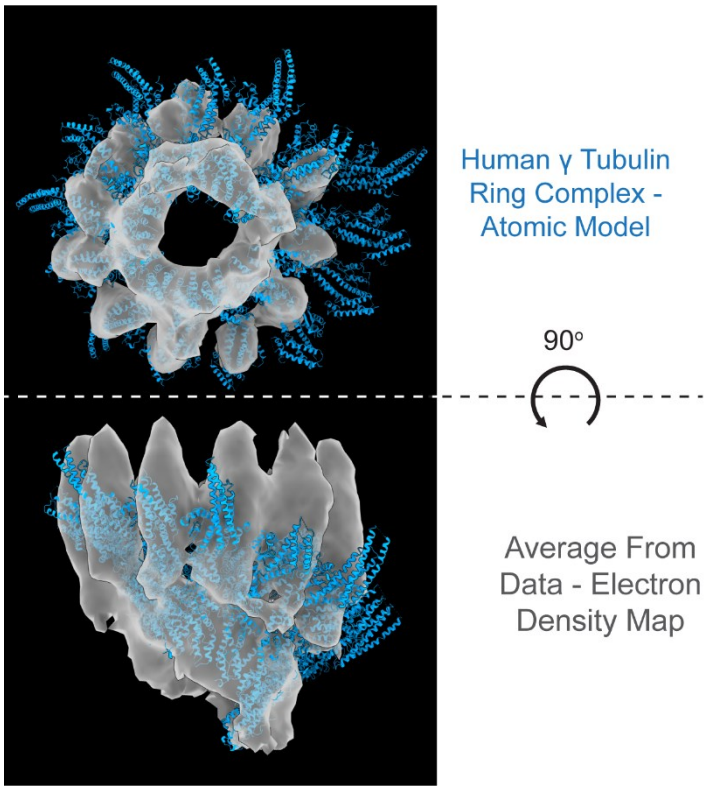

Figure 4.7.4: overlay of a human atomic model for gamma-TuRC (blue) with the average from this study (grey).

When I projected these complexes back into the data, I noticed that they did not exhibit regular organization. Instead, they were positioned randomly throughout the ribosome-excluded region, with the majority lying within the ribosome excluded core. Furthermore, the gamma-TuRCs within these complexes displayed random orientations without any preference in their bearing, such as pointing their short microtubule segments away from the centroid (Figure 4.7.5). Taken together, this data does not support previous studies suggesting that gamma-tubulin acts as a barrier to organize a specific surface of the centrosome (O'Toole *et al.*, 2012). While it is plausible that I may not have detected the complete set of gamma-TuRCs in the PCM, it is beyond unlikely that so many were missed that an impenetrable barrier could have formed out of the absent particles. This makes the data here much more consistent with older studies which show gamma-TuRCs throughout the PCM (Michelle Moritz *et al.*, 1995). In conclusion, these findings add valuable insights to our understanding of the structural organization and dynamics of gamma-TuRCs, their function, and their association with short microtubule segments within the centrosome.

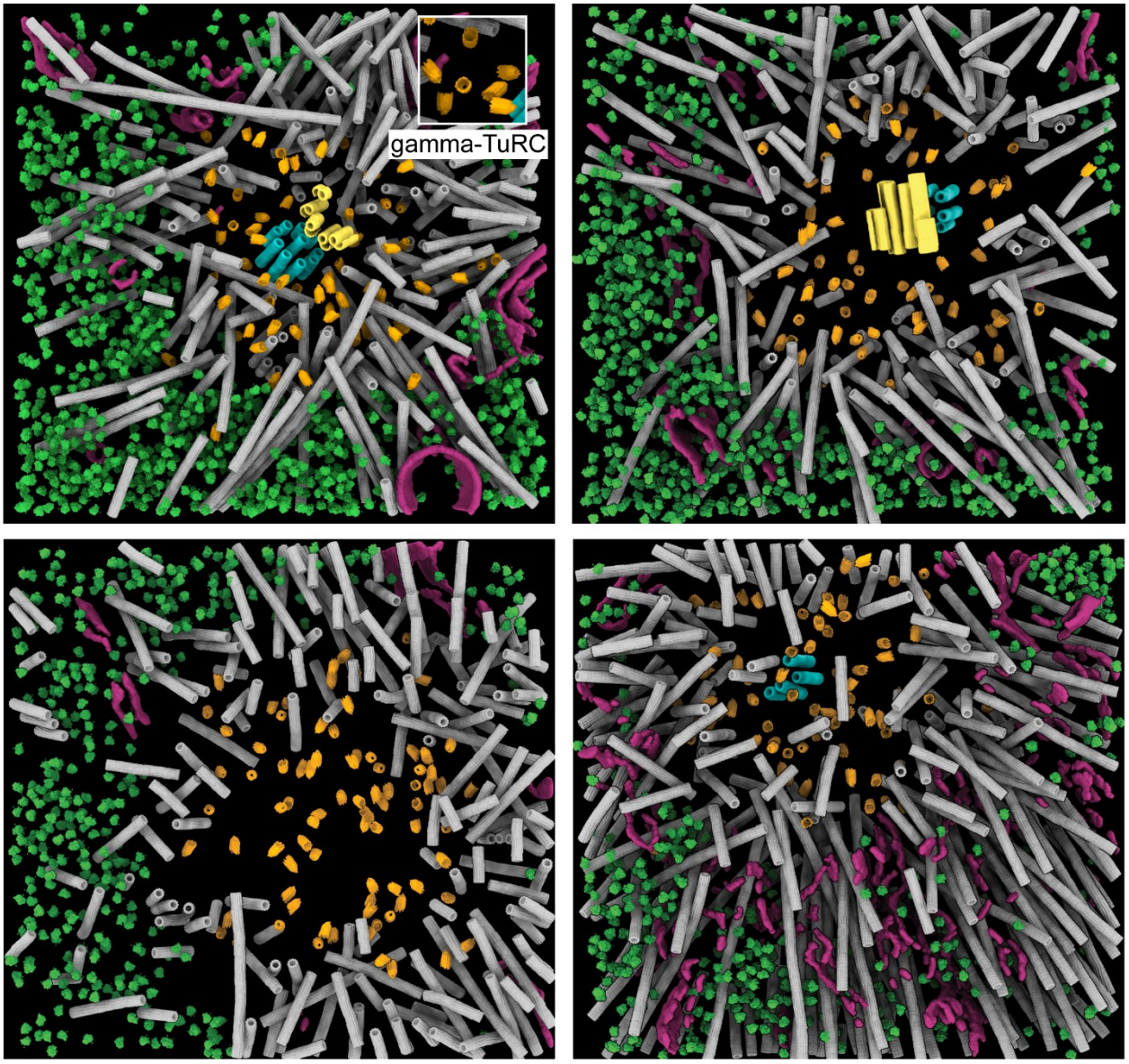

Figure 4.7.5: Result of the gamma-TuRC average placed back into the data, from all four tomograms for which particles were picked.

4.8 Identification of the centrosomal matrix

Although the microtubules, centrioles, and gamma-TuRCs occupy much of the centrosome, much of the microtubule excluded zone remained unaccounted for. However even upon first examination, it became clear that there were structures within the centrosome that had not been segmented, either in this study or in literature to date. Throughout the centrosome, a series of fine, filamentous structures

were seen (Figure 4.8.1). These were most clear in the microtubule excluded zone, as the microtubules in the other zones obscure these filaments. I estimated that these segments were 1.5 to 4.5 nm in thickness.

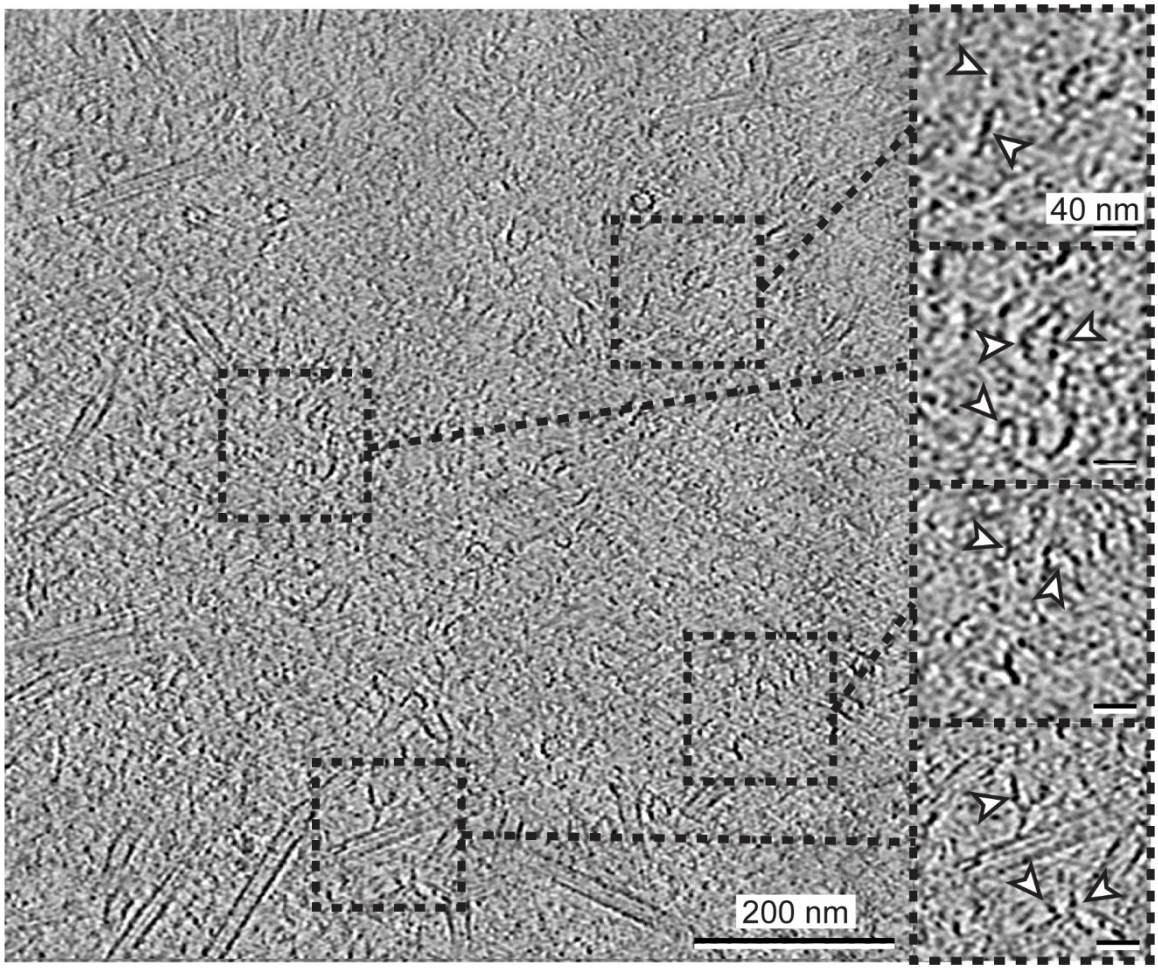

Figure 4.8.1: Identification a centrosomal matrix. Tomographic slice showing unknown filaments. Insets show magnification of indicated bound regions.

Tracing out these filaments in the raw tomograms would have proven challenging, due to the faint nature of the filaments in the inherently noisy tomogram. Simple Gaussian filtering using a wider kernel size, which was employed before for semi-automated microtubule tracing, was not appropriate in this case as this would blur out the filaments too much to be traced. Subsequently, before analyzing these unknown filaments in detail, it was necessary to denoise tomograms. To this end, cryoCARE, a deep-learning based denoising tool was used (Buchholz *et al.*, 2018). For cryoCARE to work, it needs two maps generated from the same data, where signal

will be retained but noise remains random. This can be easily done in this case, as the processing pipelines used within our lab, using Warp (Tegunov and Cramer, 2019), allows one to reconstruct tomograms from odd and even tilts respectively, which can then be used to train cryoCARE models for denoising. A lamella mask was also applied to the data for training, as this improved the result of the denoising models. All tomograms containing centrosomes were denoised in this manner, but after denoising were also lightly (1 pixel kernel) Gaussian filtered to better blur out persistent noisy elements. As the filaments were now clearer in the data (Figure 4.8.2), it became practical to move forward with segmentation and interpretation of these filaments.

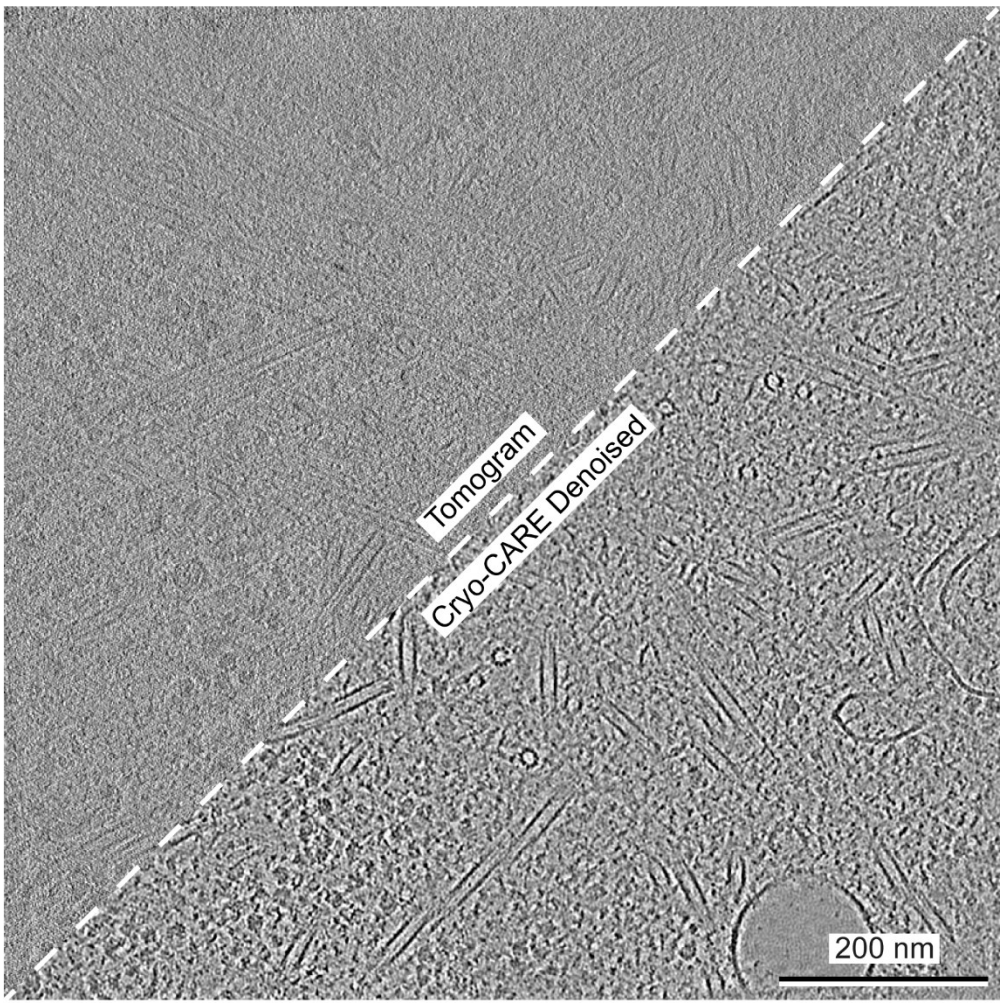

Figure 4.8.2: The effect of denoising on tomograms. An unprocessed weighted back projection is shown on the top left, with the same tomogram after processing in cryo-CARE on the bottom right.

Reliably segmenting these thin filaments still proved challenging. Several approaches were considered, including filament tracing in Amira, training of a DeePiCt model, and simple manual tracing. Given the expansive nature and large interconnectivity of the matrix, it was decided that none of these approaches were practical. Instead, I turned to use of Ilastik (Berg *et al.*, 2019). Although usually used for segmentation of light microscopy and room temperature EM images, it was employed here directly on the denoised cryo-tomograms. As these filaments were much finer and lower contrast than known components such as microtubules, any sort of classifier is likely to pick up on these as opposed to the desired meshwork. As such, it was necessary to first mask out the known components from the centrosomal volume. The segmentations corresponding to microtubules, ribosomes, membranes, and centrioles were all subtracted from the tomographic volume. Missing wedge effects and imperfect tracing means that some density in the volume was not immediately masked out by the segmentation. This was particularly noticeable for the centrioles, where the extra features such as doublets added much extra density beyond the edge of the segmentation. As such, the masked volume had to be expanded by 24 voxels (32 nm) for centrioles, 11 voxels (15 nm) for microtubules, 8 voxels (11 nm) for ribosomes, and 4 voxels (5 nm) for membranes. In the hope of seeing the connection of the matrix to the gamma-TuRCs, these complexes were not masked out, but a clear connection modality was not clear. Additionally, removing the volume of noise in the tomogram above and below the lamella was done through application of a strict lamella mask

Two modalities of Ilastik were used. On the whole 3D tomogram, the pixel classification function was run. On the central 50 xy slices (67 nm), which occupies the majority of the PCM material, Autocontext was trained, before being run on the entire volume. Autocontext is more accurate than the pixel classifier in individual slices, but only works in two dimensions, making it less effective at tracing densities through the xz and yz planes than the 3D pixel classifier. Subsequently, the

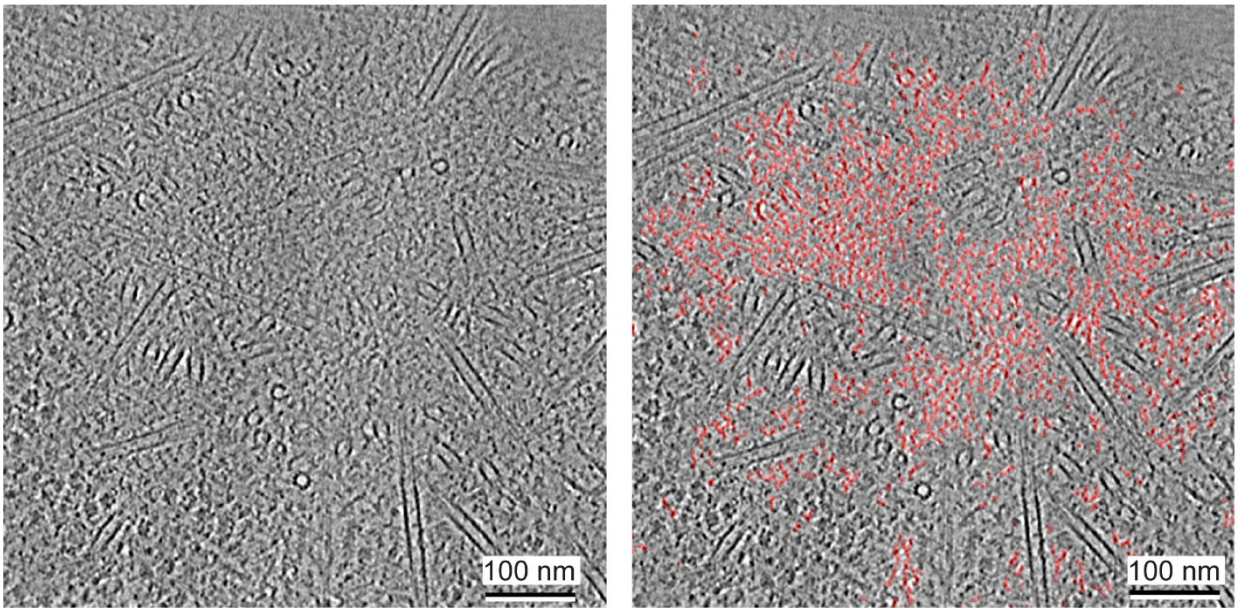

Figure 4.8.3: Centrosomal matrix tracing. A tomographic slice is shown on the left, with an overlay of the segmentation on the same tomographic slice on the right, highlighting the traced filaments within the data.

segmentations from these two functions were combined, creating a more comprehensive and complete segmentation of the PCM: if a small section was missed by one function, it would be picked up by the other (Figure 4.8.3). I performed this analysis on four tomograms, two captured during metaphase and two during anaphase, with the intention of identifying any potential differences between the two mitotic stages. However, no significant disparities were observed in the segmentations on the superficial level. The tomograms revealed that the majority of the matrix volume consisted of a single interconnected meshwork spanning the entire region excluded by ribosomes (Figure 4.8.4). Additionally, I identified segments of matrix that were not directly connected to the main body but were present in the vicinity within the tomogram, where ribosomes were also located. It is assumed that this meshwork matrix consists of the bulk of the PCM material.

In summary, the analysis uncovered filamentous structures within the centrosome that differ from known assemblies. These findings provide valuable insights into the structural organization of the PCM, furthering our understanding of its role within the centrosome.

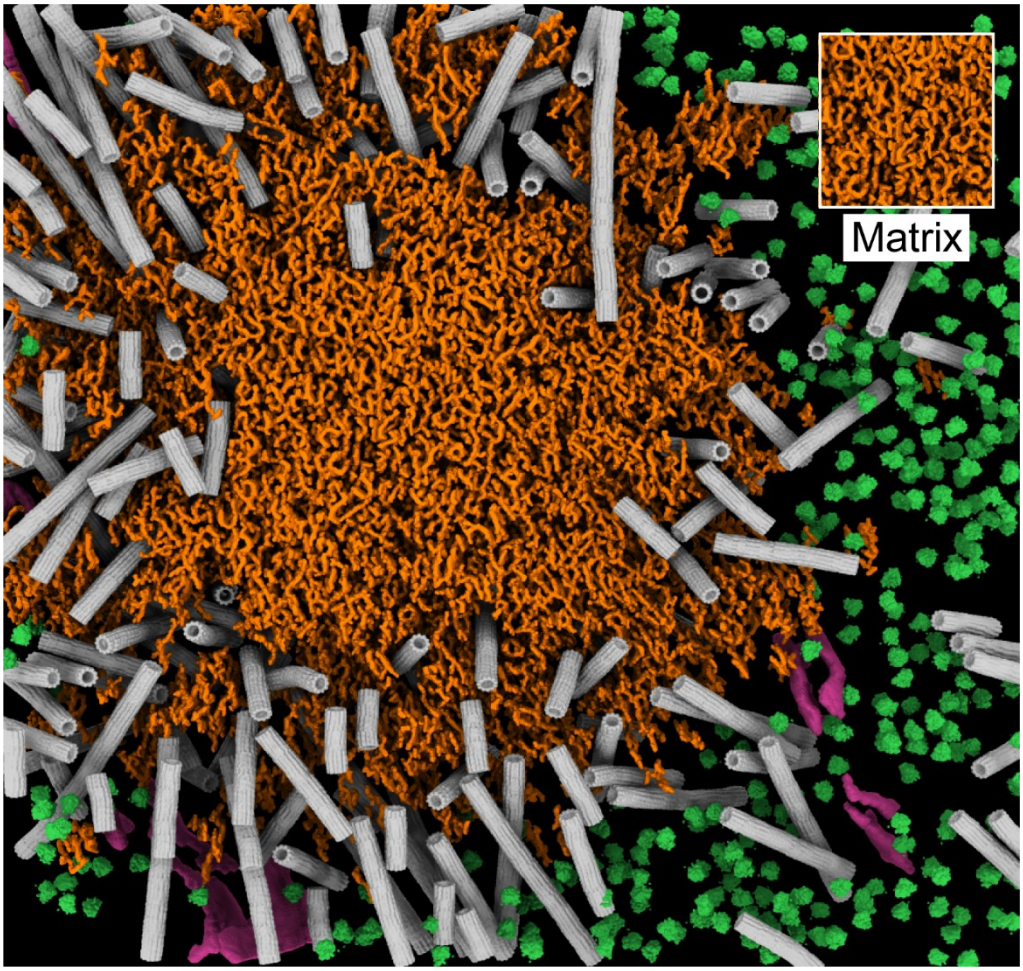

Figure 4.8.4: Result of segmentation of all unknown filaments within the tomogram, showing an interconnected mesh.

4.9 Properties of the centrosomal matrix

The PCM in *C. elegans* primarily relies on the self-assembly of the coiled-coil protein SPD-5 (Hamill *et al.*, 2002; Woodruff *et al.*, 2015). However, the nature of long-range interactions and meso-scale assembly within the functional PCM remains a subject of debate, as prior to this work it had never been directly imaged. Different models propose contrasting frameworks, including a solid, crystalline matrix (Schnackenberg *et al.*, 1998; Schnackenberg and Palazzo, 1999), a completely liquid model (Zwicker *et al.*, 2014), or a gel-like mesh (Woodruff *et al.*, 2017; Mittasch *et al.*, 2020), each with its own supporting arguments. By using the tomographic data available, and

crucially the segmentation of the PCM as shown in the previous section, it became possible to probe the properties of the matrix and relate this to the function and characteristics of the centrosome. To describe the properties of the matrix, I examined three quantitative features: the size of the pores, the number of branches at branch points, and the lengths of segments between branch points.

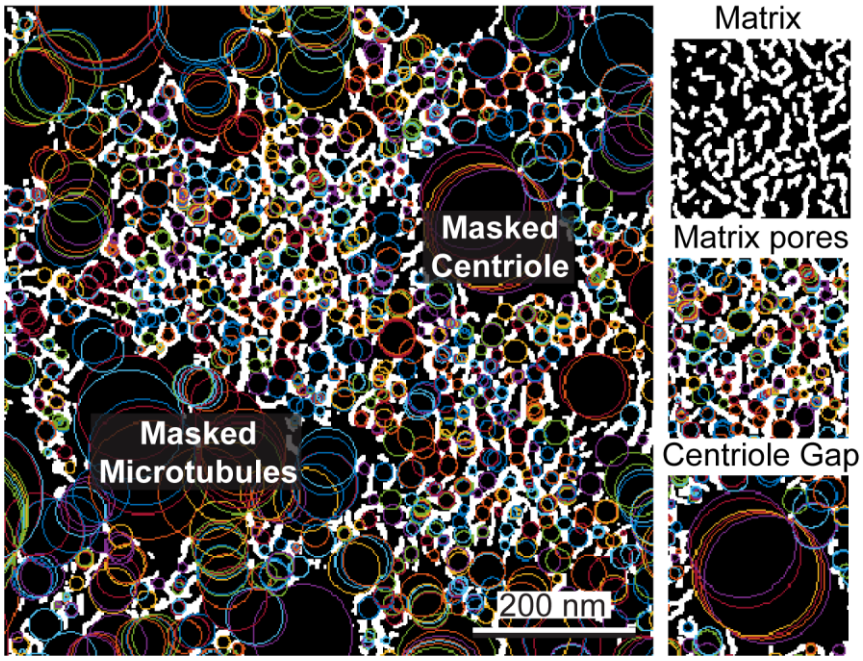

Figure 4.9.1: Matrix pore analysis. A 2D slice of matrix is shown on the left, with pores throughout. A gap corresponding to a masked centriole and a region of masked microtubules are shown. On the right are cropped regions showing the matrix without pores, with pores, and a centriole gap.

Matrix pores were determined by taking a distance transform of the entire segmented matrix, and then by finding local maxima, all within MATLAB (Figure 4.9.1). From this, it was possible to display pore sizes in a histogram, and to fit a Gaussian peak to this data (Figure 4.9.2). This histogram had two peaks, a sharp peak between 8 and 9 nm, and a second shallower peak centered at 23.2 nm. The 23.2 nm peak corresponds to the width of the microtubule mask applied in the matrix segmentation process. This histogram also had a very long tail of wider ‘pores’ which in fact corresponded to the space outside of the centrosomal matrix, which can also be ignored without affecting the biological interpretation of the data (shown on the histogram as the >40 nm bin).

This first peak however tracks to the pore size within the filamentous meshwork. It was also possible that the pores changed their width when moving from the core of the centrosome into the periphery. To investigate this, the size of pores at certain distances from the centrosome's microtubule centroid were calculated. When plotted out, both the 'pores' that exist outside the matrix and the microtubule masked pores become clearer at greater distances from the centroid, as would be expected due to the previously defined microtubule excluded zone. The smaller pores, which actually reflect the meshwork, do not change with distance from the centroid (Figure 4.9.3), meaning there is no change in pore size between the previously defined centrosomal regions.

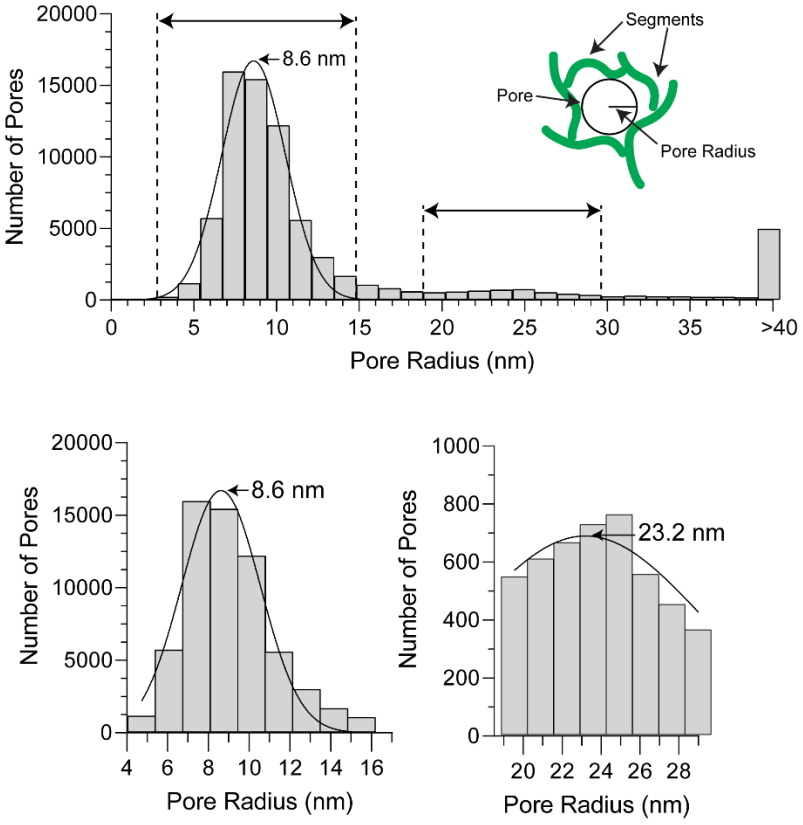

Figure 4.9.2: Histogram of pore sizes found within the matrix. Above is an overall histogram, with a Gaussian fit applied shown as a solid line. The peak of said fit (8.6 nm) is labelled. The areas between dashed lines, as indicated by a double-headed arrow, correspond to the two peaks shown beneath. The Gaussian fits for these also correspond the data shown in each graph. The top-right schematic shows how pore radii were determined.

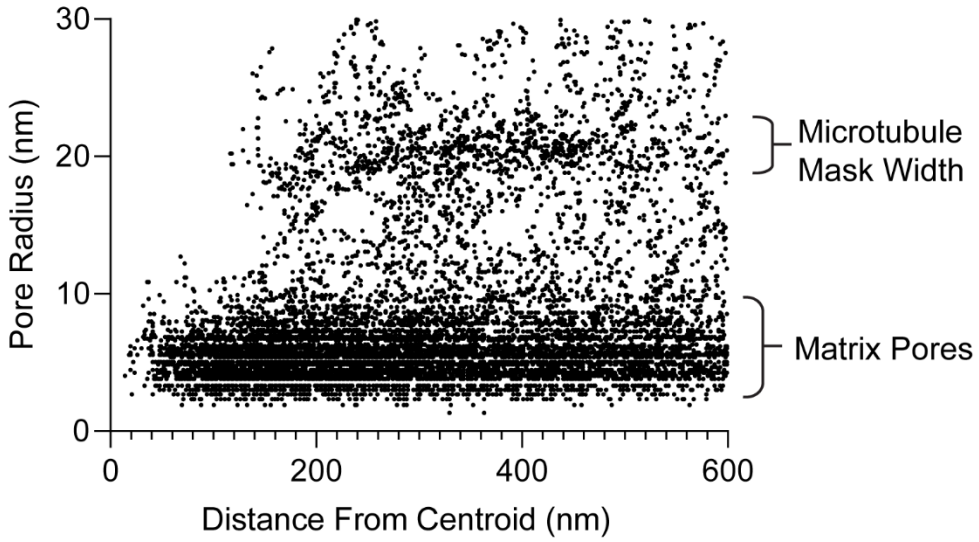

Figure 4.9.3: Pore size at distance from the centroid. Bona-fide pores corresponding to those found in the centrosomal matrix and 'pores' that arise from microtubule masking are both highlighted.

A Gaussian fit of the data histogram revealed a peak value of 8.6 nm, with a corresponding standard deviation of 1.9 nm. These pores are spacious enough to accommodate PCM client proteins, such as PLK-1 (with dimensions of 7 by 6 nm, predicted using AlphaFold2 (Jumper *et al.*, 2021)), ZYG-9 (13 by 10 nm, predicted using AlphaFold2), and tubulin dimers (5 by 8 nm, (Mandelkow *et al.*, 1995)) (Figure 4.9.4). However, due to the extended and disordered nature of certain centrosomal proteins, like TPXL-1, it is challenging to predict their confirmation within the centrosome and thus their precise interaction with this meshwork. Assembled gamma-TuRCs (30 by 20 nm in humans, (Wieczorek *et al.*, 2020)) are expected to be excluded from the matrix. Interestingly, observations indicate that gamma-TuRCs exit the mature centrosome following PLK-1 inhibition (Haren, Stearns and Lüders, 2009; Mittasch *et al.*, 2020a; Ohta *et al.*, 2021). Additionally, this data clearly shows that microtubules are capable of passing easily through the matrix, as the matrix spreads out past the microtubule excluded zone. Together this suggests that there is another mechanism to facilitate the accommodation of larger, microtubule-based complexes within the centrosome.

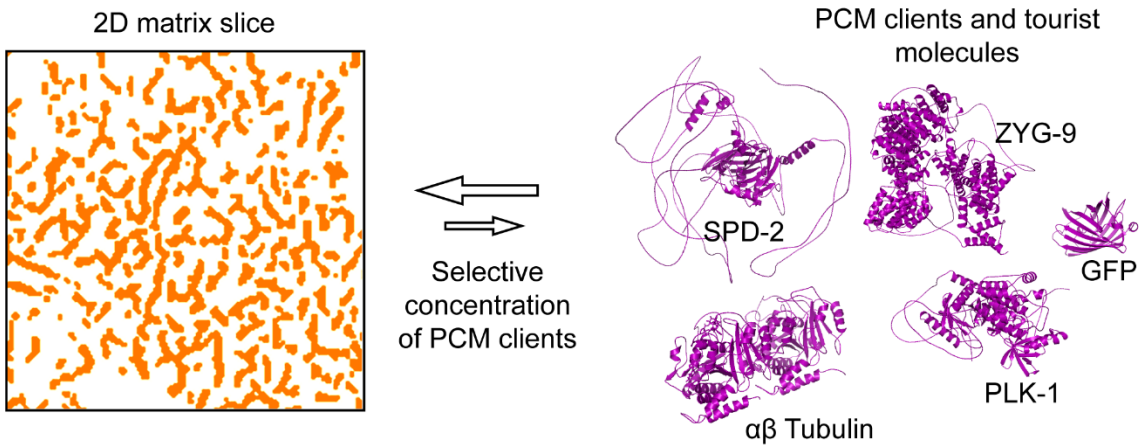

Figure 4.9.4: How matrix pores relate to PCM molecules. The pores identified are large enough to accommodate SPD-2, ZYG-9, PLK-1, αβ tubulin, and the tourist GFP, and PCM clients may then be selectively concentrated.

In order to investigate the number of branches per branch point, and the lengths of each segment, it was first necessary to skeletonize the matrix. This makes distance calculations and branch determination a much simpler affair without affecting the accuracy of output (Figure 4.9.5). By analyzing the number of segments connected at each branch point and the lengths of these segments, I gained insights into the interaction modality of molecules within the matrix. While the majority of branch points connected to three segments, which is the minimum possible as per the definition of a branch, there was some variation as 25% of branches had four or more connecting segments (Figure 4.9.6). This finding is not consistent with a lattice model of the centrosome, as if there were a crystalline skeleton making up the core of the PCM, a very regular number of branches per branch point would be expected. As such, this data indicates that the matrix is more irregularly arranged, information that is more consistent with a gel-based model of centrosomal architecture than a lattice based one.

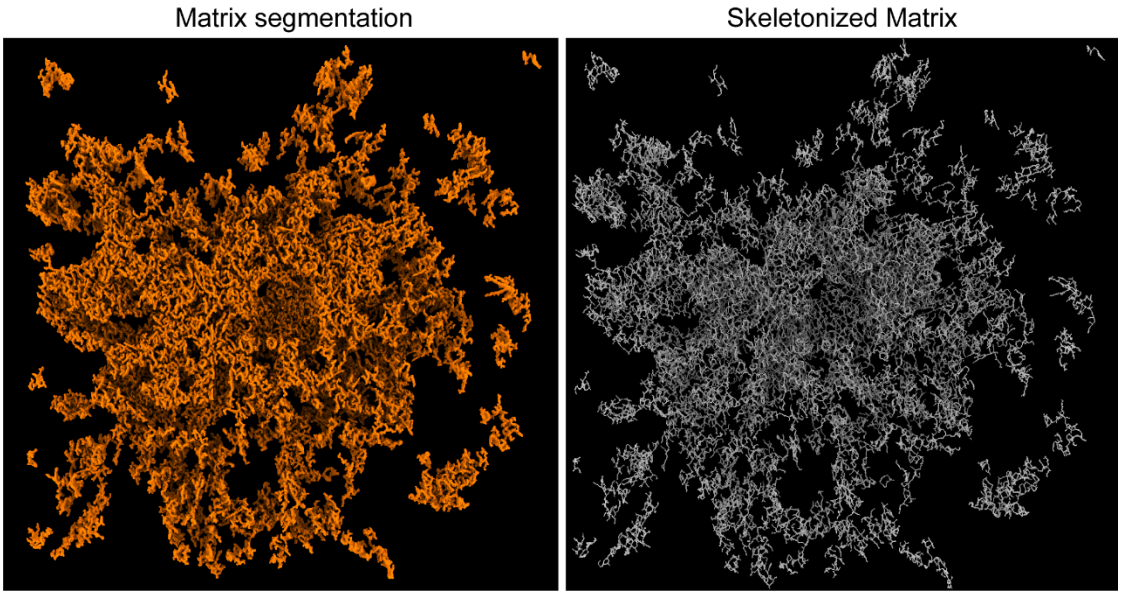

Figure 4.9.5: Example of matrix skeletonization.

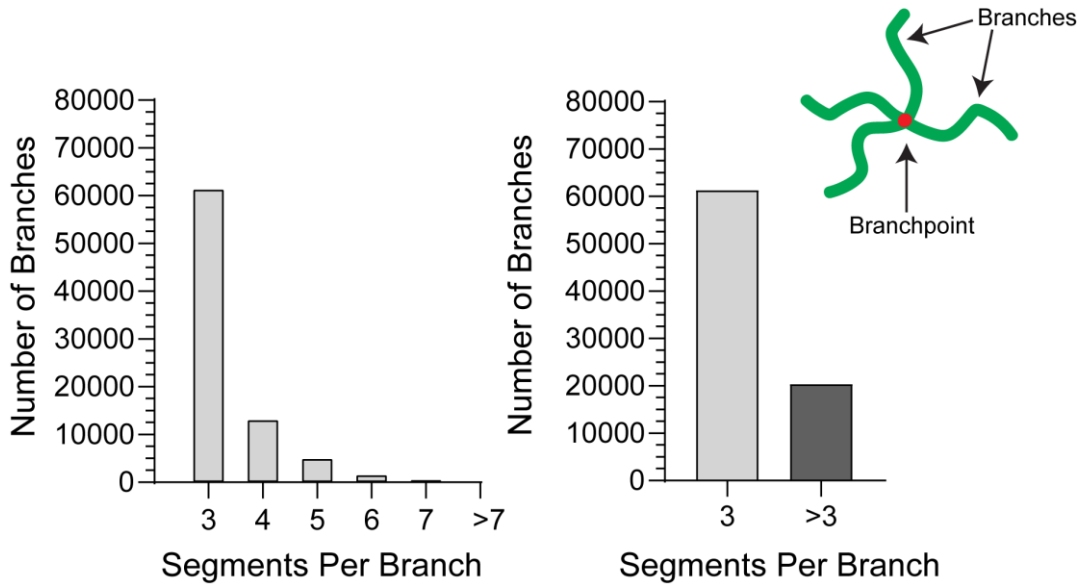

Figure 4.9.6: Number of branches per branch-point, showing both the number of connections, and the number of branch points that have three or more than three branches. A schematic identifying branches and branchpoints is also shown.

Analysis of segment lengths reinforces this viewpoint. Segments were identified, and their lengths measured using Skan (Nunez-Iglesias *et al.*, 2018). Initial observations showed many connections were under $\sqrt{3}$ (1.73) voxels. Indeed, this was the largest individual bin. This is the distance between two adjacent, but diagonal voxels, implying that segment lengths were being misread as adjacent voxels. The fear here

was that longer filaments were being misread as multiple shorter filaments punctuated by these erroneous 1 voxel long segments. It was therefore necessary to investigate the location of these small sections. Thankfully, it was quickly observed that these short 'knub' segments were only located at the end of longer segments, and therefore were not causing a misreading of segment lengths by breaking a longer segment in two. It would appear that these arise from small protrusions that appear near branch points as a part of the skeletonization step (Figure 4.9.7). This means any connection under 2 voxels, being shorter than the thickness of the filaments segmented and therefore make no biological sense, can be removed from the data without consequence.

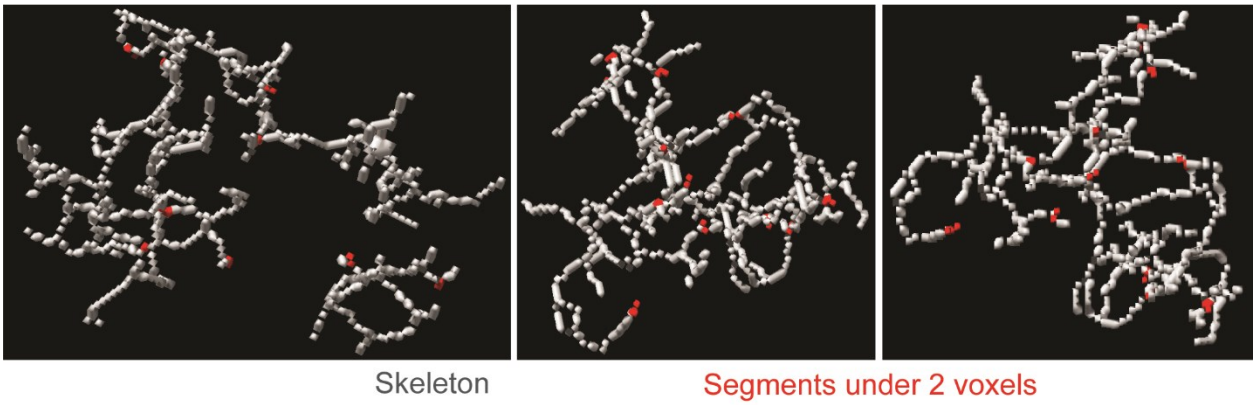

Figure 4.9.7: Identification of extremely short skeleton regions. The overall skeleton is in grey, whereas segments shorter than 2 voxels, found only at the ends of longer segments, are shown in red.

The motivation to measuring segment lengths was the expectation that it would be possible to assign molecular identity to the segments by matching the values to the lengths seen in AlphaFold2 predictions for candidates such as SPD-5 and SPD-2. However, no sharp discrete peaks were available in this data. Instead, a very broad spectrum of segment lengths was present. Given the shape of this plot, normal Gaussian fitting was inappropriate for this data. As such Lorentz fitting, which better accounts for wider data spreads, was used in its stead. This fitting had a peak value of 7.8 nm, but a great half width of 6.0 nm, preventing any definitive identification of these filaments (Figure 4.9.8). However, the molecular identity of the centrosome in

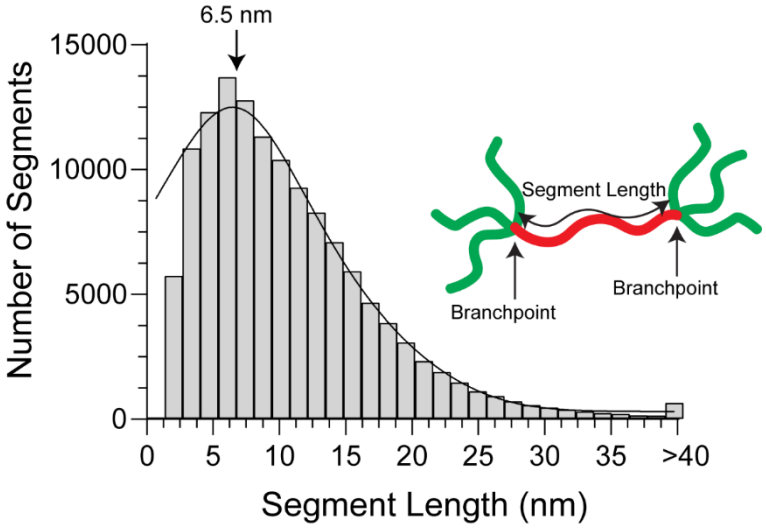

Figure 4.9.8: Histogram of segment lengths, with the sum of two Lorentz fits applied, shown as a solid line. The first peak of the fit is indicated. The schematic shows how segment lengths are defined.

C. elegans is not a complete unknown, indeed it is among the best classified and understood centrosomes out of any model organism. Given the importance of SPD-5 in this structure, I compared the information on lengths available to known structural information on this protein. The flexibility of SPD-5 makes it difficult to resolve by traditional structural biology approaches, which requires structural homogeneity for either crystallization for x-ray diffraction or averaging in single-particle cryo-EM. However, AlphaFold2 predictions of protein structure became both available and widespread over the course of this work. Both the length and width of a SPD-5 monomer (4.71 nm by 34.92 nm, Figure 4.9.9A) were inappropriate for the fits available. However, when the dimer was examined, a more promising interaction was seen. A key interaction site responsible for the multimerization of SPD-5, as identified by cross-linking mass spectrometry, is known to exist between residues 610 and 640 (Rios *et al.*, 2023). In the AlphaFold2 dimer of SPD-5, I saw a pair of interacting coiled-coils in this section, one for each monomer. The interacting region was 89.8 Å (8.98 nm) long and 19.6 Å (1.96 nm) wide. The width of this interacting region fits within the observed 1.5-4.5 nm thickness of the matrix filaments (Figure 4.9.9B). Although the 8.98 nm length of this interacting region is longer than the 7.8 nm peak segment length observed in the data, the high variability of the fit means this may be

described, albeit very imperfectly, by the distance distribution. Where the rest of the SPD-5 protein would lie remains obscured, likely due to the fact that the single flexible helices that make up much of SPD-5 dimers are too fine to be seen in these micrographs.

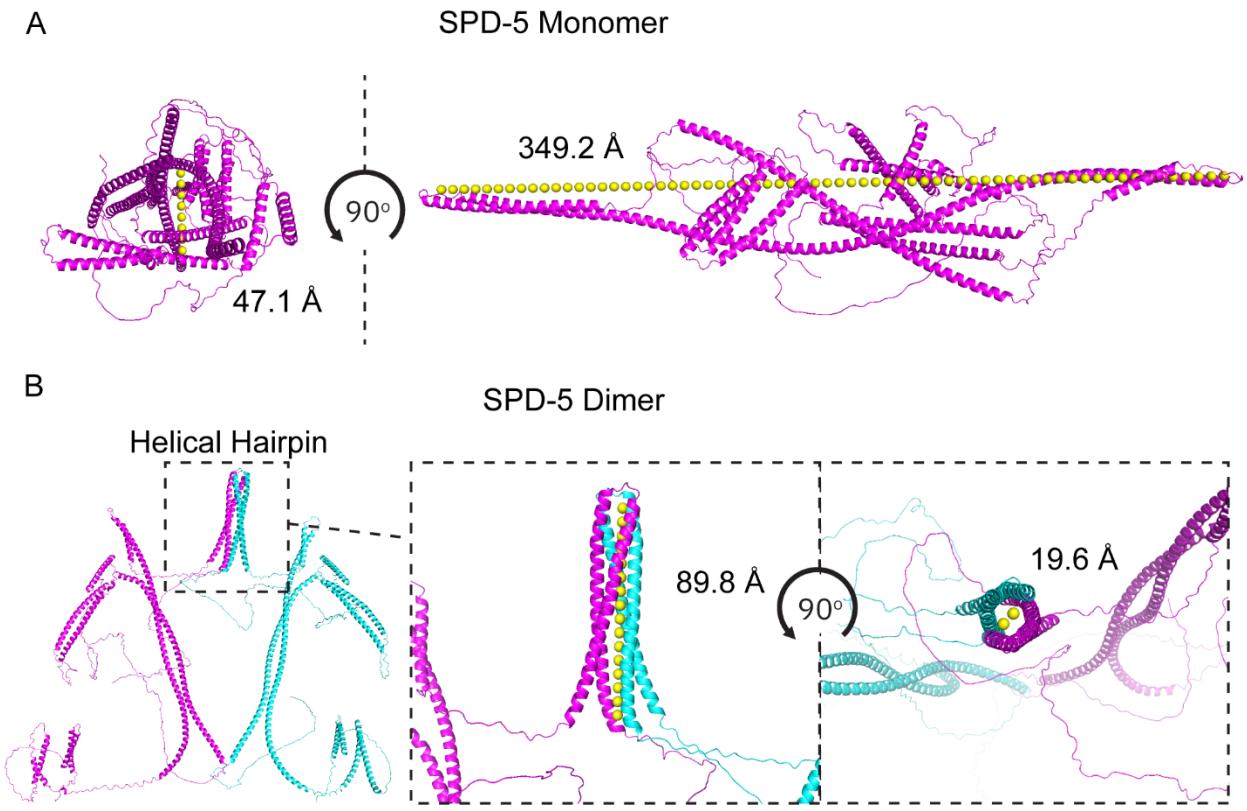

Figure 4.9.9: Alphafold2 multimer prediction of a SPD-5 homodimer, with the interacting coiled coils highlighted by a dashed box and magnified from two perspectives. The length (89.8 Å) and width (19.6 Å) of said coiled coil is shown in Ångstroms.

This observed variability in segment length and the number of branches challenges the notion of a crystalline lattice serving as an underlying skeleton of the centrosome. Conversely, the presence of discrete structures within the PCM fails to support the idea of an entirely liquid-like model. Consequently, it seems that the centrosome consists of a highly networked gel, characterized by an irregular filament matrix.

Smaller components, such as PCM client proteins, can traverse through the pores in this meshwork, while larger complexes, including gamma-TuRCs and microtubules themselves, navigate or are shuttled through this meshwork via an unknown mechanism.

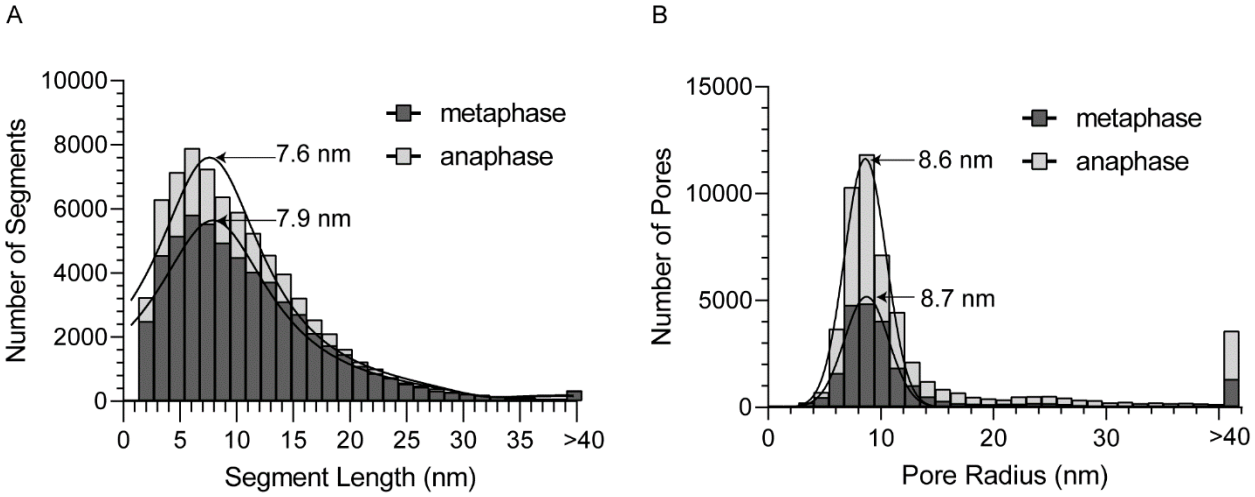

Figure 4.9.10: Comparison of PCM architecture properties between metaphase and anaphase. A: Comparison of segment lengths between the two, with a sum of two Lorentz fits applied to both. The respective peaks are indicated with arrows. B: Comparison between pore sizes between the two, with Gaussian fits applied to both and peaks again labelled.

As the structural integrity of the centrosome is known to drop at the metaphase-anaphase transition, with the centrosome becoming more labile as a result, it was thought that the metaphase matrix would display different features to the anaphase matrix. However, when the data was pooled by mitotic state as opposed to a single group, no significant difference can be seen. Metaphase centrosomes had a peak segment length of 7.9 nm and pore radius of 8.7 nm, compared to 7.6 nm segments and 8.6 nm pores in anaphase (Figure 4.9.10). The increased number of pores and segments in anaphase is simply explained by the fact that one of the anaphase lamellae is considerably thicker, and as such more PCM has been retained compared to the metaphase lamellae. How can the phenomenon of a change in physical centrosomal properties upon the metaphase-anaphase transition (Mittasch *et al.*,

2020a) be explained if no according change in architectural properties is observed? It is likely that rather than the overall architecture of centrosomes being drastically modified at this point, the assembly and strength of interaction between scaffolds is modified. Such a dynamic process, characteristic of viscoelastic gels, cannot be visualized in static cryo-ET images.

5. Discussion

In this thesis, I present a comprehensive 3D atlas of the centrosome in *C. elegans* embryonic cells as seen by cryo-ET. I developed an approach involving the plunge freezing of dissociated *C. elegans* embryonic cells, which could then be FIB milled and have mitotic centrosomes specifically targeted using CLEM. In total 12 tomograms of the wild-type centrosome were obtained, and extensively analyzed to observe the sub-compartmentalization of the PCM and the architectural role this has in organizing the mitotic spindle. Unexpectedly, as this was initially not within the scope of the study, I also unravel structural features in the centrioles that had not been previously described by the literature, which implies specialization between the mother and daughter, and possibly paints a pseudo-timeline of centriole duplication and maturation. In this discussion, I will compare the findings between *in*-vitro centrosomal protein condensates and asters with the *in-situ* findings, before discussing the practicalities of the chosen *in-situ* approach. I will then discuss the overall architecture of the centrosome, centrioles, and the roles of gamma tubulin. Finally, I will discuss the overall significance of the discovery of the porous PCM meshwork discovered as part of this study.

5.1 Microtubule asters have differing architectures from *in-situ* centrosomes

Previously, *in vitro* studies of phase-separated protein condensates have been of enormous help in understanding the role that phase separated compartments play within cells. This is also true of cryo-ET studies of these *in-vitro* condensates, where key structural properties have been uncovered, helping to unveil their molecular architecture (Patel *et al.*, 2015; Monahan *et al.*, 2017). In some cases, internal structures could even be seen (Guillén-Boixet *et al.*, 2020; Bose *et al.*, 2022).

Unfortunately, despite best efforts to reproduce the structural features of the centrosome within a test tube, the molecular-resolution centrosomal architecture (i.e. the presence of a dense meshwork) was not replicated.

That is not to say when tomograms of microtubule asters are compared to tomography of either the mitotic or interphase centrosome, no similarities are present. The mitotic centrosome was found to consist of a microtubule excluded inner region adjacent to the centrioles and a microtubule nucleation outer region. This at least is reflected in the microtubule asters, where all microtubules were seen forming in a granular outer region. This, however, is where many of the similarities end. Whereas the microtubule excluded region in mitotic centrosomes were seen to contain internal organization in the form of fine networked filaments, the microtubule aster was condensate density was continuous with no sign of internal structures. Furthermore, the microtubule condensing region in native centrosomes had the same basic structure as the microtubule free region, in that no difference in pore radius was found at different distances from the center of the centrosome. Pores are absent the *in vitro* asters, making a direct comparison impossible. Additionally, rather than the interconnected mesh, there was instead a layer of rounder granular structures in this region. Although not conclusively shown, it was speculated that this more granular region may arise from tubulin condensing on the surface, possibly unable to penetrate into the core of the condensate.

What could be the cause of these differences, and more specifically, what is present in the minimal *in vivo* centrosome that is absent *in vitro* causing these structural discrepancies? Despite the relative simplicity of the *C. elegans* centrosome, it is still a complex multiprotein structure, constantly undergoing posttranslational modifications and subject to multiple physical forces. Therefore, it could well be expected that the native centrosome has many more, and more intricate, internal structures. However, a total lack of filamentous structures within the minimal aster was surprising. It may be the case that rather than concentrating tubulin in the same

fashion as the native centrosome (Baumgart *et al.*, 2019), these asters simply act as a surface onto which tubulin can adsorb.

The asters shown in this study are not the most accurate extant *in-vitro* reflection of the *in-vivo* centrosome. They are both smaller than, and nucleate many fewer microtubules than native centrosomes. Recent unpublished work by my collaborator, Manolo Rios, has generated asters in lower concentrations of the molecular crowding agent PEG, which more closely match the size and microtubule nucleating activity of natural centrosomes. However, the protocol for creating these results in a very low concentration of final asters. While acceptable for light microscopy-based characterization, this would comprise a major challenge for cryo-ET where higher concentrations of the sample are required, as the majority of material is removed during the plunge-freezing process. Additionally, the increased size of these low-PEG asters may be so thick as to render cryo-TEM challenging. Even with the smaller asters shown in this study I had to specifically target smaller condensates as the larger ones were too thick to image through successfully. Regardless, if optimized correctly for cryo-ET studies, as must be done for all samples, these modified asters may yet prove a promising sample for *in-vitro* study of centrosomal function, something that I did not have time for over the course of this thesis, given the later success of the *in-situ* approach.

5.2 Dissociated cells are a viable sample for cryo-ET

Over the course of this thesis, I was faced with the challenge of obtaining targeted lamellae from a sample far too thick for conventional plunge freezing approaches. One approach that exists in the literature for tackling this problem is HPF followed by the cryo-lift out (Mahamid *et al.*, 2015; Schaffer *et al.*, 2019). However, technical challenges associated with this resulted in me taking a different approach: transforming a 100 µm thick worm down to the 10 µm required for plunge freezing

by stripping away the parts I was less concerned with for the study. Indeed, the actual worm itself was wholly unnecessary for my thesis, as only the easily purified embryos were the model for centrosomal studies. Rendering viable cells from these embryos requires little additional technical expertise. The fact that the cells continued to divide was of particular relevance, as this showed that the centrosomes examined were active and as such the discoveries made are reflective of wider biological relevance. Although generating a stable cell culture was seriously considered, I decided not to investigate this past the a few initial experiments, due to the associated difficulty of keeping these cells from differentiating, although differentiated single *C. elegans* cells may be of great use to researchers in other fields. Indeed, my protocol was based heavily on a pre-existing approach where dissociated cells were in turn differentiated into neuronal cells for patch clamp experiments (Christensen *et al.*, 2002).

Once plunge frozen, CLEM was used to great effect on these dissociated cells. Functionally the benefits of this were threefold: I was able to identify mitotic cells frozen on the EM grid, I localized the exact location of the centrosomes inside the lamella helping target my approaches, and I was able to determine the exact mitotic state of each centrosome imaged, building up a more complete image of this organelle through its dynamic life cycle. This demonstrates the importance of combining different imaging modalities to build the most complete picture possible of any biological process.

The approach of working with dissociated cells may, in many cases immediately unrelated to this study, prove highly beneficial (Figure 5.1). In essence, rendering a complex organism down into single cells is the basis for all cell culture work, which has already been applied to cryo-ET studies for many years (Rigort *et al.*, 2012; Mahamid *et al.*, 2016). Dissociated embryonic cells may be helpful for others attempting to perform cryo-ET on *C. elegans*. Although chosen in this case for its simple centrosomes, there are many other use cases where *C. elegans* is used as a

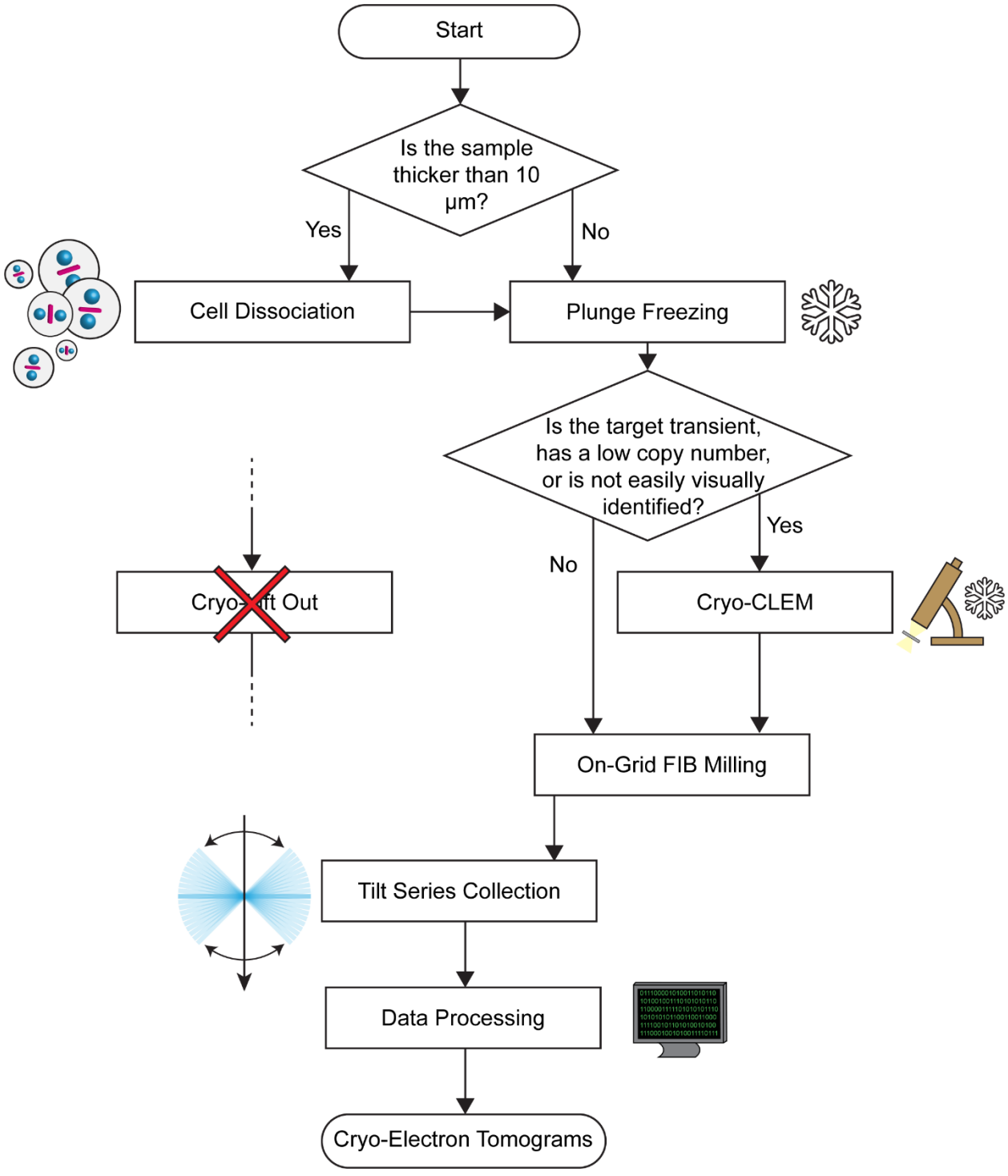

Figure 5.1: adjusted sample preparation pipeline, to exclude the cryo-lift out.

model, where cryo-ET imaging of certain processes may be beneficial and could be guided by CLEM. For example, the nematode is an important model in the study of signaling pathways (Lapierre and Hansen, 2012), environmental stressors (Rodriguez *et al.*, 2013; Kishimoto, Uno and Nishida, 2018), ageing studies (Zhang *et al.*, 2020), and studies on meiotic structures (Rog, Kohler and Dernburg, 2017). All of these fields may benefit from cryo-ET studies on embryonic cells, or differentiated cells from this embryonic stock. Furthermore, many protocols exist for differentiating cells from other model organisms (Khan *et al.*, 2016; Bresciani, Broadbridge and Liu, 2018; Wiegleb *et al.*, 2022), or tissue samples (Vieira Braga and Miragaia, 2019; Wiegleb *et al.*, 2022), for use in other protocols such as single-cell sequencing. The same principle could be applied to these cases, opening up cryo-ET to people who may have previously viewed it as impractical for their experimentation.

It is worth discussing the benefits of the cryo-lift out compared to a dissociated approach. The lift-out carries much promise, offering incredible potential to examine the native cellular environment within many thick samples, previously inaccessible to cryo-ET studies (Mahamid *et al.*, 2015; Schaffer *et al.*, 2019). More recent developments even allow this approach to be used on wider volumes of tissue, including the production of multiple sections along the length of a *C. elegans* larvae (Schiøtz *et al.*, 2023). However, this procedure is far from trivial, compared to the process of working with dissociated cells. Excluding the time and expertise required to operate a cryo-FIB, a necessary tool for almost all *in-situ* studies on intact cells, the lift-out comes with many additional technical requirements. Specifically, the faithful transfer of lamellae from the bulk sample to the grid requires much skill, with operators practicing for months until adept. Additionally, the process of milling and transferring wedges from the bulk HPF ice is a time consuming process, requiring continuous use of a FIB for several days as opposed to the relatively quick milling of individual cells plunge frozen on a grid. There is still much optimization in many steps of the protocol still to be carried out, in particular to the design of FIB shuttles and

grids to best accommodate the wedge and allow thinning within the existing architecture of the FIB.

Regardless, improvements in the technique have rendered it more accessible to researchers and it is expected this trend will continue as it is refined and institutional knowledge increases. Many core facilities across the world now offer the lift-out as part of their services offered, something that was not true at the start of this project. Additionally, as there are many biological events which it would be necessary to use this approach to image samples using cryo-ET. For example, individual cells are wholly unsuited for studies on cell-cell connections and the cell interface. Furthermore, my approach does not control for cell size beyond the use of simple cell filters. If one wanted to specifically target *C. elegans* zygotes, which are of particular relevance for studies on the synaptonemal complex involved in crossing-over events (Hurlock *et al.*, 2020), the lift-out would be required. Finally, cryo-ET on 3D cell cultures, called organoids (Sato *et al.*, 2009; Lancaster and Knoblich, 2014; Huch and Koo, 2015), is a growing field attracting much interest (D'Imprima *et al.*, 2023). To reduce these back into individual cells would render the entire exercise of using organoids useless, and as such cryo-ET studies here must be carried out via the lift-out.

5.3 Centrosome architecture is delineated by microtubules and gamma-TuRCs

The overall architecture of the centrosome has been studied before using both light and room-temperature electron microscopy (Dammermann *et al.*, 2004; Pelletier *et al.*, 2004; Fu and Glover, 2012; Lawo *et al.*, 2012; Mennella *et al.*, 2012; Sonnen *et al.*, 2012; Redemann *et al.*, 2017). These methods, having a broader field of view that allow the entire centrosomal volume to be imaged, have certain advantages over cryo-ET. However, the approach taken in this thesis, being unstained and enabling

molecular-resolution allows the integration of different scales simultaneously, letting me both examine the wide-scale architecture and the fine molecular details in subtomogram averages simultaneously within the same dataset.

In this study, I defined main centrosomal zones as a microtubule excluded and ribosome excluded zones, with the microtubule excluded zone lying within the ribosome excluded zone. These findings match previous observations of tubulin being heavily concentrated, and specifically localized, in the outer regions of the centrosome (Baumgart *et al.*, 2019), but here shown unambiguously in the form of microtubules. By combining this broad view with the resolution afforded by subtomogram averaging, I was also able to shine unparalleled detail of the organization of the microtubules. Although it was long known that *C. elegans* microtubules consist of 11 protofilaments (Chalfie and Thomson, 1982), they are shown in the centrosome to have a level of control far more precisely and accurately than implied by previous studies, with almost every single microtubule examined having the expected 11 protofilaments. This level of control is also far higher than is shown for *C. elegans* tubulin *in-vitro* (Chaaban *et al.*, 2018), implying the action of specific organizing factors present in the centriole and absent in simple buffer. Part of the microtubule organizing function of the centrosome must also include control of microtubule polarity. Previous work with EB2 comets shows 'most' microtubules are oriented away from the centrosome (Redemann *et al.*, 2017). My data mirrors this, with overall 80% of microtubules displaying their minus ends towards the centrosome, meaning their growing plus ends are moving away. However, my data also reveals both the length and position of the 'incorrectly' oriented microtubules. The negatively oriented microtubules are not only significantly shorter than the positive ones, but the majority of them both have their start and stop points within the ribosome excluded region. In essence, they start at the same position as other microtubules but are too short to exit the ribosome excluded region, or grow through into the ribosome excluded region and as such do not form part of the mitotic spindle. As such, the microtubules that go on to take part in separating chromosomes may

have better control of their polarity than the pool of spindle and non-spindle microtubules shown in this study.

As gamma-TuRCs are known to both stabilize the minus end and act as a microtubule template (Michelle Moritz *et al.*, 1995; Zheng *et al.*, 1995; Moritz *et al.*, 2000), it stands to reason that these complexes may be serving to guide the 11 protofilament nature of the microtubules in *C. elegans*. These complexes were present in the data unbound to long microtubules, the dense signal of which would have complicated the alignment process. A subtomogram average of the gamma-TuRC complex was generated as part of this thesis, the first time this complex has been shown in *C. elegans*. This complex was also found to bind a short section of microtubule, showing that it was in its active conformation. The average also contained a stabilizing ring, confirming this feature's presence within the nematode, and its upper section forming an assembly of 11-fold symmetry. This symmetric region may be responsible for imparting the strict 11 protofilaments seen in the data, which given gamma-TuRCs extensive presence within the centrosome (Michelle Moritz *et al.*, 1995; Khodjakov and Rieder, 1999), may explain the strong level of protofilament control. When, in previous work, gamma tubulin was knocked down via RNAi, the number of microtubules was unchanged but the organization of the spindle was compromised, with microtubule seen passing through the previously microtubule excluded zone (O'Toole *et al.*, 2012). It is unknown if this also compromised microtubule protofilament numbers, but formation of the centrioles was impacted. Given the random orientation of free gamma-TuRC molecules within the centrosome, it remains to be seen how these complexes function to direct microtubules away from the centrosome center.

When compared to 3.4 Å resolution structure of the complete gamma-TuRC complex from humans, one striking difference was seen, aside from the expected difference in protofilament number. Whereas the cone of the human complex had a capping structure right at its tip (Wieczorek *et al.*, 2020), in the nematode this was absent,

and a very conspicuous hole was present at the end of the ring. The authors of this, and additional studies on gamma-TuRC (Liu *et al.*, 2020; Würtz *et al.*, 2022) were unable to assign molecular identity to this tip complex, and as such it is totally absent in their molecular models, despite being present in the density maps. Its absence may be due to the fact that it is human specific, or it may be an effect of the gamma-TuRC being in an active confirmation in the data presented in this thesis. Without knowing the molecular identity of this plug, it is impossible to run the necessary bioinformatics searches that would explain this. As such for now it must remain a mystery.

Of course, not every microtubule seen in the data has 11 protofilaments. The centriolar microtubules, both mother and daughter, had 13 protofilaments without fail. How can two systems reliably nucleate different microtubule protofilament numbers, within dozens of nanometers of each other within the same cell? Although I have already postulated that gamma-TuRC is responsible for imparting the 11 protofilament nature of centrosomal microtubules, it is also known that these complexes must have a role in centriole formation as their knockdown results in elongated centriolar microtubules (O'Toole *et al.*, 2012). Nematodes also lack delta and epsilon tubulin found in centrioles and basal bodies of humans (Dutcher *et al.*, 2002). However, they have many isoforms of alpha and beta tubulin, and isoforms of beta tubulin have been shown to impact protofilament number (Ti, Alushin and Kapoor, 2018). Additionally, posttranslational modification has been shown to influence protofilament number, with acetylation on the inner face of the microtubule found to be of particular importance (Cueva *et al.*, 2012). Unfortunately a map of these modifications in *C. elegans* centrioles does not exist. Regardless, I suggest that in *C. elegans* centriolar microtubules are either composed of different tubulin isoforms than their centrosomal cousins, or are subjected to specific posttranslational modification responsible for imparting their protofilament number. The role gamma tubulins would have in relation to these is unknown.

5.4 Centrioles display structural heterogeneity

Numerous scientific investigations have been conducted to elucidate the structural characteristics of *C. elegans* centrioles, involving both light, and room temperature electron microscopy, showing its short (~150 nm) length, singlet microtubules, and the existence of the 'paddlewheel' (Pelletier *et al.*, 2006; Sugioka *et al.*, 2017; Woglar *et al.*, 2022). However, these studies were unable to discern any notable distinctions between the mother and daughter centrioles. The closest previous work has come to actively spotting structural differences between the two centrioles in any organisms arises from light microscopy work showing different patterning of PCM molecules around the mother and daughter centrioles in *Drosophila* (Fu and Glover, 2012; Mennella *et al.*, 2012), and electron microscopy showing the disappearance of the cartwheel in human mother centrioles (Paintrand *et al.*, 1992; Chrétien *et al.*, 1997). The research presented in this thesis not only reveals striking visual differences between the two, with the mother centriole showing the presence of doublet microtubules, in stark contrast to existing literature which suggests it should only have singlets (Pelletier *et al.*, 2006; Sugioka *et al.*, 2017). Furthermore, I identified intriguing variations within the b-tubule of the mother centriole. The differences between mother and daughter showing different levels of development as the centriole matures from daughter into mother. Furthermore these newfound dissimilarities strongly suggest a specialization in the functions of both the mother and daughter centrioles.

Notably, the daughter centriole exhibits a prominent cartwheel structure, which is believed to be composed of SAS-6—an essential component involved in templating the growth of procentriole microtubules. This arises from the fact that this cartwheel is the same size and shape of *in vitro* SAS-6 rings (Hilbert *et al.*, 2013; Nazarov *et al.*, 2020), and that SAS-6 is shown to localize to the same area of the centriole as the cartwheel in light microscopy (Woglar *et al.*, 2022). These observations underscore the cartwheel's role in microtubule templating during centriole assembly. Conversely,

the fully developed mother centriole, having finished its growth and adorned with a full set of microtubules, does not require such templating mechanisms. Thus, it is logically consistent, and in agreement with existing data from humans (Paintrand *et al.*, 1992; Chrétien *et al.*, 1997), that this cartwheel feature is absent in the mature mother centriole, its function having been completed. The *in-situ* approach described in this thesis may help to settle the debate as to if the inner tube consists of SAS-6 rings stacked vertically (Hatzopoulos *et al.*, 2021), or consists of a helix (Hilbert *et al.*, 2013), although this would require greater particle numbers than available in this study. Work with centrioles purified from cellular extract may be more appropriate in this case.

Compared to the daughter, the mother centriole showcases prominent features associated with centriole integrity and PCM connectivity, such as the central tube, and the novel 'outer star' structure. This central tube bears functional similarities to the helical scaffold observed in other organisms, a structure implicated in imparting physical strength to the centriole and helping to maintain its integrity (Le Guennec *et al.*, 2020). This further supports the notion that the mother centriole assumes distinctive roles in maintaining cellular structures. The outer star may be relevant in tethering the centriole to the PCM. While I was unable to precisely identify the molecular constituents of this star, experiments involving knock-down strains of SPD-2 (Cabral *et al.*, 2019) suggest that it is unlikely to be exclusively composed of this protein. This was particularly surprising, as SPD-2 not only was found to localize to the star, but approximated the shape of the star tip in symmetrized fluorescence light microscopy. The location of this star within the centriole also corresponds, albeit less closely than SPD-2, to the approximate localization of SAS-7 and PCMD-1 (Woglar *et al.*, 2022) which are known to play pivotal roles in centriole replication and tethering the centriole to the PCM (Sugioka *et al.*, 2017; Erpf *et al.*, 2019). This, combined with the star's location right at the periphery of the centriole, implicate the star as having roles in centriole tethering, however without knowing its molecular identity, this remains speculative. As, based on their AlphaFold2 predictions, SAS-7 contains

coiled-coils but PCMD-1 is unstructured, SAS-7 remains the more likely candidate of the two. Tethering and duplication are tasks specific to the mother centriole, the implication of the star in these roles reinforces the notion of functional specialization between the two centrioles.

The star and the partial b-tubule were found to occupy the region previously designated as the 'paddlewheel' in earlier room-temperature electron microscopy studies in *C. elegans* (Pelletier *et al.*, 2004, 2006; Sugioka *et al.*, 2017; Woglar *et al.*, 2022). As such, no paddlewheel, or even a structure resembling the paddlewheel, is seen in this dataset at all. My current findings instead suggest that the paddlewheel is actually a combination of the star structure and the affected b-tubule of the mother centriole. Prior evidence for the existence of the paddlewheel arose from room-temperature electron microscopy involving the use of heavy metal stains. In these cases, the accuracy of the overall image formed is limited by the fidelity of the staining. It is entirely possible that staining of these structures was ineffective, blurring the overall structure into the unclear proteinaceous density seen in the older data. As the data in this thesis is unstained and as such does not have those limitations, I propose that the discrete assemblies seen are the true structure of the mother centriole.

The partial b-tubule emerges as the site of the most significant heterogeneity within the centrioles, exhibiting variations in protofilament number ranging from 3 to 9. The extent of b-tubule formation seemed to be independent of cell cycle state: the most complete centriole seen was taken from interphase and many of the mother centrioles seen in mitosis had just 3 protofilaments. Deciphering the precise function of this b-tubule within the centriole remains a challenging question. Nevertheless, previous observations of b-tubules in basal bodies in *C. elegans* (Nechipurenko *et al.*, 2017) and other organisms (Pigino *et al.*, 2009; Klena and Pigino, 2022) as well as the centrioles of *Drosophila* (M Moritz *et al.*, 1995; Greenan *et al.*, 2018) suggest that doublet microtubules could represent a fundamental evolutionary unit upon which

additional effectors, and in the case of various other organisms including humans, a third triplet microtubule, are attached.

In summary, this study on *C. elegans* centrioles has unveiled previously unexplored nuances between the mother and daughter centrioles. The daughter centriole's prominent cartwheel and the mother centriole's central tube demonstrate specialized functions, while the novel 'outer star' structure and the partial b-tubule provide intriguing avenues for further research. The findings have significant implications for understanding the unique roles of centrioles in cellular processes and may serve as a foundation for future investigations into centriolar function and evolution across different organisms.

5.5 The centrosome consists of a gel-like porous meshwork

The existing scientific literature has put forth contrasting views on the structure and composition of the centrosome's surface. Some studies have proposed that the surface of the centrosome is defined by a layer of gamma-TuRC complexes (O'Toole *et al.*, 2012), while another suggests that it is partially membrane-bound and referred to as the 'centriculum,' consisting of layers of endoplasmic reticulum that surround the centrosome (Maheshwari *et al.*, 2023). In this research, I successfully identified the presence of gamma-TuRCs within the centrosome, but these complexes were found to be randomly positioned and oriented throughout the centrosomal volume, and do not act to delineate the centrosome surface. This is in agreement with the early studies on gamma-TuRCs, which also found distribution of these complexes throughout the centrosome (Michelle Moritz *et al.*, 1995; Moritz *et al.*, 1998). Moreover, although I observed the presence of membranes at the immediate periphery of the centrosome, it was evident that the centrosome itself was not entirely encased by the membrane, and it is more appropriate to use ribosome exclusion as a proxy for identifying the approximate boundaries of centrosomal

material. The absence of a distinct physical barrier separating the cytoplasm from the centrosome raises the question of how this spatial organization is achieved. Phase separation of the centrosome has been suggested as the mechanism by which the centrosome forms (Woodruff *et al.*, 2017), and the data shown here, seems to reinforce this model. As such I conclude that the centrosome is indeed a phase-separated organelle, as has been long considered.

Prior to this study, three plausible, yet conflicting, models were proposed to describe the formation, architecture, and behavior of the mitotic PCM. These models are the lattice model (Schnackenberg *et al.*, 1998), by which the centrosome assembles around a rigid well-structured lattice-like skeleton; the liquid model (Zwicker *et al.*, 2014), where the centrosome consists of only autocatalytic droplets of PCM; and the gel model (Woodruff *et al.*, 2017; Mittasch *et al.*, 2020), where the centrosomal matrix matures form a liquid droplet into a disordered meshwork. By analyzing the centrosome using cryo-ET, the data provides the first molecular resolution unstained view into the native structure of the centrosome, and allow the comparison of these three models.

In the tomograms, I observed and characterized an irregular, porous meshwork distributed throughout the speculated PCM region. This argues against the pure liquid model, where a smooth and invariant internal volume would be expected. This meshwork displayed highly variable segment lengths and numbers of connections per branch point, indicating that a crystalline lattice model is not consistent with these findings, where highly regular segment lengths and connections at branch points would be found instead. Not only are these two models inconsistent with the data observed, but direct evidence is seen to support the gel, or arrested condensate, model. The gel phase itself is inherently consists of two components: a cross-linked system with little flow, and a dilute phase that can pass around and through the cross-linked phase (Slomkowski *et al.*, 2011). This matches what is seen in the tomograms, with an intricate but apparently irregular meshwork throughout the centrosomal

volume, with pores large enough to accommodate known centrosomal proteins. This discovery provides an explanation for the observations made previously, identifying that the centrosome was both phase-separated, and likely to consist of a gel (Figure 5.2).

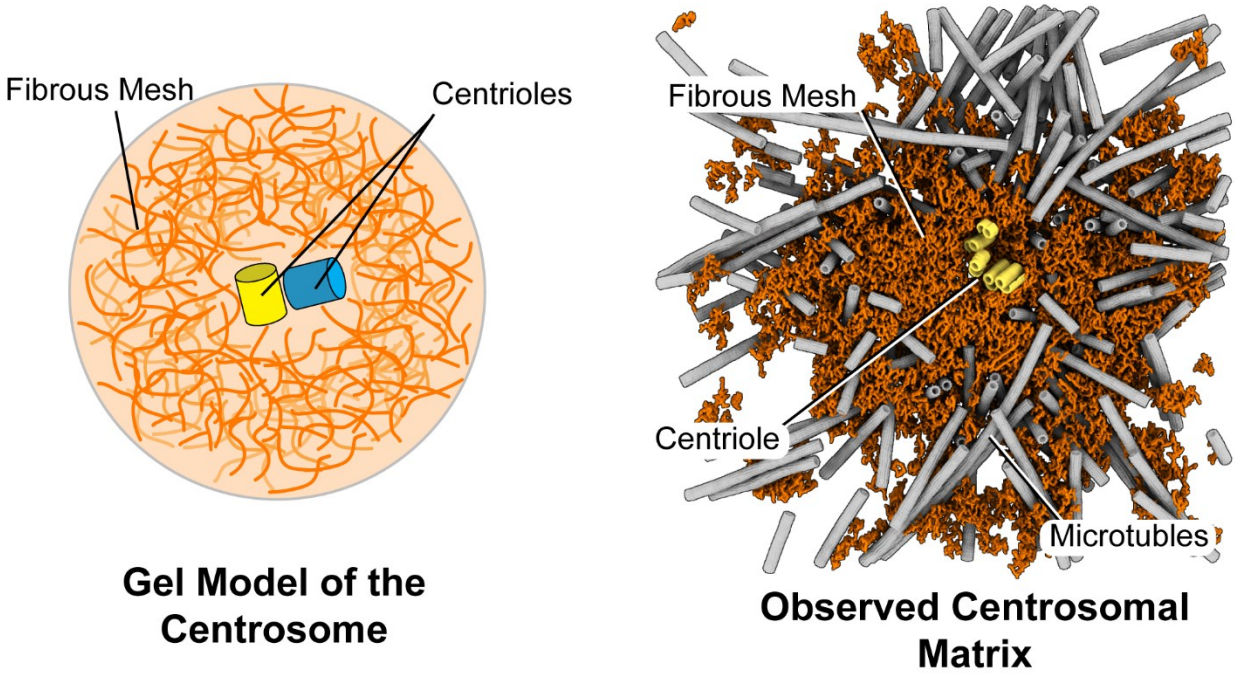

Figure 5.2: The gel model and how it relates to the data shown in this thesis. A schematic of the gel model is shown on the left, with an example of our observed matrix on the left. Both show a large number of highly interconnected filaments.

The liquid model however cannot and should not be fully discarded. It was not possible to trace out such a filamentous matrix within interphase centrosomes, despite 5 tomograms of them being collected in the study. This was because any densities seen in these centrosomes were impossible to differentiate from background noise. It therefore remains the case that the interphase centrosome could be best described as a liquid. A combination of the gel models and liquid models may therefore apply to this system, where the centrosome initially exists in a liquid-like state, in that it is ductile and undergoes local rearrangements. Upon centrosome growth at the onset of mitosis, it may remain liquid as proposed by (Zwicker *et al.*, 2014). However, during maturation it may transition into a more

cross-linked state lacking the ability to undergo local rearrangement, and strong enough to withstand pulling forces. Capturing this transition, being such a fine temporal event, is not feasible or practical within the vitreous ice required of cryo-ET. Observing if the PCM has transient and fading liquid-like properties over the course of maturation would be more appropriate of in-cell micro rheology experiments.

Despite best efforts, it was not possible to unambiguously assign identity to the meshwork based on segment lengths or number of branchpoints, ultimately because these were both found to be highly variable. However, SPD-5 is by far the most likely candidate for most of this mesh, as this protein is known to self-assemble into a scaffold, via multivalent coiled-coil interactions. The myriad nature of these interactions mirrors the broad range of segment lengths and connections seen in the data, although the one region in the protein found to be of particular importance in multimerization (Rios *et al.*, 2023) was also found to broadly match the dimensions of the peak segment length. The protein SPD-2 may also be present given its role in maintaining centrosome integrity as a crosslinking moiety (Pelletier *et al.*, 2004; Decker *et al.*, 2011), but as there is thought to be much more SPD-5 than SPD-2 in the centrosome, any signal corresponding to SPD-2 would be drowned out. Performing in-cell mass spectrometry to get a more accurate picture on the stoichiometric ratio between SPD-5, SPD-2, and other PCM proteins would help build a clearer picture of what exactly the identified meshwork consists of.

I found little difference in the structural properties of the PCM between the metaphase and anaphase centrosomes. As the ductility, lability, and strength of the PCM is known to dramatically change upon this transition (Mittasch *et al.*, 2020a), the similarity of the PCM architecture was rather surprising. As the centrosome enters anaphase, the respective action of PLK-1 and PP2A cause a drop in the phosphorylation level of SPD-5, which in turn decreases its ability to self-interact and assemble (Wueseke *et al.*, 2016; Enos *et al.*, 2018). This indicates that rather than undergoing a fundamental shift in overall structure, the PCM may be less likely to

experience internal reorganizations in its less phosphorylated state. This would in turn render the PCM less able to absorb the stresses placed upon it by the pulling forces of mitosis, and explain the phenomenon of the material shift of the centrosome. Such dynamic events are hard to capture in a relatively low number of static images.

How conserved is the PCM between species, and how applicable are these findings to wider biology? The PCM scaffolds display limited sequence homology between species, but they retain structural and functional similarities. Scaffold molecules, such as centrosomin in *Drosophila* (Timothy *et al.*, 1999) and Cdk5Rap2 in humans (Fong *et al.*, 2007; Graser, Stierhof and Nigg, 2007), are composed of multivalent proteins with coiled-coil domains, just as SPD-5 is. Given this diversity in sequence, it would not be surprising to observe differences in pore size or segment length between species. Therefore, the presence of a 'centromatrix' filament length of 12-15 nm in *S. solidissima* (Schnackenberg *et al.*, 1998) may not contradict the observed filament length centered around 7.4 nm, as these differences might be attributed to variations in scaffold molecules. Indeed, although some have interpreted these results to be a regular crystalline lattice, there is little information in the original paper to suggest the authors meant for it to be interpreted this way. What may be seen in the electron micrographs may be the same fundamental PCM matrix as shown in this thesis. Ultimately, given the similarities in overall centrosome function, formation, and molecular properties of PCM scaffold in a range of eukaryotic species, it is fair to assume that the data shown here will share common properties concerning assembly and architecture of the PCM, although evolution will have of course introduced differences in precise mechanisms.

6. Concluding remarks

In this thesis, I explored the potential of using cryo-ET in the non-conventional sample of dissociated *C. elegans* embryonic cells, prepared in such a way that they remained viable. From these data, it was possible to reveal both the broad overarching architectural details, and the finer molecular details of the centrosome. Specifically, the following conclusions were derived:

- The centrosome can be described as existing in two main zones: a ribosome excluded zone and a microtubule excluded zone. The microtubule excluded zone sits within the middle of the ribosome excluded zone and contains the centrioles. Over the course of mitosis, the radius of the microtubule excluded zone expands relative to the ribosome excluded zone.
- The centrioles are heterogeneous structures. The mother and daughter centrioles, when both are visible, show significantly different structures, such as the presence of a cartwheel in daughters that spreads past the end of the microtubules, which is absent in the mother. Furthermore, the mother centriole only has partial doublets, whereas the daughter has the singlets, as described previously. The number of protofilaments in the doublet varies between three and nine, with no apparent connection to mitotic stage.
- Mother centrioles only have a previously undescribed structure, termed the ‘outer star’. Although matching the shape and position of SPD-2 in previous light microscopy experiments (Woglar *et al.*, 2022), it does not appear to be composed of SPD-2, as knock-downs of this protein retain the outer star.
- Microtubule protofilament number is well and strictly controlled. While almost every centrosomal microtubule was found to have 11 protofilaments, centriolar microtubules all had 13 protofilaments. This demonstrates that

cells can have multiple protofilament numbers, and have strictly spatially controlled mechanisms for modulating microtubule protofilament number.

- 80% of centrosomal microtubules were found to orient their plus ends away from the centrosome and their minus ends towards it, consistent with EB2 studies (Redemann *et al.*, 2017). The remaining 20% were found to be significantly shorter and rarely extended beyond the ribosome excluded region.
- Putative gamma-TuRC in *C. elegans* can be seen templating the 11 protofilament microtubule, and has a ring section, but does not contain a plugging region at the end of said cone.
- The centrosome core is filled with a filamentous meshwork, which is likely composed of SPD-5. Segmentation of these filaments reveals an irregular, porous meshwork in the PCM, suggesting a bi-phase system and gel-like properties. The gel pores are wide enough to accommodate a number of PCM client proteins, and do not appear to change between metaphase and anaphase.

There are still mysteries of the centrosome that will need uncovering. For example, the heterogeneity of the mother centriole may be best explored with bulk purified centrioles rather than bespoke lamella prepared *in-situ*. The properties of the PCM, particularly at the crucial metaphase/anaphase transition may be further explored, and the models here expanded upon, through inclusion of in-cell mass spectrometry work to better find the molecular identify of the meshwork.

Contributions

Worm strains and proteins were generously provided by Jeff Woodruff and Manolo Rios of UT Southwestern, Dallas, USA.

Condensate and aster tomography was carried out along with Julia Mahamid, Jeff Woodruff, and Manolo Rios.

Analysis of segment lengths was made possible by scripts from Frosina Stojanovska.

Depiction of segmentations was made possible by scripts provided by Rasmus Jensen.

Ievgeniia Zagoriy assisted with room temperature light microscopy and worm maintenance.

Acknowledgments

Whilst no one ever expects a PhD to be easy, I think it's fair to say that over the years it took me to finish this I was subjected to a more-than-ideal number of global catastrophes and personal crises. And it's more than fair to say I wouldn't have lasted half as long as I did through it all without help I received from others along the way. I'd like to thank Ana Rita Rodrigues Neves for letting me steal her NGM plates for so many years, and Frosina Stojanovska for patiently explaining to me why my python scripts kept failing. I'd like to thank all my TAC members: Janosch Hennig, Yannick Schwab, and Gislene Pereira for valuable advice which helped guide this project into what it is. A special thanks of course goes to the many members of the Mahamid lab, who collectively have created an amazing atmosphere, especially to Marie and Rasmus, who volunteered to read over much of my work over the years. The EMBL Graduate Office, and in particular Monika Lachner, who never faltered in their support, deserve particular thanks.

Outside the lab, equal parts gossiping, moaning, and being terrible at Mario Kart, on the so-called therapy couch with Wolfi Hoeps and Anna Mathiodaki made stressful things much more bearable. Jenny, Aline, Max, Prachiti, Paul, and Amy acted as an emotional anchor in times of crisis and for amazing company in better days. And thank you to everyone in my predoc batch, who formed such a cohesive group and made many aspects of my time at EMBL a real pleasure.

My parents and brother deserve much credit for me having finished, for their help and offering a safe harbor in times of need. Thank you to my therapist Hannah, for talking my through the worst of it and for helping me to realize that I can actually get through this.

Finally, Jenia's kind and limitless support, up to and including picking me up from hospital (something I refuse to let her forget), made me finishing an actual possibility,

and for that I can only offer thanks on paper. Julia, thank you for giving me this opportunity in the first place mentoring me through everything, and helping to turn me into the scientist I am today.

List of abbreviations

ATP – Adenosine Triphosphate

CHAPS – (3-((3-Cholamidopropyl) Dimethylammonio)-1-Propanesulfonate)

CLEM – Correlative Light and Electron Microscopy

Cryo-EM – Cryo-Electron Microscopy

Cryo-ET – Cryo-Electron Tomography

CTF – Contrast Transfer Function

DeePiCt – Deep Picker In Context

DTT – Dithiothreitol

EGTA – Tetra(Acetoxymethyl Ester)

EM – Electron Microscopy

EMDB – Electron Microscopy Data Bank

FIB – Focused Ion Beam

FLUCS – Focused Light Induced Cytoplasmic Streaming

FSC – Fourier Shell Correlation

Gamma-TuRC – Gamma Tubulin Ring Complex

Gamma-TuSC – Gamma Tubulin Small Complex

GFP – Green Fluorescent Protein

GTP – Guanosine Triphosphate

HEPES – (4-(2-Hydroxyethyl)-1-Piperazineethanesulfonic Acid)

HPF – High Pressure Freezing

MEZ – Microtubule Excluded Zone

MTOC – Microtubule Organizing Center

NA – Numerical Aperture

NEBD – Nuclear Envelope Break Down

NGM – Nematode Growth Media

NPC – Nuclear Pore Complex

PCM – Peri-Centriolar Material

PEG – Polyethylene Glycol

PIPES – Piperazine-N,N′-Bis(2-Ethanesulfonic Acid)

REZ – Ribosome Excluded Zone

SIM – Structured Illumination Microscopy

SIRT – Simultaneous Iterative Reconstruction Technique

SNR – Signal to Noise Ratio

STED – Stimulated Emission Depletion Microscopy

STEM – Scanning Transmission Electron Microscopy

STORM – Stochastic Optical Reconstruction Microscopy

TEM – Transmission Electron Microscopy

References

Abal, M., Keryer, G. and Bornens, M. (2005) ‘Centrioles resist forces applied on centrosomes during G2/M transition’, *Biology of the Cell*, 97(6), pp. 425–434. Available at: https://doi.org/10.1042/BC20040112.

Adrian, M. *et al.* (1984) ‘Cryo-electron microscopy of viruses’, *Nature*, 308(5954), pp. 32–36. Available at: https://doi.org/10.1038/308032a0.

Al-Amoudi, A. *et al.* (2004) ‘Cryo-electron microscopy of vitreous sections’, *The EMBO Journal*, 23(18), pp. 3583–3588. Available at: https://doi.org/10.1038/sj.emboj.7600366.

Al-Amoudi, A., Studer, D. and Dubochet, J. (2005) ‘Cutting artefacts and cutting process in vitreous sections for cryo-electron microscopy’, *Journal of Structural Biology*, 150(1), pp. 109–121. Available at: https://doi.org/10.1016/j.jsb.2005.01.003.

Alberti, S. and Hyman, A.A. (2016) ‘Are aberrant phase transitions a driver of cellular aging?’, *BioEssays*, 38(10), pp. 959–968. Available at: https://doi.org/10.1002/bies.201600042.

Alvarez-Rodrigo, I. *et al.* (2019) ‘Evidence that a positive feedback loop drives centrosome maturation in fly embryos’, *eLife*, 8. Available at: https://doi.org/10.7554/eLife.50130.

Armstrong, M. *et al.* (2020) 'Microscale Fluid Behavior during Cryo-EM Sample Blotting', *Biophysical Journal*, 118(3), pp. 708–719. Available at: https://doi.org/10.1016/j.bpj.2019.12.017.

Arnold, J. *et al.* (2016) 'Site-Specific Cryo-focused Ion Beam Sample Preparation Guided by 3D Correlative Microscopy', *Biophysical Journal* [Preprint]. Available at: https://doi.org/10.1016/j.bpj.2015.10.053.

Azimzadeh, J. (2014) 'Exploring the evolutionary history of centrosomes', *Philosophical Transactions of the Royal Society B: Biological Sciences*, 369(1650), p. 20130453. Available at: https://doi.org/10.1098/rstb.2013.0453.

Azimzadeh, J. and Marshall, W.F. (2010) 'Building the centriole', *Current Biology*, 20(18), pp. R816–R825.

Banani, S.F. *et al.* (2016) 'Compositional Control of Phase-Separated Cellular Bodies', *Cell* [Preprint]. Available at: https://doi.org/10.1016/j.cell.2016.06.010.

Banterle, N. *et al.* (2020) 'Surface-catalyzed SAS-6 self-assembly directs centriole formation through kinetic and structural mechanisms', *bioRxiv*, p. 2020.09.04.283184. Available at: https://doi.org/10.1101/2020.09.04.283184.

Baumgart, J. *et al.* (2019) 'Soluble tubulin is significantly enriched at mitotic centrosomes', *Journal of Cell Biology* [Preprint]. Available at: https://doi.org/10.1083/JCB.201902069.

Beck, M. and Baumeister, W. (2016) 'Cryo-Electron Tomography: Can it Reveal the Molecular Sociology of Cells in Atomic Detail?', *Trends in Cell Biology*, 26(11), pp. 825–837. Available at: https://doi.org/10.1016/j.tcb.2016.08.006.

Berg, S. *et al.* (2019) 'ilastik: interactive machine learning for (bio)image analysis', *Nature Methods*, 16(12). Available at: https://doi.org/10.1038/s41592-019-0582-9.

Berger, C., Premaraj, N., *et al.* (2023) ‘Cryo-electron tomography on focused ion beam lamellae transforms structural cell biology’, *Nature Methods*, 20(4), pp. 499–511. Available at: https://doi.org/10.1038/s41592-023-01783-5.

Berger, C., Dumoux, M., *et al.* (2023) ‘Plasma FIB milling for the determination of structures in situ’, *Nature Communications*, 14(1), p. 629. Available at: https://doi.org/10.1038/s41467-023-36372-9.

Bharat, T.A.M., Hoffmann, P.C. and Kukulski, W. (2018) ‘Correlative Microscopy of Vitreous Sections Provides Insights into BAR-Domain Organization In Situ’, *Structure*, 26(6), pp. 879-886.e3. Available at: https://doi.org/10.1016/j.str.2018.03.015.

Bieber, A. *et al.* (2021) ‘Precise 3D-correlative FIB-milling of biological samples using METEOR, an integrated cryo-CLEM imaging system’, *Microscopy and Microanalysis*, 27(S1), pp. 3230–3232. Available at: https://doi.org/DOI: 10.1017/S1431927621011132.

Böhm, J. *et al.* (2000) ‘Toward detecting and identifying macromolecules in a cellular context: Template matching applied to electron tomograms’, *Proceedings of the National Academy of Sciences*, 97(26), pp. 14245–14250. Available at: https://doi.org/10.1073/pnas.230282097.

Bolhy, S. *et al.* (2011) ‘A Nup133-dependent NPC-anchored network tethers centrosomes to the nuclear envelope in prophase’, *Journal of Cell Biology*, 192(5), pp. 855–871. Available at: https://doi.org/10.1083/jcb.201007118.

Boltje, D.B. *et al.* (2022) ‘A cryogenic, coincident fluorescence, electron, and ion beam microscope’, *eLife*. Edited by S.R. Pfeffer and M. Kopylov, 11, p. e82891. Available at: https://doi.org/10.7554/eLife.82891.

Booy, F.P. and Pawley, J.B. (1993) ‘Cryo-crinkling: what happens to carbon films on copper grids at low temperature’, *Ultramicroscopy*, 48(3), pp. 273–280. Available at: https://doi.org/10.1016/0304-3991(93)90101-3.

Bose, M. *et al.* (2022) ‘Liquid-to-solid phase transition of oskar ribonucleoprotein granules is essential for their function in Drosophila embryonic development’, *Cell*, 185(8), pp. 1308-1324.e23. Available at: https://doi.org/10.1016/j.cell.2022.02.022.

Boveri, T. (1900) *Zellen-Studien: Über die Natur der Centrosomen*. G. Fischer (Zellen-Studien). Available at: https://books.google.de/books?id=gfQYAAAAYAAJ.

Bowler, M. *et al.* (2019) ‘High-resolution characterization of centriole distal appendage morphology and dynamics by correlative STORM and electron microscopy’, *Nature Communications*, 10(1), p. 993. Available at: https://doi.org/10.1038/s41467-018-08216-4.

Bowne-Anderson, H. *et al.* (2013) ‘Microtubule dynamic instability: A new model with coupled GTP hydrolysis and multistep catastrophe’, *BioEssays*, 35(5), pp. 452–461. Available at: https://doi.org/10.1002/bies.201200131.

‘BRB80 (5x)’ (2016) *Cold Spring Harbor Protocols*, 2016(5), p. pdb.rec086694. Available at: https://doi.org/10.1101/pdb.rec086694.

Brenner, S. (1974) ‘The genetics of Caenorhabditis elegans’, *Genetics*, 77(1), pp. 71–94. Available at: https://doi.org/10.1093/genetics/77.1.71.

Bresciani, E., Broadbridge, E. and Liu, P.P. (2018) ‘An efficient dissociation protocol for generation of single cell suspension from zebrafish embryos and larvae’, *MethodsX*, 5, pp. 1287–1290. Available at: https://doi.org/10.1016/j.mex.2018.10.009.

Brilot, A.F. *et al.* (2012) 'Beam-induced motion of vitrified specimen on holey carbon film', *Journal of Structural Biology*, 177(3), pp. 630–637. Available at: https://doi.org/10.1016/j.jsb.2012.02.003.

Brüggeller, P. and Mayer, E. (1980) 'Complete vitrification in pure liquid water and dilute aqueous solutions', *Nature*, 288(5791), pp. 569–571. Available at: https://doi.org/10.1038/288569a0.

Buchholz, T.-O. *et al.* (2018) 'Cryo-CARE: Content-Aware Image Restoration for Cryo-Transmission Electron Microscopy Data.', *arxiv*. Available at: http://arxiv.org/abs/1810.05420.

Buijsse, B. *et al.* (2020) 'Spectral DQE of the Volta phase plate', *Ultramicroscopy*, 218, p. 113079. Available at: https://doi.org/10.1016/j.ultramic.2020.113079.

Cabral, G. *et al.* (2013) 'Multiple Mechanisms Contribute to Centriole Separation in C. elegans', *Current Biology*, 23(14), pp. 1380–1387. Available at: https://doi.org/10.1016/j.cub.2013.06.043.

Cabral, G. *et al.* (2019) 'Differential Requirements for Centrioles in Mitotic Centrosome Growth and Maintenance', *Developmental Cell*, 50(3), pp. 355-366.e6. Available at: https://doi.org/10.1016/j.devcel.2019.06.004.

Castaño-Díez, D. *et al.* (2012) 'Dynamo: A flexible, user-friendly development tool for subtomogram averaging of cryo-EM data in high-performance computing environments', *Journal of Structural Biology* [Preprint]. Available at: https://doi.org/10.1016/j.jsb.2011.12.017.

Chaaban, S. *et al.* (2018) 'The Structure and Dynamics of C. elegans Tubulin Reveals the Mechanistic Basis of Microtubule Growth', *Developmental Cell* [Preprint]. Available at: https://doi.org/10.1016/j.devcel.2018.08.023.

Chalfie, M. and Thomson, J.N. (1982) 'Structural and functional diversity in the neuronal microtubules of Caenorhabditis elegans.', *Journal of Cell Biology*, 93(1), pp. 15–23. Available at: https://doi.org/10.1083/jcb.93.1.15.

Chen, M. *et al.* (2017) 'Convolutional neural networks for automated annotation of cellular cryo-electron tomograms', *Nature Methods*, 14(10), pp. 983–985. Available at: https://doi.org/10.1038/nmeth.4405.

Chen, Z. *et al.* (2022) De novo *protein identification in mammalian sperm using high-resolution* in situ *cryo-electron tomography*. preprint. Biophysics. Available at: https://doi.org/10.1101/2022.09.28.510016.

Chrétien, D. *et al.* (1997) 'Reconstruction of the Centrosome Cycle from Cryoelectron Micrographs', *Journal of Structural Biology*, 120(2), pp. 117–133. Available at: https://doi.org/10.1006/jsbi.1997.3928.

Christensen, M. *et al.* (2002) 'A primary culture system for functional analysis of C. elegans neurons and muscle cells', *Neuron* [Preprint]. Available at: https://doi.org/10.1016/S0896-6273(02)00591-3.

Conduit, P.T., Wainman, A. and Raff, J.W. (2015) 'Centrosome function and assembly in animal cells', *Nature Reviews Molecular Cell Biology*, 16(10), pp. 611–624. Available at: https://doi.org/10.1038/nrm4062.

Crowther, R.A., DeRosier, D.J. and Klug, A. (1970) 'The reconstruction of a three-dimensional structure from projections and its application to electron microscopy', *Proceedings of the Royal Society of London. A. Mathematical and Physical Sciences*, 317(1530), pp. 319–340. Available at: https://doi.org/10.1098/rspa.1970.0119.

Cueva, J.G. *et al.* (2012) ‘Posttranslational Acetylation of α-Tubulin Constrains Protofilament Number in Native Microtubules’, *Current Biology*, 22(12), pp. 1066–1074. Available at: https://doi.org/10.1016/j.cub.2012.05.012.

Dammermann, A. *et al.* (2004) ‘Centriole assembly requires both centriolar and pericentriolar material proteins’, *Developmental Cell*, 7(6). Available at: https://doi.org/10.1016/j.devcel.2004.10.015.

Danev, R. *et al.* (2014) ‘Volta potential phase plate for in-focus phase contrast transmission electron microscopy’, *Proceedings of the National Academy of Sciences of the United States of America*, 111(44), pp. 15635–15640. Available at: https://doi.org/10.1073/pnas.1418377111.

Danev, R. and Baumeister, W. (2016) ‘Cryo-EM single particle analysis with the Volta phase plate’, *eLife*. Edited by S.H.W. Scheres, 5, p. e13046. Available at: https://doi.org/10.7554/eLife.13046.

Danev, R., Tegunov, D. and Baumeister, W. (2017) ‘Using the Volta phase plate with defocus for cryo-EM single particle analysis’, *eLife*. Edited by S.H.W. Scheres, 6, p. e23006. Available at: https://doi.org/10.7554/eLife.23006.

Dawes, C.J. (1971) ‘Biological techniques in electron microscopy’.

De Harven, E. and Bernhard, W. (1956) ‘Etude au microscope électronique de l’ultrastructure du centriole chez les vertébrés’, *Zeitschrift für Zellforschung und mikroskopische Anatomie*, 45, pp. 378–398.

Decker, M. *et al.* (2011) ‘Limiting amounts of centrosome material set centrosome size in C. elegans embryos’, *Current Biology* [Preprint]. Available at: https://doi.org/10.1016/j.cub.2011.06.002.

D’Imprima, E. *et al.* (2019) ‘Protein denaturation at the air-water interface and how to prevent it’, *eLife*, 8, p. e42747. Available at: https://doi.org/10.7554/eLife.42747.

D'Imprima, E. *et al.* (2023) 'Light and electron microscopy continuum-resolution imaging of 3D cell cultures', *Developmental cell*, 58(7), pp. 616-632.e6. Available at: https://doi.org/10.1016/j.devcel.2023.03.001.

Dubochet, J. *et al.* (1982) 'Electron microscopy of frozen water and aqueous solutions', *Journal of Microscopy*, 128(3), pp. 219–237.

Dubochet, J. *et al.* (1987) 'Cryoelectron Microscopy of Vitrified Specimens', in *Cryotechniques in Biological Electron Microscopy*. Available at: https://doi.org/10.1007/978-3-642-72815-0_5.

Dubochet, J. *et al.* (1988) 'Cryo-electron microscopy of vitrified specimens', *Quarterly reviews of biophysics*, 21(2), pp. 129–228.

Dubochet, J. (1995) 'High-pressure freezing for cryoelectron microscopy', *Trends in Cell Biology*, 5(9), pp. 366–368. Available at: https://doi.org/10.1016/S0962-8924(00)89071-6.

Dubochet, J. and McDowall, A.W. (1981) 'Vitrification of pure water for electron microscopy', *Journal of Microscopy*, 124(3), pp. 3–4. Available at: https://doi.org/10.1111/j.1365-2818.1981.tb02483.x.

Dutcher, S.K. *et al.* (2002) 'ε-Tubulin is an essential component of the centriole', *Molecular biology of the cell*, 13(11), pp. 3859–3869.

Dutcher, S.K. (2003) 'Long-lost relatives reappear: identification of new members of the tubulin superfamily', *Current Opinion in Microbiology*, 6(6), pp. 634–640. Available at: https://doi.org/10.1016/j.mib.2003.10.016.

Dutcher, S.K. and Trabuco, E.C. (1998) 'The UNI3 Gene Is Required for Assembly of Basal Bodies of Chlamydomonas and Encodes δ-Tubulin, a New Member of the Tubulin Superfamily', *Molecular Biology of the Cell*, 9(6), pp. 1293–1308. Available at: https://doi.org/10.1091/mbc.9.6.1293.

Egerton, R.F. (2009) ‘Electron energy-loss spectroscopy in the TEM’, *Reports on Progress in Physics*, 72(1), p. 16502. Available at: https://doi.org/10.1088/0034-4885/72/1/016502.

Elbaum, M., Wolf, S.G. and Houben, L. (2016) ‘Cryo-scanning transmission electron tomography of biological cells’, *MRS Bulletin*, 41(07), pp. 542–548. Available at: https://doi.org/10.1557/mrs.2016.136.

Ellis, R.J. and Minton, A.P. (2003) ‘Join the crowd’, *Nature*, 425(6953), pp. 27–28. Available at: https://doi.org/10.1038/425027a.

Engel, B.D. *et al.* (2015) ‘Native architecture of the Chlamydomonas chloroplast revealed by in situ cryo-electron tomography’, *eLife*. Edited by J. Chory, 4, p. e04889. Available at: https://doi.org/10.7554/eLife.04889.

Enos, S.J. *et al.* (2018) ‘Phosphatase PP2A and microtubule-mediated pulling forces disassemble centrosomes during mitotic exit’, *Biology Open*, 7(1). Available at: https://doi.org/10.1242/bio.029777.

Erpf, A.C. *et al.* (2019) ‘PCMD-1 Organizes Centrosome Matrix Assembly in C. elegans’, *Current Biology*, 29(8). Available at: https://doi.org/10.1016/j.cub.2019.03.029.

Evans, R. *et al.* (2022) ‘Protein complex prediction with AlphaFold-Multimer’, *bioRxiv*, p. 2021.10.04.463034. Available at: https://doi.org/10.1101/2021.10.04.463034.

Faoro, R. *et al.* (2018) ‘Aberration-corrected cryoimmersion light microscopy’, *Proceedings of the National Academy of Sciences*, 115(6), pp. 1204–1209. Available at: https://doi.org/10.1073/pnas.1717282115.

Fawcett, D.W. and Porter, K.R. (1954) ‘A study of the fine structure of ciliated epithelia’, *Journal of Morphology*, 94(2), pp. 221–281.

Feng, Z. *et al.* (2017) ‘Structural Basis for Mitotic Centrosome Assembly in Flies’, *Cell*, 169(6), pp. 1078-1089.e13. Available at: https://doi.org/10.1016/j.cell.2017.05.030.

Firat-Karalar, E.N. and Stearns, T. (2014) ‘The centriole duplication cycle’, *Philosophical Transactions of the Royal Society B: Biological Sciences*, 369(1650). Available at: https://doi.org/10.1098/rstb.2013.0460.

Fong, K.-W. *et al.* (2007) ‘CDK5RAP2 Is a Pericentriolar Protein That Functions in Centrosomal Attachment of the γ-Tubulin Ring Complex’, *Molecular Biology of the Cell*, 19(1), pp. 115–125. Available at: https://doi.org/10.1091/mbc.e07-04-0371.

Fu, J. and Glover, D.M. (2012) ‘Structured illumination of the interface between centriole and peri-centriolar material’, *Open Biology*, 2(AUG). Available at: https://doi.org/10.1098/rsob.120104.

Fukuda, Y. *et al.* (2015) ‘Electron cryotomography of vitrified cells with a Volta phase plate’, *Journal of Structural Biology*, 190(2), pp. 143–154. Available at: https://doi.org/10.1016/j.jsb.2015.03.004.

Fulton, A.B. (1982) ‘How crowded is the cytoplasm?’, *Cell*, 30(2), pp. 345–347. Available at: https://doi.org/10.1016/0092-8674(82)90231-8.

Fung, H.K.H. *et al.* (2022) ‘Genetically encoded multimeric tags for intracellular protein localisation in cryo-EM’, *bioRxiv*, p. 2022.12.10.519870. Available at: https://doi.org/10.1101/2022.12.10.519870.

Fygenson, D.K., Braun, E. and Libchaber, A. (1994) ‘Phase diagram of microtubules’, *Physical Review E*, 50(2), pp. 1579–1588. Available at: https://doi.org/10.1103/PhysRevE.50.1579.

Galaz-Montoya, J.G. *et al.* (2015) ‘Single particle tomography in EMAN2’, *Journal of Structural Biology*, 190(3), pp. 279–290. Available at: https://doi.org/10.1016/j.jsb.2015.04.016.

Gall, J.G. (2004) ‘Early Studies on Centrioles and Centrosomes’, in *Centrosomes in Development and Disease*, pp. 1–15. Available at: https://doi.org/10.1002/3527603808.ch1.

Gilbert, S.F. (2000) ‘Early Development of the Nematode Caenorhabditis elegans’, *Developmental Biology* [Preprint].

Glaeser, R.M. (2013) ‘Invited Review Article: Methods for imaging weak-phase objects in electron microscopy’, *Review of Scientific Instruments*, 84(11), p. 111101. Available at: https://doi.org/10.1063/1.4830355.

Glaeser, R.M. *et al.* (2016) ‘Factors that Influence the Formation and Stability of Thin, Cryo-EM Specimens’, *Biophysical Journal*, 110(4). Available at: https://doi.org/10.1016/j.bpj.2015.07.050.

Glaeser, R.M. and Taylor, K.A. (1978) ‘Radiation damage relative to transmission electron microscopy of biological specimens at low temperature: a review’, *Journal of Microscopy*, 112(1), pp. 127–138. Available at: https://doi.org/10.1111/j.1365-2818.1978.tb01160.x.

Gopalakrishnan, J. *et al.* (2011) ‘Sas-4 provides a scaffold for cytoplasmic complexes and tethers them in a centrosome’, *Nature Communications*, 2(1). Available at: https://doi.org/10.1038/ncomms1367.

Gorelick, S. *et al.* (2019) ‘PIE-scope, integrated cryo-correlative light and FIB/SEM microscopy’, *eLife*. Edited by S. Subramaniam, J. Kuriyan, and J.M. Plitzko, 8, p. e45919. Available at: https://doi.org/10.7554/eLife.45919.

Gould, R.R. and Borisy, G.G. (1977) ‘The pericentriolar material in Chinese hamster ovary cells nucleates microtubule formation’, *Journal of Cell Biology*, 73(3), pp. 601–615. Available at: https://doi.org/10.1083/jcb.73.3.601.

Graham, L. and Orenstein, J.M. (2007) ‘Processing tissue and cells for transmission electron microscopy in diagnostic pathology and research’, *Nature Protocols*, 2(10), pp. 2439–2450. Available at: https://doi.org/10.1038/nprot.2007.304.

Graser, S., Stierhof, Y.-D. and Nigg, E.A. (2007) ‘Cep68 and Cep215 (Cdk5rap2) are required for centrosome cohesion’, *Journal of Cell Science*, 120(24), pp. 4321–4331. Available at: https://doi.org/10.1242/jcs.020248.

Greenan, G.A. *et al.* (2018) ‘Insights into centriole geometry revealed by cryotomography of doublet and triplet centrioles’, *eLife*, 7, p. e36851. Available at: https://doi.org/10.7554/eLife.36851.

Grigoriev, I. *et al.* (2008) ‘STIM1 Is a MT-Plus-End-Tracking Protein Involved in Remodeling of the ER’, *Current Biology*, 18(3), pp. 177–182. Available at: https://doi.org/10.1016/j.cub.2007.12.050.

Guichard, P. *et al.* (2013) ‘Native architecture of the centriole proximal region reveals features underlying its 9-fold radial symmetry’, *Current Biology* [Preprint]. Available at: https://doi.org/10.1016/j.cub.2013.06.061.

Guillén-Boixet, J. *et al.* (2020) ‘RNA-Induced Conformational Switching and Clustering of G3BP Drive Stress Granule Assembly by Condensation’, *Cell*, 181(2), pp. 346–361. Available at: https://doi.org/10.1016/j.cell.2020.03.049.

Hagen, W.J.H., Wan, W. and Briggs, J.A.G. (2017) ‘Implementation of a cryo-electron tomography tilt-scheme optimized for high resolution subtomogram averaging’, *Journal of Structural Biology*, 197(2), pp. 191–198. Available at: https://doi.org/10.1016/j.jsb.2016.06.007.

Hamill, D.R. *et al.* (2002) ‘Centrosome maturation and mitotic spindle assembly in C. elegans require SPD-5, a protein with multiple coiled-coil domains’, *Developmental Cell* [Preprint]. Available at: https://doi.org/10.1016/S1534-5807(02)00327-1.

Han, K.F., Sedat, J.W. and Agard, D.A. (1995) ‘Mechanism of image formation for thick biological specimens: exit wavefront reconstruction and electron energy-loss spectroscopic imaging’, *Journal of microscopy*, 178(2), pp. 107–119.

Haren, L., Stearns, T. and Lüders, J. (2009) ‘Plk1-Dependent Recruitment of γ-Tubulin Complexes to Mitotic Centrosomes Involves Multiple PCM Components’, *PLOS ONE*, 4(6), p. e5976.

Hashizume, C. *et al.* (2013) ‘Nucleoporin Nup62 maintains centrosome homeostasis’, *Cell Cycle* [Preprint]. Available at: https://doi.org/10.4161/cc.26671.

Hatzopoulos, G.N. *et al.* (2021) ‘Tuning SAS-6 architecture with monobodies impairs distinct steps of centriole assembly’, *Nature Communications*, 12(1). Available at: https://doi.org/10.1038/s41467-021-23897-0.

Henderson, R. (1995) ‘The potential and limitations of neutrons, electrons and X-rays for atomic resolution microscopy of unstained biological molecules’, *Quarterly Reviews of Biophysics*, 28(2), pp. 171–193. Available at: https://doi.org/DOI: 10.1017/S003358350000305X.

Hilbert, M. *et al.* (2013) ‘Caenorhabditis elegans centriolar protein SAS-6 forms a spiral that is consistent with imparting a ninefold symmetry’, *Proceedings of the National Academy of Sciences*, 110(28), pp. 11373–11378. Available at: https://doi.org/10.1073/pnas.1302721110.

Himes, B.A. and Zhang, P. (2018) ‘emClarity: software for high-resolution cryo-electron tomography and subtomogram averaging’, *Nature Methods*, 15(11), pp. 955–961. Available at: https://doi.org/10.1038/s41592-018-0167-z.

Holehouse, A.S. and Pappu, R.V. (2018) ‘Functional Implications of Intracellular Phase Transitions’, *Biochemistry* [Preprint]. Available at: https://doi.org/10.1021/acs.biochem.7b01136.

Hrabe, T. *et al.* (2012) 'PyTom: A python-based toolbox for localization of macromolecules in cryo-electron tomograms and subtomogram analysis', *Journal of Structural Biology*, 178(2), pp. 177–188. Available at: https://doi.org/10.1016/j.jsb.2011.12.003.

Huch, M. and Koo, B.-K. (2015) 'Modeling mouse and human development using organoid cultures', *Development*, 142(18), pp. 3113–3125.

Hurlock, M.E. *et al.* (2020) 'Identification of novel synaptonemal complex components in C. elegans.', *The Journal of cell biology*, 219(5), p. e201910043. Available at: https://doi.org/10.1083/jcb.201910043.

Ishihara, K. *et al.* (2014) 'Microtubule nucleation remote from centrosomes may explain how asters span large cells', *Proceedings of the National Academy of Sciences*, 111(50), pp. 17715–17722. Available at: https://doi.org/10.1073/pnas.1418796111.

Jakobsen, L. *et al.* (2011) 'Novel asymmetrically localizing components of human centrosomes identified by complementary proteomics methods', *The EMBO Journal*, 30(8), pp. 1520–1535. Available at: https://doi.org/10.1038/emboj.2011.63.

Jansen, G., Weinkove, D. and Plasterk, R.H.A. (2002) 'The G-protein γ subunit gpc-1 of the nematode C.elegans is involved in taste adaptation', *The EMBO Journal*, 21(5), pp. 986–994. Available at: https://doi.org/10.1093/emboj/21.5.986.

Jumper, J. *et al.* (2021) 'Highly accurate protein structure prediction with AlphaFold', *Nature*, 596(7873), pp. 583–589. Available at: https://doi.org/10.1038/s41586-021-03819-2.

Kellenberger, E. *et al.* (1992) 'Artefacts and morphological changes during chemical fixation', *Journal of microscopy*, 168(2), pp. 181–201.

Kelley, K. *et al.* (2022) 'Waffle Method: A general and flexible approach for improving throughput in FIB-milling', *Nature Communications*, 13(1), p. 1857. Available at: https://doi.org/10.1038/s41467-022-29501-3.

Khan, S.J. *et al.* (2016) 'A rapid, gentle and scalable method for dissociation and fluorescent sorting of imaginal disc cells for mRNA sequencing', *Fly*, 10(2), pp. 73–80. Available at: https://doi.org/10.1080/19336934.2016.1173296.

Khodjakov, A. and Rieder, C.L. (1999) 'The Sudden Recruitment of γ-Tubulin to the Centrosome at the Onset of Mitosis and Its Dynamic Exchange Throughout the Cell Cycle, Do Not Require Microtubules', *Journal of Cell Biology*, 146(3), pp. 585–596. Available at: https://doi.org/10.1083/jcb.146.3.585.

Kim, J., Lee, K. and Rhee, K. (2015) 'PLK1 regulation of PCNT cleavage ensures fidelity of centriole separation during mitotic exit', *Nature communications*, 6(1), p. 10076.

Kimanius, D. *et al.* (2021) 'New tools for automated cryo-EM single-particle analysis in RELION-4.0', *Biochemical Journal*, 478(24), pp. 4169–4185. Available at: https://doi.org/10.1042/BCJ20210708.

Kishimoto, S., Uno, M. and Nishida, E. (2018) 'Molecular mechanisms regulating lifespan and environmental stress responses', *Inflammation and Regeneration*, 38(1), p. 22. Available at: https://doi.org/10.1186/s41232-018-0080-y.

Klein, S. *et al.* (2021) 'Post-correlation on-lamella cryo-CLEM reveals the membrane architecture of lamellar bodies', *Communications Biology*, 4(1), p. 137. Available at: https://doi.org/10.1038/s42003-020-01567-z.

Klena, N. *et al.* (2020) 'Architecture of the centriole cartwheel-containing region revealed by cryo-electron tomography', *The EMBO Journal*, 39(22), p. e106246. Available at: https://doi.org/10.15252/embj.2020106246.

Klena, N. and Pigino, G. (2022) ‘Structural Biology of Cilia and Intraflagellar Transport’, *Annual Review of Cell and Developmental Biology*, 38(1), pp. 103–123. Available at: https://doi.org/10.1146/annurev-cellbio-120219-034238.

Klumpe, S. *et al.* (2021) ‘A modular platform for automated cryo-FIB workflows’, *eLife*. Edited by A.T. Brunger, R.W. Aldrich, and B. Carragher, 10, p. e70506. Available at: https://doi.org/10.7554/eLife.70506.

Kobayashi, T. and Dynlacht, B.D. (2011) ‘Regulating the transition from centriole to basal body’, *Journal of Cell Biology*, 193(3), pp. 435–444. Available at: https://doi.org/10.1083/jcb.201101005.

Kollmannsberger, P. *et al.* (2017) ‘The small world of osteocytes: connectomics of the lacuno-canalicular network in bone’, *New Journal of Physics*, 19(7), p. 73019. Available at: https://doi.org/10.1088/1367-2630/aa764b.

Kops, G.J.P.L. and Gassmann, R. (2020) ‘Crowning the Kinetochore: The Fibrous Corona in Chromosome Segregation’, *Trends in Cell Biology*, 30(8), pp. 653–667. Available at: https://doi.org/10.1016/j.tcb.2020.04.006.

Kremer, J.R., Mastronarde, D.N. and McIntosh, J.R. (1996) ‘Computer visualization of three-dimensional image data using IMOD’, *Journal of Structural Biology*, 116(1), pp. 71–76. Available at: https://doi.org/10.1006/jsbi.1996.0013.

Kuriyama, R. and Borisy, G.G. (1981) ‘Centriole cycle in Chinese hamster ovary cells as determined by whole-mount electron microscopy.’, *Journal of Cell Biology*, 91(3), pp. 814–821. Available at: https://doi.org/10.1083/jcb.91.3.814.

Lam, V. and Villa, E. (2021) ‘Practical approaches for cryo-FIB milling and applications for cellular cryo-electron tomography’, *cryoEM: Methods and Protocols*, pp. 49–82.

Lancaster, M.A. and Knoblich, J.A. (2014) ‘Generation of cerebral organoids from human pluripotent stem cells’, *Nature protocols*, 9(10), pp. 2329–2340.

Langford, R.M. and Clinton, C. (2004) ‘In situ lift-out using a FIB-SEM system’, *Micron*, 35(7), pp. 607–611. Available at: https://doi.org/10.1016/j.micron.2004.03.002.

Laos, T., Cabral, G. and Dammermann, A. (2015) ‘Isotropic incorporation of SPD-5 underlies centrosome assembly in C. elegans’, *Current Biology*, 25(15), pp. R648–R649. Available at: https://doi.org/10.1016/j.cub.2015.05.060.

Lapierre, L.R. and Hansen, M. (2012) ‘Lessons from C. elegans: signaling pathways for longevity’, *Trends in Endocrinology & Metabolism*, 23(12), pp. 637–644. Available at: https://doi.org/10.1016/j.tem.2012.07.007.

Lawo, S. *et al.* (2012) ‘Subdiffraction imaging of centrosomes reveals higher-order organizational features of pericentriolar material’, *Nature Cell Biology*, 14(11), pp. 1148–1158. Available at: https://doi.org/10.1038/ncb2591.

Le Guennec, M. *et al.* (2020) ‘A helical inner scaffold provides a structural basis for centriole cohesion’, *Science Advances* [Preprint]. Available at: https://doi.org/10.1126/sciadv.aaz4137.

Lee, N.K. *et al.* (2018) ‘DeepFinder: An integration of feature-based and deep learning approach for DNA motif discovery’, *Biotechnology & Biotechnological Equipment*, 32(3), pp. 759–768. Available at: https://doi.org/10.1080/13102818.2018.1438209.

Leidel, S. *et al.* (2005) ‘SAS-6 defines a protein family required for centrosome duplication in C. elegans and in human cells’, *Nature Cell Biology*, 7(2), pp. 115–125. Available at: https://doi.org/10.1038/ncb1220.

Li, G. and Moore, J.K. (2020) ‘Microtubule dynamics at low temperature: evidence that tubulin recycling limits assembly’, *Molecular Biology of the Cell*, 31(11), pp. 1154–1166. Available at: https://doi.org/10.1091/mbc.E19-11-0634.

Li, S. (2022) ‘Cryo-electron tomography of enveloped viruses’, *Trends in Biochemical Sciences*, 47(2), pp. 173–186. Available at: https://doi.org/10.1016/j.tibs.2021.08.005.

Li, X. *et al.* (2013) ‘Electron counting and beam-induced motion correction enable near-atomic-resolution single-particle cryo-EM’, *Nature Methods*, 10(6), pp. 584–590. Available at: https://doi.org/10.1038/nmeth.2472.

Liu, P. *et al.* (2020) ‘Insights into the assembly and activation of the microtubule nucleator γ-TuRC’, *Nature*, 578(7795), pp. 467–471. Available at: https://doi.org/10.1038/s41586-019-1896-6.

Liu, S., Pokrovskaya, I.D. and Storrie, B. (2023) ‘High-Pressure Freezing Followed by Freeze Substitution: An Optimal Electron Microscope Technique to Study Golgi Apparatus Organization and Membrane Trafficking BT - Golgi: Methods and Protocols’, in Y. Wang, V.V. Lupashin, and T.R. Graham (eds). New York, NY: Springer US, pp. 211–223. Available at: https://doi.org/10.1007/978-1-0716-2639-9_13.

Lucas, B.A. *et al.* (2021) ‘Locating macromolecular assemblies in cells by 2D template matching with cisTEM’, *eLife*. Edited by E.H. Egelman et al., 10, p. e68946. Available at: https://doi.org/10.7554/eLife.68946.

Lüders, J. and Stearns, T. (2007) ‘Microtubule-organizing centres: a re-evaluation’, *Nature Reviews Molecular Cell Biology*, 8(2), pp. 161–167. Available at: https://doi.org/10.1038/nrm2100.

Mahamid, J. *et al.* (2015) ‘A focused ion beam milling and lift-out approach for site-specific preparation of frozen-hydrated lamellas from multicellular organisms’, *Journal of Structural Biology* [Preprint]. Available at: https://doi.org/10.1016/j.jsb.2015.07.012.

Mahamid, J. *et al.* (2016) 'Visualizing the molecular sociology at the HeLa cell nuclear periphery', *Science* [Preprint]. Available at: https://doi.org/10.1126/science.aad8857.

Maheshwari, R. *et al.* (2023) 'A membrane reticulum, the centriculum, affects centrosome size and function in Caenorhabditis elegans', *Current Biology*, 33(5), pp. 791-806.e7. Available at: https://doi.org/10.1016/j.cub.2022.12.059.

Mandelkow, E. *et al.* (1995) 'On the structure of microtubules, tau, and paired helical filaments', *Neurobiology of Aging*, 16(3), pp. 347–354. Available at: https://doi.org/10.1016/0197-4580(95)00026-B.

Marko, M. *et al.* (2007) 'Focused-ion-beam thinning of frozen-hydrated biological specimens for cryo-electron microscopy', *Nature Methods* [Preprint]. Available at: https://doi.org/10.1038/nmeth1014.

Mastronarde, D.N. (2018) 'Advanced Data Acquisition From Electron Microscopes With SerialEM', *Microscopy and Microanalysis*, 24(S1), pp. 864–865. Available at: https://doi.org/10.1017/s1431927618004816.

Mastronarde, D.N. and Held, S.R. (2017) 'Automated tilt series alignment and tomographic reconstruction in IMOD', *Journal of Structural Biology*, 197(2), pp. 102–113. Available at: https://doi.org/10.1016/j.jsb.2016.07.011.

Matsuo, K. *et al.* (2012) 'Kendrin is a novel substrate for separase involved in the licensing of centriole duplication', *Current biology*, 22(10), pp. 915–921.

Matsuura, K. *et al.* (2004) 'Bld10p, a novel protein essential for basal body assembly in Chlamydomonas : localization to the cartwheel, the first ninefold symmetrical structure appearing during assembly', *Journal of Cell Biology*, 165(5), pp. 663–671. Available at: https://doi.org/10.1083/jcb.200402022.

Matthews, L.R. *et al.* (1998) 'ZYG-9, a Caenorhabditis elegans protein required for microtubule organization and function, is a component of meiotic and mitotic

spindle poles', *Journal of Cell Biology* [Preprint]. Available at: https://doi.org/10.1083/jcb.141.5.1159.

Mazia, D., Harris, P.J. and Bibring, T. (1960) 'The multiplicity of the mitotic centers and the time-course of their duplication and separation', *The Journal of Cell Biology*, 7(1), pp. 1–20.

McGuffin, L.J., Bryson, K. and Jones, D.T. (2000) 'The PSIPRED protein structure prediction server', *Bioinformatics*, 16(4), pp. 404–405. Available at: https://doi.org/10.1093/bioinformatics/16.4.404.

Mennella, V. *et al.* (2012) 'Subdiffraction-resolution fluorescence microscopy reveals a domain of the centrosome critical for pericentriolar material organization', *Nature Cell Biology* [Preprint]. Available at: https://doi.org/10.1038/ncb2597.

Mitchison, T. and Kirschner, M. (1984) 'Dynamic instability of microtubule growth', *Nature* [Preprint]. Available at: https://doi.org/10.1038/312237a0.

Mittasch, M. *et al.* (2018) 'Non-invasive perturbations of intracellular flow reveal physical principles of cell organization', *Nature Cell Biology*, 20(3), pp. 344–351. Available at: https://doi.org/10.1038/s41556-017-0032-9.

Mittasch, M. *et al.* (2020) 'Regulated changes in material properties underlie centrosome disassembly during mitotic exit', *Journal of Cell Biology*, 219(4). Available at: https://doi.org/10.1083/JCB.201912036.

Moens, P.B. and Rapport, E. (1971) 'Synaptic structures in the nuclei of sporulating yeast, Saccharomyces cerevisiae (hansen)', *Journal of Cell Science*, 9(3), pp. 665–677. Available at: https://doi.org/10.1242/jcs.9.3.665.

Monahan, Z. *et al.* (2017) 'Phosphorylation of the FUS low-complexity domain disrupts phase separation, aggregation, and toxicity', *EMBO J.*, 36, p. 2951.

Moor, H. (1987) ‘Theory and practice of high pressure freezing.’, in. Available at: https://api.semanticscholar.org/CorpusID:124588434.

Moritz, Michelle *et al.* (1995) ‘Microtubule nucleation by γ-tubulin-containing rings in the centrosome’, *Nature*, 378(6557), pp. 638–640. Available at: https://doi.org/10.1038/378638a0.

Moritz, M *et al.* (1995) ‘Three-dimensional structural characterization of centrosomes from early Drosophila embryos.’, *The Journal of cell biology*, 130(5), pp. 1149–1159. Available at: https://doi.org/10.1083/jcb.130.5.1149.

Moritz, M. *et al.* (1998) ‘Recruitment of the γ-Tubulin Ring Complex to Drosophila Salt-stripped Centrosome Scaffolds’, *Journal of Cell Biology*, 142(3), pp. 775–786. Available at: https://doi.org/10.1083/jcb.142.3.775.

Moritz, M. *et al.* (2000) ‘Structure of the γ-tubulin ring complex: a template for microtubule nucleation’, *Nature Cell Biology*, 2(6), pp. 365–370. Available at: https://doi.org/10.1038/35014058.

Murk, J. *et al.* (2003) ‘Influence of aldehyde fixation on the morphology of endosomes and lysosomes: quantitative analysis and electron tomography’, *Journal of microscopy*, 212(1), pp. 81–90.

Nakajo, M. *et al.* (2022) ‘Centrosome maturation requires phosphorylation-mediated sequential domain interactions of SPD-5’, *Journal of Cell Science*, 135(8), p. jcs259025. Available at: https://doi.org/10.1242/jcs.259025.

Naydenova, K., Jia, P. and Russo, C.J. (2020) ‘Cryo-EM with sub–1 Å specimen movement’, *Science*, 370(6513), pp. 223–226. Available at: https://doi.org/10.1126/science.abb7927.

Nazarov, S. *et al.* (2020) ‘Novel features of centriole polarity and cartwheel stacking revealed by cryo-tomography’, *The EMBO Journal*, 39(22), p. e106249. Available at: https://doi.org/10.15252/embj.2020106249.

Nechipurenko, I.V. *et al.* (2017) 'Centriolar remodeling underlies basal body maturation during ciliogenesis in Caenorhabditis elegans', *eLife*. Edited by O. Hobert, 6, p. e25686. Available at: https://doi.org/10.7554/eLife.25686.

Nickell, S. *et al.* (2005) 'TOM software toolbox: Acquisition and analysis for electron tomography', *Journal of Structural Biology*, 149(3), pp. 227–234. Available at: https://doi.org/10.1016/j.jsb.2004.10.006.

Nievergelt, A.P. *et al.* (2018) 'High-speed photothermal off-resonance atomic force microscopy reveals assembly routes of centriolar scaffold protein SAS-6', *Nature nanotechnology*, 13(8), pp. 696–701. Available at: https://doi.org/10.1038/s41565-018-0149-4.

Nigg, E.A. and Holland, A.J. (2018) 'Once and only once: mechanisms of centriole duplication and their deregulation in disease', *Nature Reviews Molecular Cell Biology*, 19(5), pp. 297–312. Available at: https://doi.org/10.1038/nrm.2017.127.

Nigg, E.A. and Stearns, T. (2011) 'The centrosome cycle: Centriole biogenesis, duplication and inherent asymmetries', *Nature Cell Biology*, 13(10), pp. 1154–1160. Available at: https://doi.org/10.1038/ncb2345.

Nogales, E. and Wang, H.-W. (2006) 'Structural intermediates in microtubule assembly and disassembly: how and why?', *Current Opinion in Cell Biology*, 18(2), pp. 179–184. Available at: https://doi.org/10.1016/j.ceb.2006.02.009.

Nunez-Iglesias, J. *et al.* (2018) 'A new Python library to analyse skeleton images confirms malaria parasite remodelling of the red blood cell membrane skeleton', *PeerJ*. Edited by M. Ferreira, 6, p. e4312. Available at: https://doi.org/10.7717/peerj.4312.

Ohta, M. *et al.* (2021) 'Polo-like kinase 1 independently controls microtubule-nucleating capacity and size of the centrosome', *Journal of Cell Biology*, 220(2), p. e202009083. Available at: https://doi.org/10.1083/jcb.202009083.

Oosterheert, W. *et al.* (2022) 'Structural basis of actin filament assembly and aging', *Nature*, 611(7935), pp. 374–379. Available at: https://doi.org/10.1038/s41586-022-05241-8.

O'Reilly, F.J. *et al.* (2020) 'In-cell architecture of an actively transcribing-translating expressome', *Science*, 369(6503), pp. 554–557. Available at: https://doi.org/10.1126/science.abb3758.

Orlova, E.V. and Saibil, H.R. (2011) 'Structural Analysis of Macromolecular Assemblies by Electron Microscopy', *Chemical Reviews*, 111(12), pp. 7710–7748. Available at: https://doi.org/10.1021/cr100353t.

O'Rourke, S.M. *et al.* (2011) 'A Survey of New Temperature-Sensitive, Embryonic-Lethal Mutations in C. elegans: 24 Alleles of Thirteen Genes', *PLoS ONE*. Edited by A. Hart, 6(3), p. e16644. Available at: https://doi.org/10.1371/journal.pone.0016644.

O'Toole, E. *et al.* (2012) 'The role of γ-tubulin in centrosomal microtubule organization', *PLoS ONE* [Preprint]. Available at: https://doi.org/10.1371/journal.pone.0029795.

O'Toole, E.T., Winey, M. and McIntosh, J.R. (1999) 'High-Voltage Electron Tomography of Spindle Pole Bodies and Early Mitotic Spindles in the Yeast Saccharomyces cerevisiae', *Molecular Biology of the Cell*, 10(6), pp. 2017–2031. Available at: https://doi.org/10.1091/mbc.10.6.2017.

Özlü, N. *et al.* (2005) 'An Essential Function of the C. elegans Ortholog of TPX2 Is to Localize Activated Aurora A Kinase to Mitotic Spindles', *Developmental Cell*, 9(2), pp. 237–248. Available at: https://doi.org/10.1016/j.devcel.2005.07.002.

Paintrand, M. *et al.* (1992) 'Centrosome organization and centriole architecture: Their sensitivity to divalent cations', *Journal of Structural Biology*, 108(2), pp. 107–128. Available at: https://doi.org/10.1016/1047-8477(92)90011-X.

Palazzo, R.E. *et al.* (1999) ‘Centrosome maturation’, in R.E. Palazzo and G.P.B.T.-C.T. in D.B. Schatten (eds) *The Centrosome in Cell Replication and Early Development*. Academic Press, pp. 449–470. Available at: https://doi.org/10.1016/S0070-2153(99)49021-0.

Passmore, L.A. and Russo, C.J. (2016) ‘Chapter Three - Specimen Preparation for High-Resolution Cryo-EM’, in R.A.B.T.-M. in E. Crowther (ed.) *The Resolution Revolution: Recent Advances In cryoEM*. Academic Press, pp. 51–86. Available at: https://doi.org/10.1016/bs.mie.2016.04.011.

Patel, A. *et al.* (2015) ‘A Liquid-to-Solid Phase Transition of the ALS Protein FUS Accelerated by Disease Mutation’, *Cell*, 162(5), pp. 1066–1077. Available at: https://doi.org/10.1016/j.cell.2015.07.047.

Pelletier, L. *et al.* (2004) ‘The Caenorhabditis elegans centrosomal protein SPD-2 is required for both pericentriolar material recruitment and centriole duplication’, *Current Biology* [Preprint]. Available at: https://doi.org/10.1016/j.cub.2004.04.012.

Pelletier, L. *et al.* (2006) ‘Centriole assembly in Caenorhabditis elegans’, *Nature*, 444(7119). Available at: https://doi.org/10.1038/nature05318.

Penczek, P.A. (2010) ‘Chapter One - Fundamentals of Three-Dimensional Reconstruction from Projections’, in G.J.B.T.-M. in E. Jensen (ed.) *Cryo-EM, Part B: 3-D Reconstruction*. Academic Press, pp. 1–33. Available at: https://doi.org/10.1016/S0076-6879(10)82001-4.

Petry, S. *et al.* (2013) ‘Branching Microtubule Nucleation in Xenopus Egg Extracts Mediated by Augmin and TPX2’, *Cell*, 152(4), pp. 768–777. Available at: https://doi.org/10.1016/j.cell.2012.12.044.

Pettersen, E.F. *et al.* (2004) ‘UCSF Chimera—A visualization system for exploratory research and analysis’, *Journal of Computational Chemistry*, 25(13), pp. 1605–1612. Available at: https://doi.org/10.1002/jcc.20084.

Pettersen, E.F. *et al.* (2021) ‘UCSF ChimeraX: Structure visualization for researchers, educators, and developers’, *Protein Science*, 30(1), pp. 70–82. Available at: https://doi.org/10.1002/pro.3943.

Pfeffer, S. and Mahamid, J. (2018) ‘Unravelling molecular complexity in structural cell biology’, *Current Opinion in Structural Biology*, 52, pp. 111–118. Available at: https://doi.org/10.1016/j.sbi.2018.08.009.

Phillips, M.A. *et al.* (2020) ‘CryoSIM: super-resolution 3D structured illumination cryogenic fluorescence microscopy for correlated ultrastructural imaging’, *Optica*, 7(7), pp. 802–812. Available at: https://doi.org/10.1364/OPTICA.393203.

Pierson, J. *et al.* (2011) ‘Exploring vitreous cryo-section-induced compression at the macromolecular level using electron cryo-tomography; 80S yeast ribosomes appear unaffected’, *Journal of Structural Biology*, 173(2), pp. 345–349. Available at: https://doi.org/10.1016/j.jsb.2010.09.017.

Pigino, G. *et al.* (2009) ‘Electron-tomographic analysis of intraflagellar transport particle trains in situ’, *Journal of Cell Biology*, 187(1), pp. 135–148. Available at: https://doi.org/10.1083/jcb.200905103.

Plitzko, J.M., Rigort, A. and Leis, A. (2009) ‘Correlative cryo-light microscopy and cryo-electron tomography: from cellular territories to molecular landscapes’, *Current Opinion in Biotechnology*, 20(1), pp. 83–89. Available at: https://doi.org/10.1016/j.copbio.2009.03.008.

Porta-de-la-Riva, M. *et al.* (2012) ‘Basic Caenorhabditis elegans methods: Synchronization and observation’, *Journal of Visualized Experiments* [Preprint], (64). Available at: https://doi.org/10.3791/4019.

Pyle, E. and Zanetti, G. (2021) ‘Current data processing strategies for cryo-electron tomography and subtomogram averaging’, *Biochemical Journal*, 478(10), pp. 1827–1845. Available at: https://doi.org/10.1042/BCJ20200715.

Qiao, R. *et al.* (2012) 'SAS-6 coiled-coil structure and interaction with SAS-5 suggest a regulatory mechanism in C. elegans centriole assembly', *EMBO Journal*, 31(22). Available at: https://doi.org/10.1038/emboj.2012.280.

Ranganathan, S. and Shakhnovich, E.I. (2020) 'Dynamic metastable long-living droplets formed by sticker-spacer proteins', *eLife*. Edited by J.D. Faraldo-Gómez et al., 9, p. e56159. Available at: https://doi.org/10.7554/eLife.56159.

Redemann, S. *et al.* (2014) 'The segmentation of microtubules in electron tomograms using Amira', *Mitosis: Methods and Protocols*, pp. 261–278.

Redemann, S. *et al.* (2017) 'C. elegans chromosomes connect to centrosomes by anchoring into the spindle network', *Nature Communications*, 8. Available at: https://doi.org/10.1038/ncomms15288.

Rigort, A. *et al.* (2012) 'Focused ion beam micromachining of eukaryotic cells for cryoelectron tomography', *Proceedings of the National Academy of Sciences of the United States of America* [Preprint]. Available at: https://doi.org/10.1073/pnas.1201333109.

Rios, M.U. *et al.* (2023) 'A central helical hairpin in SPD-5 enables centrosome strength and assembly', *bioRxiv*, p. 2023.05.16.540868. Available at: https://doi.org/10.1101/2023.05.16.540868.

Robinow, C.F. and Marak, J. (1966) 'A fiber apparatus in the nucleus of the yeast cell.', *The Journal of cell biology*, 29(1). Available at: https://doi.org/10.1083/jcb.29.1.129.

Robinson, C.V., Sali, A. and Baumeister, W. (2007) 'The molecular sociology of the cell', *Nature*, 450(7172), pp. 973–982. Available at: https://doi.org/10.1038/nature06523.

Rodriguez, M. *et al.* (2013) ‘Worms under stress: C. elegans stress response and its relevance to complex human disease and aging’, *Trends in Genetics*, 29(6), pp. 367–374. Available at: https://doi.org/10.1016/j.tig.2013.01.010.

Rog, O., Kohler, S. and Dernburg, A.F. (2017) ‘The synaptonemal complex has liquid crystalline properties and spatially regulates meiotic recombination factors’, *eLife*, 6, p. e21455.

Rohou, A. and Grigorieff, N. (2015) ‘CTFFIND4: Fast and accurate defocus estimation from electron micrographs’, *Journal of Structural Biology*, 192(2), pp. 216–221. Available at: https://doi.org/10.1016/j.jsb.2015.08.008.

Rusu, M. *et al.* (2012) ‘Automated tracing of filaments in 3D electron tomography reconstructions using Sculptor and Situs’, *Journal of Structural Biology*, 178(2), pp. 121–128. Available at: https://doi.org/10.1016/j.jsb.2012.03.001.

Sato, T. *et al.* (2009) ‘Single Lgr5 stem cells build crypt-villus structures in vitro without a mesenchymal niche’, *Nature*, 459(7244), pp. 262–265. Available at: https://doi.org/10.1038/nature07935.

Schaffer, M. *et al.* (2017) ‘Optimized cryo-focused ion beam sample preparation aimed at in situ structural studies of membrane proteins’, *Journal of Structural Biology* [Preprint]. Available at: https://doi.org/10.1016/j.jsb.2016.07.010.

Schaffer, M. *et al.* (2019) ‘A cryo-FIB lift-out technique enables molecular-resolution cryo-ET within native Caenorhabditis elegans tissue’, *Nature Methods* [Preprint]. Available at: https://doi.org/10.1038/s41592-019-0497-5.

Scheres, S.H.W. (2010) ‘Classification of Structural Heterogeneity by Maximum-Likelihood Methods’, in *Methods in Enzymology*. Elsevier, pp. 295–320. Available at: https://doi.org/10.1016/S0076-6879(10)82012-9.

Scheres, S.H.W. (2014) ‘Beam-induced motion correction for sub-megadalton cryo-EM particles’, *eLife*. Edited by W. Kühlbrandt, 3, p. e03665. Available at: https://doi.org/10.7554/eLife.03665.

Scheres, S.H.W. and Chen, S. (2012) ‘Prevention of overfitting in cryo-EM structure determination’, *Nature Methods*, 9(9), pp. 853–854. Available at: https://doi.org/10.1038/nmeth.2115.

Schindelin, J. *et al.* (2012) ‘Fiji: an open-source platform for biological-image analysis’, *Nature Methods*, 9(7), pp. 676–682. Available at: https://doi.org/10.1038/nmeth.2019.

Schiøtz, O.H. *et al.* (2023) ‘Serial Lift-Out – Sampling the Molecular Anatomy of Whole Organisms’, *bioRxiv*, p. 2023.04.28.538734. Available at: https://doi.org/10.1101/2023.04.28.538734.

Schnackenberg, B.J. *et al.* (1998) ‘The disassembly and reassembly of functional centrosomes in vitro’, *Proceedings of the National Academy of Sciences*, 95(16), pp. 9295–9300. Available at: https://doi.org/10.1073/pnas.95.16.9295.

Schnackenberg, B.J. and Palazzo, R.E. (1999) ‘Identification and function of the centrosome centromatrix’, *Biology of the Cell*, 91(6), pp. 429–438. Available at: https://doi.org/10.1111/j.1768-322X.1999.tb01098.x.

Schwartz, O. *et al.* (2019) ‘Laser phase plate for transmission electron microscopy’, *Nature Methods*, 16(10), pp. 1016–1020. Available at: https://doi.org/10.1038/s41592-019-0552-2.

Shaw, P.J. (2006) ‘Comparison of Widefield/Deconvolution and Confocal Microscopy for Three-Dimensional Imaging’, in. Available at: https://api.semanticscholar.org/CorpusID:45959689.

Slomkowski, S. *et al.* (2011) ‘Terminology of polymers and polymerization processes in dispersed systems (IUPAC Recommendations 2011)’, *Pure and Applied Chemistry*, 83, pp. 2229–2259.

Sluder, G. and Begg, D.A. (1985) ‘Experimental analysis of the reproduction of spindle poles’, *Journal of Cell Science*, 76(1), pp. 35–51.

Smith, N.S. *et al.* (2006) ‘High brightness inductively coupled plasma source for high current focused ion beam applications’, *Journal of Vacuum Science & Technology B: Microelectronics and Nanometer Structures Processing, Measurement, and Phenomena*, 24(6), pp. 2902–2906.

Sonnen, K.F. *et al.* (2012) ‘3D-structured illumination microscopy provides novel insight into architecture of human centrosomes’, *Biology Open* [Preprint]. Available at: https://doi.org/10.1242/bio.20122337.

Sosa, H. and Chrétien, D. (1998) ‘Relationship between moiré patterns, tubulin shape, and microtubule polarity’, *Cell Motility*, 40(1), pp. 38–43. Available at: https://doi.org/10.1002/(SICI)1097-0169(1998)40:1<38::AID-CM4>3.0.CO;2-B.

Spehner, D. *et al.* (2020) ‘Cryo-FIB-SEM as a promising tool for localizing proteins in 3D’, *Journal of Structural Biology*, 211(1), p. 107528. Available at: https://doi.org/10.1016/j.jsb.2020.107528.

Stalling, D., Westerhoff, M. and Hege, H.C. (2005) ‘Amira: A highly interactive system for visual data analysis’, in *Visualization Handbook*. Available at: https://doi.org/10.1016/B978-012387582-2/50040-X.

Stölken, M. *et al.* (2011) ‘Maximum likelihood based classification of electron tomographic data’, *Journal of Structural Biology*, 173(1), pp. 77–85. Available at: https://doi.org/10.1016/j.jsb.2010.08.005.

Strange, K., Christensen, M. and Morrison, R. (2007) ‘Primary culture of Caenorhabditis elegans developing embryo cells for electrophysiological, cell

biological and molecular studies', *Nature Protocols*, 2(4), pp. 1003–1012. Available at: https://doi.org/10.1038/nprot.2007.143.

Sugioka, K. *et al.* (2017) 'Centriolar SAS-7 acts upstream of SPD-2 to regulate centriole assembly and pericentriolar material formation', *eLife*, 6. Available at: https://doi.org/10.7554/eLife.20353.

Sui, H. and Downing, K.H. (2010) 'Structural basis of interprotofilament interaction and lateral deformation of microtubules', *Structure (London, England : 1993)*, 18(8), pp. 1022–1031. Available at: https://doi.org/10.1016/j.str.2010.05.010.

Tacke, S. *et al.* (2021) 'A streamlined workflow for automated cryo focused ion beam milling', *Journal of Structural Biology*, 213(3), p. 107743. Available at: https://doi.org/10.1016/j.jsb.2021.107743.

Tegunov, D. *et al.* (2021) 'Multi-particle cryo-EM refinement with M visualizes ribosome-antibiotic complex at 3.5 Å in cells', *Nature Methods*, 18(2), pp. 186–193. Available at: https://doi.org/10.1038/s41592-020-01054-7.

Tegunov, D. and Cramer, P. (2019) 'Real-time cryo-electron microscopy data preprocessing with Warp', *Nature Methods*, 16(11), pp. 1146–1152. Available at: https://doi.org/10.1038/s41592-019-0580-y.

de Teresa-Trueba, I. *et al.* (2023) 'Convolutional networks for supervised mining of molecular patterns within cellular context', *Nature Methods*, 20(2), pp. 284–294. Available at: https://doi.org/10.1038/s41592-022-01746-2.

Thompson, R.F. *et al.* (2016) 'An introduction to sample preparation and imaging by cryo-electron microscopy for structural biology', *Methods*, 100, pp. 3–15. Available at: https://doi.org/10.1016/j.ymeth.2016.02.017.

Thorne, R.E. (2020) 'Hypothesis for a mechanism of beam-induced motion in cryo-electron microscopy', *IUCrJ*, 7, pp. 416–421.

Ti, S.-C., Alushin, G.M. and Kapoor, T.M. (2018) ‘Human β-Tubulin Isotypes Can Regulate Microtubule Protofilament Number and Stability’, *Developmental Cell*, 47(2), pp. 175-190.e5. Available at: https://doi.org/10.1016/j.devcel.2018.08.014.

Tilney, L.G. *et al.* (1973) ‘Microtubules: evidence for 13 protofilaments’, *The Journal of cell biology*, 59(2), pp. 267–275.

Timothy, L.M. *et al.* (1999) ‘The Centrosomin protein is required for centrosome assembly and function during cleavage in Drosophila’, *Development*, 126(13), pp. 2829–2839. Available at: https://doi.org/10.1242/dev.126.13.2829.

Tivol, W.F., Briegel, A. and Jensen, G.J. (2008) ‘An improved cryogen for plunge freezing’, *Microscopy and Microanalysis*, 14(5), pp. 375–379. Available at: https://doi.org/10.1017/S1431927608080781.

Tollervey, F. *et al.* (2022) ‘Cryo-electron tomography of reconstituted biomolecular condensates’, in *Phase-Separated Biomolecular Condensates: Methods and Protocols*. Springer, pp. 297–324.

Toro-Nahuelpan, M. *et al.* (2020) ‘Tailoring cryo-electron microscopy grids by photo-micropatterning for in-cell structural studies’, *Nature Methods*, 17(1). Available at: https://doi.org/10.1038/s41592-019-0630-5.

Tsou, M.-F.B. and Stearns, T. (2006) ‘Mechanism limiting centrosome duplication to once per cell cycle’, *Nature*, 442(7105), pp. 947–951. Available at: https://doi.org/10.1038/nature04985.

Tuijtel, M.W. *et al.* (2019) ‘Correlative cryo super-resolution light and electron microscopy on mammalian cells using fluorescent proteins’, *Scientific Reports*, 9(1), p. 1369. Available at: https://doi.org/10.1038/s41598-018-37728-8.

Turoňová, B. *et al.* (2017) ‘Efficient 3D-CTF correction for cryo-electron tomography using NovaCTF improves subtomogram averaging resolution to 3.4Å’, *Journal of*

Structural Biology, 199(3), pp. 187–195. Available at: https://doi.org/10.1016/j.jsb.2017.07.007.

Turoňová, B. *et al.* (2020) 'Benchmarking tomographic acquisition schemes for high-resolution structural biology', *Nature Communications*, 11(1), p. 876. Available at: https://doi.org/10.1038/s41467-020-14535-2.

Van Beneden, E. and Neyt, A. (1887) 'Nouvelles recherches sur la maturation de l'oeuf, la fécondation et la division cellulaire', *Bull. Acad. R. Sci. Belg*, 147, pp. 215–298.

Vieira Braga, F.A. and Miragaia, R.J. (2019) 'Tissue Handling and Dissociation for Single-Cell RNA-Seq', in V. Proserpio (ed.) *Single Cell Methods*. New York, NY: Springer New York (Methods in Molecular Biology), pp. 9–21. Available at: https://doi.org/10.1007/978-1-4939-9240-9_2.

Villa, E. *et al.* (2013) 'Opening windows into the cell: focused-ion-beam milling for cryo-electron tomography', *Current Opinion in Structural Biology*, 23(5), pp. 771–777. Available at: https://doi.org/10.1016/j.sbi.2013.08.006.

Wagner, F.R. *et al.* (2020) 'Preparing samples from whole cells using focused-ion-beam milling for cryo-electron tomography', *Nature protocols*, 15(6), pp. 2041–2070.

Wan, W. *et al.* (2020) 'STOPGAP: A Software Package for Subtomogram Averaging and Refinement', *Microscopy and Microanalysis*, 26(S2), pp. 2516–2516. Available at: https://doi.org/10.1017/S143192762002187X.

Wan, W. and Briggs, J.A.G. (2016a) 'Cryo-Electron Tomography and Subtomogram Averaging', in *Methods in Enzymology*. Available at: https://doi.org/10.1016/bs.mie.2016.04.014.

Wan, W. and Briggs, J.A.G. (2016b) 'Cryo-Electron Tomography and Subtomogram Averaging', in *Methods in Enzymology*.

Wang, C., Wojtynek, M. and Medalia, O. (2023) ‘Structural investigation of eukaryotic cells: From the periphery to the interior by cryo-electron tomography’, *Advances in Biological Regulation*, 87, p. 100923. Available at: https://doi.org/10.1016/j.jbior.2022.100923.

Wang, J.T. *et al.* (2017) ‘Centriole triplet microtubules are required for stable centriole formation and inheritance in human cells’, *eLife*. Edited by A.A. Hyman, 6, p. e29061. Available at: https://doi.org/10.7554/eLife.29061.

Wang, T. *et al.* (2022) ‘Deep Active Learning for Cryo-Electron Tomography Classification’, in *2022 IEEE International Conference on Image Processing (ICIP)*. *2022 IEEE International Conference on Image Processing (ICIP)*, Bordeaux, France: IEEE, pp. 1611–1615. Available at: https://doi.org/10.1109/ICIP46576.2022.9898002.

Weber, M.S., Wojtynek, M. and Medalia, O. (2019) ‘Cellular and Structural Studies of Eukaryotic Cells by Cryo-Electron Tomography’, *Cells*, 8(1). Available at: https://doi.org/10.3390/cells8010057.

Weigert, M. *et al.* (2018) ‘Content-aware image restoration: pushing the limits of fluorescence microscopy’, *Nature Methods*, 15(12), pp. 1090–1097. Available at: https://doi.org/10.1038/s41592-018-0216-7.

Wheeler, J.R. *et al.* (2016) ‘Distinct stages in stress granule assembly and disassembly’, *eLife*, 5, p. e18413. Available at: https://doi.org/10.7554/eLife.18413.

Wieczorek, M. *et al.* (2020) ‘Asymmetric Molecular Architecture of the Human γ-Tubulin Ring Complex’, *Cell*, 180(1), pp. 165-175.e16. Available at: https://doi.org/10.1016/j.cell.2019.12.007.

Wiegleb, G. *et al.* (2022) ‘Tissue dissociation for single-cell and single-nuclei RNA sequencing for low amounts of input material’, *Frontiers in Zoology*, 19(1), p. 27. Available at: https://doi.org/10.1186/s12983-022-00472-x.

Wilson, E.B. (1925) *The cell in development and heredity*. Macmillan.

Wittmann, T., Hyman, A. and Desai, A. (2001) 'The spindle: a dynamic assembly of microtubules and motors', *Nature cell biology*, 3(1), pp. E28–E34.

Woglar, A. *et al.* (2022) 'Molecular architecture of the C. elegans centriole', *PLOS Biology*, 20(9), p. e3001784.

Wolff, G. *et al.* (2019) 'Mind the gap: Micro-expansion joints drastically decrease the bending of FIB-milled cryo-lamellae', *Journal of Structural Biology*, 208(3), p. 107389. Available at: https://doi.org/10.1016/j.jsb.2019.09.006.

Woodruff, J.B. *et al.* (2015) 'Regulated assembly of a supramolecular centrosome scaffold in vitro', *Science*, 348(6236), pp. 808–812. Available at: https://doi.org/10.1126/science.aaa3923.

Woodruff, J.B. *et al.* (2017) 'The Centrosome Is a Selective Condensate that Nucleates Microtubules by Concentrating Tubulin', *Cell*, 169(6), pp. 1066–1077. Available at: https://doi.org/10.1016/j.cell.2017.05.028.

Wu, X. *et al.* (2019) 'Template-based and template-free approaches in cellular cryo-electron tomography structural pattern mining'.

Wueseke, O. *et al.* (2014) 'The Caenorhabditis elegans pericentriolar material components SPD-2 and SPD-5 are monomeric in the cytoplasm before incorporation into the PCM matrix', *Molecular Biology of the Cell*, 25(19), pp. 2984–2992. Available at: https://doi.org/10.1091/mbc.e13-09-0514.

Wueseke, O. *et al.* (2016) 'Polo-like kinase phosphorylation determines Caenorhabditis elegans centrosome size and density by biasing SPD-5 toward an assembly-competent conformation', *Biology Open* [Preprint]. Available at: https://doi.org/10.1242/bio.020990.

Würtz, M. *et al.* (2022) ‘Modular assembly of the principal microtubule nucleator γ-TuRC’, *Nature Communications*, 13(1), p. 473. Available at: https://doi.org/10.1038/s41467-022-28079-0.

Zachs, T. *et al.* (2020) ‘Fully automated, sequential focused ion beam milling for cryo-electron tomography’, *eLife*. Edited by A.P. Carter and J. Kuriyan, 9, p. e52286. Available at: https://doi.org/10.7554/eLife.52286.

Zamora, I. and Marshall, W.F. (2005) ‘A mutation in the centriole-associated protein centrin causes genomic instability via increased chromosome loss in Chlamydomonas reinhardtii’, *BMC Biology*, 3(1), p. 15. Available at: https://doi.org/10.1186/1741-7007-3-15.

Zhang, K. (2016) ‘Gctf: Real-time CTF determination and correction’, *Journal of Structural Biology*, 193(1), pp. 1–12. Available at: https://doi.org/10.1016/j.jsb.2015.11.003.

Zhang, S. *et al.* (2020) ‘Caenorhabditis elegans as a useful model for studying aging mutations’, *Frontiers in endocrinology*, 11, p. 554994.

Zheng, S. *et al.* (2022) ‘AreTomo: An integrated software package for automated marker-free, motion-corrected cryo-electron tomographic alignment and reconstruction’, *Journal of Structural Biology: X*, 6, p. 100068. Available at: https://doi.org/10.1016/j.yjsbx.2022.100068.

Zheng, S.Q. *et al.* (2017) ‘MotionCor2: anisotropic correction of beam-induced motion for improved cryo-electron microscopy’, *Nature Methods*, 14(4), pp. 331–332. Available at: https://doi.org/10.1038/nmeth.4193.

Zheng, Y. *et al.* (1995) ‘Nucleation of microtubule assembly by a γ-tubulin-containing ring complex’, *Nature*, 378(6557), pp. 578–583. Available at: https://doi.org/10.1038/378578a0.

Zheng, Z. *et al.* (2018) ‘A Complete Electron Microscopy Volume of the Brain of Adult Drosophila melanogaster’, *Cell*, 174(3), pp. 730-743.e22. Available at: https://doi.org/10.1016/j.cell.2018.06.019.

Zwicker, D. *et al.* (2014) ‘Centrosomes are autocatalytic droplets of pericentriolar material organized by centrioles’, *Proceedings of the National Academy of Sciences*, 111(26), pp. E2636–E2645. Available at: https://doi.org/10.1073/pnas.1404855111.

Zwicker, D., Hyman, A.A. and Julicher, F. (2015) ‘Suppression of Ostwald ripening in active emulsions’, *Phys. Rev. E*, 92, p. 12317.